

**KU LEUVEN**

**ULB** UNIVERSITÉ  
LIBRE  
DE BRUXELLES

**KU LEUVEN  
ARENBERG DOCTORAL SCHOOL**  
Faculty of Engineering Science

**UNIVERSITE LIBRE  
DE BRUXELLES**  
Faculty of Engineering

# Vibro-acoustics of rotating electric machines

## Prediction, validation and solution

**Fabien Chauvicourt**

Supervisors:

Prof. dr. ir. W. Desmet

Prof. dr. ir. J.C. Gyselinck

Dissertation presented in partial fulfillment of the requirements for the degree of:

- Doctor of Engineering Science (PhD): Mechanical Engineering (KU Leuven)
- Docteur en Science de l'ingénieur et technologie (Université Libre de Bruxelles)

June 2018



# **Vibro-acoustics of rotating electric machines**

Prediction, validation and solution

**Fabien CHAUVICOURT**

Examination committee:

Prof. dr. A. Bultheel, chair at preliminary defence

Prof. dr. ir. A. Deraemaeker (ULB), chair at public defence and assessor

Prof. dr. ir. W. Desmet, supervisor

Prof. dr. ir. J.C. Gyselinck, supervisor

Dr. ir. C.T. Faria (Siemens Industry Software NV), assessor

Prof. dr. ir. K. Gryllias (KUL), assessor

Dr. ir. E. Deckers (KUL)

Prof. dr. ir. D. Pissoort (KUL)

Prof. dr. ir. M. Boltežar (University of Ljubljana)

Dissertation presented in partial fulfillment of the requirements for the degree of:

- Doctor of Engineering Science (PhD): Mechanical Engineering (KU Leuven)
- Docteur en Science de l'ingénieur et technologie (Université Libre de Bruxelles)

June 2018

© 2018 KU Leuven – Faculty of Engineering Science  
Uitgegeven in eigen beheer, Fabien Chauvicourt, Celestijnenlaan 300 box 2402, B-3001 Leuven (Belgium)

Alle rechten voorbehouden. Niets uit deze uitgave mag worden vermenigvuldigd en/of openbaar gemaakt worden door middel van druk, fotokopie, microfilm, elektronisch of op welke andere wijze ook zonder voorafgaande schriftelijke toestemming van de uitgever.

All rights reserved. No part of the publication may be reproduced in any form by print, photoprint, microfilm, electronic or any other means without written permission from the publisher.

# Acknowledgments

Before starting my PhD, I was told: "Your PhD is your baby". And hereby I would like to thank each and everyone of you who participated in accompanying this great adventure for this baby to grow and become adult.

First thanks go to my promotors Prof. Johan Gyselinck and Prof. Wim Desmet. The multi-physical problematics involved in my 4 year work required both your full participation. Johan, beside the leveraging to electric machine theory that you gave me, you taught me how important rigorousness is. Wim, despite your business, you always gave me appropriate feedback and if necessary quickly orientated me to the right person to ask for more details on particular issues. I would also like to extend my gratitude to every member of my examination committee for taking the time to provide relevant feedback after having thoroughly been through the dissertation. Having those three components at the table allowed me to present my work as it is now.

I wanted to personally thank who I consider my mentor during this period Cassio: Muito Obrigado. There is much to say but I will be concise. You always valued my work, and motivated me to go beyond the limits. More importantly now it is my turn to value your tremendous availability that allowed me to efficiently tackle every day problems, your high capacity of quickly understanding any problematics and your get-to-the-point strategy even on topics you do not master. It has been (is) a pleasure working with you and I am looking forward for our near & far future collaborations.

Next to that, there is a fundamental aspect to mention: the working environment. I am very thankful to the entire Engineering Services (ES) department who provided me great technical support and friendly environment. Amongst the many people of the division, I would like to thank Stefano for his fruitful assistance to my questions and the technicians (Nico, Henri and Gunther) for their constant availability. Not to mention the RTD group from whom I earned the most from great socialization and integration through lunch breaks and

from lovely social events. It is hardly possible to list every person I met in this team given the huge student turnover, yet I am giving it a try. Thanks to: Gustavo for your infinite politeness, Fabio for your sarcastic jokes, Xueji for the laughs we shared, ZhongZhe for your availability, Giorgio for your love about pineapple, Caoimhe for selling me Galway as mighty crack, Lisa for true friendship, etc... (sorry I cannot pursue, I am told to submit the dissertation).

I am also very thankful to the people I met in both universities. First from the PMA team of KUL, mainly interacted through the MHF meetings, where many interesting and valued works are presented on a monthly basis. Second from part of the BEAMS team of ULB, where I had the chance to spend a few weeks running various experiments along with great colleagues: Julien and Yves.

I always say that "teaching is learning". Beside all the students that I stood alongside and contributed actively in my every day life, I would like to particularly emphasize my gratitude to two students I supervised from whom I learned a lot by teaching, and without whom this dissertation would not be here now. Egi Nazeraaj, you were my first student and we can both agree that our cooperation was rewarding on both sides. Your curiosity and devotion upon engineering fit mine and encourage our (professional and personal) friendship. Anna Bartalotta, not only I but the entire RTD team enjoyed working with you. I taught you how to learn, you taught me how to teach.

Where would this thesis be without financial support? Quite nowhere I suppose. Therefore I would like to acknowledge the financial support of the European Commission via the Marie Curie ITN project called ADvanced Electric Powertrain Technology (ADEPT), grant number 607361. The networking and training capabilities brought by the project were immense and still grow nowadays. Special thanks to the fellows: Pietro, Sabrina, Kesavan, Stjepan, Andrii, Arkadiusz, Georgios, Mitrofan, Nenad, Simon, Wei, Anton and Korawich; I am proud to being part of this great multi-cultural and multi-competence team.

In Leuven I also met so many great people that it would be close-to-impossible to list every single one. From the numerous Italians at the coffee corner (Emilio, Simone, Simona, Alessandro, Umberto, Claudio, Luca,...) to the French team (Valène, Jonathan, Alice, Karim, Adrien) who participated in after work discussions.

Enfin le plus important pour moi: ma famille. Je ne le montre pas clairement, je l'avoue, mais vous êtes ma force. Ce doctorat a été ponctué de beaucoup d'étapes difficiles qui racontent notre histoire familiale. J'ai une pensée très émue pour Mamie qui nous a quittés soudainement, et à Papi qui reste tout de même fort. A Papé et Grand-Mère et mes cousins que je ne vois que trop

rarement. A Maman qui trouve sûrement que je ne la contacte pas assez, je m'en excuse. A Papa qui est par chance proche en Belgique. A mon frère Denis, qui vit sa vie à fond, comme à son habitude. Mais je voudrais particulièrement saluer mon frère Rémi qui nous a, à tous, donné une leçon de VIE; je pense souvent à toi, et je suis très fier d'être ton frère.

Une autre partie de moi concerne Arthur et sa famille, et cela, depuis 16 ANS quoi! Vous m'avez très tôt considéré comme un fils adoptif, et j'en ai fait de même: vous êtes ma famille adoptive. Arthur, je me souviendrai toujours du moment où je t'ai demandé de jouer au basket avec moi, toi même tu sais. Que toutes ces petites choses continuent.

Et non, je ne t'ai pas oubliée: ma YonYon. Tu connais déjà mon histoire que tu partages avec moi depuis maintenant quelques années (je ne vais pas compter, ça nous rend vieux). Tu m'as accompagné dans les moments difficiles, mais aussi dans les meilleurs. J'espère être à la hauteur pour rendre la pareille. Que notre petite vie pleine de voyages se poursuive tranquillement, merci d'être là.

Finally I am ending this part by a quote that reflects my engineering and life approach towards problem solving, hoping to inspire anyone of you.

*"Nothing in life is to be feared, it is only to be understood. Now is the time to understand more, so that we may fear less". - Marie Curie*





# Abstract

The increase of greenhouse gas emission is commonly accepted to largely contribute to global warming, in part due to the massive use of non-renewable fossil energy sources. It is a reason why recently, beside other industrial sectors, electric mobility has been considered as the next generation for transportation systems. But the electrification of a vehicle introduces new challenges in its design since it involves different domains of expertise than the ones from Internal Combustion Engine (ICE) vehicles. In particular, Noise, Vibration and Harshness (NVH) comfort is significantly affected by powertrain changes, *i.e.* from ICE to electric machine. High levels of unpleasant acoustic noise from resonances may occur but can be addressed numerically to support decision making processes early enough in the design stages. The accurate prediction of its radiated acoustic noise then requires a thorough multi-physical understanding, from the system-level (electric machine) to the component-level (stator and rotor cores).

First from a system-level point of view, two multi-physical modeling frameworks that use different model simplifications were implemented. By comparing simulated results to experimental measurements at each physical step of the modeling flow (electromagnetic, vibration, acoustic), it was shown that both models are accurate enough for pre-designing phases. It was also shown that considering only the stator core to contribute to the vibro-acoustic behavior of electric machines is a valid assumption.

Second from a component-level point of view, the rotor and the stator core were investigated. The rotor influence on the complete machine structural dynamics was assessed. Beside the validated effects of different rotor topologies on the radiated noise, an analytical model was successfully developed to explain the occurrence of a particular vibration mode; whose explanation was still not offered in literature. In parallel, the stator core was studied, essentially because it is composed of hundreds of thin laminations stacked together which introduce difficulties in understanding its structural behavior. The effects of

the laminations on the structural behavior of the stator core were studied numerically and experimentally as well. Two modeling guidelines were thus provided depending on the mode shape of interest and the computational resources available. The experimental studies consolidated these two modeling approaches, and also permitted to highlight the importance of looking at the damping properties. Therefore it was shown that different lamination stacking techniques could affect significantly this damping.

Finally the influence of the stacking technique (gluing, welding) on the structural behavior of the laminated compound motivated the implementation of an alternative solution to the mitigation of resonance phenomenon responsible for high level of acoustic noise. By using a skewed distribution of welding or glue lines, the technique aims at forcing laminations to vibrate with different phases which generates friction between them. The induced damping increases and then depends on the introduced asymmetry and on the mode shape considered. This innovative technique was validated experimentally and showed up to 7 times higher structural damping and 10 dB reduction in structural transfer function amplitudes.

# Beknopte samenvatting

De toename van de uitstoot van broeikasgassen wordt algemeen aanvaard als een belangrijke bijdrage aan de opwarming van de aarde, ten dele door het massale gebruik van niet-hernieuwbare fossiele energiebronnen. Dit is een reden waarom onlangs, naast andere industriële sectoren, elektrische mobiliteit wordt beschouwd als de volgende generatie voor transportsystemen. Maar de elektrificatie van een voertuig introduceert nieuwe uitdagingen in zijn ontwerp omdat het andere domeinen van expertise omvat dan die van interne verbrandingsmotor ICE voertuigen. Met name het comfort van geluid en trillingen (NVH) wordt aanzienlijk beïnvloed door veranderingen in de aandrijflijn, van ICE naar elektrische machine. Hoge niveau van onaangename akoestische ruis van resonanties kan optreden, maar kan numeriek worden aangepakt om besluitvormingsprocessen vroeg genoeg in de ontwerpstadia te ondersteunen. De nauwkeurige voorspelling van zijn afgestraalde akoestische ruis vereist dan een grondig multi-fysisch begrip, van het systeemniveau (elektrische machine) tot het componentniveau (stator- en rotorkernen).

Ten eerste werden vanuit systeemniveau twee multi-fysische modelleringskaders met verschillende modelvereenvoudigingen geïmplementeerd. Door gesimuleerde resultaten te vergelijken met experimentele metingen bij elke fysieke stap van de modelleringsstroom (elektromagnetisch, trillingen, akoestisch), werd aangetoond dat beide modellen nauwkeurig genoeg zijn voor de voorontwerp fases. Er werd ook aangetoond dat alleen de stator kern in overweging nemen als bijdrage aan het vibro-akoestische gedrag van elektrische machines, een geldige aanname is.

Ten tweede werden de rotor en de stator kern onderzocht vanuit een component-niveau oogpunt. De invloed van de rotor op de volledige structurele dynamica van de machine werd beoordeeld. Naast de gevalideerde effecten van verschillende rotortopologieën op de uitgestraalde ruis, is met succes een analytisch model ontwikkeld om het optreden van een bepaalde trillingsvorm te verklaren waarvoor in literatuur nog steeds geen verklaring werd gegeven. Parallel daaraan werd de stator kern bestudeerd, voornamelijk omdat deze

is samengesteld uit honderden dunne gestapelde lamellen die moeilijkheden veroorzaken bij het begrijpen van het structurele gedrag ervan. De effecten van de lamineringen op het structurele gedrag van de statorkern werden numeriek en ook experimenteel bestudeerd. Er werden dus twee modelleerrichtlijnen voorzien, afhankelijk van welke trillingsvorm van belang is en de beschikbare rekenhulpmiddelen. De experimentele studies consolideerden deze twee modelbenaderingen en lieten ook het belang van het in rekening nemen van de dempingseigenschappen naar voren komen. Daarom werd aangetoond dat verschillende lamineringsstapelingsstechnieken deze demping aanzienlijk zouden kunnen beïnvloeden.

Tenslotte motiveerde de invloed van de stapeltechniek (lijmen, lassen) op het structurele gedrag van de gelamineerde verbinding de implementatie van een alternatieve oplossing voor het mitigeren van resonantieverschijnselen die verantwoordelijk zijn voor een hoog niveau akoestische ruis. Door een scheve verdeling van las- of lijmlijnen te gebruiken, is de methode erop gericht frictie tussen de lamellen te genereren door ze te laten trillen met verschillende fasen. De geïnduceerde demping neemt toe en hangt af van de geïntroduceerde asymmetrie en van de beschouwde trillingsvorm. Deze innovatieve techniek werd de techniek experimenteel gevalideerd en tot 7 keer hogere structurele demping en 10 dB reductie in de amplitude van de structurele overdrachtsfunctie getoond.

# Résumé

Le réchauffement climatique est largement influencé par l'augmentation des émissions de gaz à effets de serre, en partie à cause de l'utilisation massive de sources d'énergie fossiles non renouvelables. C'est la raison pour laquelle récemment, la mobilité électrique prend graduellement de l'importance et est de plus en plus considérée comme la suite logique pour des systèmes de transportation plus écologiques. Cependant, de nouveaux défis émergent de cette électrification de nos véhicules. Leur conception implique des domaines de compétences différents de ceux précédemment requis, tel que ceux utilisés dans les véhicules à moteur à combustion interne. Le confort, généralement lié à la notion de Noise, Vibration and Harshness (NVH), est particulièrement affecté par les changements associés à la chaîne de traction. Des problèmes de niveaux de bruit acoustique élevés associés à un son désagréable provenant de phénomènes de résonances peuvent se produire. Ils peuvent toutefois être étudiés numériquement en amont afin de renforcer les prises de décision suffisamment tôt dans les étapes de conception. Une prédiction précise du bruit acoustique rayonné nécessite alors une compréhension multi-physique complète, tant au niveau du système (machine électrique) qu'au niveau des composants (noyaux du stator et du rotor).

Tout d'abord d'un point de vue du système, deux cadres de modélisation multi-physiques utilisant différentes simplifications de modèles ont été mis en œuvre. En comparant les résultats simulés à des mesures expérimentales à chaque étape physique du procédé de modélisation (électromagnétique, vibratoire, acoustique), il a été montré que les deux modèles étaient suffisamment précis pour les phases de pré-conception. Il a également été montré qu'il était suffisant de considérer simplement le noyau du stator dans la caractérisation du comportement vibro-acoustique des machines électriques.

Ensuite, du point de vue des composants, le rotor et le noyau du stator ont été étudiés. L'influence du rotor sur le comportement mécanique de la machine a été évaluée. Outre les effets validés de différentes topologies de rotor sur

le bruit rayonné, un modèle analytique a été développé avec succès dans le but d'expliquer l'apparition d'un mode de vibration particulier; dont l'état de l'art n'expliquait pas minutieusement l'apparition jusqu'à maintenant. En parallèle, le noyau du stator a été étudié, notamment en raison du fait qu'il est composé de plusieurs centaines de lamelles empilées et attachées qui rendent la compréhension la compréhension de son comportement vibratoire difficile. Les effets de ces lamelles sur le comportement structurel du noyau du stator ont alors été investigués numériquement et expérimentalement. Deux suggestions de modélisation ont été fournies en fonction de la déformée modale d'intérêt mais aussi des ressources de calcul disponibles. Les études expérimentales ont confortés ces deux approches, et ont aussi permis de souligner l'importance de l'amortissement sur le comportement vibratoire du stator. Ainsi il a été montré que différentes techniques d'empilement des lamelles pouvait affecté considérablement cet amortissement.

Enfin cette dernière étude sur l'influence de la technique d'empilement (collage, soudure) sur le comportement structurel du stator a motivé l'implémentation d'une solution alternative pour atténuer les phénomènes de résonance responsables du bruit acoustique désagréable. En utilisant une distribution asymétrique des lignes de soudure ou de collage, la technique tend à forcer les lamelles à vibrer en différence de phase ce qui provoque des frottements entre elles. L'amortissement induit se trouve augmenté et dépend alors de l'assymétrie introduite ainsi que de la déformée modale considérée. Cette technique innovante a été validée expérimentalement et a montré un amortissement jusqu'à 7 fois plus élevé et une réduction de 10 dB des amplitudes de la fonction de transfert structurelle.

# List of abbreviations

- 1D, 2D, 3D** One, Two, Three Dimensions
- AC** ..... Alternative Current
- ADEPT** .. ADvanced Electric Powertrain Technology
- ANOVA** .. ANalysis Of VAriances
- ATV** ..... Acoustic Transfer Vector
- BEM** ..... Boundary Elements Method
- CAD** ..... Computer Aided Drawing
- DC** ..... Direct Current
- DOF** ..... Degree-Of-Freedom
- DSP** ..... Digital Signal Processing
- EMA** ..... Experimental Modal Analysis
- EV(s)** ..... Electrical Vehicle(s)
- FE** ..... Finite Element
- FEA(s)** ... Finite Element Analysis(es)
- FFT** ..... Fast Fourier Transform
- FRF(s)** ... Frequency Response Function(s)
- ICE(s)** .... Internal Combustion Engine(s)
- IM(s)** ..... Induction Machine(s)
- MAC** ..... Modal Assurance Criterion

---

<b>MDOF</b>	....	Multiple Degree-Of-Freedom
<b>mmf</b>	.....	MagnetoMotive Force
<b>NV</b>	.....	Noise and Vibration
<b>NVH</b>	.....	Noise, Vibration and Harshness
<b>OASPL</b>	...	OverAll Sound Pressure Level
<b>PM(s)</b>	....	Permanent Magnet(s)
<b>PMSM(s)</b>		Permanent Magnet Synchronous Machine(s)
<b>RoM</b>	.....	Rules of Mixture
<b>RVE</b>	.....	Representative Volume Element
<b>SDOF</b>	.....	Single Degree-Of-Freedom
<b>SPL</b>	.....	Sound Pressure Level
<b>SRM(s)</b>	...	Switched Reluctance Machine(s)
<b>SynRM(s)</b>		Synchronous Reluctance Machine(s)



# List of symbols

## Symbols

$\omega$	Angular frequency (rad/s)
$H_{mag}$	Magnetic field intensity magnitude
$B_r, B_\theta, B_z$	Magnetic flux density in radial, azimuthal and axial direction
$\mu$	Permeability
$\Phi$	Magnetic flux magnitude
$R_e$	Reluctance
$F_{Lorentz}$	Lorentz force
$[\bar{\sigma}_{Maxwell}]$	Maxwell stress tensor
$\sigma_r, \sigma_\theta, \sigma_z$	Stress in radial, azimuthal and axial direction
$x(t), \dot{x}(t), \ddot{x}(t)$	Displacement, Velocity, Acceleration in time domain
$X$	Displacement in frequency/Laplace domain
$[H]$	Transfer function matrix
$H_{OI}(\omega)$	FRF matrix coefficient for input $I$ and output $O$
$[M]$	Mass matrix
$[K]$	Stiffness matrix
$[D]$	Damping matrix
$\omega_k$	Natural frequency of mode $k$ (rad/s)

$f_k$	Natural frequency of mode $k$ (Hz)
$\xi_k$	Modal damping of mode $k$
$Q_k$	Scaling factor of mode $k$
$\{X_k\}$	Modal vector for mode $k$
$[L]$	Modal participation factor matrix
$v_n$	Surface velocity field
$p, P$	Acoustic pressure in time and frequency domain
$\rho_0$	Fluid density
$c_{sound}$	Sound velocity
$L_p$	SPL
$p_{rms}$	Root-mean-square value of the pressure $p$
$f_{order}$	Frequency of orders
$N_{rot}$	Rotational speed
$Q_r$	Number of rotor poles
$Q_s$	Number of stator slots
$n_o$	Order harmonic
$n_r$	Radial mode order
$n_z$	Axial mode order
$R$	Stator end-tooth radius
$R_m$	Stator mean radius
$E$	Young's modulus
$\rho$	Mass density
$s_f$	Stacking factor
$n_s$	Number of steel sheets
$t_s$	Thickness of one sheet
$L_{stack}$	Thickness of the lamination stack

$h$	Stator yoke height
$G_z$	Stator teeth weight
$G_w$	Winding weight
$G_y$	Yoke weight
$b_z$	Stator mean tooth width
$h_s$	Stator tooth height
$[C]$	Elasticity matrix with coefficients $C_{ij}$
$\{\epsilon\}$	Strain tensor
$\nu$	Poisson ratio
$G$	Shear modulus
$\lambda^{(n)}, \mu^{(n)}$	Lamé coefficients
$S_H$	FRF-sum
$P_{nom}, T_{nom}, N_{nom}$	Nominal power, torque, speed
$T_{av}$	Average torque
$K_T$	Torque ripple factor
$\Delta T$	Mean absolute deviation of torque
$w(x, t)$	Transverse deflection of a beam
$(EI)$	Flexural rigidity
$(\rho A)$	Linear density
$\delta t$	Time increment
$f_s$	Sampling frequency
$\delta \theta$	Angle increment
$\theta$	Rotation angle
$T$	Torque
$\delta f$	Frequency resolution
$F_r, F_\theta, F_z$	Forces in radial, azimuthal and axial direction

---

$\eta_r$	Resonance factor for spatial harmonic $n_r$
$\Im$	Imaginary part
$\Re$	Real part
$\sigma^2$	Variance
$\sigma_m^2$	Pooled variance
$G_k$	FRF-sum amplitude of mode $k$

#### Operators and notations

$\{\bullet\}$	Vector
$[\bullet]$	Matrix
$\bullet^T$	Transpose
$\bullet^*$	Complex conjugate
$\nabla^2$	Laplace operator

# Contents

<b>Abstract</b>	<b>v</b>
<b>Contents</b>	<b>xvii</b>
<b>List of Figures</b>	<b>xxiii</b>
<b>List of Tables</b>	<b>xxix</b>
<b>1 Introduction</b>	<b>1</b>
1.1 Research context . . . . .	1
1.1.1 Characteristics of acoustic noise in electric drives and challenges . . . . .	2
1.1.2 Objectives of the thesis . . . . .	5
1.2 Original contributions . . . . .	6
1.3 Dissertation outline . . . . .	7
<b>2 General notions behind magnetic noise</b>	<b>9</b>
2.1 Fundamentals of rotating electric machines . . . . .	9
2.1.1 Basic electromagnetic formulations . . . . .	10
2.1.2 Fundamental principle of rotating electric motors . . . . .	11
2.1.3 Common motor types in EVs . . . . .	13

2.1.4	Force production calculation . . . . .	16
2.2	Fundamentals of structural dynamics . . . . .	17
2.2.1	Introduction to modal analysis . . . . .	18
2.2.2	Calculation of the modal characteristics . . . . .	19
2.2.3	Calculation of the forced response . . . . .	23
2.3	Fundamentals of acoustic transfer systems . . . . .	23
2.4	Typical measured acoustic noise from a rotating electric machine	25
<b>3</b>	<b>The multi-physical nature of magnetic noise</b>	<b>29</b>
3.1	Simulation of magnetic noise during run-up . . . . .	29
3.1.1	FE Models . . . . .	30
3.1.2	Analytical models . . . . .	36
3.2	Reference experimental data . . . . .	40
3.3	Result comparisons . . . . .	42
3.3.1	Input currents . . . . .	42
3.3.2	Force wave distribution . . . . .	43
3.3.3	Structural vibrations and acoustic radiation . . . . .	43
3.3.4	Computational time considerations . . . . .	50
3.4	Intermediate conclusions . . . . .	51
<b>4</b>	<b>Rotor influences on the electric machine vibro-acoustic behavior</b>	<b>53</b>
4.1	Common rotor design changes . . . . .	54
4.2	Effects on the radiated magnetic noise . . . . .	54
4.2.1	Case study definition . . . . .	55
4.2.2	Electromagnetic model and torque ripple assessment . . . . .	56
4.2.3	Structural and acoustic model . . . . .	59
4.2.4	Results . . . . .	60
4.3	Effects on the assembly structural dynamics . . . . .	64

4.3.1	FE identification of RHC mode . . . . .	65
4.3.2	Experimental validations of the RHC mode occurrence .	69
4.3.3	Experimental evaluation of the rotor structural dynamics responsibilities . . . . .	73
4.3.4	Mathematical validation of the hypothesis . . . . .	76
4.4	Intermediate conclusions . . . . .	82
4.4.1	Conclusions on the effects on the radiated magnetic noise	82
4.4.2	Conclusions on the effects on the assembly structural dynamics . . . . .	83
<b>5</b>	<b>The laminated cores structural dynamics</b>	<b>85</b>
5.1	Typical modes related to laminated cylindrical cores . . . . .	85
5.2	1D Analytical models ( <b>Ring</b> ) . . . . .	87
5.3	2D FE model . . . . .	90
5.4	3D FE model with homogenized material properties . . . . .	91
5.4.1	Isotropic behavior . . . . .	92
5.4.2	Orthotropy and Transverse isotropy . . . . .	93
5.5	Model comparison and validation: A case study . . . . .	101
5.5.1	Reference experimental tests . . . . .	101
5.5.2	Stator core models . . . . .	103
5.5.3	Comparisons . . . . .	107
5.5.4	Material parameter sweep and optimization . . . . .	109
5.6	Effects of the number of laminations . . . . .	114
5.6.1	Experimental setup and validation . . . . .	114
5.6.2	Results . . . . .	118
5.7	Effects of the stacking technology . . . . .	119
5.7.1	Experimental setup . . . . .	123
5.7.2	Results . . . . .	124

5.8	Intermediate conclusions . . . . .	126
5.8.1	Final remarks on stator model comparisons . . . . .	126
5.8.2	Conclusions on the effects of the number of laminations . . . . .	128
5.8.3	Conclusions on the effects of the stacking technology . . . . .	129
<b>6</b>	<b>On a novel attachment method of the laminations of the stator core for improved NV performances</b>	<b>131</b>
6.1	Vibration reduction techniques . . . . .	132
6.2	Conceptualization . . . . .	133
6.2.1	Motivation . . . . .	133
6.2.2	On forcing transversal asymmetry . . . . .	137
6.3	Experimental validations . . . . .	139
6.3.1	Manufacturing procedure . . . . .	139
6.3.2	Testing procedure . . . . .	141
6.3.3	Significance evaluation . . . . .	143
6.4	Results . . . . .	145
6.4.1	The effects on axial, shearing and anti-symmetric modes . . . . .	145
6.4.2	The effects on pure radial modes $A(n_r, 0)$ . . . . .	150
6.4.3	Hypotheses validations . . . . .	156
6.5	Intermediate conclusions . . . . .	161
<b>7</b>	<b>Conclusions</b>	<b>165</b>
7.1	Multi-physical nature of magnetic noise . . . . .	165
7.2	The laminated cores structural dynamics . . . . .	166
7.3	Original lamination stacking for vibration damping purposes . . . . .	168
7.4	Future work . . . . .	170
<b>A</b>	<b>Cylindrical symmetries formulation</b>	<b>173</b>



<b>B Steady-state versus Transient responses</b>	<b>177</b>
<b>Bibliography</b>	<b>181</b>
<b>Curriculum Vitae</b>	<b>195</b>



# List of Figures

1.1	Transfer paths in an electric powertrain . . . . .	3
1.2	Measured acoustic pressure of an SRM powertrain during run-up	5
2.1	Electromagnetic system (in motoring operation) . . . . .	10
2.2	Simple magnetic core subjected to a magnetic field . . . . .	11
2.3	Example of an electric machine architecture - case of an IM exploded view [9] . . . . .	12
2.4	Example of a cross-section of an 8/6 SRM . . . . .	12
2.5	Classification of rotating electric machines . . . . .	13
2.6	Operation example of an 8/6 SRM . . . . .	14
2.7	Cross-section example of four machines - (a), (b) and (c) are pictures taken from [6] . . . . .	14
2.8	Surface line integration of the Maxwell stress tensor . . . . .	17
2.9	Vibrating system . . . . .	18
2.10	Acoustic system . . . . .	23
2.11	Typical acoustic spectrograms for run-up tests, taken from literature	26
3.1	Detailed FE modeling flow . . . . .	30
3.2	Electromagnetic mesh quality study: Results of convergence (left) and mesh geometry and magnetic flux lines for one magnetostatic problem (right) . . . . .	31

3.3	2D electromagnetic mesh and force integration line . . . . .	32
3.4	Illustration of the nodal forces transformation process . . . . .	33
3.5	Structural mesh quality study: Results of convergence . . . . .	34
3.6	3D structural mesh and force application nodes . . . . .	35
3.7	3D acoustic mesh and vibration velocity surface application to the acoustic system . . . . .	36
3.8	Analytical modeling flow . . . . .	36
3.9	Equivalent ring representation of the stator core . . . . .	37
3.10	SRM 2 measurement colormap during run-up . . . . .	41
3.11	Current profiles: (a) currents versus time at 1,000 rpm, (b) current versus frequency at 1,000 rpm, (c) current versus frequency for every calculated speed . . . . .	42
3.12	Radial force profile at 1,000 rpm: (a) versus time and angle position, (b) versus time for four different application points, (c) versus angular position for three different time instants, (d) versus time and spatial harmonics . . . . .	44
3.13	Radial acceleration results for (a) FE models and (b) analytical models . . . . .	45
3.14	Radial acceleration order cut results . . . . .	47
3.15	Acoustic pressure results for (a) FE Models and (b) Analytical models . . . . .	48
3.16	Acoustic pressure order cut results . . . . .	49
4.1	A quarter of the geometry and magnetic flux lines of the Rotor 1 (a), 2 (b), 3 (c) and 4 (d), with each complete machine stator (white) plus rotor (green) mass . . . . .	56
4.2	Torque vs. Speed curve of analyzed SynRM . . . . .	56
4.3	Magnetic flux density at 4,400 rpm with Rotor 1, versus time and angle position . . . . .	57
4.4	Radial force profiles at a fixed time instant, along the air-gap circumference, and for different rotors at 4,400 rpm . . . . .	58
4.5	Output torque waveform for the different rotors at 4,400 rpm . . . . .	58

4.6	Torque ripple for the different rotors . . . . .	60
4.7	(a) Structural mesh, (b) Ovalization mode $A(2,0)$ , (c) Triangular mode $A(3,0)$ and (d) Square mode $A(4,0)$ of the stator . . . . .	61
4.8	Acoustic pressure for the different rotors . . . . .	61
4.9	Average order cuts $L_p(n_o)$ for the different rotors . . . . .	62
4.10	OASPL for the different rotors . . . . .	63
4.11	Exploded view of the PMSM meshes composing the assembly . . . . .	66
4.12	Simulated modal characteristics of SRM 1 (left) and PMSM (right) . . . . .	68
4.13	Measurement setup for PMSM . . . . .	70
4.14	Measurement setup for SRM 2 . . . . .	70
4.15	Mesh resolution for IM assembly . . . . .	70
4.16	Linearity check example for IM . . . . .	71
4.17	Reciprocity check example for IM . . . . .	72
4.18	Undeformed assembly (left) and its RHC mode shape estimated from EMA (right) . . . . .	73
4.19	Mesh resolution for the rotors . . . . .	74
4.20	Two first bending modes for Rotor A and B from EMA, the plain lines follow the measurement points of the green line described in Fig. 4.15 . . . . .	75
4.21	Five-beam structure under study . . . . .	76
4.22	5-beam equivalent parametrization process . . . . .	80
4.23	Flexible mode shapes of the five-beam structure . . . . .	82
5.1	Illustration of the twinned $B(2,1)$ modes . . . . .	87
5.2	Principle of multi-scale homogenization for a laminated stack - Figure taken from [78] . . . . .	98
5.3	Base unit cell used for parameter identification . . . . .	99
5.4	Examples of two RVE simulations . . . . .	100
5.5	Cross-section and profile of the stator core under study . . . . .	101

5.6	Experimental setup; (left) Test.lab geometry, (right) Test setup	102
5.7	FRF-sum for the 12-8 SRM under study . . . . .	103
5.8	Illustration of the stator core models modeling flow . . . . .	104
5.9	3D-mesh validated . . . . .	106
5.10	<b>Ortho</b> RVE representation . . . . .	107
5.11	Parameter sweep analyses . . . . .	110
5.12	Simulation process for optimization (1 iteration) . . . . .	111
5.13	Optimization results, each blue line corresponds to a parametriza- tion that permits to reach the optimum P-value . . . . .	113
5.14	Representation of some samples (from left to right): 1, 10, 178 and 528 laminas, with their measurement discretization . . . . .	115
5.15	Reciprocity checks for different stacks and directions . . . . .	117
5.16	Axial bending mode shapes $E(n_r, 0)$ of 10 lamination stack . . . . .	118
5.17	FRFs-sum in axial excitation case for different lamination stacks	119
5.18	Estimated natural frequencies for axial bending modes $E(n_r, 0)$	120
5.19	Main radial mode shapes of the full stator; undeformed (grey) and deformed (black) . . . . .	120
5.20	FRFs-sum in radial excitation case for different lamination stacks	121
5.21	Estimated natural frequencies for radial modes $A(n_r, 0)$ and $B(n_r, 1)$ . . . . .	121
5.22	Pictures and test discretization of the specimens . . . . .	124
5.23	Main mode shapes of the welded stator core; undeformed (grey) and deformed (black) . . . . .	125
5.24	FRFs-sum of radial components for glue-bonded and welded stator cores . . . . .	125
6.1	Welding event and induced residual stresses - T = temperature	134
6.2	Residual stresses effects on mode $A(2, 0)$ (a) and $A(3, 0)$ (b) . . . . .	135
6.3	Residual stresses effects on mode $B(2, 1)$ . . . . .	135

6.4	Illustration of viscous (a) and Coulomb (b) damping in the case relative displacement occurs . . . . .	136
6.5	Illustration of the damping occurrence for specific modes - NB: Vector amplitudes are informative only . . . . .	136
6.6	Illustration of the novel lamination attachment method for welding with four weld lines . . . . .	137
6.7	Illustration of the damping occurrence when using skew-weld/glue - NB: Vector amplitudes are informative only . . . . .	138
6.8	Production line process - Gluing and welding cases . . . . .	140
6.9	Test specimens under study . . . . .	142
6.10	FRF-sum for 35_180_g and 50_180_g . . . . .	146
6.11	FRF-sum for 35_200_g and 35_200_sg . . . . .	146
6.12	FRF-sum for 35_180_g, 35_180_w and 35_180_sw . . . . .	147
6.13	FRF-sum for 35_180_g, 35_180_sw and 35_180_gsw . . . . .	147
6.14	Modal damping comparison for glued cores of different lamination thicknesses . . . . .	151
6.15	Modal damping comparison for glued and skew-glued cores . . . . .	152
6.16	Modal damping comparison for glued, welded and skew-welded cores . . . . .	154
6.17	Modal damping of glued, skew-welded and glued + skew-welded cores . . . . .	155
6.18	Example of a linearity check for the skew-welded core: (a) input autopower (RMS) spectrum, (b) FRF results for different input levels, (c-d-e) zooms on the FRF peaks . . . . .	157
6.19	Complete MAC analysis for different stator manufactures - matrices	159
6.20	Layered MAC analysis for different stator manufactures . . . . .	160
A.1	Representation of axial symmetry; the example of $C(0,0)$ mode deformation . . . . .	174
A.2	Representation of axial asymmetry; the example of $A(2,0)$ mode deformation . . . . .	174

A.3	Representation of radial symmetry; the example of $A(2, 0)$ mode deformation . . . . .	174
A.4	Representation of radial asymmetry; the example of $B(1, 1)$ mode deformation . . . . .	175
A.5	Representation of transversal symmetry; the example of $A(2, 0)$ mode deformation . . . . .	175
A.6	Representation of transversal asymmetry; the example of $B(2, 3)$ mode deformation . . . . .	176
A.7	Representation of transversal antisymmetry; the example of $B(2, 1)$ mode deformation . . . . .	176
B.1	Transient and steady-state responses of a SDOF system in time (a) and frequency (b) domain . . . . .	178
B.2	Excitation frequency versus time (a), its frequency spectrum (b) and the response (c) of the SDOF system to linear sweep and stepped-sine sweep excitations . . . . .	179



# List of Tables

3.1	SRM 2 geometry parametrization . . . . .	38
3.2	Structural characteristics results, N/M - Not Measured, N/A - Not Applicable . . . . .	43
3.3	Average computational time for both models per steady-state operating point . . . . .	50
4.1	Machine's geometry parameters . . . . .	55
4.2	Torque ripple function of the rotor topology and the rotational speed . . . . .	59
4.3	Base characteristics of the electric machines studied (Conf. = Confidential) . . . . .	65
4.4	Natural frequency (in Hz) results of the FE simulations for SRM 1 and PMSM (w/o = without, w/ = with, N/A = Not Applicable, OR = Out of Range) . . . . .	67
4.5	Experimental setups for PMSM, SRM 2 and IM (w/o = without, w/ = with) . . . . .	71
4.6	Experimentally estimated natural frequencies (in Hz) for PMSM, SRM 2 and IM (w/o = without, w/ = with, N/A = Not Applicable, OR = Out of Range) . . . . .	72
4.7	Experimental setups for IM (w/o = without, w/ = with) and different rotors . . . . .	74

4.8	Experimentally estimated natural frequencies (in Hz) for IM (w/o = without, w/ = with, N/A = Not Applicable, OR = Out of Range) . . . . .	75
4.9	Equivalent parameters . . . . .	81
4.10	Results for the equivalent beam structures, (*) = the assembly is modeled without the stator . . . . .	82
5.1	Typical vibrational modes of a stator core (Part I), (*) twinned modes occur . . . . .	88
5.2	Typical vibrational modes of a stator core (Part II), (*) twinned modes occur . . . . .	89
5.3	Simulations performed for parameter identification . . . . .	99
5.4	Characteristics of the stator core under study . . . . .	102
5.5	Isotropic material properties of the composite compounds . . .	105
5.6	Model parameters . . . . .	108
5.7	Model and experimental results comparisons of the natural frequencies . . . . .	109
5.8	Optimal material parameters compared to <b>Iso</b> 's . . . . .	113
5.9	Natural frequencies: calculated with optimal material parameters compared to measured . . . . .	114
5.10	Lamination stacks under investigation; H = Hammer, S = Shaker	115
5.11	Modal characteristics for axial modes $E(n_r, 0)$ ; (-) Not appearing	122
5.12	Modal characteristics for radial modes $A(n_r, 0)$ and $B(n_r, 1)$ ; (-) Not captured . . . . .	122
5.13	Modal characteristics for radially excited modes; (-) Not appearing	126
5.14	Model advantages and disadvantages; (- -) Very bad, (-) Bad, (+) Good, (++) Very good . . . . .	127
6.1	Test specimens built . . . . .	141
6.2	Material characteristics . . . . .	141
6.3	EMAs results . . . . .	149

6.4	Significance levels for the samples tested, effect of lamination thickness . . . . .	150
6.5	Significance levels for the samples tested, effects of skew-gluing	152
6.6	Significance levels for the samples tested, effects of skew-welding	153
6.7	Significance levels for the samples tested, glue + skew-welding effect . . . . .	155
6.8	Modal damping estimations (half-power technique) for skew-welding core and different input voltage levels to the shaker (equivalent to force levels) . . . . .	158
6.9	Complete MAC analysis for different stator manufactures - diagonal values . . . . .	159
6.10	Layered MAC analysis for different stator manufactures - diagonal values . . . . .	161
A.1	Symmetry definitions of global parameter $\Upsilon, \forall(r, \theta, z)$ , N/A - Not Applicable . . . . .	173



# Chapter 1

## Introduction

### 1.1 Research context

In the context of global warming, several industry sectors have been developing greener technologies to reduce greenhouse gases emissions. Amongst these sectors, transportation has a significant ecological footprint which is expected to be attenuated by the expansion of electric mobility. Indeed at first electric trains, now Electrical Vehicles (EVs) [38] and then electric aircrafts [8] are thought to be the next generation of transportation systems. But replacing Internal Combustion Engines (ICE) with electric machines is not trivial: countries need to provide larger access to charging infrastructures to replace gas stations while industry has to reorganize their competence centers towards more electrical engineering.

This expanding engineering field faces similar system performance requirements than for ICE such as system efficiency, output power, maximum torque, maximum speed and comfort. Several machine technologies can be used to fulfill these requirements but EV manufacturers tend to choose Induction Machines (IMs) or Permanent Magnet Synchronous Machines (PMSMs) over other machines, because they are either cheap to produce or easy to control, respectively. Yet another crucial requirement related to market demands in the long-term perspective emerges nowadays: the cost of rare-earth material. IMs and PMSMs might be subjected to higher cost over the years because they use expensive materials, either copper or Permanent Magnets (PMs). Given the growing market of EVs, the European Commission therefore encourages research to tackle this near future problem [20].

The ADEPT (ADvanced Electric Powertrain Technology) project [114], from which this research work takes its grant, is a perfect example of growing research developments towards rare-earth-material-free electric machines for EVs. It focuses on reluctance machines such as Switched Reluctance Machines (SRMs) and Synchronous Reluctance Machines (SynRMs). Having no copper on the rotor nor PMs on the rotor/stator cores, these types of electric machines are significantly cheaper to manufacture. Because of several disadvantages these types of machines have not been integrated in commercial EVs so far: control strategies require proper switching schemes to allocate for rotating field input, output torque ripple is significantly higher than for the conventional machines, and acoustic noise may be particularly high and prohibitive from a psycho-acoustic point of view. In short, reluctance machines tend to be cheaper than currently used IMs and PMSMs as they lack or comprise few rare-earth materials, but challenges emerge from the control and comfort sides.

This dissertation mainly focuses on the comfort aspect, referred to as Noise, Vibration and Harshness (NVH) behavior, of electric machines for traction applications.

### 1.1.1 Characteristics of acoustic noise in electric drives and challenges

Overall acoustic noise in traction vehicles can be categorized in three parts: powertrain noise, tyre noise from the tyre/road contact and wind noise from the wind hitting the vehicle. Typically for ICE vehicles, engine noise is the most predominant noise at low speed, then tyre noise becomes more important at medium speed and finally wind noise dominates at high speed [39]. For current EVs, powertrain noise is lower than tyre and wind noises such that these vehicles are often considered quiet at low speed [83].

However the way a human perceives sound, and thus also noise, is not only about overall levels but also about its quality, notably its frequency content. For instance, high frequency tones with constant power over time (*e.g.* whistle) are usually not appreciated. Obviously this appreciation is subjective and therefore it is evaluated using objective sound quality metrics such as loudness, sharpness, frequency masking and A-weighting [21]. Nowadays, electric powertrain noise is essentially masked by other noises but high tones can still be perceived and be predominant, especially if SRM or SynRM are chosen.

In order to define the contribution of each part to the overall NVH comfort in vehicle traction, a source-transfer-receiver approach [123] is often adopted. The vehicle passenger and/or driver represents the receiver. In the case of acoustic

noise he/she ultimately receives sound coming from airborne components shaped by the interior topology of the vehicle cabin. But in general the source excites a structure that, by vibrating, generates pressure fluctuations to the surrounding fluid. The pressure variations are assimilated to acoustic noise; we talk about vibro-acoustics. The energy transmission system, also called transfer path, represents everything between the source and the receiver. It is defined by stiffness, damping and mass characteristics. The input energy coming from the source can employ a multitude of different paths to reach the receiver. For instance the tyre/road interface exhibits two aspects: airborne sound radiation is generated when the tyre surface interacts with the road surface; on the other hand, it causes a structure-borne phenomenon from which forces are transmitted from the wheel to the vehicle body, and then from the vehicle body to the air of the passenger cabin as acoustic noise.

In electric powertrains, the acoustic noise sources are usually described in literature in terms of their influence on the receiver frequency spectra and categorized in three different transfer paths [56, 129]: the aerodynamic, mechanical and magnetic noises. Fig. 1.1 pictures the different energy transfer paths represented in an electric powertrain system.

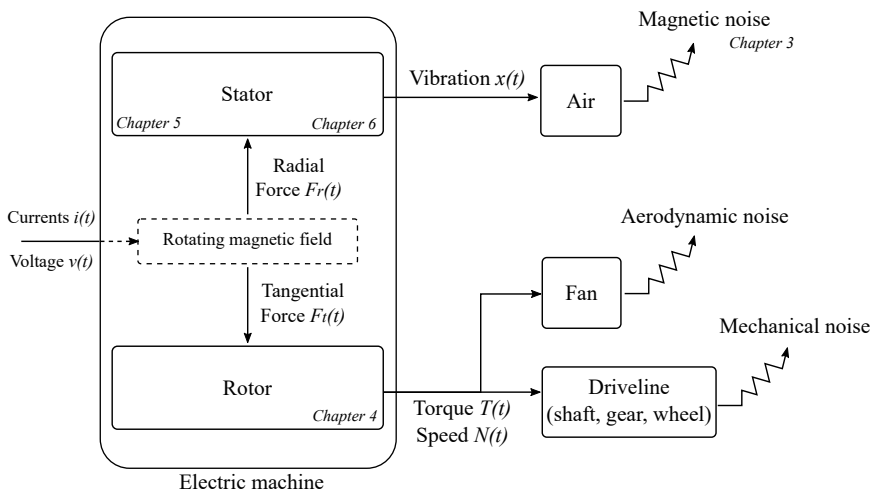


Figure 1.1: Transfer paths in an electric powertrain

*Aerodynamic noise* [56, 129] (e.g. motor fans, air flow turbulences) essentially originates from motor cooling fans that create air flow turbulence while rotating. The sound pressure level they radiate is increasing as the rotational speed increases, and it usually becomes the most important acoustic contributor at high speeds. Several solutions exist to reduce their contribution to the overall

emitted noise [129, 121]. One of the most interesting solution is the use of liquid cooling [46]. Despite eliminating fan-originated noise, aerodynamic losses still contribute to noise radiation. Since this physical phenomenon involves fluid dynamics and has a fairly low overall contribution in liquid-cooled designs [46], aerodynamic noises are not addressed in the scope of this thesis.

*Mechanical noise* [56, 129] (*e.g.* bearings, shaft whirling, rotor unbalance, brakes) is caused by the mechanical contact of parts and components of which the interference provokes a vibratory response of the bodies, finally producing noise. Often these interferences are located at the bearings/gears and result from rotor unbalance. Refined alignments and axial preloads with dedicated springs are solutions to that matter [145]. Despite their potential large acoustic influence on the low frequencies (20 Hz to 300 Hz), proper manufacturing, calibration and alignment of the machines is assumed so the mechanical sources are not addressed in this thesis.

*Magnetic noise* [56, 129, 74] (*e.g.* inverter noise from switches, motor vibrations from magnetic flux fluctuations) originates from the electrical currents traversing the coils of the machine which generates a rotating magnetic field in the air gap. The induced magnetic flux density fluctuations translate into magnetic forces that excite the stator core, which in turn produces stator vibrations and acoustic noise at the end. They occur at relatively high frequencies (between 400 Hz and 20 kHz) and are characterized by three main features:

1. the **electronically induced ripples** are caused by the artificial production of sine current waves in the phases. The poor representation of the sine wave gets amplified into noise components. It is usually characterized by high frequency noise ( $> 5$  kHz) and potentially disturbs the human ear significantly [14]. Counter-actions exist [70] and for instance involve various pulsewidth modulation schemes [115] or active-noise reduction methods [17]. However these ripples are related to the power electronics so they have not been addressed in this thesis.
2. the **orders** whose frequencies linearly depend on the rotational speed and on the number of rotor poles [5]. They physically represent the number of times per second a stator tooth meets a rotor pole. They immediately emanate from the radial force distribution (in time and space) that acts on the transferring structure *i.e.* the stator, and therefore contain fundamental and harmonics frequencies.
3. the **resonance phenomena** whose frequencies are fixed and depend only on the vibrating transfer structure. For traction applications, the resonance frequencies of interest are mostly greater than 400 Hz.



Fig. 1.2 illustrates a typical acoustic pressure measurement (up to 5 kHz) 1 m away from a SRM during acceleration [93], *i.e.* run-up. The most significant components are attributed to the magnetic noise, as previously described, and generate high tonal noise which is generally unappreciated by the human receiver. Psycho-acoustic metrics (tonality, sharpness, loudness) support these claims [21, 90, 14] and justify why magnetic noise is often considered the largest contributor to the overall acoustic noise of electric machine drives [121, 50, 74]. Hence this thesis focuses on magnetic noise.

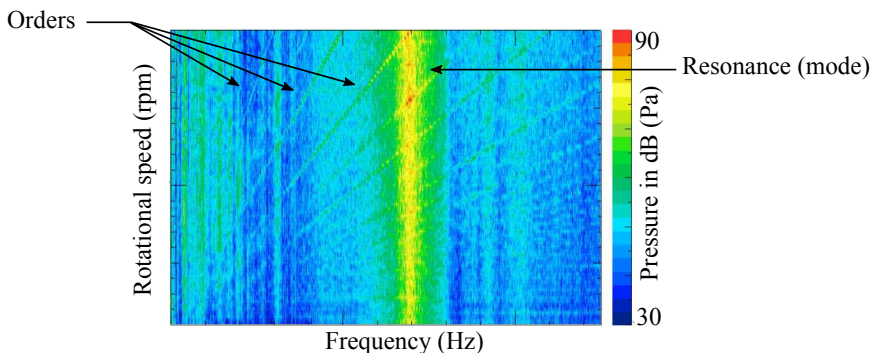


Figure 1.2: Measured acoustic pressure of an SRM powertrain during run-up

The prediction of such phenomena is a great asset to define early in the design stage an optimum system configuration. Moreover since magnetic noise originates from a multi-physical process that involves electrical and mechanical engineering disciplines, it is fundamental to understand the principles within both domains of competences. The induced magnetic forces are relatively consistently calculated but they excite the rotor and stator of the electric machines, possibly showing complex structural behavior due to their assembly and composition. On the one hand, the rotor may show particular coupling modes due to its connection to the machine housing through the bearings. On the second hand, the stator is made of hundreds of steel laminations (to minimize eddy current losses), which introduce structural dynamics modeling difficulties and thus challenges.

### 1.1.2 Objectives of the thesis

The main objective of this thesis is to propose solutions to the prediction and the reduction of acoustic noise, and particularly magnetic noise, of electric machines. The challenges in modeling at a component level (laminated stator and rotor cores) has to be overcome to reinforce the validity of the multi-

physics system-level (electric machine) simulations. These simulations aim at supporting decision making processes during design phases. The model's accuracy is essential to ensure, but computational time/cost has also to be taken into consideration.

Experimental tests are used to improve the model representation of the laminated structural dynamics, at the component level, *i.e.* stator and rotor cores. They contribute to various analyses that consolidate known trends, but also provide design refinement guidelines for NVH comfort improvements.

It is important to note that in this dissertation, the focus and studies are emphasized on inner rotor radial-flux rotating electric machines designed for EV powertrain applications - within the context of ADEPT project - even though the developed methods are expendable to other electric machine applications *e.g.* small machinery, wind-turbines, etc.

## 1.2 Original contributions

The research presented in this thesis gave rise to a number of original contributions that were shared with an international audience through peer-reviewed conference publications and presentations, journal articles and ADEPT project seminars. The research documents are either already published or in the process of publication, see Section "List of Publications". The most important contributions are:

- Proper multi-physics modeling processes for the vibro-acoustic simulation of an electric machine are defined;
- The rotor influence on the complete machine structural dynamics is assessed, and an analytical model explains the occurrence of a particular mode that was still not given a clear explanation in literature;
- A relevant modeling strategy for the vibrational behavior of laminated stator cores is defined thanks to comparison of simulation models and experimental results;
- An alternative solution to the attenuation of the resonance phenomenon responsible for large acoustic noise emissions is proposed and validated experimentally.

## 1.3 Dissertation outline

The thesis comprises three main parts. In the first part, the multi-physical system-level modeling framework for the vibro-acoustics of an electric machine is described, and the best modeling practices are defined. The second part focuses on the component-level insight gains and their modeling. Relevant linear modeling strategies are described and experimentally validated for laminated stator cores. The importance of collecting information regarding structural dynamics at the component-level is also highlighted by investigating the rotor. Numerical, experimental and analytical analyses support the conclusions on its effects on the electric machine vibrational behavior. Finally the third part formulates the idea of introducing a mismatch between magnetic forces and stator mode shapes for overall vibration reduction and frictional damping activation between laminations. The hypothesis is validated experimentally. Fig. 1.1 pinpoints the chapters associated to each investigated problem.

**Chapter 1** introduces the problem and motivates the required investigation work. The objectives and novel contributions of the work are highlighted.

**Chapter 2** provides the basic concepts of electrical and mechanical engineering that permit to understand and pursue investigations. The necessity of taking both domains of competences into account is justified by the explanation of the multi-physical problem to tackle.

**Chapter 3** starts by defining the multi-physical modeling flow concept for the simulation of magnetic noise from an electric machine. The multi-physical approach is then detailed and applied at several levels of model complexity which limitations are compared with test data. Given the large contribution from resonance phenomena to magnetic noise, NVH comfort improvement strategies finally emphasize on the necessity to accurately predict/understand the component-level structural behavior.

**Chapter 4** focuses on the influence of rotor dynamics on the complete machine structural behavior. The effects of different rotor topologies on magnetic noise are studied numerically, and its influences on the assembly vibrational behavior are highlighted numerically and experimentally. An innovative analytical model explains the newly identified modal characteristics of an electric machine assembly incorporating the rotor.

**Chapter 5** is dedicated to the structural dynamics of laminated cores. Different modeling techniques with various levels of complexity are described and used for comparison with test results. Advantages and disadvantages are listed and an optimization procedure proposes the definition of best practices for the lamination modeling. Then several component-level and manufacture changes

are studied experimentally in order to have a complete physical understanding of the lamination structural dynamics.

**Chapter 6** hypothesizes a structural solution to magnetic noise radiation: the implementation of axial-asymmetric stiffness within the lamination stacking process of machine cores. The hypothesis is validated experimentally with various attachment techniques. Damping improvements are significant and the developed technique can be considered as an alternative manufacturing procedure.

**Chapter 7** summarizes the most relevant conclusions of the work and gives recommendations for future research activities.

## Chapter 2

# General notions behind magnetic noise

When a rotating electric machine operates, a multitude of physical phenomena are involved, going from electrical to mechanical domains, but also fluid-dynamics and thermal processes. As explained in the previous chapter, magnetic noise is generated through a vibro-acoustic phenomenon in which the excitation source is electrical. Its prediction therefore requires fundamental knowledge in various engineering disciplines that this chapter will provide. Given that a comprehensive description of every aspect would go beyond the scope of the present thesis, a general introduction to electric machines and corresponding electromagnetic notions is given in Section 2.1. The concepts of structural dynamics and acoustic are similarly explained in Sections 2.2 and 2.3 to form the initial description of the vibro-acoustic process under study. Then the typical measured acoustic noise in rotating electric machines is presented in Section 2.4, and highlights the need for multi-physical machine design.

### 2.1 Fundamentals of rotating electric machines

Rotating electric machines convert electrical energy into rotational mechanical energy or vice versa, cf Fig. 2.1. From the input of currents and voltage, a magnetic field is generated. Its spatial distribution depends on many factors (pole/slot combination, machine type and topology). The induced magnetic flux in the air gap produces magnetic forces of radial and tangential nature that apply on both the rotor and the stator. Tangential forces generate torque

whereas radial forces may excite the stator which inherently activates vibration phenomena.

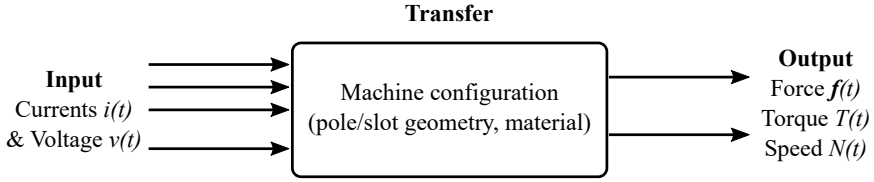


Figure 2.1: Electromagnetic system (in motoring operation)

### 2.1.1 Basic electromagnetic formulations

Although the goal of this thesis is not to provide deep insight into electric machine types, a fundamental knowledge of the principles governing the energy conversion from electrical inputs to a rotating mechanical motion is required.

Ampere's law states that the line integral of the magnetic field intensity  $\{H_{mag}\}$  (in A/m) along any closed path  $c$  equals the total current  $\{I\}$  enclosed by this path:

$$\{I\} = \oint_c \{H_{mag}\} \cdot dl \quad (2.1)$$

When considering the magnetic core of Fig. 2.2 (of circumference  $l_c$ ) surrounded by a coil of  $N$  turns traversed by a current  $i$ , and assuming uniform field of magnitude  $H_{mag}$ , the magneto-motive force  $mmf$  is given by:

$$mmf = Ni = H_{mag}l_c \quad (2.2)$$

The density of the flux lines generated in the magnetic field  $\{H_{mag}\}$ , *i.e.* the magnetic flux density  $\{B\}$ , is defined by:

$$\{B\} = \mu\{H_{mag}\} \quad \text{in tesla (T)} \quad (2.3)$$

where  $\mu$  is the permeability of the material. It represents the capability of the material to let magnetic flux pass. The flux magnitude  $\Phi$  reads:

$$\Phi = BA = \left( \mu \frac{mmf}{l_c} \right) A = \frac{mmf}{R_e} \quad \text{in weber (Wb)} \quad (2.4)$$

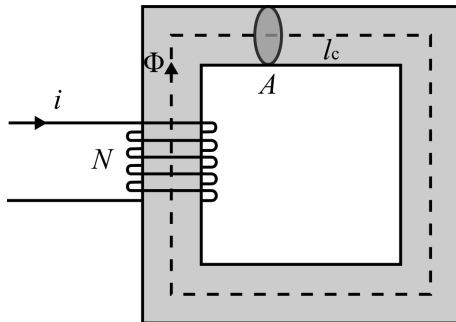


Figure 2.2: Simple magnetic core subjected to a magnetic field

where  $A$  is the surface area perpendicular to the direction of the flux lines, and  $R_e$  is the reluctance of the magnetic core. Eq. (6.6) shows that the flux produced by the  $mmf$  is inversely proportional to the reluctance  $R_e$ , which is analogous to Ohm’s law ( $I = V/R$ ) in electric circuits. Furthermore such as in the electric domain, the flux (current) tends to find the magnetic field path (electric circuit) with the lowest reluctance (resistance): law of minimal reluctance. A force density is then produced when current density  $\{j\}$  flows through a conductor in a flux density  $\{B\}$ , and is called the Lorentz force density  $\{F_{Lorentz}\}$ :

$$\{F_{Lorentz}\} = (\{j\} \times \{B\}) \quad \text{in N/m}^3 \tag{2.5}$$

### 2.1.2 Fundamental principle of rotating electric motors

In general, rotating electric machines are composed of a fixed stator and a rotating rotor. An example of the architecture of an IM is shown in Fig. 2.3. The rotor is mounted on bearings that are attached to the stator. A transversal cut of the stator plus rotor assembly is defined and shown in Fig. 2.4. It is essentially used during the electromagnetic design phase of the machine. The stator is generally composed of a core, made of hundreds of thin steel sheets called laminations, windings that carry electrical currents, and possibly permanent magnets for some machines. Similarly, the rotor is composed of laminations, a shaft and potentially windings and permanent magnets depending on the electric machine considered. The stator and rotor cores’ circumference are divided respectively in  $Q_s$  stator poles (also called stator teeth or slots) and  $Q_r$  rotor poles (also called rotor teeth or slots). An electric machine is then

conventionally denoted  $Q_s/Q_r$  "machine type"; e.g. a 8-stator pole, 6-rotor pole SRM is written 8/6 SRM.

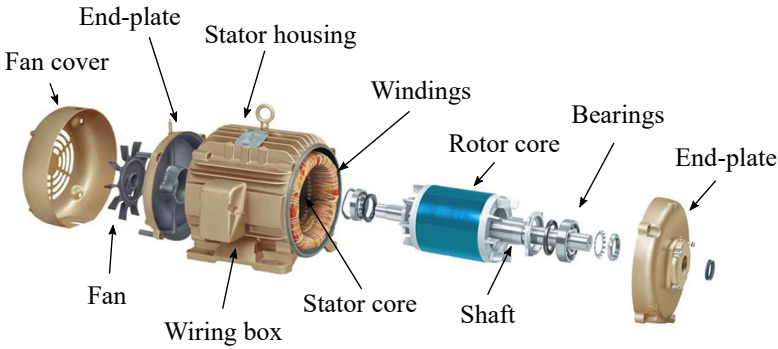


Figure 2.3: Example of an electric machine architecture - case of an IM exploded view [9]

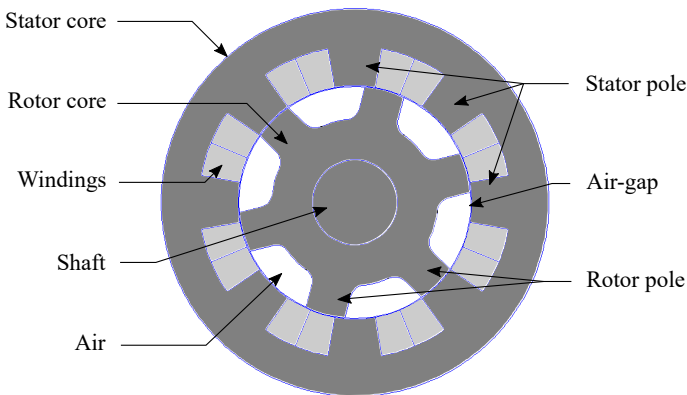


Figure 2.4: Example of a cross-section of an 8/6 SRM

By applying currents with different phases to the windings, this architecture permits to generate a rotating magnetic field that induces a tangential force which produces a torque applied to the rotor shaft; thus forced to rotate. A large variety of machine categories emerge from the combination of different coil locations, the use of permanent magnets for constant magnetic field generation, and the number of slot/poles; which show various performance characteristics. Fig. 2.5 shows a classification of the categories of rotating electric machines, split in Direct Current (DC) and Alternating Current (AC) categories.



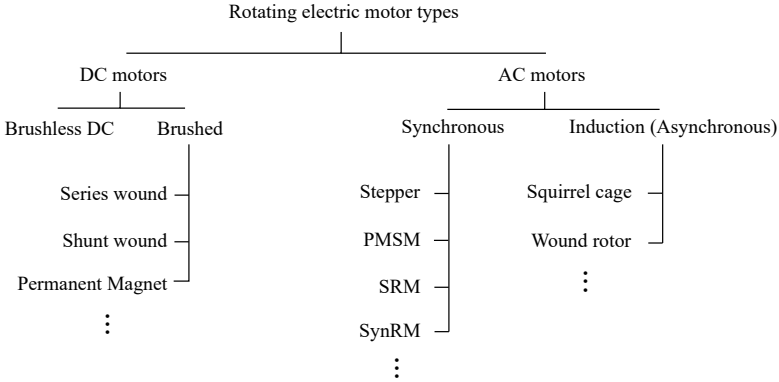


Figure 2.5: Classification of rotating electric machines

It is not of the present dissertation interest to thoroughly explain the functioning principles of each of them, yet it is important to understand how rotational motion is created from electromagnetic interactions. Hence the working principle of an SRM is further described, illustrated in Fig. 2.6 and inspired by [93, 89], while other machine functioning principles are accessible in literature [57].

In SRMs, windings are present only in the stator slots and associated coils are fed two by two such that the number of phases is equal to half the number of stator poles  $Q_s$ . As described in Section 2.1.1, currents traversing the coils create a magnetic field at the excited stator pole, which attract the nearest rotor pole, following the principle of minimum reluctance. The rotor is in the aligned position (1). Then the neighboring phase is excited while the previous one is gradually deactivated. A set of unaligned rotor poles are attracted to the new excited stator pole; the rotor is in an unaligned position (2) and (3). Finally another aligned position is reached again at step (4). Hence the mechanical rotation is ensured by sequential excitation of the phases.

### 2.1.3 Common motor types in EVs

Overviews on the most common motor used in EVs are already provided in literature [24, 25, 89], and a non-exhaustive list is given below, with the illustration of some of these machines' cross-section in Fig. 2.7.

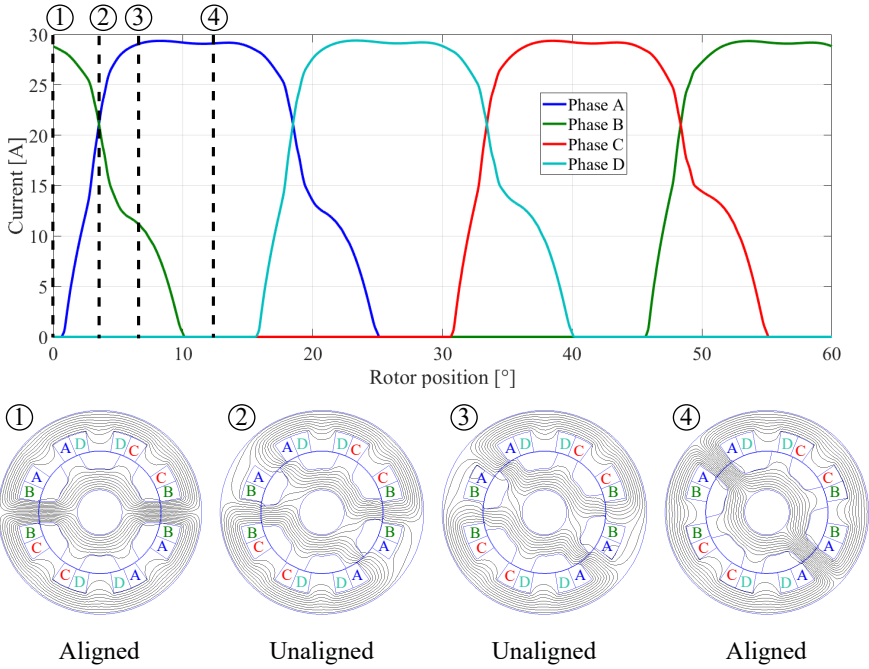


Figure 2.6: Operation example of an 8/6 SRM

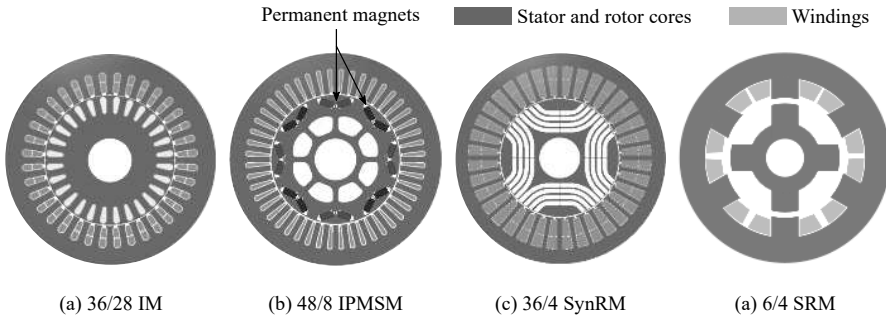


Figure 2.7: Cross-section example of four machines - (a), (b) and (c) are pictures taken from [6]

### Direct Current (DC) machines

DC machines used to be widely adopted for EVs (Fiat Panda Elettra, Mazda Bongo, Conceptor G-Van, etc [31]) because they do not need complex control strategies. A DC current carrying armature is connected to the supply end

through commutator segments and brushes while the armature is placed between north and south poles of a permanent or electro magnet. The Lorentz force from Eq. (2.5) is produced and generates a rotating motion of the rotor.

Although they benefit from simple control, they suffer from frequent maintenance requirements and low efficiency. Commutators increase torque ripple and limit the motor speed while brushes add friction interferences. The development of power electronics in the last decades made the Alternating Current (AC) machines more attractive for EVs.

### **Induction Machines (IMs)**

Amongst AC machines, IMs are extensively used in modern EVs (Fiat Seicento Elettra, Ford T!ink city, GM EV1, Tesla models, etc [31]) because they are cheaper, they show higher power density and they are more efficient than DC motors. AC currents in the stator windings produce a rotating magnetic flux that induces currents in the short-circuited rotor windings (Faraday's law). By tending to cancel the former stator flux (Lenz's law), the delayed induced rotor flux generates an electromagnetic torque on the rotor.

The advancements in power converters to allocate for multi-phase AC designs allowed the technology to be implemented easily in industry and vehicles. However it suffers from lower efficiency at high loads (compared to other machine types), cooling problems and narrow speed range.

### **Permanent Magnet Synchronous Machines (PMSMs)**

PMSMs are the most used electric motors nowadays in EVs (Toyota Prius, Honda EV Plus, Nissan Altra, Toyota RAV4, Nissan Leaf, etc [31]) for their high power density due to high-energy PMs, high efficiency and cooling capabilities by removing copper in the rotor. Contrarily to IMs, the rotor magnetic flux is fixed by PMs located inside (Interior PMSM) or outside (Surface-mounted PMSM) the rotor structure. It makes the control simple to implement, and sinusoidal (or trapezoidal) multi-phase AC currents can be injected to generate the rotating flux.

However, the main drawbacks are the limited resources of rare-earth materials used to manufacture PMs, which inherently induces a higher cost. Additionally the magnets are subjected to demagnetization at high temperatures, which is usually addressed by flux-weakening.

## Synchronous Reluctance Machines (SynRMs)

SynRMs are not used at the moment in commercial EVs, but are potential candidate to PMSM and IM replacements. By relying solely on the minimum reluctance principle, they use the saliency of the rotor to generate torque. They essentially benefit from the fact that they use cheap materials and they show high efficiency. The improvements in power converter technologies allow real time position sensing that facilitates the machine control.

Yet the rotor geometry composed of flux-barriers brings two drawbacks: it makes the rotor harder to manufacture, and it can break when subjected to high rotational speeds (because of centrifugal forces). Torque ripple is also a significant disadvantage of SynRMs.

## Switched Reluctance Machines (SRMs)

Interest is growing for SRMs implementation in EVs (Chloride Lucas, [31]), given the recent developments in power converters. Similarly as the SynRMs, they generate only reluctance torque [68] and their simpler construction and the absence of windings and PMs on the rotor make them particularly cheap and robust. They can also sustain high temperatures and are better suited for high speed operations than SynRMs.

Nonetheless they show relatively low power density (*e.g.* compared to PMSMs) and a position measurement is almost constantly required in the control loop [89]; preventing from feeding with pure sinusoidal current. In fact controlling such machine is also complex because of non-linearities involved in fringing effects and high saturation levels of the iron [89]. Larger current levels are required to produce similar torque, and induce significantly high torque ripple. Finally SRMs radiate particularly large acoustic noise due to resonances and high current ripples. For a long time, this last characteristic has prevented SRMs from being used in noise-sensitive applications such as in automotive industry.

### 2.1.4 Force production calculation

In any of the machine type cases, the force produced  $\{F\}$  by the electromagnetic events can be calculated using the Maxwell stress tensor [53]. It is derived from the Lorentz force and Ampere's law.

$$\{F\} = \oiint_S [\bar{\sigma}_{Maxwell}] \cdot \{n\} dS \quad \text{in newton (N)} \quad (2.6)$$

where  $\{n\}$  is the unit vector pointing out of the surface S, and  $[\bar{\sigma}_{Maxwell}]$  is the Maxwell stress tensor:

$$[\bar{\sigma}_{Maxwell}] = \frac{1}{\mu_0} \begin{bmatrix} B_r^2 - B^2/2 & B_r B_\theta & B_r B_z \\ B_\theta B_r & B_\theta^2 - B^2/2 & B_\theta B_z \\ B_z B_r & B_z B_\theta & B_z^2 - B^2/2 \end{bmatrix} \quad (2.7)$$

where  $B^2 = B_r^2 + B_\theta^2 + B_z^2$ , in the cylindrical coordinate system  $(r, \theta, z)$ . Fig. 2.8 illustrates the surface line integration of the Maxwell stress tensor for 2D analyses.

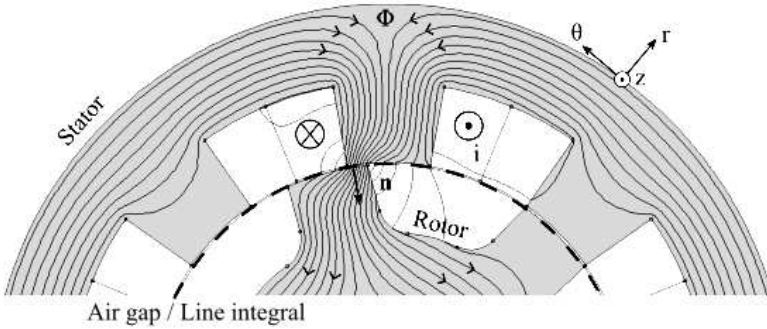


Figure 2.8: Surface line integration of the Maxwell stress tensor

## 2.2 Fundamentals of structural dynamics

Vibrating structures are transferring energy mechanically, see Fig 2.9, from an input excitation, that can be localized (equivalent to a force in newton - N) or distributed (equivalent to a pressure in N/m<sup>2</sup>), through the structural transfer path to an external receiver in the form of vibration (displacement, velocity, acceleration). While most of the energy is transferred, a part is dissipated giving rise to the notion of structural damping. Modal analysis is commonly used to characterize the transfer path.

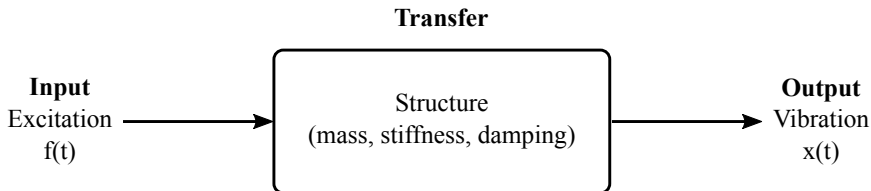


Figure 2.9: Vibrating system

## 2.2.1 Introduction to modal analysis

Any linear time invariant vibrating structure can be fully characterized by so-called modes [58]. They represent particular deformations (mode shapes) whose amplitudes are decreased through damping ratio and that occur at specific frequencies (natural frequencies). They uniquely depend on the structure's properties (geometry, mass, stiffness, damping) and its boundary conditions, and can be calculated by modal analysis. In the digital world, the number of modes composing a structure immediately relates to the number of Degrees-Of-Freedom (DOFs) that shape the system. Real structures however are continuous and consequently have an infinite number of modes (also DOFs). Since modes are associated to particular natural frequencies and that in practice one is interested in definite frequency bandwidths, it is reasonable to describe a structure using a reduced discretized system of a finite number of DOFs, namely a Multiple Degree-Of-Freedom (MDOF) system. Modal analysis concepts are introduced further, and thorough details on how to obtain the equations below are available in literature [58].

For a MDOF system with  $N$  DOFs, the force equilibrium states the balance between inertial, damping, elastic and external forces to derive the equation of motion:

$$[M]\{\ddot{x}(t)\} + [D]\{\dot{x}(t)\} + [K]\{x(t)\} = \{f(t)\} \quad (2.8)$$

where  $[M]$ ,  $[D]$  and  $[K]$  are respectively the mass, damping and stiffness matrices of size  $N \times N$ , while  $\{x(t)\}$  and  $\{f(t)\}$  are the displacement and force vectors ( $N \times 1$ ). Translating Eq. (2.8) from the time domain (time variable  $t$ ) to the Laplace domain (variable  $p$ ), and assuming zero initial displacement and velocity, yields:

$$([M]p^2 + [D]p + [K]) \{X(p)\} = \{F(p)\} \quad (2.9)$$

The transfer function matrix  $[H(p)]$  is defined as,

$$[H(p)] = [[M]p^2 + [D]p + [K]]^{-1} \quad (2.10)$$

The determinant is called the system characteristic equation, which roots compose the system poles  $\lambda_k$  and  $\lambda_k^*$ . The free vibration of an undamped system, *i.e.*  $[D] = [0]$  and  $F = 0$ , permits to define the eigenvalue problem. Assuming the solution of  $\{X\}$  to be harmonic yields:

$$\forall \omega, \quad (-[M]\omega^2 + [K])\{X(\omega)\} = \{0\} \quad (2.11)$$

The non-trivial solution  $\{X\} \neq \{0\}$  of this system of  $N$  algebraic homogeneous equations gives  $N$  eigenvalues  $\omega_k$ , the natural frequencies (rad/s) corresponding to  $N$  eigenvectors  $\{X_k\}$  ( $N \times 1$ ), the mode shapes. Therefore the mode shapes and natural frequencies only depend on the  $[M]$  and  $[K]$  matrices, *i.e.* on the structure geometry and material properties. Finally along the frequency axis ( $j\omega$ ), the transfer function matrix  $[H(p)]$  becomes the Frequency Response Function (FRF) matrix  $[H(\omega)]$  and can be written as follows [58],

$$[H(p)]\Big|_{p=j\omega} = [H(\omega)] = \sum_{k=1}^N \frac{[A_k]}{j\omega - \lambda_k} + \frac{[A_k]^*}{j\omega - \lambda_k^*} \quad (2.12)$$

$$\text{where } \lambda_k = -\xi_k\omega_k + j\sqrt{1 - \xi_k^2}\omega_k$$

where  $\xi_k$  is the modal damping ratio and the terms  $[A_k]$  and  $[A_k]^*$  are the residues which depend on the scaling factor  $Q_k$  and the modal vectors  $\{X_k\}$ .

$$\forall k \in [1..N], \quad A_k = Q_k\{X_k\}\{X_k\}^t \quad (2.13)$$

It is important to notice that if the previous calculations are performed for a Single DOF (SDOF) system, the transfer function matrix of a  $N$ -DOF system is the sum of  $N$  SDOF transfer functions; also known as the modal superposition principle [58].

## 2.2.2 Calculation of the modal characteristics

Any continuous structure can be discretized using  $N$  DOFs, and consequently characterized by unique modes that are defined by natural frequencies  $\omega_k$ , mode

shapes  $\{X_k\}$  and damping ratios  $\xi_k$ . The calculation of these parameters permits to fully characterize the structure and is required for further analyses. Numerical methods are commonly used and employ Finite Element (FE) methods to that matter, while Experimental Modal Analyses serve the calculation of the modal parameters from a measured dataset.

## Finite Element Analysis (FEA)

Although the aim of this thesis is not to describe the details of performing FEA but rather to make use of this type of analysis, it is necessary to explain some of its concepts. Further details of the FEAs are extensively available in literature [35, 150] and are employed in many different engineering fields: heat transfer, electromagnetics and structural. The FEA generally follows a six-step standard procedure described below with the application interest of modal analysis:

- 1. Define the problem:** From the equation of equilibrium, one has to solve the eigenproblem of Eq. (2.11).
- 2. Approximate field variables:** Select the element type and order. A continuous structure is discretized by a finite number of elements. The type (1D, 2D, 3D,...), order (linear, quadratic) and geometry (triangle, hexahedron...) of the elements define shape functions used in the calculations of the element matrices.
- 3. Define the finite element mesh:** The mesh is composed by all the elements attached together. Significant result discrepancies might occur while using two different meshes, so it is crucial to introduce useful practices for setting up a relevant mesh. It is important to consider: a trade-off between accuracy and calculation time (both are inversely affected by the mesh refinement), the dimensionality (a 3D analysis is not always required, and 1D or 2D elements might be sufficient), a trade-off between the order versus the number of elements used, the compatibility (continuity has to be ensured between elements of different types) and distortion (too much deformed elements may lead unreliable results).
- 4. Calculate and assemble the problem matrices:** Each element matrix is computed using the virtual work principle. Translated into the element local domain by means of the Jacobian matrix, each element matrix can be assembled to form the global system matrices. For modal analysis, the element stiffness and mass matrices are calculated using the stress-strain relationship from the theory of linear elasticity.



5. **Solve the system** of linear equations: The real eigenvalue problem of Eq. (2.11) needs to be solved through matrix inversion iterations. Several eigenvalue extraction methods exist to solve efficiently different sizes of problems: the iterative Lanczos method, the reduction Householder method, etc [112].
6. **Post-process**: The solution of the real eigenvalue problem, *i.e.* undamped natural frequencies and mode shapes, being solved, it is important to verify the results for instance by checking the satisfaction of the boundary conditions, the solution convergence and their physical meaning consistency.

It is important to note that the damping is not modelled. It is hard to estimate the damping matrix by computational means because of the various damping phenomena occurring, *e.g.* friction, viscous damping [10]. But it plays a significant role in the output vibrations. Modal damping is commonly assumed, and supposes that the damping matrix  $[D]$  is diagonal in the real mode basis. In this case, the damping matrix is linked to the modal damping ratio  $\xi_k$  of each mode  $k$  by

$$\forall k \in [1..N], \quad 2\xi_k\omega_k = \{X_k\}^T [D] \{X_k\} \quad (2.14)$$

$\xi_k$  is usually estimated beforehand from experience or experimental results.

### Experimental Modal Analysis (EMA)

The modal characteristics of a structure are estimated experimentally through Experimental Modal Analysis (EMA), which is carefully explained in [58]. In short, FRF measurements serve the construction of a measured MDOF FRF matrix  $[H(\omega)]$  that is curve-fit to its theoretical formulation of Eq. (2.12). For every structure to test, a standard procedure is followed:

1. **Setup the test**: A large part of the experiments consists in the testing setup definition. The boundary conditions (free-free, fixed) are chosen based on the goals of the tests, the choice on the number of measurement points (measurement discretization) as well as the excitation type (hammer, shaker) and locations have to be based on the frequency range of interest and the available sensors. For intrinsic characteristic estimation of a structure, free-free boundary conditions are reproduced by hanging the system with flexible ropes given that they shall eliminate the interference

between flexible and rigid modes by allocating the latter at very low frequency; *e.g.* less than 1 Hz.

- 2. Verify measurement consistency** from Digital Signal Processing (DSP) metrics: From an input ( $I$ ) force, one captures the output ( $O$ ) acceleration and calculates the FRF matrix coefficients  $H_{OI}(\omega)$  with a dedicated method (H1, H2 or Hv [58]). For each coefficient calculation several similar measurements are performed and the sets of identical coefficients are averaged to eliminate random noise. Linearity has to be checked as well. Every real structure is intrinsically non-linear, but linearity can be assumed to some extent in order to perform the parameter identification through linear modal analysis. A linearity test verifies if the ratio output/input corresponding to any FRF is input-independent. It can be evaluated by performing several tests with different forces input levels. A reciprocity condition implies that the waves follow the same transfer path independently from the input location, *i.e.*  $H_{OI}(\omega) = H_{IO}(\omega)$ . One can verify that by measuring the FRF from an input force at a point A and output acceleration at a point B and then reversing the experiment by applying a force on point B and measuring the response at point A. The closeness between the two FRFs corroborates the reciprocity. Repeatability principle can be seen in two aspects: the sample repeatability and the test repeatability. The first states that two identical samples tested within the same operational configuration should demonstrate an equal structural behavior, while the second states that two similar tests of the same sample should show an equal structural behavior.
- 3. Estimate modal parameters:** The modal model used to extract the modal parameters corresponds to the linear mathematical parametric equation 2.12. Curve-fitting of each FRF  $H_{OI}(\omega)$  is a common solution to collect the unknown values although it is not trivial to implement. Advanced algorithms shall be used such as Least Squares Complex Exponential (LSCE) [55] and PolyMAX [100].
- 4. Validate the modal model:** The estimated modal parameters are immediately correlated with the raw measurement data using different validation metrics. The synthesized FRFs show measurable discrepancies from their equivalent measured FRFs. The Modal Assurance Criterion (MAC) matrix, the mode participation, complexity and phase collinearity are also metrics that evaluate the validity of the modal model chosen.

### 2.2.3 Calculation of the forced response

After completing the calculation of the transfer characteristics, it is necessary to compute the forced response of the system to a given excitation. The output displacement  $\{X(\omega)\}$  which is the forced response to harmonic excitation is simply derived from the multiplication of the FRF matrix  $[H(\omega)]$  with the excitation force vector  $\{F(\omega)\}$ :

$$\{X(\omega)\} = [H(\omega)]\{F(\omega)\} \tag{2.15}$$

A measure of the excitation efficiency of each DOF for each mode is defined as the modal participation factor matrix  $[L]$  [58],

$$[L] = [Q_1\{X_1\} \dots Q_N\{X_N\} \quad Q_1^*\{X_1\}^* \dots Q_N^*\{X_N\}^*]^t \tag{2.16}$$

It can be used extensively to know the best excitation location to (de)activate certain modes, and is therefore used in the upcoming Chapter 6 to attenuate noise.

## 2.3 Fundamentals of acoustic transfer systems

Vibrating structures also transfer energy acoustically (Fig 2.10). An input vibration velocity  $v(t)$  of a structural volume generates particle displacements in the vicinity of the structure surface that partially travels through the surrounding medium and produces pressure fluctuations as output. Humans transform this acoustic energy into an electrical signal through the ear system [44]; sound is then perceived by the human receiver.

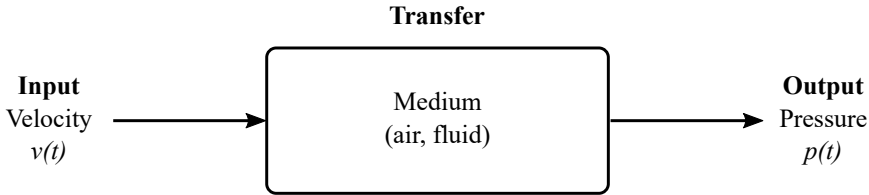


Figure 2.10: Acoustic system

In general terms, sound propagation follows the acoustic wave equation. It is derived from the Helmholtz wave equation applied to the propagation of longitudinal waves [130]:

$$\nabla^2 p - \frac{1}{c_0^2} \frac{\partial^2 p}{\partial t^2} = 0 \quad (2.17)$$

where  $\nabla^2$  is the Laplace operator,  $p(\mathbf{M}, t)$  the complex acoustic pressure (in pascal - Pa),  $\mathbf{M}$  the point where the pressure is calculated and  $c_0$  the sound velocity. The solutions of Eq. (2.17) are obtained by separation of variables:

$$p(r_0, t, \omega) = \Re[P(r_0, \omega)e^{j\omega t}] \quad (2.18)$$

where  $r_0$  is the distance from the source to the receiver point and  $\omega$  the angular frequency, and Green's theorem (in free- space) gives the solutions of Eq. (2.17) via the Kirchoff-Helmholtz integral formulation [130]:

$$P(r_0, \omega) = \frac{1}{4\pi} \oint_S \left( j\omega\rho_0 v_n(\omega) \frac{e^{-jk_0 r_0}}{r_0} + p_S(\omega) \frac{\partial}{\partial n} \frac{e^{-jk_0 r_0}}{r_0} \right) dS \quad (2.19)$$

where  $S$  is the closed surface,  $\rho_0$  the mass density of the surrounding fluid,  $v_n$  the sound particle velocity normal to  $S$  (*i.e.* direction  $n$ ),  $k_0 = \omega/c_0$  the wave number and  $p_S$  the sound pressure on  $S$ . This formulation provides the starting point for many numerical formulations, *e.g.* the Boundary Elements Method (BEM) for unbounded domains [67]. After constructing and solving the matrix system, the pressures and normal velocities are known for each element of the boundary surface  $S$ . Eq. (2.19) can be directly used to compute the pressure at each desired field point location.

However such simulation may be computationally expensive due to the fact that the system matrices need to be solved for each frequency and load case. The Acoustic Transfer Vector (ATV) concept [49] introduces input-output vector relations  $\{atv(r_0, \omega)\}$  that are reused for any load case and make the computations much faster. The ATV characterizes the transfer between the normal structural velocity  $v_n$  of a vibrating surface at a node of the mesh and the sound pressure  $P(r_0, \omega)$  at a specific field point at a distance  $r_0$ :

$$P(r_0, \omega) = \{atv(r_0, \omega)\}^T \{v_n(\omega)\} \quad (2.20)$$

Finally the human ear captures significant differences of sound pressure in a logarithmic scaling. Therefore the Sound Pressure Level (SPL)  $L_p$  is often defined:

$$L_p = 10 \log_{10} \left( \frac{p_{rms}^2}{p_0^2} \right) \quad \text{in dB} \quad (2.21)$$

where  $p_0 = 20 \mu\text{Pa}$  is the pressure threshold from which the human ear perceives something, *i.e.* reference pressure, and  $p_{rms}$  is the root-mean-squared value of the pressure.

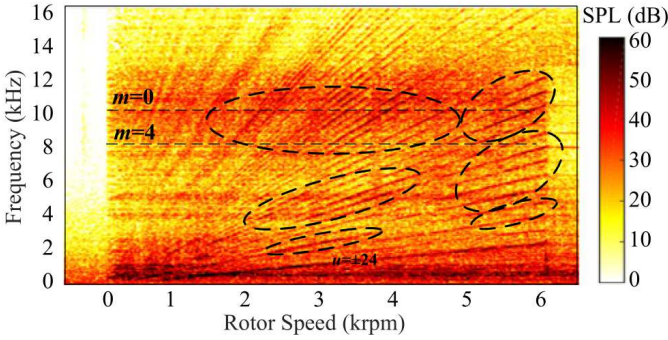
## 2.4 Typical measured acoustic noise from a rotating electric machine

In traction applications, the electric machine never operates at constant speed and torque conditions, *i.e.* in steady-state configuration. That is one of the reasons why acoustic sound radiated by a rotating electric machine is often measured in run-up/down conditions, *i.e.* when the machine is accelerating/decelerating. It allows identifying critical operating points quickly in terms of NVH comfort.

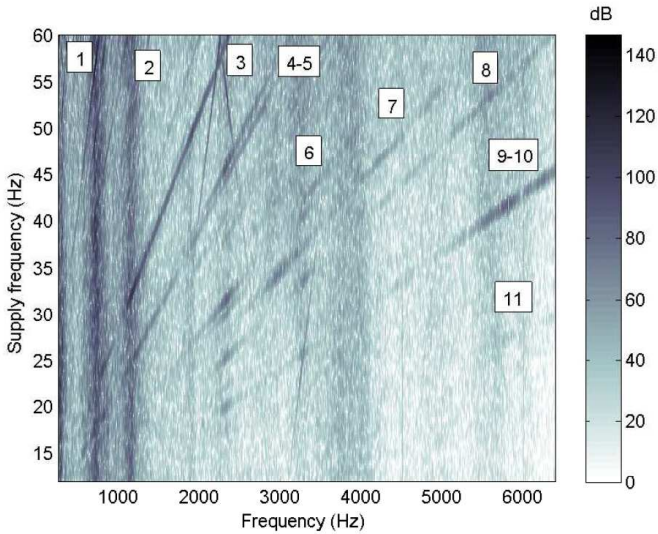
Acoustic noise radiated by rotating electric machines is typically characterized by their magnetic noise components described in Section 1.1.1: order lines, resonance phenomena and switching frequency components. Fig. 1.2 introduces these characteristics from an acoustic signal measurement of an 8/6 SRM during a run-up using its spectrogram displayed as a colormap, *i.e.* a 3D plot where the magnitude is represented with a color scale. Essentially a spectrogram is obtained by computing the Short Time Fourier Transform [54] of the time signal to be characterized, *e.g.* acoustic pressure, force, acceleration vibration, etc. It represents the series of spectra that are calculated over intervals (windows) of the complete signal and thus depends on the tracked quantity (time or machine speed) and its time-harmonic (*i.e.* frequency) arrays. Numerous authors present the acoustic noise of rotating electric machines in this colormap form. For example, Dong et al. [40] present the acoustic spectrogram (represented as a colormap) of a 12/8 SRM and Le Besnerais [74] measures it from a small IM. Fig. 2.11 illustrates the colormaps they obtain from their run-up tests.

Dong et al. show the frequency on the y-axis and the rotor speed on the x-axis. In that case the horizontal lines linked to high SPL amplitudes indicate resonance phenomena of the structure [19], *i.e.* mode excitation. The oblique lines are the order lines [47]: a factor times the rotational speed is called an order; if the rotational speed is referred to as order 1, two times the rotation speed is order 2. In rotating electric machines this factor is defined by the number of rotor poles  $Q_r$  such that the frequency of the orders  $f_{\text{order}}$  reads

$$f_{\text{order}}(N_{rot}, Q_r, n_o) = \frac{N_{rot}}{60} \times Q_r \times n_o, \quad n \in \mathbb{N}^* \quad (2.22)$$



(a) Picture taken from [40]



(b) Picture taken from [74]

Figure 2.11: Typical acoustic spectrograms for run-up tests, taken from literature

where  $N_{rot}$  is the rotor speed (in rpm) and  $n_o$  the order harmonic. In fact the amplitude of the signal along each order line can be displayed against the rotational speed or against the frequency and is referred to as order cuts [47]. Their amplitude depends on the machine itself and originates from the magnetic flux density distribution. Some orders can vanish because of geometry reasons, *e.g.* Fiedler et al. [45] define a method to quantify the harmonic content, both spatial and time, of SRMs and find particular topologies that suppress the occurrence of certain orders.

Le Besnerais [74] decides to swap the x and y axes, such that resonance phenomena correspond to vertical lines and look to contribute significantly to acoustic noise. The vertical line at 700 Hz is briefly correlated with a stator bending mode excitation which no published literature offers a thorough explanation of its occurrence, while the one at 1.1 kHz corresponds to the so-called ovalization mode [45], later described in Section 5.1. The order lines are observable but no link with the number of rotor poles and the rotational speeds can be set because this data is not provided by the author. Yet one can notice that the contribution of some orders to the acoustic noise is low compared to others.

Supported by both literature cases presented above and others [41, 42, 19, 76], it is assumed that the magnetic noise components dominate acoustic noise radiated by rotating electric machines. Resonance phenomena significantly contribute to the acoustic sound radiation and potentially generate unpleasant noise due to their high tonality characteristics. The orders also play a non-negligible role in comfort definition and consequently have to be considered.





## Chapter 3

# The multi-physical nature of magnetic noise

Predicting magnetic noise is essential to propose adequate solutions to overall NV improvements of an electric machine, and as seen in the previous chapter, its modeling requires a multi-physical approach. This presupposes that each step of the multi-physical modeling simulation has to correlate with experimental data, and with as little computational efforts as possible. Therefore in Section 3.1 two multi-physical modeling frameworks are developed and employ different levels of complexity. They are applied to an SRM from which reference test data is presented in Section 3.2. Finally the simulated results for both models are compared with the reference measured ones at each physical step of the multi-physical simulation process in Section 3.3.

### 3.1 Simulation of magnetic noise during run-up

The multi-physical simulation process for the magnetic noise calculation might employ different levels of complexity but it always follows the general physical transfer flow of Fig. 1.1. From the feeding current waveforms, the machine geometry and the material parameters, one can calculate the air-gap magnetic flux density and thus the induced force density applied on the stator. The forces are input of the structural transfer system (*i.e.* the stator) which radiates energy in the form of acoustic pressure fluctuations. This method is commonly utilized for magnetic noise prediction [41, 42, 19].

Because of the multi-physical approach employed and its associated computational burden, one of the first assumptions when calculating the acoustic pressure emitted by an electric machine during a run-up case is to represent an acceleration phenomenon as a set of successive steady-state operations. In this situation, the multi-physical modeling process to go from electrical input to acoustic output is followed for every single operating point that reconstructs the discretized run-up/down. Thus being neglected, additional contributions from transient phenomena happening in between the considered points are discussed separately in Appendix B.

This Section presents two multiple steady-state approaches of different computational complexities that are used for the multi-physical simulation of an 8 slots-6 poles SRM, later referred to as SRM 2. It is important to mention that any effect from the windings, the slot liners, the winding potting, the cooling jacket, the housing and the end-plates is neglected. In fact the laminated stator core is usually one of the largest contributors to the stiffness and mass of the complete machine and therefore plays a significant role in its modal characteristics [56], compared to windings [141], housing [139] and other components [109].

### 3.1.1 FE Models

The method in one of its most detailed approaches involves FE models in all the physical domains. The modeling flow of such method is illustrated in Fig. 3.1 and described below with the example of SRM 2.

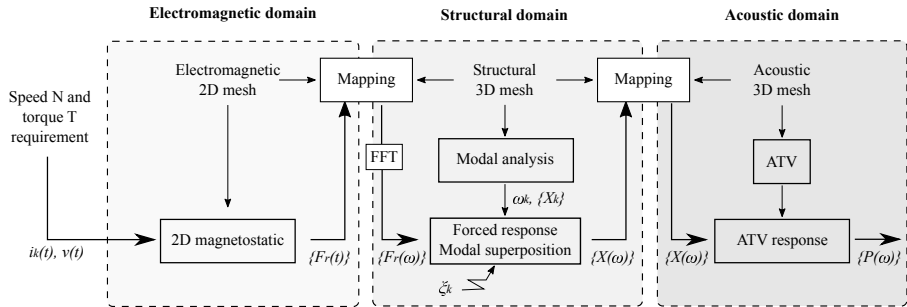


Figure 3.1: Detailed FE modeling flow

## Electromagnetic domain

For each simulation, fixed values of speed  $N_{rot}$  and torque  $T$  are associated with steady currents and voltages waveforms. A 2D magnetostatic problem is defined for the electromagnetic model. This assumption is relevant when, because of particular geometry and boundary conditions, the magnetic field can be supposed uniform along the axis of symmetries. In radial-flux machines, it is equivalent to neglecting the end-windings effects, which is a common assumption made in literature [74, 33]. The magnetostatic problem in 2D FE solves Eq. (2.1) and Eq. (2.3). Here the magnetostatic field solution is computed using the open-source software FEMM. The 2D mesh is generated carefully by taking magnetic mesh quality constraints into account, *i.e.* fine mesh at the air gap [107, 97]. A convergence analysis was performed in order to validate the mesh created. For different mesh sizes, the resultant magnetic flux density at the air gap is plotted in Fig. 3.2. It can be seen that the magnetic flux density is not affected significantly by the mesh sizes. Therefore the final mesh was chosen with an airgap mesh size of 0.5 mm and the rest of the geometry (iron, coil, air) with a mesh size of 5 mm; leading to the 20,968-node mesh shown in Fig. 3.3. In fact it is important to note that it is not possible to use a coarser mesh due to the meshing algorithm embedded in FEMM which does not provide a mesh at the airgap coarser than the airgap length, jointly with the fact that the end results are mostly affected by the mesh discretization in the airgap interfaces [107, 97].

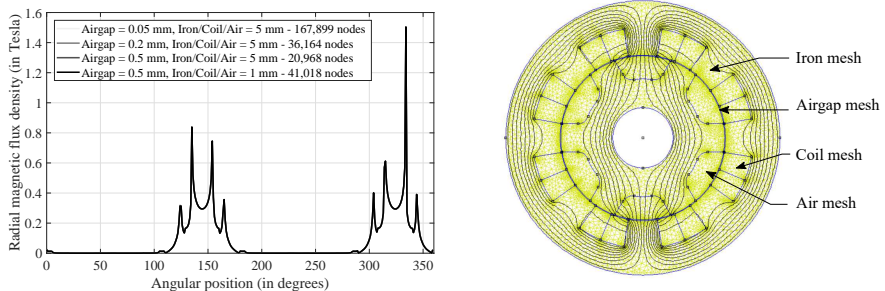


Figure 3.2: Electromagnetic mesh quality study: Results of convergence (left) and mesh geometry and magnetic flux lines for one magnetostatic problem (right)

Additionally, the input current waveforms are discretized with a sampling frequency  $f_s$ . For each time increment  $\delta t = 1/f_s$ , the rotor is rotated over an angle  $\delta\theta$  and the field solution is recalculated. In theory a full mechanical rotation needs to be simulated, but it is computationally expensive. Thus one

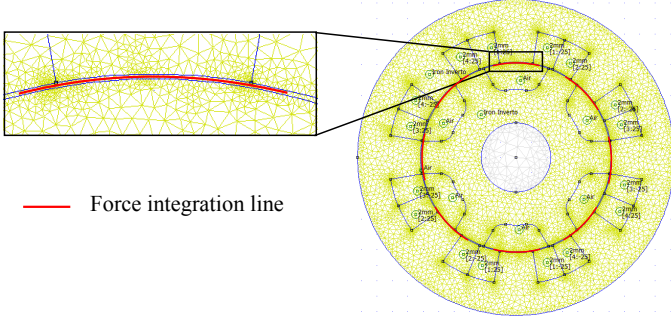


Figure 3.3: 2D electromagnetic mesh and force integration line

can exploit the machine symmetries to simulate a fraction  $\theta$  (in degree) of a complete rotation. Each fraction incorporates  $n_\tau$  field solution calculations and leads to an output solution of time period  $\tau$ .

$$\tau = n_\tau \delta t = \frac{60}{N_{rot}} \frac{\theta}{360} \quad \text{in seconds} \quad (3.1)$$

It is important to recognize that the signals are to be transferred to the frequency domain for later forced response calculations, see Section 2.2.3. Hence special care arises on the choice of  $\delta t$  (thus  $\delta\theta$ ) and  $\tau$ , as mentioned in [74]. DSP theory tells us that  $\delta t$  should be at least inferior to the inverse of  $2f_{max}$  [58] ( $10f_{max}$  is considered) where  $f_{max}$  is the maximum frequency of interest, and that the frequency resolution  $\delta f$  in the frequency domain strictly equals the inverse of  $\tau$ . If  $\tau$  is too small, the frequency resolution  $\delta f$  becomes too rough, so one can repeat the signal fragment  $p$  times as suggested in Annex B. Indeed it leads to a  $p$ -times finer frequency resolution  $\delta f/p$ . Finally, the magnetic flux density in the middle line of the air-gap  $\{B(t)\}$  is collected:

$$\text{for each } (N_{rot}, T), \quad \{B(t)\} = \{B(\underbrace{\delta t, \dots, \tau, \dots, p\tau - \delta t, p\tau}_{p\theta \text{ rotations}})\} \quad (3.2)$$

From this magnetic flux density, the force density  $\{\sigma(t)\}$  acting on the stator can be calculated using Eq. (2.7). Several authors investigate the added value of incorporating the tangential component contribution but conclude that it is not significant to the magnetic noise emission [36]. Hence it is assumed that the magnetic flux density contributes to the force production only with its radial component  $B_r$ , leading to the nodal radial force  $\{F_r(t)\}$

$$\text{for each } (N_{rot}, T), \quad \{F_r(t)\} = -\frac{\{B_r(t)\}^2}{2\mu_0} d\theta L_{stack} \quad \text{in newton} \quad (3.3)$$

where  $d\theta$  is the distance on which the magnetic flux density is integrated to provide nodal variables, and  $L_{stack}$  is the stator length. This step corresponds to Fig. 3.4a. Then for computational reasons and having a low curvature at the tooth-end region allows us to simplify the force  $\{F_r(t)\}$  to one resultant force  $\{F_r(t)\}_{eq}$  per stator tooth (illustrated in Fig. 3.4b),

$$\text{for each } (N_{rot}, T), \quad \{F_r(t)\}_{eq} = \frac{\sum_1^{n_{forces}} \{F_r(t)\}}{n_{forces}} \quad \text{in newton} \quad (3.4)$$

where  $n_{forces}$  is the number of nodal forces along the integration line of Fig. 3.3 ( $n_{forces} = 7$  in Fig. 3.4a). Finally, for the use in 3D models, one has to extrude this resultant force along the stator length. It leads to an axial discretization of  $n_{forces,3D}$  nodal forces ( $n_{forces,3D} = 4$  in Fig. 3.4c) with the value  $\{F_r(t)\}_{eq,3D}$  expressed by,

$$\text{for each } (N_{rot}, T), \quad \{F_r(t)\}_{eq,3D} = \frac{\{F_r(t)\}_{eq}}{n_{forces,3D}} \quad \text{in newton} \quad (3.5)$$

It is important to note that vector notation  $\{\bullet\}$  is used because the quantities are distributed discretely along the mesh nodes.

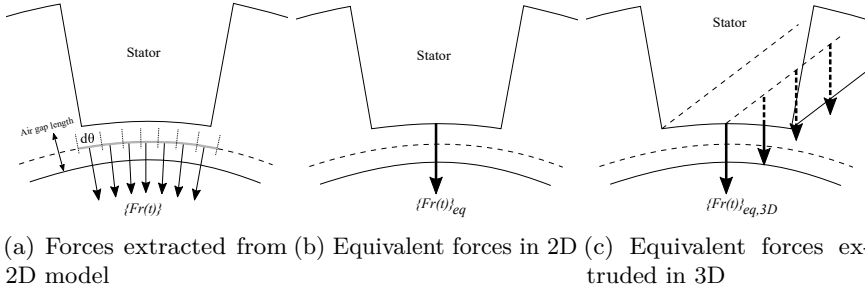


Figure 3.4: Illustration of the nodal forces transformation process

## Structural domain

For the structural domain, solely the stator core is modeled as the energy transfer. The housing and the rotor are supposed not to play a significant role

in magnetic noise generation. The notation of the stator modes " $X(x, x)$ " is described in the upcoming Section 5.1.

Given the different field equations to solve from the magnetic to the structural domain, the meshes are different. So a structural mesh for the stator core is created as suggested in Section 2.2.2, *i.e.* the mesh is validated in terms of fulfilling the trade-off accuracy versus computational time, by computing natural frequencies of the flexible modes between 1 Hz and 5 kHz, for different mesh sizes. Fig. 3.5 shows the results of the convergence analysis for the different mesh sizes (metric equivalent to the number of nodes). The model with the finest mesh provides the reference results. The convergence is assumed sufficient when the natural frequencies do not exceed 5% error compared to these reference values. At the same time, it is expected to have a computationally efficient model that runs in an acceptable time, *e.g.* several minutes. Finally, the chosen structural mesh is built from a 5 mm mesh size which leads to a composition of 246,023 3D linear tetrahedron elements (TETRA4 in Nastran formulation) containing 52,465 nodes; and is shown in Fig. 3.6.

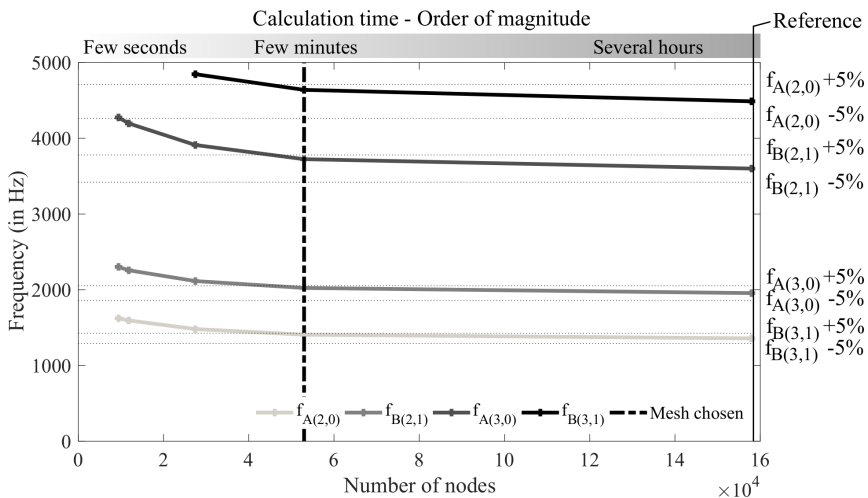


Figure 3.5: Structural mesh quality study: Results of convergence

The magnetic forces  $\{F_r(t)\}_{eq,3D}$  are distributed along the nodes located at the stator end-teeth of the electromagnetic mesh and need to be transferred to corresponding nodes of the structural mesh. At the same time, the work produced by the forces needs to be conserved. A conservative force mapping algorithm [3] is thus used. Later a Fast Fourier Transform (FFT) analysis permits to obtain the Discrete Fourier Transform of the time-domain forces  $\{F_r(t)\}_{eq,3D}$ , *i.e.* forces in the frequency-domain  $\{F_r(\omega)\}_{eq,3D}$ .

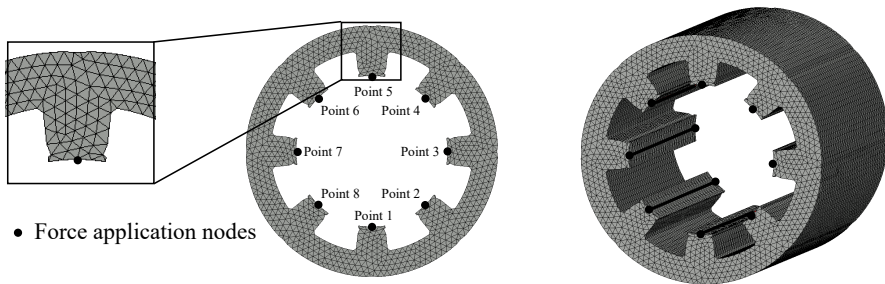


Figure 3.6: 3D structural mesh and force application nodes

As a first approximation, isotropic material properties from manufacturer datasheet are used for the M300-35A steel composing the stator core; *i.e.* Young's modulus of 185 GPa, mass density of  $7,650 \text{ kg/m}^3$  and poisson ratio of 0.287. The associated model is later referred to as **Iso**. The upcoming Section 5.8.1 will discuss thoroughly the consequences of using such material simplification. Modal analysis is performed with free-free boundary conditions to eliminate the test rig contributions to the overall structural dynamics. Modal damping is defined from literature trends [128, 125, 101]; the pure radial modes  $A(n_r, 0)$  are assigned modal damping values of  $\xi_{A(n_r,0)} = 0.001$ , while the anti-symmetric modes  $B(n_r, 1)$  are given values of  $\xi_{B(n_r,1)} = 0.005$ .

The forced vibration response displacement  $\{X(\omega)\}$  is finally calculated from the modal superposition technique [62], as described in Section 2.2.3.

### Acoustic domain

The vibratory energy from the outer surface of the stator core is transferred to the air medium through an acoustic 3D FE mesh. Similarly as for the translation from the electromagnetic to the structural domain, the field equations of the structural and the acoustic domains require different mesh quality. The acoustic mesh needs to envelop the complete core. Its element size is determined by the wavelength of the maximum frequency of interest. In theory it should be extended up to the microphone receiver locations, but this would require too much computational effort. Hence an artificial boundary with no reflection is defined and truncates the acoustic medium; it refers to Automatically Matched Layer (AML) [4]. Fig. 3.7 illustrates the acoustic mesh used for SRM 2.

After giving material properties to the air fluid, the ATV (implemented in LMS Virtual.Lab® FE software package) is calculated and the pressure spectrum

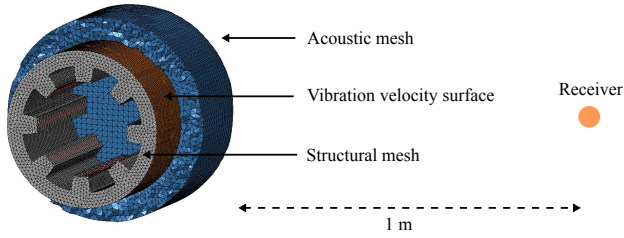


Figure 3.7: 3D acoustic mesh and vibration velocity surface application to the acoustic system

$\{P(\omega)\}$  at a chosen sink (e.g. a microphone, human ear, etc) is computed through Eq. (2.20). In general the sink receiver is located one meter away from the vibrating source as depicted in Fig. 3.7.

### 3.1.2 Analytical models

The method presented in the previous Section can be quite accurate however it follows a cumbersome process, given all the FE meshes and calculations involved. Analytical models benefit from convenient implementation and relatively high computational speed. The modeling flow of such method is illustrated in Fig. 3.8 and described below with the example of the SRM 2 under study.

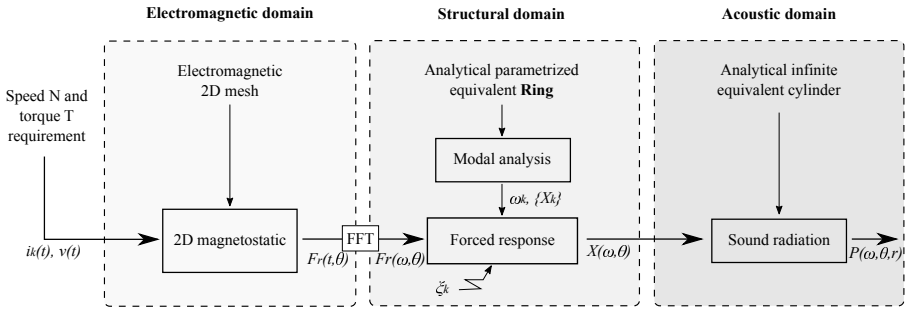


Figure 3.8: Analytical modeling flow

#### Electromagnetic domain

The resultant magnetic forces  $\{F_r(t)\}_{eq}$  computed in the 2D model of Section 3.1.1 are used as well in this part because the purpose is to compare the



vibro-acoustic models.

### Structural domain

In this approach the force is fully represented by its azimuthal  $\theta$  and temporal  $t$  discrete distribution, while for the previous FE method the mesh was defining the spatial distribution which led to a force vector  $\{F_r(t)\}_{eq}$ , now to  $F_r(t, \theta)$ . Hence a force mapping is not necessary.

An FFT is performed and leads to a frequency-distributed force  $F_r(\omega, \theta)$ . Similarly to the previous method, special attention is required on the sampling frequency  $f_s$  and on the signal total period  $\tau$ . Additionally the spatial-FFT  $F_r(\omega, n_r)$  of  $F_r(\omega, \theta)$  can be calculated. The spatial harmonic is defined with the mode order  $n_r$ , which follows the notation of the pure-radial modes described in the upcoming Section 5.1, because in the ring model only these modes occur.  $F_r(\omega, n_r)$ , denoted FFT 2D  $F_r(t, \theta)$ , is an interesting indicator to identify the contribution of the force wave on each pure radial modes, and is also required to calculate the vibration forced response.

Regarding the modal analysis, the stator core is modeled as an equivalent circular ring that contains corrective coefficients to take the third dimension into account [61] as depicted in Fig. 3.9. The natural frequencies  $f_{A(n_r, 0)}$  of this free-free circular ring are obtained by [82],

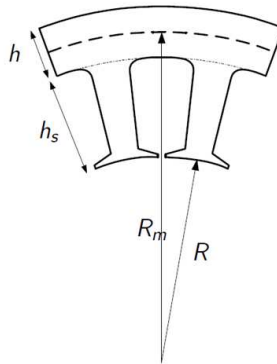


Figure 3.9: Equivalent ring representation of the stator core

$$f_{A(n_r,0)} = \begin{cases} f_{C(0,0)} = \frac{1}{2\pi R_m} \sqrt{\frac{E}{s_f \Delta \rho}} & \text{for } n_r = 0 \\ f_{A(1,0)} = f_{C(0,0)} \sqrt{\frac{2}{1+\kappa^2 \frac{\Delta_m}{\Delta}}} & \text{for } n_r = 1 \\ f_{C(0,0)} \kappa \frac{n_r(n_r^2-1)}{\sqrt{n_r^2+1}} \frac{1}{\sqrt{1+\kappa^2 \left(\frac{n_r^2-1}{n_r^2+1}\right) [3+n_r^2(4+\frac{\Delta_m}{\Delta})]}} & \text{for } n_r \geq 2 \end{cases} \quad (3.6)$$

where  $n_r$  is the radial mode order,  $R_m$  the stator mean radius,  $E$  the Young's modulus of elasticity and  $\rho$  the mass density. The remaining parameters relate to the machine topology and are described as follows,

$$\text{Stacking factor: } s_f = \frac{n_s \cdot t_s}{L_{stack}},$$

$$\text{Relative mass increase due to windings and teeth: } \Delta = 1 + \frac{G_z + G_w}{G_y}, \quad (3.7)$$

$$\kappa = \frac{1}{2\sqrt{3}} \frac{h}{R_m},$$

$$\Delta_m = 1 + \frac{Q_r}{2\pi R_m} \frac{12b_z h_s^3}{h^3} \left[ \frac{1}{3} + \frac{h}{2h_s} + \left( \frac{h}{2h_s} \right)^2 \right] \frac{G_z + G_w}{G_z}$$

where  $n_s$  is the number of steel sheets,  $t_s$  the thickness of one sheet,  $L_{stack}$  the length of the full lamination stack,  $h$  the stator yoke height,  $G_z$  the stator teeth weight,  $G_w$  the winding weight,  $G_y$  the yoke weight,  $Q_r$  the number of rotor poles,  $b_z$  the stator mean tooth width, and  $h_s$  the stator tooth height. In the thesis, this model is referred to as **Ring**. For SRM 2, the equivalent parameters are given in Table 3.1.

Table 3.1: SRM 2 geometry parametrization

Parameter	Unit	Value
$R$	mm	61.80
$R_m$	mm	92.45
$h$	mm	20.10
$L_{stack}$	mm	185
$E$	GPa	185

The output vibration displacement  $X(\omega)$  is calculated using the forced response formulation of the **Ring** model [82, 74, 121] with the same modal damping

values  $\xi_{n_r}$  as in previous Section 3.1.1.  $X(\omega)$  is the sum of the displacement contributions  $X(\omega, n_r)$  from each mode  $n_r$  given by,

$$X(\omega, n_r) = \begin{cases} \frac{RR_m}{Eh} \frac{F_r(\omega, n_r)}{2\pi RL_{stack}} \eta(\omega, n_r) & \text{for } n_r = 0, 1 \\ \frac{RR_m}{Eh} \left[ \frac{1+3\kappa^2(\kappa^2-1)}{\kappa^2(\kappa^2-1)^2} \right] \frac{F_r(\omega, n_r)}{2\pi RL_{stack}} \eta(\omega, n_r) & \text{for } n_r \geq 2 \end{cases} \quad (3.8)$$

$\eta(\omega, n_r)$  is the resonance factor for the spatial harmonic  $n_r$  allocating for dynamical effects,

$$\eta(\omega, n_r) = \frac{1}{\sqrt{\left(1 - \left(\frac{\omega}{2\pi f_{A(n_r,0)}}\right)^2\right)^2 + \left(\frac{2\xi_{n_r}\omega}{2\pi f_{A(n_r,0)}}\right)^2}} \quad (3.9)$$

It is interesting to notice that when the force and mode shape meet the same spatial distribution at the same frequency with no damping, *i.e.*  $\omega = 2\pi f_{A(n_r,0)}$  and  $\xi_{n_r} = 0$ ,  $\eta$  goes to infinity which gives an infinite displacement; *i.e.* resonance effect.

### Acoustic domain

The acoustic pressure is calculated from the acoustic power generated by a radiator. Timar et al. [122] describe three acoustic-source models commonly employed for the stator radiation factor modeling: the spherical model, the cylindrical model and the plane-radiator model. They correspond to different  $L_{stack}/R_m$  ratios that stand from 0.5 to 2, from 2 to 3 and above 3, respectively. For our case, this ratio equals 2.3 so the sound radiator considered in the acoustic model is an infinite cylinder. The use of the infinitely long cylinder model is questionable since the stator length is finite. However the work of Gieras et al. [50] on the validity of considering infinite cylinder length model against finite cylinder length model comforts us using the infinitely long cylinder assumption.

The sound pressure  $p(t, \theta, r_0)$  at a distance  $r_0$  and an angle  $\theta$  from the radiating surface is determined in the time domain by the summation/superposition of negative and positive rotating vibration waves coming from each mode  $n_r$  [140]

$$p(t, \theta, r_0) = \int_{\omega=-\infty}^{+\infty} \underbrace{\sum_{n_r=-\infty}^{+\infty} P(\omega, n_r, r_0) e^{jn_r\theta} e^{j\omega t}}_{P(\omega, \theta, r_0)} d\omega \quad (3.10)$$

where, for an infinite cylinder radiator,

$$P(\omega, n_r, r_0) = -\frac{j\rho_0 c}{\frac{dH_{n_r}^{(2)}(k_0 r_0)}{d(k_0 r_0)}} H_{n_r}^{(2)}(k_0 r_0) \dot{X}(\omega, n_r) \quad (3.11)$$

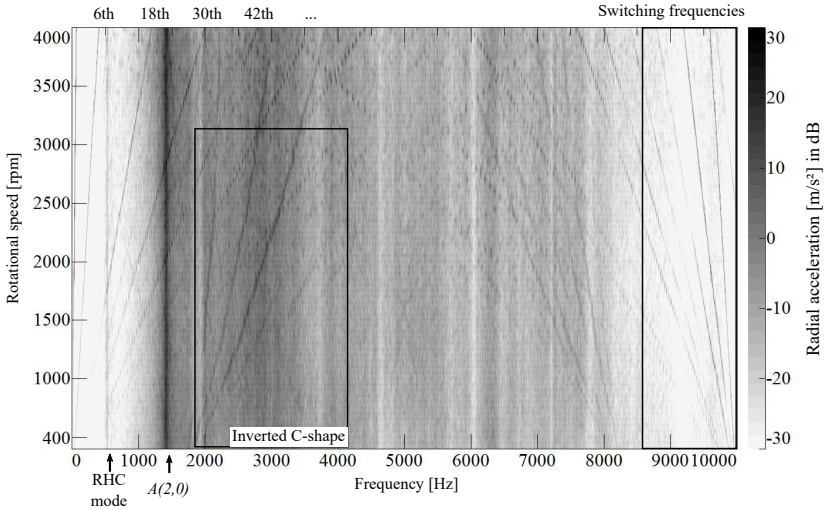
with  $\rho_0$  the air mass density,  $c$  the sound velocity in the air,  $H_{n_r}^{(2)}$  the  $n_r$ <sup>th</sup> order Hankel function of the second kind and  $k_0 = \omega/c$  the acoustic wave number. The  $n_r$ <sup>th</sup> spatial-harmonic velocity  $\dot{X}(\omega, n_r)$  contributing to the total particle velocity simply corresponds to the radial velocity of the radiating surface:

$$\dot{X}(\omega, n_r) = j\omega X(\omega, n_r) \quad (3.12)$$

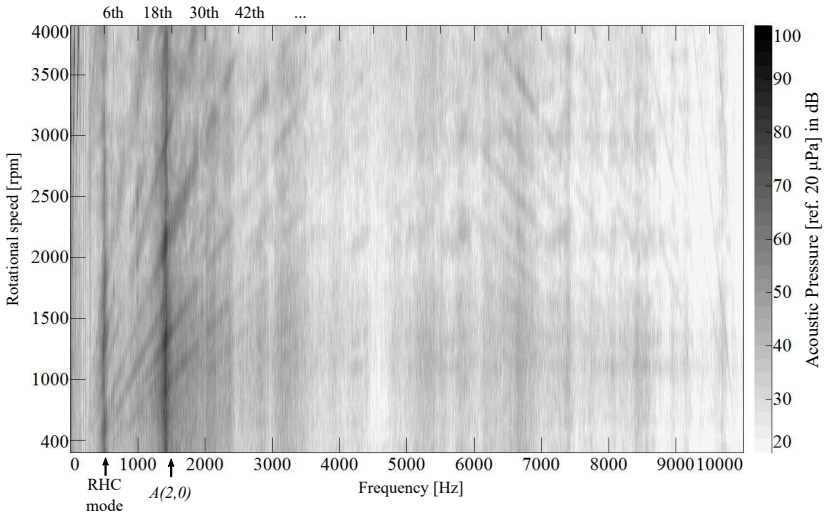
## 3.2 Reference experimental data

Experimental results described below are the reference from which accuracy assessment on the developed multi-physical models are performed. The measurements were performed on SRM 2 hanged to emulate free-free vibrations. It is then not necessary to model the test bench and simplifies the correlation process. Moreover the measurements were done in accelerating condition (run-up) at no load. Fig. 3.10 illustrates (a) the acceleration vibration measured at an outer surface point of SRM 2 and (b) the acoustic pressure measured one meter away from SRM 2.

Resonance phenomena can be observed as vertical darker lines and are synonyms of mode excitations; a detailed EMA is later performed on SRM 2 in Section 4.3.2 and identifies clearly the two major excited modes to be the ovalization mode  $A(2, 0)$  at 1,409 Hz and the Rotor Housing Coupling (RHC) mode at 534 Hz described in the upcoming Sections 5.1 and 4.3, respectively. The switching frequency at 10 kHz is also observable with its frequencies multiple of 6. The orders multiple of 6 dominate the response as well, as expected by Eq. (2.22), although even numbers of 6-multiples tend to vanish (*i.e.* 12, 24, 36, etc). The reason to this extinction is purely geometric and has to do with the number of poles/slots as explained by Fiedler et al. [45]. Additionally the so-called



(a) Acceleration measurements



(b) Acoustic pressure measurements

Figure 3.10: SRM 2 measurement colormap during run-up

inverted C-shape originates from the hysteresis control that induces current ripple thus force oscillations, and thus structural vibrations [108, 91].

### 3.3 Result comparisons

In this Section, the results for each step of the multi-physical simulation process are presented, for both modelling strategies considered.

#### 3.3.1 Input currents

As mentioned in Section 2.1.3, an SRM is not fed by sinusoidal currents due to its non-linearity behavior and the fact that the rotor position is in the control loop as well. Therefore the four currents ( $I_A, I_B, I_C, I_D$ ) that feed SRM 2 are taken from experimental measurements as input to the models and are shown in Fig. 3.11 (a) at 1,000 rpm. The FFT of the phase A current is displayed in Fig. 3.11 (b) at 1,000 rpm and extended for every rotational speed case in Fig. 3.11 (c).

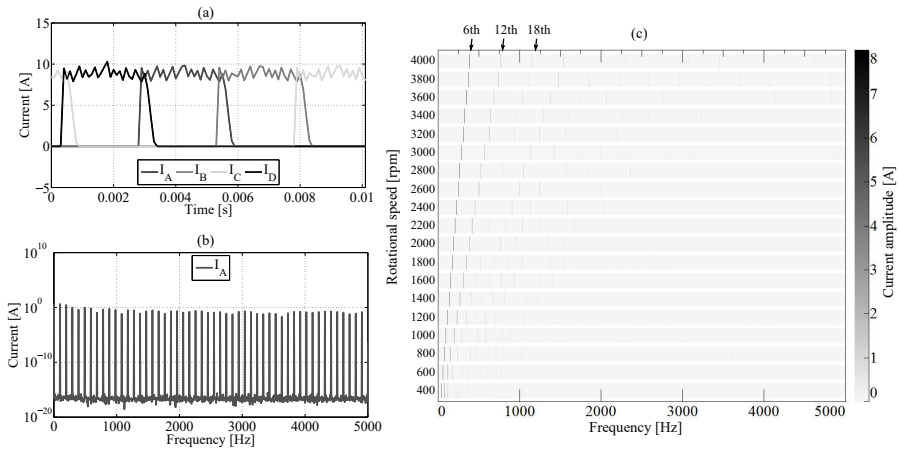


Figure 3.11: Current profiles: (a) currents versus time at 1,000 rpm, (b) current versus frequency at 1,000 rpm, (c) current versus frequency for every calculated speed

The frequency  $f_{order}$  of the orders is clearly observable and follows the behavior of Eq. (2.22). Indeed here the number of rotor poles is equal to  $p = 6$  so one can expect fundamental order frequency at 100 Hz for 1,000 rpm case, as shown

in Fig. 3.11 (b) and further extended in 3.11 (c). Harmonics of the fundamental frequency are present as well, although with lower amplitudes.

### 3.3.2 Force wave distribution

The resultant radial force wave distribution characteristic at 1,000 rpm is shown in Fig. 3.12. At first (a) the force profile is given depending on time and the angle position. It is important to mention that the spatial discretization is so small (8 points along the circumference) that it was decided to use large color bands to be able to see magnitudes changes over time, although the forces apply only at located nodes. Then (b), for four fixed force application points (denoted in Fig. 3.6), the force wave time distribution is given, and (c) for three fixed time instants, the force wave spatial distribution is plotted. Finally it is interesting to present the time and space harmonics of the force wave distribution (d), *i.e.* the FFT 2D.

The radial forces are exclusively negative, see Fig. 3.12 (a), which makes sense as the magnetic flux pulls the stator teeth inwards. Additionally the modes activated by these forces (at 1,000 rpm) can be determined. The odd spatial harmonic components are null which indicates that pure radial modes of odd  $n_r$  values are hardly excited by these forces, see Fig. 3.12 (d). On the other hand, the zero and even spatial harmonics are significantly present in the force profile, which can be problematic for the remaining pure radial modes activation, denoted  $A(2n_r, 0)$  modes which notation is further described in Section 5.1.

### 3.3.3 Structural vibrations and acoustic radiation

First the structural characteristics obtained with the two different models are confronted to the experimental results in Table 3.2. Only frequencies between 1 Hz and 5 kHz are considered.

Table 3.2: Structural characteristics results, N/M - Not Measured, N/A - Not Applicable

	Mass	Mode natural frequency (Hz)			
	kg	$A(2, 0)$	$B(2, 1)$	$A(3, 0)$	$B(3, 1)$
Experiments	50.0	1,409	N/M	3,430	N/M
<b>Iso</b>	22.0	1,395 (-1.0%)	2,009	3,697 (+7.8%)	4,621
<b>Ring</b>	21.5	1,176 (-16.5%)	N/A	3,129 (-8.8%)	N/A

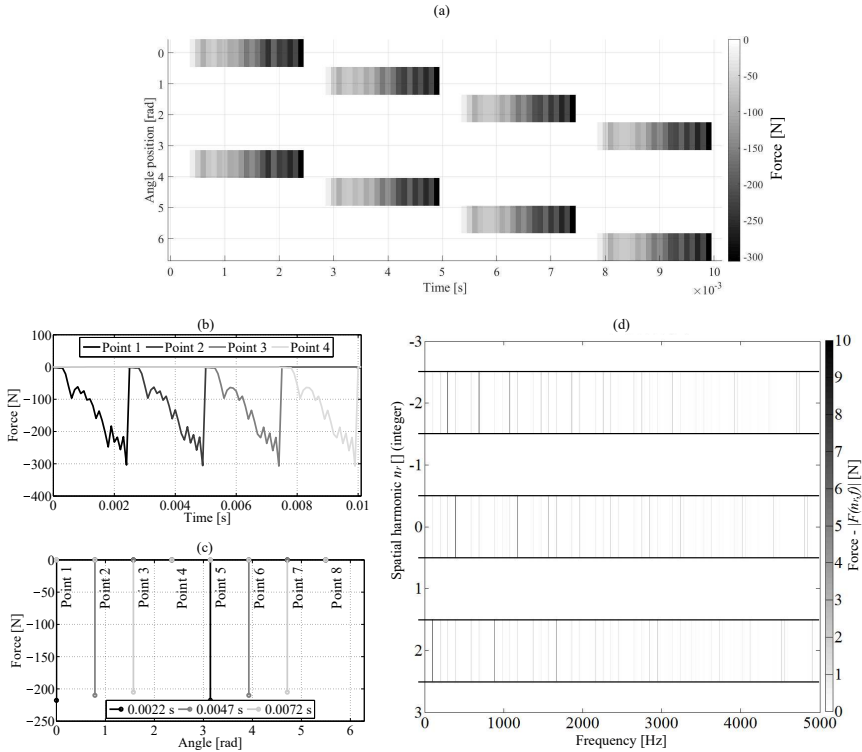


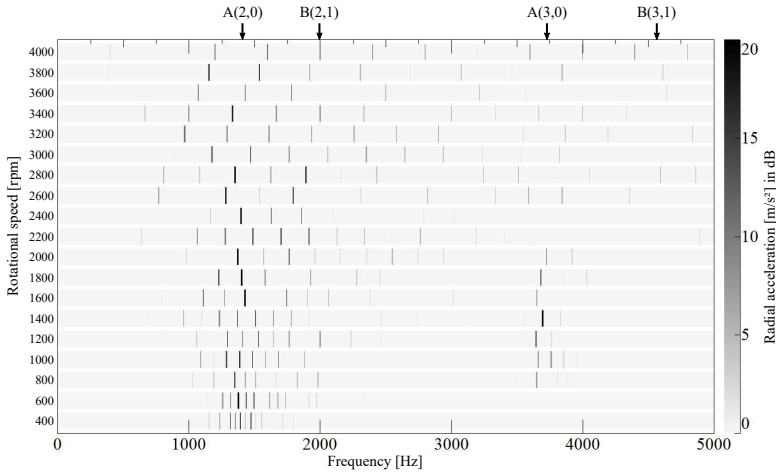
Figure 3.12: Radial force profile at 1,000 rpm: (a) versus time and angle position, (b) versus time for four different application points, (c) versus angular position for three different time instants, (d) versus time and spatial harmonics

Despite the natural frequency discrepancies of about  $\pm 10\%$ , one can consider the model accuracy sufficient knowing that only the stator core is modeled, whereas the complete (assembled) machine is tested in Section 3.2. Naturally the anti-symmetric modes  $B(n_r, 1)$  (see Section 5.1 for mode notations) are not captured by the **Ring** model, as mentioned in Section 3.1.2. However they are considered in **Iso** with the previously defined damping values, and also contribute to the acoustic noise of the machine.

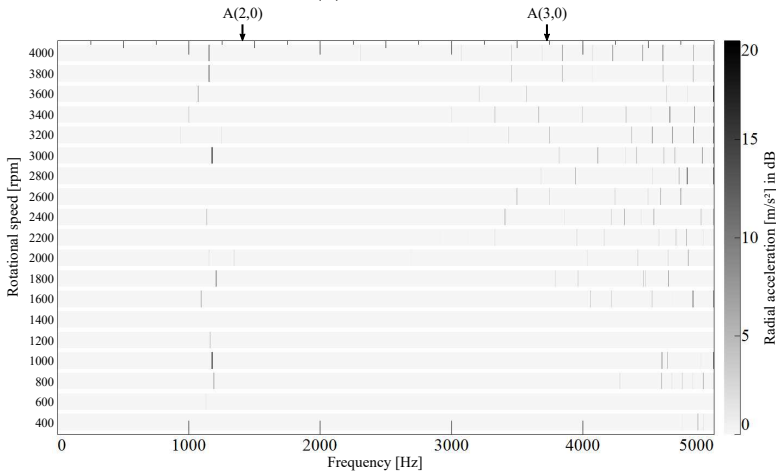
Fig. 3.13 shows the radial acceleration spectrum  $\ddot{X}(\omega)$  at an outer surface point of the stator core for every speed case, and both multi-physical modeling strategies.

Resonance phenomena and order lines are observable in both modeling cases, yet with different behaviors. As expected from the force distribution of Fig. 3.12 (c),





(a) FE Models



(b) Analytical models

Figure 3.13: Radial acceleration results for (a) FE models and (b) analytical models

the triangle mode  $A(3, 0)$  is hardly excited because the third spatial-harmonic component is null. Similarly the anti-symmetric modes  $B(n_r, 1)$  are not excited because the force profile does not vary axially. The ovalization mode  $A(2, 0)$  is activated, with increased vibration amplitudes around its frequency. However the vertical line that defines a resonance does not appear as in Fig. 3.10. This is due to the fact that steady-state operations do not take transient effects into account; these latter ones contain extra frequency components on the force side which excite easily certain modes. This fundamental phenomenon is explained further in Annex B and justifies the need for transient forces in run-up simulations. Additionally, since the operational speed cases are not all calculated but discretized for computational-cost reasons, the critical operating points where orders cross a resonance are not necessarily considered.

The occurring orders are all (even and odd) multiples of 6 as expected by Eq. (2.22), but odd multiples of 6 should vanish because of symmetries [45]. In fact when order cuts are performed for the six first multiples of 6 (6, 12, 18, 24, 30 and 36), as shown in Fig. 3.14, lower amplitudes for odd multiple of 6 orders are not clearly observable in comparison to the even ones. The phenomenon is essentially observable for higher order numbers where acceleration values are significantly higher than lower orders. On the other hand resonance phenomena are observable, yet with quite large amplitude discrepancies, either due to the use of inaccurate damping or from the inaccurately estimated mode's natural frequency. It is also important to note that having computed more speed/load cases would provide better discretization of the results, thus enlarging conclusion capabilities in terms of resonance amplitude, with the obvious disadvantage of increasing the computational efforts. But overall considering the assumptions of the models, the structural response trends correlate with experiments, although increased accuracy is required and may be coped by characterizing modal parameters in more details.

Regarding the acoustic sound radiation, Fig. 3.15 shows the acoustic pressure spectrum at a receiver one meter away from the outer surface of the stator core for every speed case, and both modeling strategies adopted.

As mentioned previously for acceleration results, resonance and order phenomena can be observed in the acoustic pressure spectrum. The ovalization mode  $A(2, 0)$  shows the highest pressure amplitude components compared to the triangle  $A(3, 0)$  and anti-symmetric modes  $B(n_r, 1)$ . Order cuts are performed similarly as for acceleration results, see Fig. 3.16, and demonstrate particularly the importance of resonance effects on the acoustic response. **Iso** and **Ring** modeling strategies show similar results with respect to acoustic results.

However it is important to note that in both acceleration and acoustic simulated results, the RHC mode at 534 Hz is not captured. Since it shows quite high

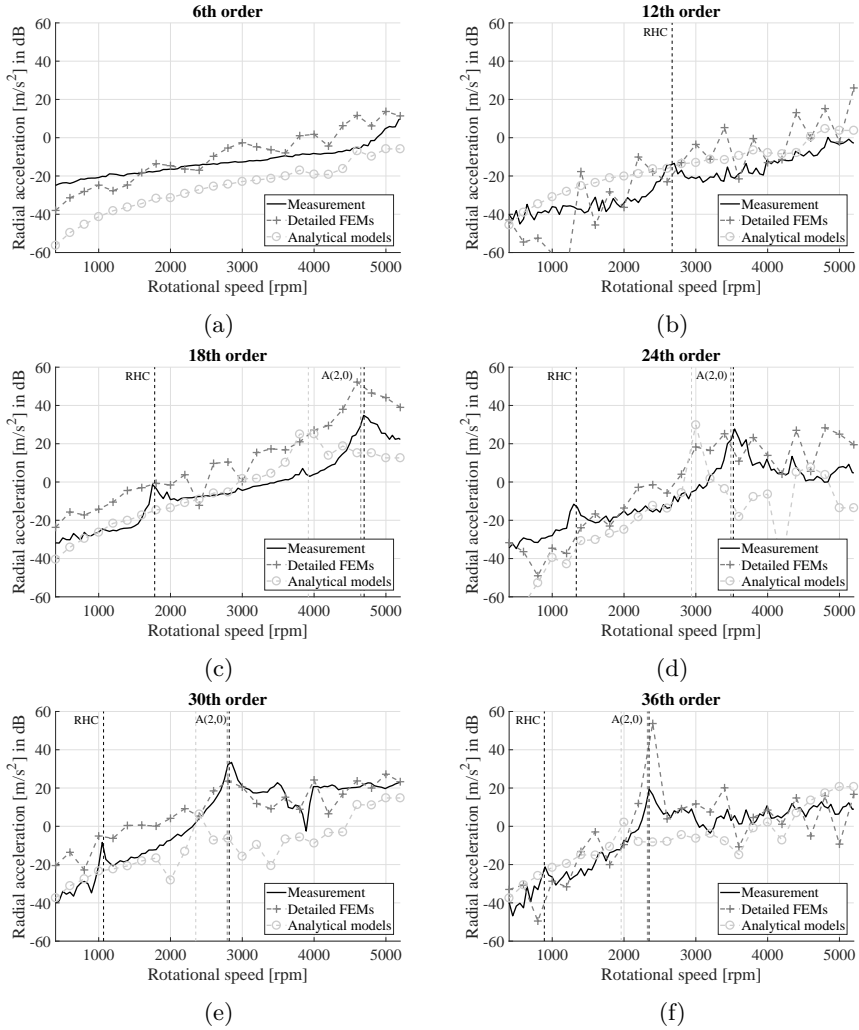
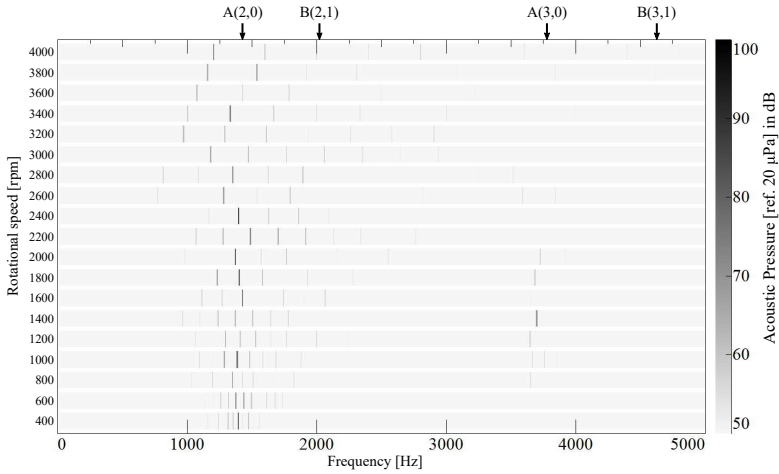
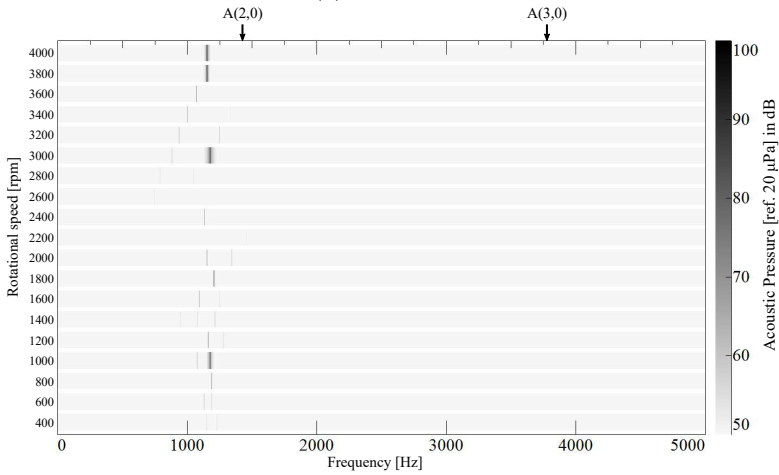


Figure 3.14: Radial acceleration order cut results



(a) FE Models



(b) Analytical models

Figure 3.15: Acoustic pressure results for (a) FE Models and (b) Analytical models

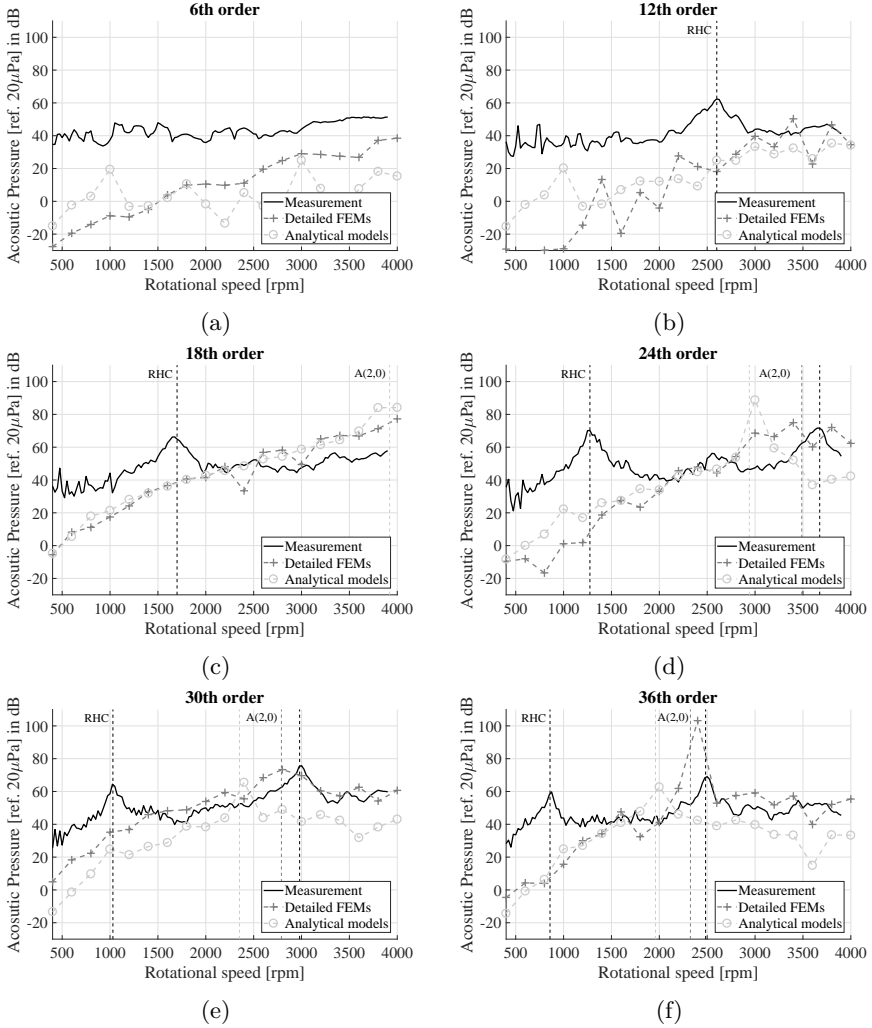


Figure 3.16: Acoustic pressure order cut results

acoustic pressure amplitude, the occurrence of the RHC mode is thoroughly investigated in the upcoming Section 4.3.

### 3.3.4 Computational time considerations

It was noted previously that a higher discretization of load/speed cases can provide smoother results, thus allowing the extension of the conclusions in terms of amplitudes at resonances. However computational efforts are immediately impacted by such consideration. The common trade-off accuracy-computational effort is therefore defined.

Despite the capability of both models to provide relevant results, their computational cost is of interest in early design stages. Table 3.3 indicates the average computational time for both models per steady-state operating point to calculate, on a laptop Intel Core i7 4800MQ CPU (2.7 GHz) with 16 GB RAM memory. The code implemented for the analytical models was manually optimized to run as fast as possible, yet following hardware limitations, and the FE models were solved using the commercial software package LMS Virtual.Lab®.

Table 3.3: Average computational time for both models per steady-state operating point

Domain	Model step	FE models	Analytical models
Electromagnetic	400,...,4000 rpm		700,...,70 s
Structural	Modal analysis	60 s	0.0065 s
	Forced response	60 s	0.0060 s
Acoustic	ATV	3000 s	-
	Acoustic response	60 s	1.64 s

The electromagnetic simulations spend different amount of time depending on the operating point, since each steady-state simulation has different rotational period lengths but with the same time step. Moreover, since the structural and acoustic responses rely on multiplication operations, their computations can be optimized by running modal analysis and ATV once. Yet the FE models are much slower compared to the analytical ones. It is also important to mention that the model implementation is not taken into account and requires significantly more time for the FE models than for the analytical models.

### 3.4 Intermediate conclusions

The multi-physical nature of magnetic noise was thoroughly investigated by comparing, at each physical step of magnetic noise generation, experimental measurements with two different models of different complexities. The first modeling approach entirely uses FE models (**Iso**) while the second one adopts analytical formulations (**Ring**) to compute magnetic noise. Both modeling strategies were applied to a SRM which was tested experimentally.

The feeding currents were measured and input of an electromagnetic model where currents were transferred into magnetic forces. It is important to note that given the focus on vibro-acoustic analyses, only one electromagnetic model was used for both multi-physical modeling strategies. Furthermore due to the practical difficulties to place force sensors in the air gap, no force measurement could be done. However the simulated forces follow the expected signature, *i.e.* the order frequencies  $f_{order}$  are observable. Additionally their spatial distribution contains significant even harmonic components (see Fig. 3.12 (c)) which are subjected to excite  $A(2n_r, 0)$  modes.

Regarding the structural domain where magnetic forces are transferred into structural vibrations, several discrepancies could be observed. Yet, the accuracy was considered acceptable at this stage, especially given the significant assumptions made for the **Ring** model and the fact that only the stator core was modeled. Then calculating the forced response permitted to identify the resonance and order phenomena, see Fig. 3.13. As expected from the force spatial harmonics, the modes  $A(3, 0)$  and  $B(3, 1)$  are not excited as compared to mode  $A(2, 0)$ . However resonances are not activated for every operational case, unlike in experiments, because transient phenomena are not incorporated in the force profile, see Annex B. The order cuts from Fig. 3.14 correlate with the trend expectations and measurements. **Iso** still shows higher accuracy than **Ring** essentially because of modal characteristics higher accuracy.

Regarding the acoustic domain where structural vibration velocity is transferred into acoustic pressure fluctuations, similar conclusions to the ones drawn in the structural domain were given. The mode  $A(2, 0)$  is responsible for the most critical resonance effect such as in the experiments, see Fig. 3.15. Order cuts from Fig. 3.16 emphasize the importance of resonance phenomena on the acoustic spectrum signature of the machine, and thus on the higher accuracy brought by **Iso** compared to **Ring**. Moreover, it was shown that the RHC mode significantly contributes to the acoustic noise radiation, and therefore will be investigated further in Section 4.3.

Finally it was noticed that the assumption of considering only the stator core as the energy transfer is sufficient to obtain relevant accuracy. From computational

efforts perspectives, the analytical model **Ring** is particularly interesting for pre-designing phases while the FE model **Iso** has to be considered when higher accuracy is requested and time is less problematic. However given that resonance phenomena considerably affect magnetic noise, it is suggested to predict as accurately as possible each component structural characteristics, notably the rotor influence (linked to RHC mode) and the laminated stator core (linked to  $A(2,0)$  mode).



## Chapter 4

# Rotor influences on the electric machine vibro-acoustic behavior

The rotor is the term that describes the assembly of the laminated rotor core with the rotating driving shaft. For higher overall performance (efficiency, power density) the rotor core geometry is often optimized while the shaft is kept the same. However slight changes on the rotor core topology induce different magnetic field distribution and are expected to play a non-negligible role in magnetic noise emission. At the same time due to its connections to the assembly, the shaft interferes with the assembly structural dynamics and immediately affects the radiated acoustic noise.

Therefore this chapter starts by giving a non-exhaustive list of the common rotor core design changes in Section 4.1, with their effects on the machines' performances inherently affecting NV behavior. Different rotor core topologies of a SynRM are then numerically modeled in Section 4.2 and permit to assess the importance of taking small geometry changes into account, in terms of acoustic outcome and torque ripple. Finally the structural dynamics interference of the rotor on the complete assemblies of different machine sizes and types is investigated in Section 4.3.

## 4.1 Common rotor design changes

The rotor is extensively studied in literature, essentially because it transfers the electrical energy into mechanical torque and speed, which process involves losses and ripples. Significant performance improvements can be achieved from the optimization of the rotor core cross section topology. In the case where PMs are used, their shape is of utmost importance. The machine losses and the produced torque are immediately impacted and justify optimization schemes to be employed [66, 73]. More generally for electric machines with or without PMs, the number and geometry of the rotor poles is a key-component of overall performance improvements. Azizi et al. use the Taguchi optimization design procedure for the rotor geometry and manage to maximize the torque to current ratio of a SynRM [12]. Zhang et al. also increase power density and torque density of their machine by optimizing a claw-pole rotor material, dimensions and construction [147]. Another interesting research work is the one from Chitroju et al. [30] who propose the concept of non-skewed asymmetrical rotor slots. In fact, based on Annex A wording, they introduce a number of radial symmetries that is different from the number of poles. In other words, the pole width varies along the circumference. They directly obtain acoustic noise reduction by tuning the magnetic forces output.

In fact regarding acoustic noise attenuation, researchers tend to focus on torque ripple reduction techniques [99]. Machine designers look at skewing as a method to reduce torque ripple. The rotor poles are skewed distributed such that they are radially symmetric and transversally asymmetric (see Appendix A for symmetry definition). The skew pattern is defined by a skew angle. Wang et al. apply numerically different skew angles to a brushless doubly-fed IM and identify significant torque ripple reduction capabilities [136]. Sugiura et al. propose a stepped skewing technique and claim by experimental validations a significant reduction of losses [116]. However no link between torque ripple and acoustic noise is made available to our knowledge.

## 4.2 Effects on the radiated magnetic noise

The geometry of the stator end teeth and rotor poles affect the magnetic flux lines and thus the force produced [30]. In order to define the influence of the rotor topology on the emitted magnetic noise, several rotor topologies of a SynRM are modeled in a multi-physical simulation framework (thoroughly detailed in Section 3.1.1). The study also permits to evaluate the link between torque ripple and acoustic noise.

### 4.2.1 Case study definition

A SynRM rotor comprises flux barriers that force the magnetic flux to traverse flux paths. The geometry of these barriers have direct effects on the flux distribution at the air gap hence the acoustic noise emitted. The SynRM under study is tailored for automotive electric powertrain application; *i.e.* the nominal power, torque and rotational speed of the machine are respectively  $P_{nom} = 22$  kW,  $T_{nom} = 100$  Nm and  $N_{nom} = 2100$  rpm. In this frame, several parameters are fixed and displayed in Table 4.1. Only the rotor geometry influence is investigated such that the stator topology remains unchanged.

Table 4.1: Machine's geometry parameters

Parameter	Unit	Value
Number of stator slots ( $Q_s$ )	-	24
Number of rotor poles ( $Q_r$ )	-	4
Air gap length	mm	1
Rotor diameter	mm	171
Stator outer diameter	mm	300

Four different rotor topologies are investigated; each is presented with flux lines in Fig. 4.1. They show various design choices of the flux barriers geometries. The first topology (a) is very similar to what can be found in literature [88, 69] and is used as base shape for further rotor structure optimization [64, 103]. The second topology (b) comprises rectangular-shaped barriers. The third rotor topology (c) is derived from the second one by removing the piece of steel enclosing the fourth flux barrier. These two topologies are considered to sense topology change influences. Finally, the fourth rotor (d) contains flux barriers whose geometry is obtained using curves equation derived from Zhukovski's function and permits a significant torque ripple reduction [43]. For the sake of consistency, let us call them respectively Rotor 1, 2, 3 and 4.

It is important to notice that Rotor 4 has significant lower mass which is an interesting asset to this topology. The induced lower inertia to the shaft provides higher acceleration capabilities to the powertrain.

Due to their computational cost, the analyses are run at particular rotational speeds and torques taken from the torque vs. speed curve. Steady state analyses are performed on those particular points shown in Fig. 4.2. The chosen velocities correspond to a discretization along the maximum torque and power lines; *i.e.* between 1600 rpm and 4800 rpm with steps of 400 rpm. For conciseness in the

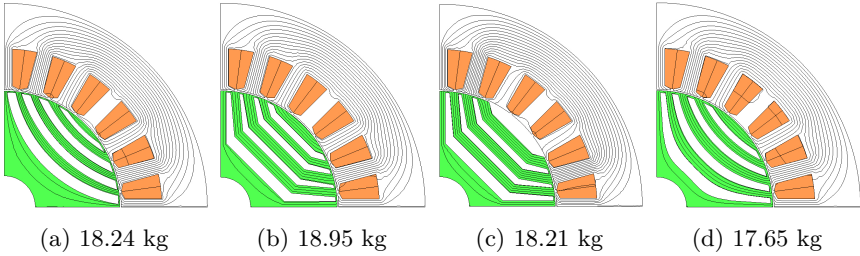


Figure 4.1: A quarter of the geometry and magnetic flux lines of the Rotor 1 (a), 2 (b), 3 (c) and 4 (d), with each complete machine stator (white) plus rotor (green) mass

rest of this study, the operating points will be referred to their rotational speed, although they also correspond to different torque requirements.

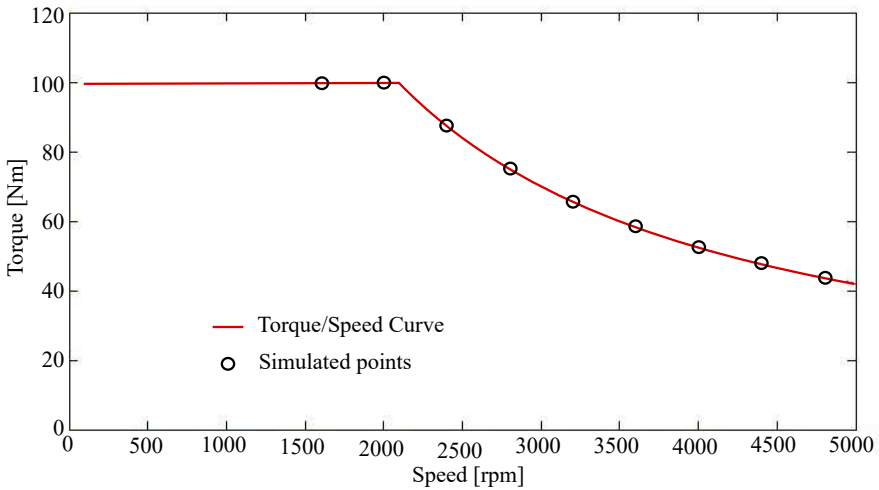


Figure 4.2: Torque vs. Speed curve of analyzed SynRM

### 4.2.2 Electromagnetic model and torque ripple assessment

A 2D magnetostatic analysis is carried out in JMAG® for each operating point of interest (see Section 3.1.1). The symmetry of the machine allows to run the simulation for 45 degrees of mechanical rotation, which significantly decreases the computation time. The sampling frequency is set to 50 kHz to guarantee the

observation of phenomena within the human audible range. The input feeding current for the studied SynRM is a pure sinusoidal three phase current (star connection). The supply frequency  $f_e$  (in Hz) ensures the required rotational speed  $N_{rot}$  (in rpm) and is given by:

$$f_e = \frac{Q_r}{2} \frac{N_{rot}}{60} \quad (4.1)$$

The magnetic flux density obtained for Rotor 1 at 4,400 rpm is shown in Fig. 4.3. The force along the air gap is immediately derived from Eq. (2.7), and the spatial distribution of the radial force calculated is shown in Fig. 4.4 at a fixed time instant for each rotor topology. This graph demonstrates that the flux barrier shape affects the magnetic flux density, and thus the force profile [98].

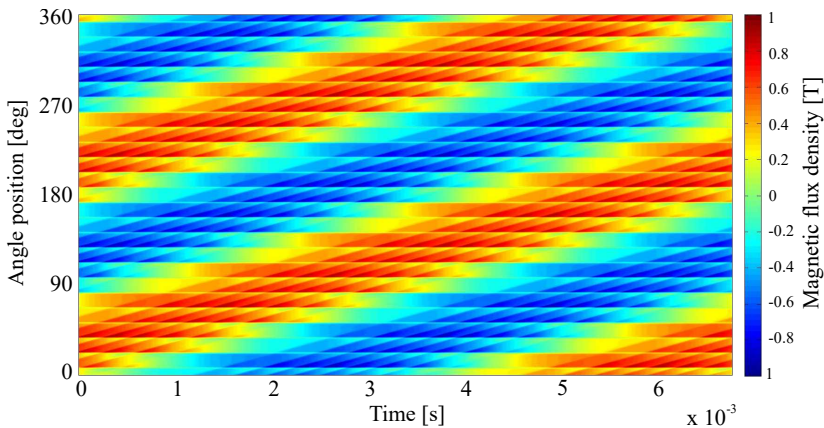


Figure 4.3: Magnetic flux density at 4,400 rpm with Rotor 1, versus time and angle position

Moreover the output torque versus time at 4400 rpm is displayed in Fig. 4.5 for every rotor topology, it is noticeable that the average torque  $T_{av}$  is achieved for all the rotor design cases. However its ripple varies significantly depending on the rotor topology. Its factor  $K_T$  is calculated as expressed in [26] together with its mean absolute deviation  $\Delta T$  calculated within the period  $T_0$ ,

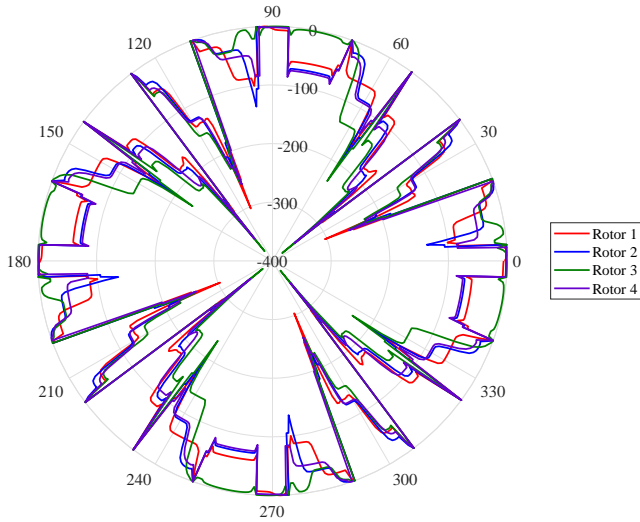


Figure 4.4: Radial force profiles at a fixed time instant, along the air-gap circumference, and for different rotors at 4,400 rpm

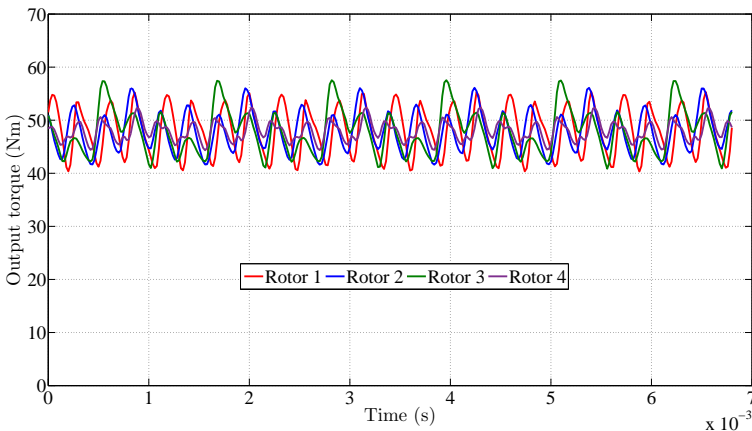


Figure 4.5: Output torque waveform for the different rotors at 4,400 rpm

$$K_T(N_{rot}) = \left( \frac{T_{max}(N_{rot}) - T_{min}(N_{rot})}{T_{av}(N_{rot})} \right) \times 100 \quad (\text{in } \%) \quad (4.2)$$

$$\Delta T(N_{rot}) = \frac{1}{T_0} \int_{T_0} |T(N_{rot}, t) - T_{av}(N_{rot})| dt \quad (\text{in Nm}) \quad (4.3)$$

$K_T$  and  $\Delta T$  are considered as relative and peak-to-peak torque ripples, respectively. They are functions of the rotational speed  $N_{rot}$  and the rotor topology as shown in Table 4.2.  $K_T$  is shown in Fig. 4.6. Rotor 1 produces the highest absolute torque ripple whereas Rotor 3 gives the highest relative torque ripple. Rotor 2 shows slightly lower torque ripples even though the variations between each speed are higher. It is important to notice that Rotor 4 is indeed optimized for torque ripple reduction, both absolute and relative [43].

Table 4.2: Torque ripple function of the rotor topology and the rotational speed

Speed $N_{rot}$ in [rpm]	Rotor 1		Rotor 2		Rotor 3		Rotor 4	
	$\Delta T$ in [Nm]	$K_T$ in [%]	$\Delta T$ in [Nm]	$K_T$ in [%]	$\Delta T$ in [Nm]	$K_T$ in [%]	$\Delta T$ in [Nm]	$K_T$ in [%]
1,600	8.88	32.9	6.99	34.8	7.67	37.6	4.17	18.7
2,000	8.67	32.4	7.06	34.8	7.86	37.2	4.15	18.6
2,400	7.96	33.9	6.12	34.5	6.68	36.9	3.44	18.8
2,800	6.77	33.3	5.27	32.6	5.82	36.3	2.92	18.1
3,200	5.92	35.3	4.04	28.5	5.13	39.6	2.55	21.0
3,600	5.03	33.4	4.27	34.1	4.44	36.9	2.11	18.6
4,000	4.56	34.8	4.33	39.0	4.06	39.1	1.99	20.8
4,400	3.91	31.5	3.17	30.2	3.49	34.9	1.56	16.8
4,800	6.78	32.5	6.59	34.2	6.55	36.8	4.98	19.0
Average	6.50	33.3	5.32	33.6	5.74	37.3	3.10	18.9

### 4.2.3 Structural and acoustic model

The structural and acoustic models used are described carefully in Section 3.1.1 but the main characteristics of the models are summarized further. The structural model makes the following assumptions:

- The **3D mesh** is defined from a detailed Computer Aided Drawing (CAD) and is composed of about 50,000 linear hexagonal elements (CHEXA8). It is important to note that the choice of the mesh size is the result of an accuracy/computational time trade-off as explained in Section 3.1.1.
- The steel constituting the stator core follows an **isotropic behavior** with the following mechanical parameters: a Young's modulus of 185 GPa, a Poisson coefficient of 0.287 and mass density of 7,650 kg.m<sup>-3</sup>.

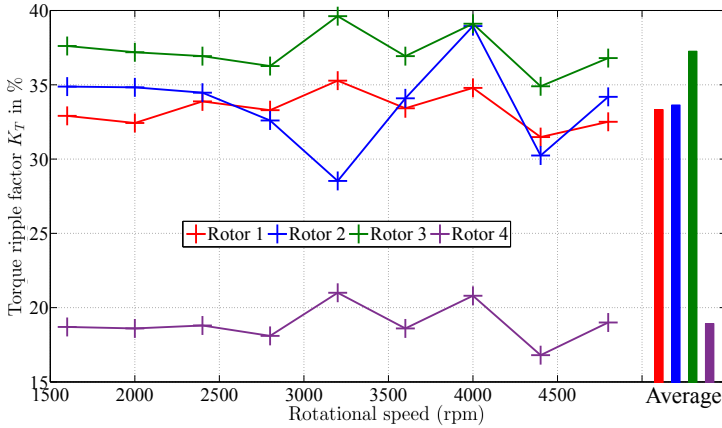


Figure 4.6: Torque ripple for the different rotors

- The **stator core only** is transferring the mechanical energy, *i.e.* the windings, slot liners, housing, cooling jacket and the rotor are not part of the structural model

The consequences of using this rather simplified structural model are described in Section 3.3.3. Once the mesh and material properties are set, the modal analysis is carried out in LMS Virtual.Lab®. Fig. 4.7 shows the undeformed structural mesh together with three modes (and their natural frequency) of the considered stator core within the frequency range of study, *i.e.* from 10 to 5 kHz.

The forced response follows the modal superposition principle detailed in Section 2.2.3, having the time-domain forces translated in the frequency domain by means of FFT. It is also required to perform a conservative mesh mapping from the forces distribution in the electromagnetic mesh transferred to the structural mesh as described in Section 3.1.1.

The acoustic pressure at one meter away from the stator outer surface is then evaluated through an ATV analysis as described in Section 3.1.1.

## 4.2.4 Results

The computed sound pressure is shown for the four rotor topologies in Fig. 4.8. For each operating point simulated, the frequency spectrum of the pressure



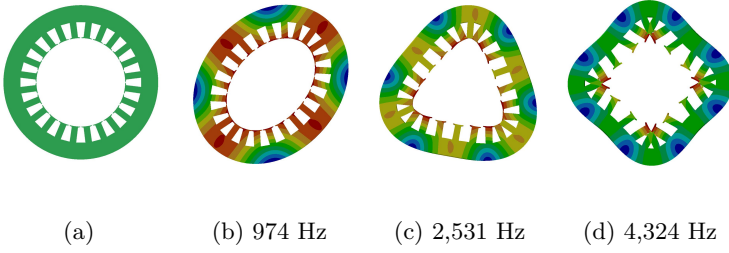


Figure 4.7: (a) Structural mesh, (b) Ovalization mode  $A(2,0)$ , (c) Triangular mode  $A(3,0)$  and (d) Square mode  $A(4,0)$  of the stator

magnitude is color-coded.

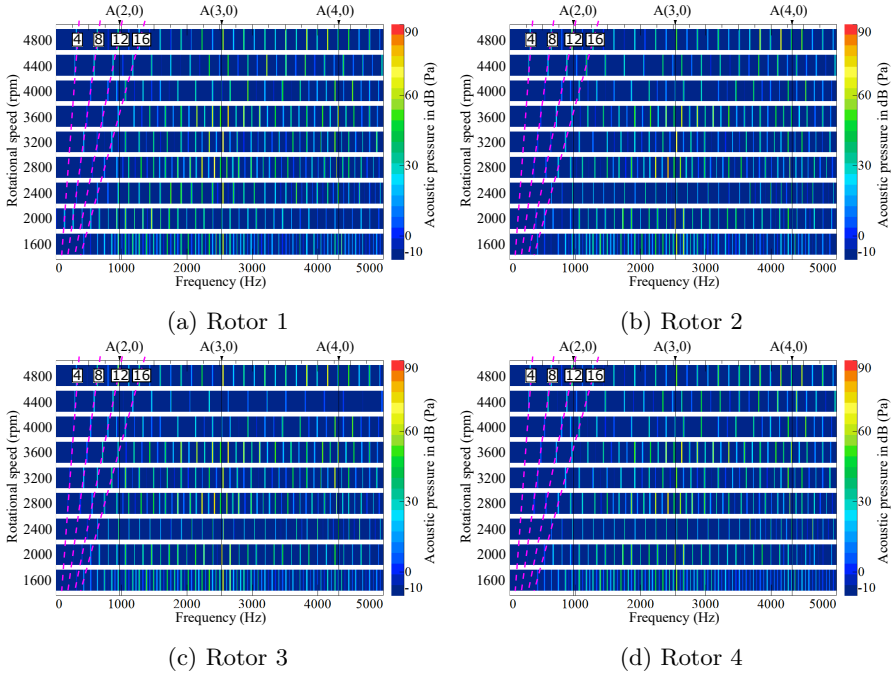


Figure 4.8: Acoustic pressure for the different rotors

Alike any rotating machine, one can notice the regular peaks of amplitude corresponding to the orders, see Section 2.4. The frequency of these orders  $f_{order}$  is derived from Equation (2.22). Since here the number of rotor poles is equal to 4 ( $Q_r = 4$ ), it is expected to see multiples of the 4<sup>th</sup> order. This

phenomenon is verified in Fig. 4.8. In order to identify the orders that are the most critical, average values of the orders are calculated depending on the rotor topology. Let us call  $P(n_o, N_{rot})$  the acoustic pressure for each harmonic  $n_o$  and every rotational speed  $N_{rot}$ . The idea is to define the arithmetic mean acoustic pressure  $\bar{P}_{N_{rot}}(n_o)$  radiated by each order  $n_o$  through the speeds  $N_{rot}$ . Then an averaged SPL  $L_p(n_o)$  is defined with regard to the reference pressure  $P_0 = 20 \mu\text{Pa}$ :

$$L_p(n_o) = 20 \log_{10} \left( \frac{\bar{P}_{N_{rot}}(n_o)}{P_0} \right) \quad \text{in dB} \quad (4.4)$$

The metric described above is calculated per order and is compiled in Fig. 4.9. It indicates the acoustic noise level is not heavily influenced by the first orders, *i.e.* 4<sup>th</sup> and 8<sup>th</sup>. However, at this stage, no immediate conclusion can be drawn on the effects of the rotor geometry on the acoustic pressure.

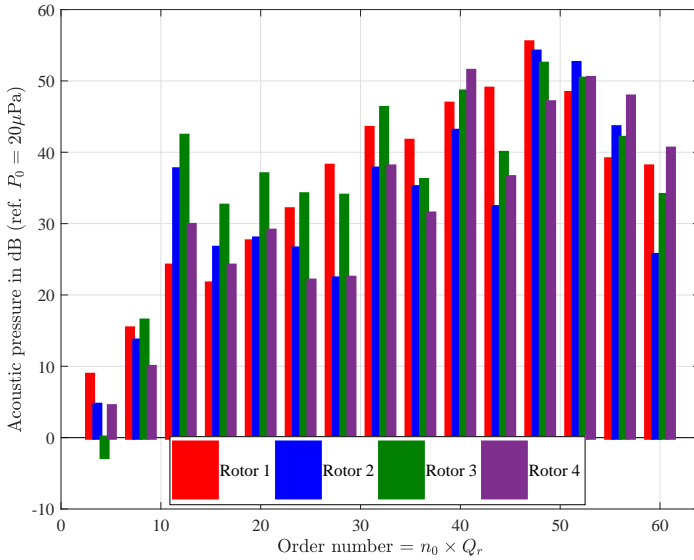


Figure 4.9: Average order cuts  $L_p(n_o)$  for the different rotors

$f_{order}$  is immediately linked to the magnetic force excitation and a resonance phenomenon might arise when the force pattern excites a structural mode of the stator, *i.e.* an order frequency  $f_{order}$  is equal to a natural frequency, and the force spatial distribution is similar to the mode shape. This phenomenon happens

close to the triangle mode  $A(3,0)$  at 2,531 Hz for all the rotor topologies simulated. The ovalization mode  $A(2,0)$  does not seem to be significantly excited, which indicates a low amplitude of the 2<sup>nd</sup> spatial order of the forces.

The previous indicators do not permit to define the best rotor topology. Hence a relevant indicator to quantitatively correlate the pressures from each rotor simulation at every rotational speed is the OverAll Sound Pressure Level (OASPL), as it gives an estimation of the SPL in dB that is produced by the machine at each speed  $N_{rot}$ ,

$$OASPL_{N_{rot}} = 10 \log_{10} \left( \int_{f_{min}}^{f_{max}} S_{N_{rot}}(f) df \right) \quad (4.5)$$

where  $f_{min}$  and  $f_{max}$  define the frequency range, *i.e.* from 10 Hz to 5 kHz, and  $S_{N_{rot}}$  the frequency spectrum of the pressure fluctuation for the rotational speed  $N_{rot}$ . Fig. 4.10 shows the  $OASPL_{N_{rot}}$  values for each rotational speed and rotor topology.

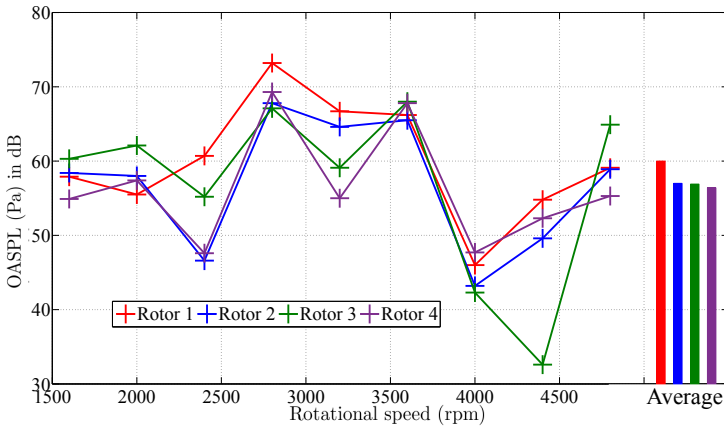


Figure 4.10: OASPL for the different rotors

Rotor 1 has the highest levels for most of the speeds. It is further confirmed by the arithmetic average which is 3 dB above the other geometries. On the other hand, it is interesting to see that the  $\overline{OASPL}$  is the lowest for Rotor 4.

Finally comparing Fig. 4.10 with Fig. 4.6 permits to verify if there is a link between torque ripple and acoustic noise. The  $OASPL$  has no trivial relation with the torque ripple itself. Indeed Rotor 3 and 4 give respectively the highest

and lowest torque ripple, yet this trend is not followed by the *OASPL*. No direct relationship could be established to link the torque ripple variations to the *OASPL* ones, which questions some current NVH optimization strategies that focus uniquely on torque ripple minimization [99].

Finally former design from Rotor 1 is to be avoided because of higher acoustic noise; the lack of flux-barrier from Rotor 3 is to be avoided because of high torque ripple; and Rotor 4 is to be preferred to Rotor 2 because of large torque ripple reduction and a little more acoustic pressure diminution.

### 4.3 Effects on the assembly structural dynamics

Not only from an air-borne point of view but also from a structure-borne point of view should an electric machine radiate acoustic noise due to the rotor mechanical joints to the housing. Rotor unbalances and eccentricities have a known impact on the vibration outcomes [75]. For instance these may introduce unbalanced magnetic pull [146, 143, 29] responsible for extra order frequency excitation.

Beside these unbalance-related issues, the topology of the assembly itself may also encourage resonance phenomena emerging from to rotor/housing interferences. One often refers to as shaft whirling [75]. It is essentially related to shaft vibrational resonances that happen either when the rotor stands still and when the rotor rotates. As seen in [117], the first associated flexible mode shape happens when the rotor is static. The natural frequency of this mode does not depend on the rotational speed and only shows planar deformations. On the other hand, whenever the rotor starts turning, this planar motion becomes 3D *i.e.* the rotor center traces out a circle; yet the natural frequency of the corresponding mode is equal to the planar motion case (non rotating) and is independent on the rotational speed. In fact, the rotational speed influences the mode frequency only starting from the second mode shape. For instance this mode shape shows asymmetric deformation with respect to the transverse center of the machine. Additionally the split in natural frequencies due to forward and backward whirl are only observed for second (and higher) modes [117]. The stiffness of the bearings affect the output frequency of any of these modes, *i.e.* non rotating and rotating, and in particular the lower order modes [94].

In our case, the resonance to be identified does not vary with rotational speed as seen in [40, 74] and in Fig. 3.10. Therefore it is sufficient to consider planar motion in the next analyses, and to look into non rotating modes. Bearing stiffnesses are still not to be neglected and will be evaluated based on previous

Table 4.3: Base characteristics of the electric machines studied (Conf. = Confidential)

Parameter	Unit	SRM 1	PMSM	SRM 2	IM
Machine type	-	SRM	PMSM	SRM	IM
Number of slots/poles	-	16/12	12/10	8/6	Conf.
Number of phases	-	4	3	4	Conf.
Rated power	W	30,000	365	15,000	22,000
Max. speed	rpm	14,000	500	12,000	Conf.
Approx. Mass	kg	41	3	50	125
Approx. Volume	m <sup>3</sup>	7.4x10 <sup>-3</sup>	6.5x10 <sup>-4</sup>	4.4x10 <sup>-3</sup>	2.6x10 <sup>-2</sup>
FEA performed	-	Yes	Yes	No	No
Tests performed	-	No	Yes	Yes	Yes

study on similar machines [13]. It is interesting to note that they may be neglected when the first rotor mode is the only study interest [94].

At first the structural dynamics of four electric machines (with attached rotor) of different sizes and types are numerically investigated. The occurrence of a critical mode, referred to as Rotor Housing Coupling (RHC) mode, is then validated experimentally, and the rotor intrinsic dynamics responsibilities on its characteristics are assessed experimentally. Finally an analytical model is developed to explain this particular mode. Table 4.3 summarizes the machines studied. It is important to recognize that these investigations are made on such an amount of different specimens in order to cover a broad range of machines and to better support the claims.

### 4.3.1 FE identification of RHC mode

A structural FEA of SRM 1 is performed first without and with rotor attached to it through the bearings. A similar second analysis is then carried out on the smaller PMSM in order to verify if particular behaviors related to the rotor attachment happen for other machine sizes. The methodology employed to model the assembly of SRM 1 and PMSM essentially follows the steps below:

1. **Mesh** each assembly component using the detailed CAD information. Each mesh is validated again to ensure a relevant accuracy/computation time

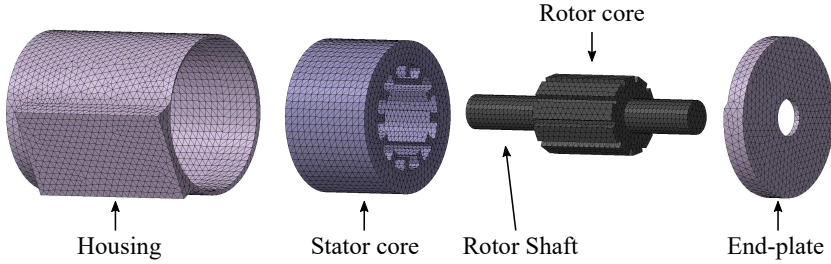


Figure 4.11: Exploded view of the PMSM meshes composing the assembly

trade-off, see Section 3.1.1. The meshes created for PMSM components are depicted in Fig. 4.11;

2. Define **component connections**. Except the rotor shaft to housing contact, all the components have got compatible meshes such that the degrees of freedom of the connecting mesh points are equal. The particular bearing connection is modelled carefully using CELAS1 elements (with translation stiffness equal to  $1.3e8$  N/m, value validated in [13]) from Nastran solver that define finite stiffness connections;
3. Define **material properties**. Isotropic properties are used here for the aluminum and steel that compose the assembly. More advanced models for the laminated stator and rotor cores are developed in Chapter 5, and are not of the present Chapter focus;
4. Run **modal analysis** for natural frequency determination.

The modal characteristics obtained from the FE modal analyses of SRM 1 and PMSM are further described. The modes between 10 Hz and 5,200 Hz are of main interest since this is the common range in which critical resonances occur in these categories of e-machines. Table 4.4 gathers the natural frequencies obtained for the four analyses performed: SRM 1 without and with rotor, PMSM without and with rotor. The "End-plate modes" correspond to modes that involve only the end-plate motion and are therefore not of the present study interest, such as the "Other modes" that relate to modes dependent of the specific machine geometry. The common stator-related modes are identified and noted in conformity with the upcoming Section 5.1, *i.e.*  $A(2,0)$ ,  $A(2,0)$  twin and  $B(2,1)$ . It is interesting to notice that the natural frequency of the ovalization mode  $A(2,0)$  is not significantly shifted due to the attachment of the massive rotor component. Therefore it is not necessary to simulate the rotor when one wants to capture the pure radial modal frequencies.

Table 4.4: Natural frequency (in Hz) results of the FE simulations for SRM 1 and PMSM (w/o = without, w/ = with, N/A = Not Applicable, OR = Out of Range)

	SRM 1	SRM 1	PMSM	PMSM
	w/o rotor	w/ rotor	w/o rotor	w/ rotor
FE mass (kg)	22.4	40.8	2.9	3.2
Modes				
End-plate modes	> 2,400	N/A	> 2,048	N/A
RHC mode	N/A	1,033	N/A	4,587
RHC mode twin	N/A	1,503	N/A	OR
$A(2,0)$	1,666	1,676	5,055	5,080
$A(2,0)$ twin	1,717	1,725	5,145	5,167
$B(2,1)$	2,607	2,917	OR	OR
Other modes	> 2,644	> 3,060	OR	> 5,200

Yet a particular mode occurs solely when the rotor is attached to the structure. Fig. 4.12 gives a first illustration of this novel mode shape together with the undeformed mesh and the ovalization  $A(2,0)$  modes for both machines simulated. Whereas this mode will be further refined (and called RHC mode) in the next sub-sections of this Chapter it can be characterized, at this stage, by the following features:

1. It corresponds to the **first flexible mode** of the assembly, *i.e.* its lowest natural frequency even lower than the ovalization mode  $A(2,0)$
2. It is **rotor-dependent** since it is activated only when the rotor is attached to the assembly
3. It has a **particular shape** that involves rotor, stator and end-plate bending

Particularly from the fact that the RHC mode can induce shaft and stator bending, it can affect significantly safety and comfort quality [96]. Additionally researchers show a mode excited at low frequency (prior the ovalization) such as Le Besnerais [74] (page 53) who captures a bending mode at the lowest natural frequency for his electric machine. But no explanation of the phenomenon is further offered in literature, eventually due to the absence of measurements at the rotor. The next Section 4.3.2 validates experimentally the occurrence of this mode.

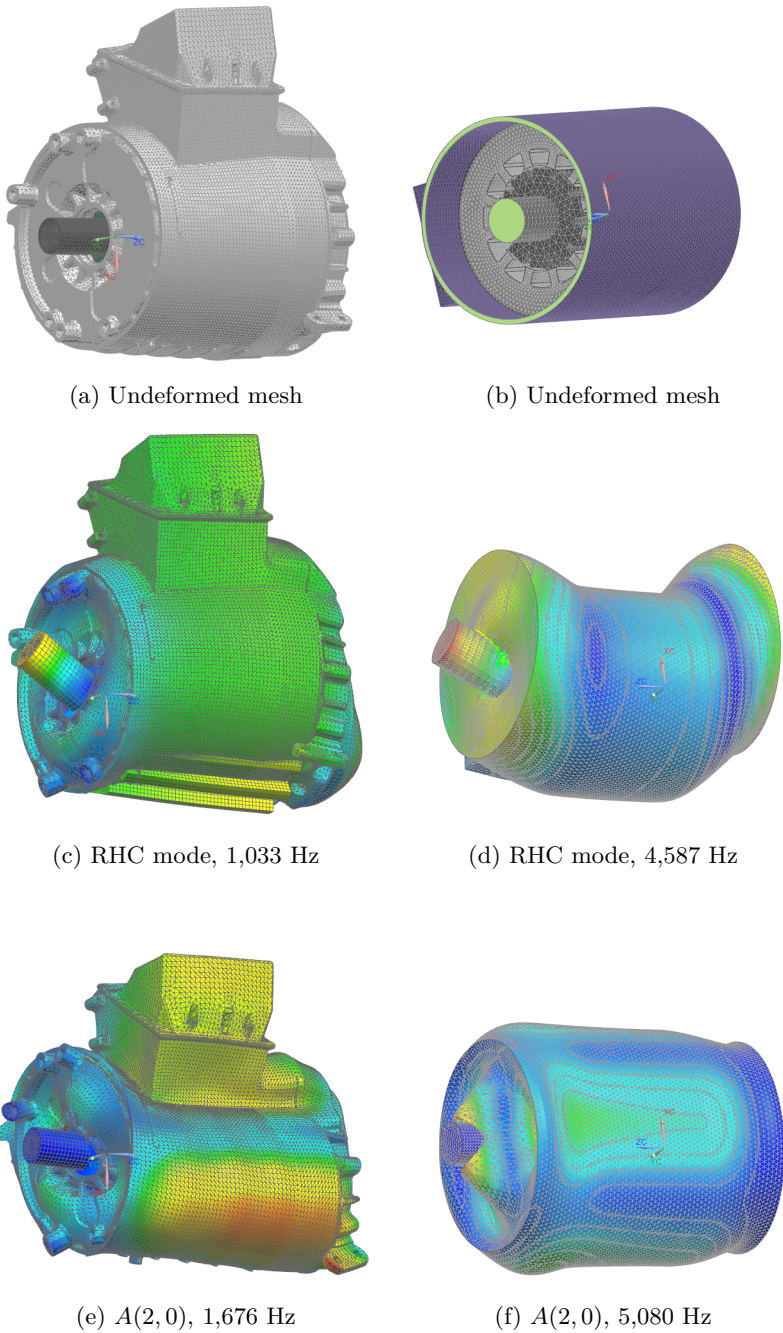


Figure 4.12: Simulated modal characteristics of SRM 1 (left) and PMSM (right)



### 4.3.2 Experimental validations of the RHC mode occurrence

Three different experimental studies are carried out on the three electric machines available: PMSM, SRM 2 and IM. For each structure, a dedicated experimental campaign is developed according to requirements of Section 2.2 (free vibration, hanging ropes, coherence, linearity, etc). Then the results from EMAs are collected to validate the occurrence of the RHC mode when a rotor is attached to the assembly.

#### Experimental setup principle

Similarly to the previous FEAs, several levels of assemblies are investigated for each available machine under test. PMSM, SRM 2 and IM are tested without and with rotor. EMA is used [58] to identify/measure these systems modal parameters, which principle is thoroughly explained in Section 2.2.2.

An impact hammer (PCB Piezotronics SN20541) and a miniature shaker (LMS Qsource SN045) allow achieving consistent, repeatable and coherent measurements up to 2.8 kHz and 5.5 kHz, respectively. Whenever the shaker is employed, its settings are the following: white noise input from 100 Hz to 8 kHz as a burst random signal (80% burst time, 0.025s burst ramp time) and 50 averages for FRF H1 estimation [58]. Whenever the hammer is employed, 15 hits are averaged; coherence, flat input autopowers and double impacts are consistently checked throughout measurements. This H1 estimator is used because it is assumed that the input signals for modal tests (shaker and hammer) are not noisy compared to the output signals. Moreover, specific boundary conditions are properly defined to ensure free-free vibrations to be measured, as described in Section 2.2.2.

The accelerometers discretization of the tested specimen is chosen such that modes of interest are captured. In particular measurement points are located on the rotor shaft in order to identify the RHC mode. Fig. 4.13, Fig. 4.14 and Fig. 4.15 show the actual test setup, with the accelerometer discretization used in LMS Test.Lab for each machine. Note that for IM, no picture is given because of confidentiality reasons.

Table 4.5 compiles the experimental information: the machine tested, the specimens that are subjected to complete EMAs, their respective mass and geometry discretization, and the excitation device used as input to the FRFs.

As described in Section 2.2, an important note to mention is that EMAs rely on the linearity principle. Indeed when the measured FRFs are acquired one needs to extract the modal characteristics *i.e.* the natural frequencies and damping

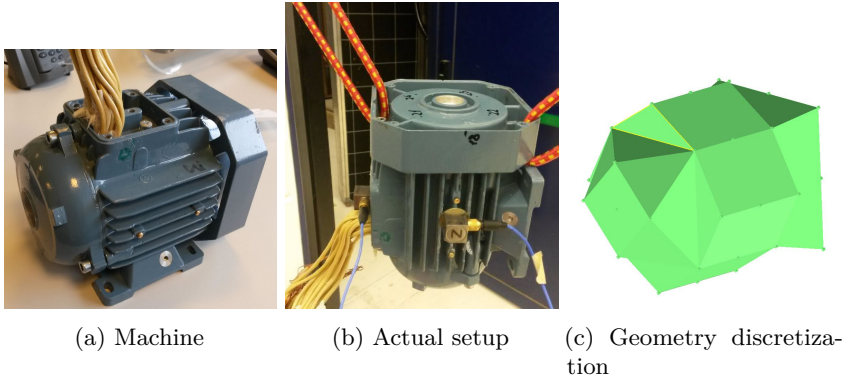


Figure 4.13: Measurement setup for PMSM

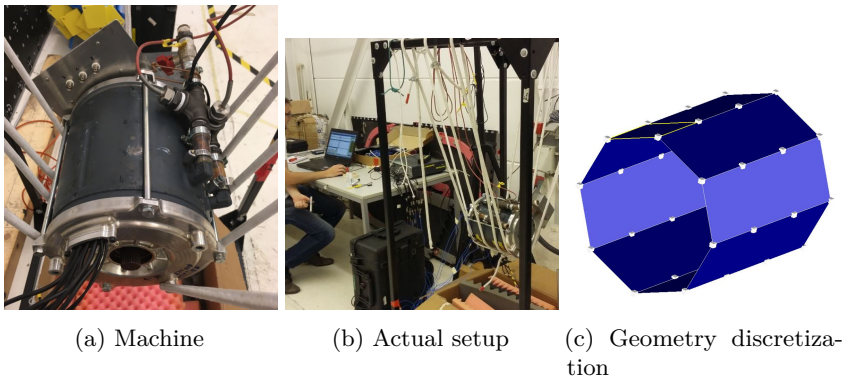


Figure 4.14: Measurement setup for SRM 2

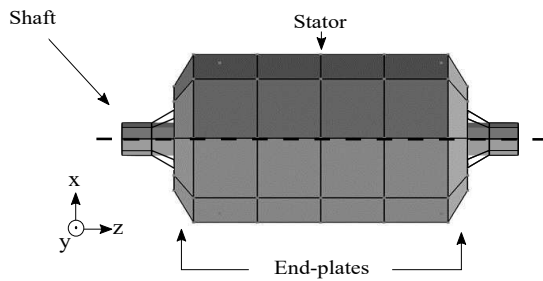


Figure 4.15: Mesh resolution for IM assembly

Table 4.5: Experimental setups for PMSM, SRM 2 and IM (w/o = without, w/ = with)

Machine	Specimen	Mass (kg)	Number of measurement points	Excitation device
PMSM	w/o Rotor	2.9	12 x 3D	Hammer
	w/ Rotor	3.2	12 x 3D	Hammer
SRM 2	w/o Rotor	37	32 x 3D	Hammer
	w/ Rotor	50	32 x 3D	Hammer
IM	w/o Rotor	85	58 x 3D	Shaker
	w/ Rotor	122	58 x 3D	Shaker

ratios. This extraction process usually assumes a linear mathematical parametric equation for each of the measured FRFs  $H_{ij}(\omega)$ . The present measurement campaigns consequently include a deep validation step of the linearity of each structure by means of typical checks such as reciprocity and linearity [58], see Section 2.2. The linearity check should show similar FRFs for different input levels, while the reciprocity check should show similar FRFs for reversed input/output measurements. Fig. 4.16 and Fig. 4.17 respectively illustrate a linearity and a reciprocity check for the IM.

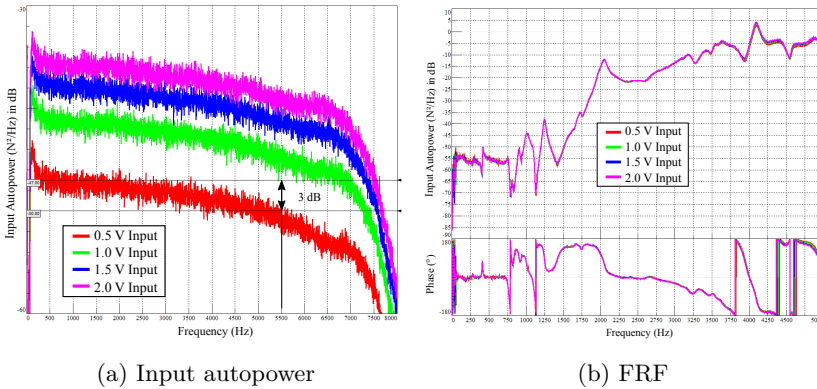


Figure 4.16: Linearity check example for IM

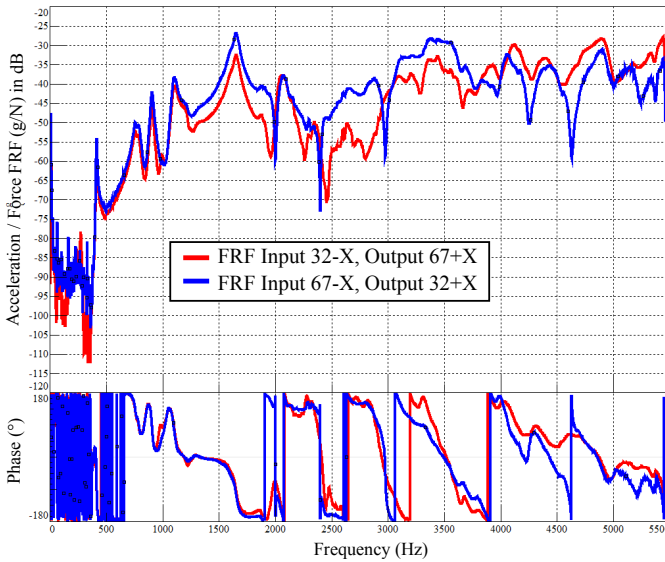


Figure 4.17: Reciprocity check example for IM

## EMAs results

PolyMAX [100] implemented in LMS Test.lab software is used for the EMAs since it allows for fast parameter estimation along with large identification capabilities for highly damped structures. The results of the EMAs are presented in Table 4.6. Several conclusions can be drawn at this stage, considering also the FE results of Section 4.3.1.

Table 4.6: Experimentally estimated natural frequencies (in Hz) for PMSM, SRM 2 and IM (w/o = without, w/ = with, N/A = Not Applicable, OR = Out of Range)

Machine	Specimen	RHC mode	$A(2, 0)$
PMSM	w/o Rotor	-	5,003
	w/ Rotor	4,522	4,995
SRM 2	w/o Rotor	-	1,406
	w/ Rotor	534	1,409
IM	w/o Rotor	-	N/A
	w/ Rotor	414	N/A

The ovalization mode natural frequency is not affected by the presence of the rotor for any of the machine. Moreover, the RHC mode occurs at the lowest natural frequency of each assembly. Its estimated shape from EMAs is depicted in Fig. 4.18 and is similar to the simulated one of Fig. 4.12.

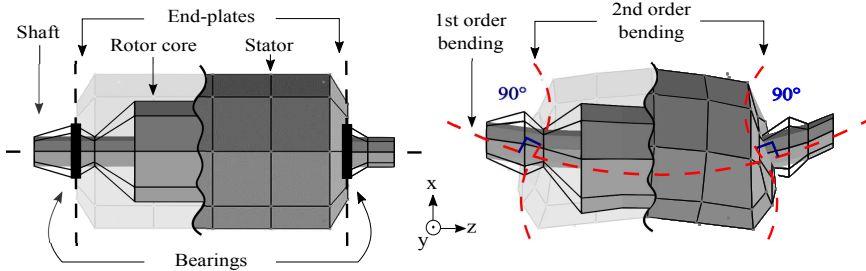


Figure 4.18: Undeformed assembly (left) and its RHC mode shape estimated from EMA (right)

In fact, it implies a first order bending of the rotor and housing, and a second order bending of the end-plates. However since the first order bending of the rotor depends on its stiffness and mass, it is expected to have different assembly structural dynamics by using different rotors (showing different structural dynamics). This will be evaluated in the next Section.

An important note that will be used for later modeling purposes is the relative angle between the end-plate and the rotor at their contact point. It is a constant value of approximately  $90^\circ$  and is representative of a fixed rotational degree-of-freedom at the bearing locations.

### 4.3.3 Experimental evaluation of the rotor structural dynamics responsibilities

The rotor intrinsic structural dynamics are expected to contribute to the RHC mode modal characteristics. Hence to evaluate this statement, two rotors (meant for IM), namely Rotor A and Rotor B, are tested experimentally with and without their corresponding machine housing.

#### Experimental setup principle

Since the IM was already tested with and without a rotor in the previous Section 4.3.2, the identical test setup is employed for the next analyses with Rotor A and Rotor B. Additionally the intrinsic structural dynamics of each rotor is required

Table 4.7: Experimental setups for IM (w/o = without, w/ = with) and different rotors

Specimen	Mass (kg)	Number of measurement points	Excitation device
IM w/ Rotor A	122	58 x 3D	Shaker
IM w/ Rotor B	128	58 x 3D	Shaker
Rotor A	37	12 x 3D	Hammer
Rotor B	43	12 x 3D	Hammer

to compare appropriately with each assembly behavior. Therefore another setup has to be defined for the rotors' structural dynamics measurements. An impact hammer (PCB Piezotronics SN20541) is employed, 15 hits are averaged for FRF H1 estimation; coherence, flat input autopowers and double impacts are consistently checked throughout measurements. Elastic hanging ropes are adequately chosen to ensure free-free vibrations to be measured, as described in Section 2.2.2. Regarding the accelerometer positions, only bending modes are of interest since they are the ones involved in the novel mode. Hence only points following the green line in Fig. 4.19 are measured. Table 4.7 compiles the experimental information: the specimen tested with their respective mass and geometry discretization, and the excitation device used as input to the FRFs.

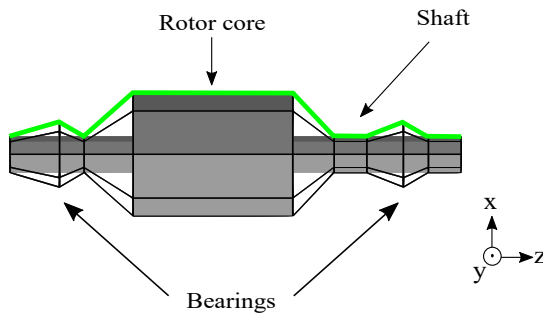


Figure 4.19: Mesh resolution for the rotors

It is important to mention that linearity and reciprocity have been constantly checked before any EMA.

**EMAs results**

The EMAs, which results are presented in Table 4.8, identify the RHC mode when attaching a rotor to the assembly (Fig. 4.18). They also extract beam-like bending motions for the single rotors, referred to as bending modes (Fig. 4.20).

Table 4.8: Experimentally estimated natural frequencies (in Hz) for IM (w/o = without, w/ = with, N/A = Not Applicable, OR = Out of Range)

Specimen	RHC mode	A(2, 0)
IM w/o Rotor	-	N/A
IM w/ Rotor A	414	N/A
IM w/ Rotor B	351	N/A
	1 <sup>st</sup> bending	2 <sup>nd</sup> bending
Rotor A	1,011	1,647
Rotor B	676	1,325

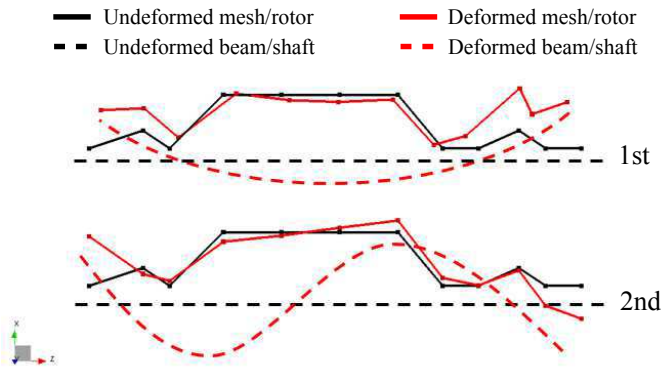


Figure 4.20: Two first bending modes for Rotor A and B from EMA, the plain lines follow the measurement points of the green line described in Fig. 4.15

Knowing that Rotor A is lighter than Rotor B, one could expect the Rotor A natural frequencies higher than for Rotor B. But stiffness inversely affects the natural frequencies as well, and may counter act mass variation effects. Here the frequencies discrepancies are not entirely justified by the mass variation so that Rotor A is stiffer than Rotor B. In parallel the IM with Rotor A shows stiffer RHC mode behavior than the IM with Rotor B. Furthermore the natural frequency of such mode is quite low despite the high natural frequencies of the assembly standalone components.

It is therefore hypothesized that the combination of both beam-like bending motions of the rotor and end-plates couple these components at the bearing locations. The assembly becomes less constrained (more flexible) for this type of coupled motion such that it translates in a low-frequency mode subjected to generate resonance phenomenon. Yet the intrinsic structural dynamics of each component is supposed to affect the characteristics of this mode, as it was concluded experimentally previously.

### 4.3.4 Mathematical validation of the hypothesis

An analytical model that simplifies the electric machine system to a combination of beams is developed to provide a physical explanation of the previously identified RHC mode rather than a validation of it for further use.

#### Analytical model formulation

The presented analytical model simplifies the rotor plus stator assembly of Fig. 4.18 to a combination of five homogeneous beams with specific connections and boundary conditions. Fig. 4.21 presents the structure and the local coordinate systems ( $O_i, x_i, w_i$ ) for each beam  $i = 1, 2, 3, 4, 5$ .

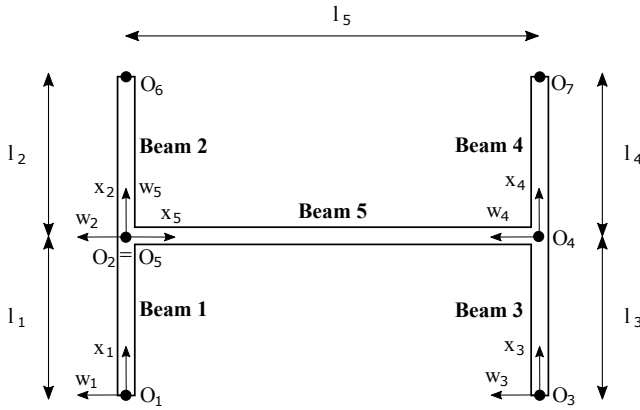


Figure 4.21: Five-beam structure under study

For the investigation purposes, the beams only show transverse deflections  $w_i(x_i, t)$  such that Euler-Bernoulli beam formulation is used. The corresponding free vibration equation for each beam  $i$  reads [104]:



$$(EI)_i \frac{\partial^4 w_i}{\partial x_i^4}(x_i, t) + (\rho A)_i \frac{\partial^2 w_i}{\partial t^2}(x_i, t) = 0 \quad (4.6)$$

where  $(EI)_i$ ,  $(\rho A)_i$  and  $l_i$  are the flexural rigidity ( $\text{Nm}^2$ ), the linear density ( $\text{kg/m}$ ) and the length (m) of the beam  $i$ , respectively. The separation of variables technique defines the displacement of each beam  $i$  as the product of the spatial  $W_i(x_i)$  and the time  $T(t)$  parts [11]:

$$w_i(x_i, t) = W_i(x_i) \cdot T(t) \quad (4.7)$$

Substituting Eq. (4.7) into Eq. (4.6) gives Eq. (4.8) and Eq. (4.9),

$$(EI)_i \frac{d^4 W_i}{dx_i^4}(x_i) - (\rho A)_i \omega^2 W_i(x_i) = 0 \quad (4.8)$$

$$\frac{d^2 T}{dt^2} + \omega^2 T(t) = 0 \quad (4.9)$$

where  $\omega$  is the angular frequency in rad/s. While the solution of Eq. (4.9) defines a sinusoidal expression for  $T(t)$ , the general solution of Eq. (4.8) is:

$$W_i(x_i) = U_{i1} \cosh(\beta_i x_i) + U_{i2} \sinh(\beta_i x_i) + U_{i3} \cos(\beta_i x_i) + U_{i4} \sin(\beta_i x_i) \quad (4.10)$$

with  $\beta_i^4 = \frac{(\rho A)_i \omega^2}{(EI)_i}$ . The 20 constants  $U_{ij}$  are calculated from the boundary conditions. In the frame of analyzing the RHC mode, the model assumes the stator core and housing to be fixed relatively to the end-plates bending motion. This assumption is reasonable for larger machines where the stator contributes to a large amount of mass and stiffness to the full assembly. The beams 1, 2, 3 and 4 corresponding to the end-plates are clamped, *i.e.* at points  $O_1$ ,  $O_3$ ,  $O_6$  and  $O_7$  (stator attachment points). It yields,

$$\begin{aligned}
O_1 : \quad W_1(0) = 0 \quad , \quad \frac{dW_1}{dx_1}(0) = 0 \\
O_3 : \quad W_3(0) = 0 \quad , \quad \frac{dW_3}{dx_3}(0) = 0 \\
O_6 : \quad W_2(l_2) = 0 \quad , \quad \frac{dW_2}{dx_2}(l_2) = 0 \\
O_7 : \quad W_4(l_4) = 0 \quad , \quad \frac{dW_4}{dx_4}(l_4) = 0
\end{aligned} \tag{4.11}$$

The coupling at points  $O_2$  and  $O_4$  is modeled using: the continuity principle of the end-plate, the axial infinitely rigid assumption, and a specific rigidity that fixes the relative rotation between the two components. The continuity of the end-plates induces equal rotation at the connections. The displacements at these points are considered null to accommodate for the limitation of the Euler-Bernoulli theory, where no axial displacement is allowed. It is interesting to note that this assumption does not allocate for any possible rigid axial translation of Beam 5; any rigid motion is neglected in this model. Finally assuming infinite axial rigidity of the beams means equal rotation and bending moment between the end-plate and rotor beams [105]. The mathematical derivation of these boundary conditions at the connections  $O_2$  and  $O_4$  are summarized as follows:

$$\begin{aligned}
O_2 : \quad \left\{ \begin{array}{l} W_1(l_1) = W_2(0) = 0 \quad , \quad W_5(0) = 0 \quad , \\ \frac{dW_1}{dx_1}(l_1) = \frac{dW_2}{dx_2}(0) = \frac{dW_5}{dx_5}(0) \quad , \\ (EI)_1 \frac{d^2W_1}{dx_1^2}(l_1) = (EI)_5 \frac{d^2W_5}{dx_5^2}(0) \end{array} \right. \\
O_4 : \quad \left\{ \begin{array}{l} W_3(l_3) = W_4(0) = 0 \quad , \quad W_5(l_5) = 0 \quad , \\ \frac{dW_3}{dx_3}(l_3) = \frac{dW_4}{dx_4}(0) = \frac{dW_5}{dx_5}(l_5) \quad , \\ (EI)_3 \frac{d^2W_3}{dx_3^2}(l_3) = (EI)_5 \frac{d^2W_5}{dx_5^2}(l_5) \end{array} \right.
\end{aligned} \tag{4.12}$$

Substituting the boundary conditions of Eq. (4.11) and Eq. (4.12) in Eq. (4.10) gives a linear system of 20 equations with the 20 unknowns  $U_{ij}, (i, j) \in [1, 2, 3, 4, 5; 1, 2, 3, 4]$ :

$$[M]_{20 \times 20} \cdot \{U\}_{20 \times 1} = \{0\}_{20 \times 1} \quad (4.13)$$

A non-trivial solution exists if and only if the determinant of  $[M]$  is equal to zero; the roots are called the natural frequencies  $\omega_n$  of the system in rad/s. Each  $\omega_n$  corresponds to a unique combination  $\{U_n\}$  of the coefficients  $U_{ij}$  that satisfy Eq. (4.13). In other words the vectors  $\{U_n\}$  compose the null space of  $[M]$ , namely the mode shapes of the system.

### Equivalent parametrization

In order to predict quickly relevant natural frequencies comparable to experimental ones, the developed analytical model requires representative material properties and beam dimensions. This part proposes a methodology to define equivalent beam parameters from a reference framework in order to evaluate more realistically the effects of rotor dynamics upon the machine assembly behavior.

The equivalent flexural rigidity  $\overline{(EI)}$  and linear density  $\overline{(\rho A)}$  of the beams are derived following the parametrization process described hereafter and pictured in Fig. 4.22.

Each component (end-plate and rotor) is isolated and studied separately. Their free vibration characteristics are analyzed by a simplified analytical model, detailed FE model or experimental campaign. In particular their natural frequencies and masses are collected and represent the reference parameters. The equivalent beams are parametrized such that both the natural frequency and mass fit these reference values. For mass coherence, one obtains the equivalent linear masses  $\overline{(\rho A)}$ :

$$\overline{(\rho A)} = \begin{cases} \overline{(\rho A)}_r = \frac{m_r}{l_r} & \text{for the rotor} \\ \overline{(\rho A)}_{ep} = \frac{m_{ep}}{l_{ep}} & \text{for the end-plate} \end{cases} \quad (4.14)$$

where  $m_r$  and  $m_{ep}$  are the reference masses of the rotor and the end-plate, respectively. The lengths of the rotor ( $l_r$ ) and end-plate ( $l_{ep}$ ) beams correspond to the rotor shaft length and the end-plate diameter, respectively. In addition

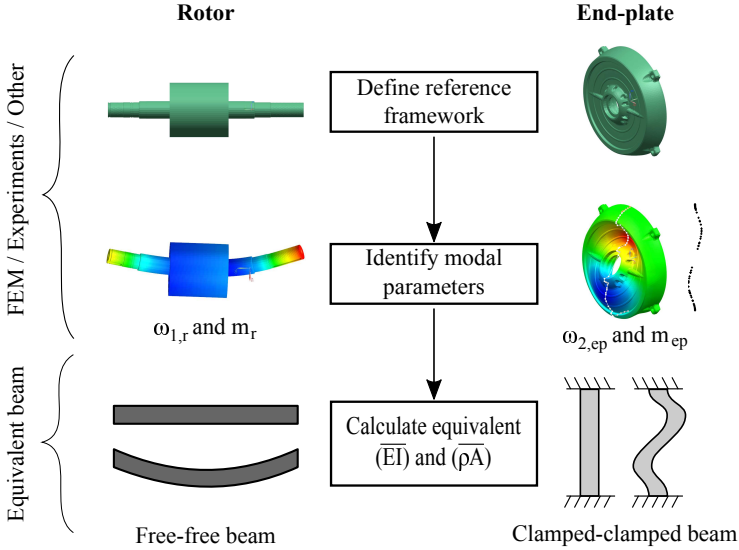


Figure 4.22: 5-beam equivalent parametrization process

only the first and second order bending modes are of interest given the focus on the RHC mode. Hence the rotor first bending and the end-plate second bending modes give the following equivalent flexural rigidity  $\overline{(EI)}$ :

$$\overline{(EI)} = \begin{cases} \left( \frac{\omega_{1,r}}{\beta_{1,r}^2} \right)^2 \cdot \overline{(\rho A)}_r & \text{for the rotor} \\ \left( \frac{\omega_{2,ep}}{\beta_{2,ep}^2} \right)^2 \cdot \overline{(\rho A)}_{ep} & \text{for the end-plate} \end{cases} \quad (4.15)$$

where  $\omega_{1,r}$  and  $\omega_{2,ep}$  are the reference natural frequencies in rad/s of the modes of interest, and with  $\beta_{1,r}$  and  $\beta_{2,ep}$  derived from the boundary conditions of the beams. In order to consider the assembly boundaries early in the process, the rotor is assumed free at both ends and each end-plate is studied clamped at the connection-to-stator ends. Substituting the solution of these beam types [104] with Eq. (4.14) in Eq. (4.15) gives:

$$\overline{(EI)} = \begin{cases} \overline{(EI)}_r = \frac{\omega_{1,r}^2 m_r l_r^3}{22.3733^2} & \text{for the rotor} \\ \overline{(EI)}_{ep} = \frac{\omega_{2,ep}^2 m_{ep} l_{ep}^3}{61.6727^2} & \text{for the end-plate} \end{cases} \quad (4.16)$$

## Results

The methodology described above is applied to IM. The experimental campaign carried out in Section 4.3.2 is used as the reference framework from which equivalent parameters are calculated. The equivalent parameters obtained are listed in Table 4.9.

Table 4.9: Equivalent parameters

Parameter	Unit	Value
$\overline{(\rho A)}_r$ (Rotor A)	kg/m	92.5
$\overline{(\rho A)}_r$ (Rotor B)	kg/m	107.5
$\overline{(\rho A)}_{ep}$	kg/m	6.1
$\overline{(EI)}_r$ (Rotor A)	Nm <sup>2</sup>	$1.9 \times 10^5$
$\overline{(EI)}_r$ (Rotor B)	Nm <sup>2</sup>	$9.9 \times 10^4$
$\overline{(EI)}_{ep}$	Nm <sup>2</sup>	$1.7 \times 10^4$

The five first flexible mode shapes obtained with the equivalent parameters are displayed in Fig. 4.23 and the simulated natural frequencies are shown in Table 4.10.

On the one hand the RHC mode is well captured and corresponds to the first flexible mode of the system (lowest natural frequency). Then it is interesting to point the significant natural frequency difference between each component taken separately while the assembly RHC mode occurs at a much lower frequency than any of the natural frequencies of its components. It indicates that the connection of these components at the bearings introduces a significant amount of rotational inertia to the end-plate and shaft beams. The five-beam model provides a good estimation of the RHC mode natural frequency, despite the significant assumptions made, and therefore is a relevant analytical tool to predict the dynamic phenomenon early in the design stage.

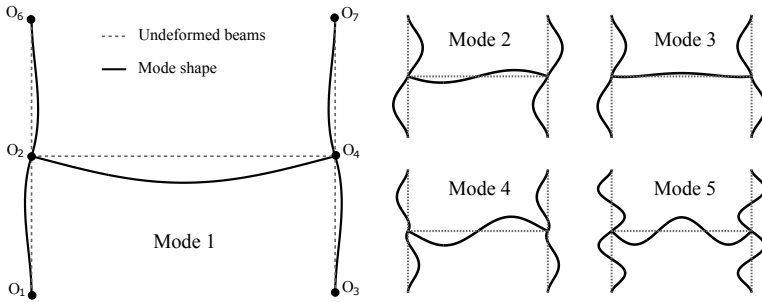


Figure 4.23: Flexible mode shapes of the five-beam structure

Table 4.10: Results for the equivalent beam structures, (\*) = the assembly is modeled without the stator

	Mass [kg]		Natural frequency [Hz]		
	Ref.	Experiment	Ref.	Experiment	Five-beam model
Rotor A		$m_r = 37.0$		$\omega_{1,r}/2\pi = 1,011$	$\omega_{1,r}/2\pi = 1,011$
Rotor B		$m_r = 43.0$		$\omega_{1,r}/2\pi = 676$	$\omega_{1,r}/2\pi = 676$
End-plate		$m_{ep} = 2.45$		$\omega_{2,ep}/2\pi = 3,248$	$\omega_{2,ep}/2\pi = 3,248$
Assembly w/ Rotor A*		41.9		$\omega_1/2\pi = 414$	$\omega_1/2\pi = 492$
Assembly w/ Rotor B*		47.9		$\omega_1/2\pi = 351$	$\omega_1/2\pi = 359$

## 4.4 Intermediate conclusions

### 4.4.1 Conclusions on the effects on the radiated magnetic noise

The coupled electromagnetic-vibroacoustic FE modeling framework presented in Section 3.1.1 was used to determine the rotor topology influence on the NV behavior of a SynRM. Using the same stator, four different rotors were numerically analyzed and permitted to assess on their different effects on the emitted noise.

Early in the simulation process one can say that, as seen in Fig. 4.4, the radial force profile is immediately impacted by the rotor topology while torque ripple

(see Table 4.2) significantly differs from one topology to another.

The corresponding simulated acoustic pressure varies as well depending on the rotor topology. However acoustic pressure colormaps of Fig. 4.8 and order cut analyses of Fig. 4.9 did not clearly identify noise spectrum differences brought by different rotor topologies. They still revealed that high acoustic pressure magnitudes are more concentrated around the highest orders.

Moreover, significant discrepancies of *OASPL* were depicted in Fig. 4.10, depending on the rotor topology. They can reach 10 dB differences from one topology to another, which demonstrates the necessity to take the flux-barriers design into account for NV optimization perspectives. More generally the rotor topology of an electric machine can significantly influence the radiated magnetic noise.

Nevertheless it is important to mention that the *OASPL* discrepancies do not necessarily mean that the other topologies would be quieter, because of the averaging process involved in the calculation of the *OASPL*; but it is a relevant indicator of a quieter machine when the operating points are chosen wisely (*e.g.* critical speed activating resonance). In fact by this study it was also emphasized that relevant metrics have to be defined to assess the sound quality for further optimization implementations. For instance, torque ripple and the *OASPL* were shown from Fig. 4.10 and 4.6 not to be in a trivial relationship; although torque ripple is often considered for noise reduction strategies.

#### 4.4.2 Conclusions on the effects on the assembly structural dynamics

The mechanical connection of the rotor to the assembly housing at the bearings introduces a structural transfer for vibrations to occur.

The FEAs performed on two different electric machines identified in Fig. 4.12 the occurrence of a specific mode that is activated only when a rotor is attached to the housing. This Rotor Housing Coupling (RHC) mode involves rotor and stator first order bending and end-plate second order bending. Moreover, it corresponds to the electric machine assembly mode with the lowest frequency. These two characteristics suggest that this mode can be responsible for resonances implicating shaft vibrations and acoustic disturbances.

The RHC mode was also identified experimentally on three different machines of different sizes and Fig. 4.18 shows that the experimentally identified RHC mode shape is similar to the previously simulated one. The mode also corresponds to the first natural frequency of the structure for any electric machine considered.

Moreover it was hypothesized that given the involvement of the first order bending of the rotor and its dependency on the rotor stiffness and mass, using different rotors (with different structural dynamics) would lead to different assembly structural dynamics. The hypothesis was validated experimentally by performing two EMAs on the same machine but with two different rotors attached (Table 4.8): the stiffer assembly (for the RHC mode) corresponds to the stiffer rotor.

Finally the frequency of such RHC mode is quite low despite the high natural frequencies of the assembly standalone components. It presupposes that the beam-like bending motions of the rotor and end-plates are coupled particularly at their bearing connections. In order to better understand the RHC mode, the analytical model that simplifies the assembly to a five-beam structure was developed. It captures correctly the RHC mode shape (Fig. 4.23) and allocates for intrinsic rotor dynamic influences previously noticed (Table 4.10). Similarly as seen experimentally, the RHC mode occurs at a much lower frequency than any natural frequency of its components. A significant amount of rotational inertia is introduced to the end-plate and shaft beams.

It is important to note that the frequency of ovalization mode  $A(2,0)$  is not significantly affected by any of the changes; *i.e.* with or without rotor, which validates the fact that the stator core contributes to most of the stiffness and mass for this type of modes.



# Chapter 5

## The laminated cores structural dynamics

In order to ensure reliable multi-physical simulation models, it is necessary to investigate further the component responsible for high tonal noise. In the electric machines of interest (inner-rotor, radial-flux) the stator core is the major contributor to acoustic noise through its excited mode, inducing a resonance phenomenon. But its laminated nature gives modeling challenges and behavior ambiguities, which this chapter addresses and clarifies.

At first the typical modes of vibration of the laminated cylindrical cores are presented in Section 5.1, as a base for modal definitions of the similarly shaped stator core. Sections 5.2 to 5.3 present several structural models of this component, with increasing levels of complexity, that are compared to experimental results in Section 5.5. Then in order to gather thorougher physical understanding of the dynamics induced by the laminations, some effects are investigated such as the number of laminations in Section 5.6 and the stacking technology in Section 5.7.

### 5.1 Typical modes related to laminated cylindrical cores

The typical mode shapes of laminated cores present in rotating electric machines are extensively studied and identified in literature. Weilharter et al. [141] for

instance identify experimentally the mode shapes that occur on a laminated stator core with windings. But more generally it is possible to compare the modes of the stator core to the modes of an equivalent simplified circular cylinder. Shen et al. [111] define five categories of mode shapes for thin cylinders while Wang et al. [134] incorporate another mode shape concerning thick cylinders, which all together can define completely the modes of a laminated stator core.

The mode shapes are characterized by particular combinations  $(n_r, n_z)$  of radial mode order  $n_r$  and axial mode order  $n_z$ . In other words,  $2n_r$  represents the number of nodal radii of the  $r$ th mode, and  $n_z$  represents the number of nodal cross sections along the stack length. Additionally azimuthal, torsion, shearing and axial motions of different orders define other types of mode shapes. The six categories obtained by Wang et al. [134] for thick cylinders are listed below.

- A. Pure radial modes:** The deformation of this kind of modes is only radial in the sense that the cylinder cross-section remains the same along its axial length. Also, the cross-section stays in its plane normal to the cylinder axial axis. An example is shown in Table 5.1 for a stator core, and their frequencies are denoted  $f_{A(n_r,0)}$  throughout the thesis.
- B. Radial motion with radial shearing modes:** For this type of modes, the cross-section varies along the axial length and the circumferential cross-sections do not remain plane. Three examples are shown in Table 5.1 for a stator core, and their frequencies are denoted  $f_{B(n_r,n_z)}$  throughout the thesis. Additionally, particular B modes with odd  $n_z$  are called **anti-symmetric** because they are anti-symmetric to the median cross-sectional plane of the cylinder/core.
- C. Extensional modes:** The cross-section is simply stretched inwards/outwards with a constant amplitude along the azimuthal direction. Some authors refer to them as **breathing modes**. An example is shown in Table 5.1 for a stator core, and their frequencies are denoted  $f_{C(n_r,n_z)}$  throughout the thesis.
- D. Circumferential modes:** Adjacent segmental elements expand or contract one by one in the azimuthal direction, and axial deformations are generated by this motion. An example is shown in Table 5.1 for a stator core, and their frequencies are denoted  $f_{D(n_r,n_z)}$  throughout the thesis.
- E. Axial bending modes:** The structure simply bends axially with in-phase edges ( $n_z = \text{even}$ ) or out-of-phase edges ( $n_z = \text{odd}$ ). The circumferential lines define nodal lines depending on  $n_z$ . Two examples are shown in Table 5.2 for a stator core, and their frequencies are denoted  $f_{E(n_r,n_z)}$  throughout the thesis.

**F. Global modes:** This category gathers a few other possible mode shapes that can behave as: a simple beam vibrating in transverse direction (F(a)), a bar vibrating in torsion (F(b)), or as a rod vibrating in a longitudinal direction (F(c)). Three examples are shown in Table 5.2 for a stator core, and their frequencies are denoted  $f_{F(i)(n_r, n_z)}$  throughout the thesis.

Table 5.1 and 5.2 give examples of the modes shapes of a basic stator core for each category, together with natural frequencies calculated in an FE model. The stator FE model (**Iso**) is further explained in the upcoming Section 5.4.1. Yet the natural frequencies are given such that one can locate each mode with respect to the other ones, for a relevant example.

On top of these, the modes of categories A, B, D, E and F(a) are found to be **twinned**; *i.e.* in theory they are two modes of the same shape occurring at the same frequency with a space phase difference of  $\frac{\pi}{2}$  [61, 51]. They actually correspond to mode shapes associated to sin and cos functions. In the case of a perfectly axi-symmetric structure (*e.g.* a circular ring without teeth), the natural frequencies of these two modes are identical. For the stator core, the teeth bring non-symmetry to the system and therefore the twin mode shapes occur at slightly different natural frequencies. Figure 5.1 illustrates the twinned modes of B(2,1).

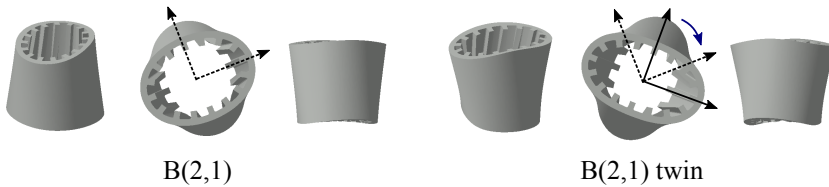






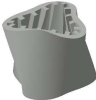
















Figure 5.1: Illustration of the twinned B(2,1) modes

## 5.2 1D Analytical models (Ring)



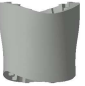












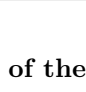
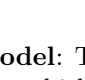
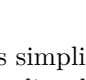
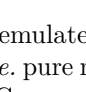
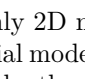
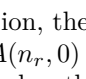
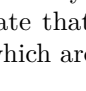
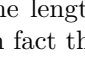
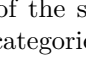
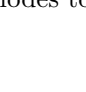








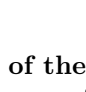
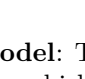
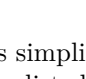
The simplest models for the laminated stator cores are analytical. Timar et al. [121] simulate the laminated stator as a circular ring with equivalent parameters as depicted previously in Section 3.1.2 (see Fig. 3.9). Numerous studies investigate extensions to this model, in order to allocate for mass, windings and frame effects. Hubert et al. [61] extend it by using a corrective coefficient to take the third dimension into account. This modeling approach is commonly used by many authors such as Gieras et al. [50] and Maliti et al. [82], among others [74, 91]. Eq. (3.6) permits to compute the natural frequencies of

Table 5.1: Typical vibrational modes of a stator core (Part I), (\*) twinned modes occur

Category <i>cat</i>	Mode shape example			$(n_r, n_z)$	Frequency $f_{cat(n_r, n_z)}$ (Hz)
Initial				-	-
A				<b>(2,0)*</b>	890
				(3,0)*	2437
				(4,0)*	4502
				(5,0)*	6959
B				(2,1)*	1315
				<b>(3,1)*</b>	3086
				(4,1)*	5219
				(5,1)*	7677
				(2,2)*	5995
C				(3,2)*	6233
				<b>(4,2)*</b>	7829
				(5,2)*	10117
				(2,3)*	11105
				(3,3)*	11117
D				(4,3)*	12496
				(5,3)*	O/R
				(0,0)	7087
				(0,1)	7065
C				(0,2)	8020
				(0,3)	11690
				(1,1)*	10090
D				(1,2)*	13223

a free-free circular ring from Hubert's model. The details on how to obtain this equation are given in [61]. It essentially originates from D'Alembert theorem, also known as the forces equilibrium principle.

Table 5.2: Typical vibrational modes of a stator core (Part II), (\*) twinned modes occur

Category <i>cat</i>	Mode shape example	$(n_r, n_z)$	Frequency $f_{cat(n_r, n_z)}$ (Hz)	
E				$(1,0)^*$ 5564
				$(2,0)^*$ 8037
				$(3,0)^*$ 12285
F(a)				$(1,1)^*$ O/R
				$(2,1)^*$ 13232
				$(3,1)^*$ O/R
F(b)				$(1,2)^*$ 7156
				$(1,3)^*$ 11094
F(c)				$(0,1)$ 7579
				$(0,2)$ O/R
F(c)				$(0,1)$ 13868
				$(0,2)$ O/R

**Assumptions of the model:** This simplified model of the stator core works under specific assumptions which are listed below:

- Since it can emulate only 2D motion, the model captures solely the in-plane modes, *i.e.* pure radial modes  $A(n_r, 0)$  and the extensional/breathing mode  $C(0, 0)$ . Consequently, the core length is taken into account only by mass change of the system. Cai et al. [22, 23] analytically and experimentally corroborate that the length of the stator is negligible on the in-plane modes, which are in fact the categories A and  $C(0, 0)$  simulated here.
- Shearing strains are neglected. It is a valid assumption knowing that the critical modes to target are not involving strain deformations, and that

several authors validate this assumption experimentally like Hubert et al. [61].

- The stator teeth are not modelled in detail, and affect only the system mass. Den Hartog [34], p.166, states that the stator teeth highly influence the total kinetic energy of the core but less the deformation energy. Belmans et al. [18] even show numerically that the extra modes brought by the teeth occur at frequencies much higher than the audible range. It is therefore reasonable to neglect them in the structural dynamics calculation in terms of flexural rigidity changes but not in terms of mass.
- The laminated nature of the core is taken into account by a stacking factor  $s_f$ ; although it basically allocates for mass removal by considering the air plus insulation layers between each lamination sheet [61, 74].

### 5.3 2D FE model

Despite the high gains in terms of computational resources and time required by the 1D analytical models, they have limited accuracy improvements. FE models are usually the solution employed to fill this gap. In theory, each lamination composing the core can be modelled but it would lead to millions of DOFs and thus hardly computable model, and without necessarily yielding higher accuracy results.

A solution to this problem is to model only the cross-section of the stator core via a 2D FE model. Indeed, as stated in literature [113, 142, 22, 23] and verified experimentally [28] (in the upcoming Section 5.6, the author also reaches these conclusions), the natural frequencies of pure radial modes  $f_{A(n_r,0)}$  depend strongly on the cross-section geometry. The stack length does not affect their value significantly. To the author's knowledge, no reference exists on the use of 2D shell elements in FE to calculate the natural frequencies of a laminated stator core. Therefore it is proposed in this thesis to model the stator core as a 2D component.

A 2D mesh is created from the cross-section geometry of the stator core. Then the shell elements that compose the structure (CQUAD4 in Nastran language [1]) are attributed isotropic property that corresponds to the electrical steel grade used for the laminations. The idea of the **Shell** model is to use a material model that depends only on known parameters which are the steel isotropic properties (given by manufacturers' datasheet). The stacking factor is not always known either such that the steel thickness is used as the shell element thickness. The details of solving the FE model are given in Section 2.2.2.

### Assumptions of the model:

- The model captures in-plane modes, *i.e.* pure radial modes  $A(n_r, 0)$  and the extensional/breathing mode  $C(0, 0)$ ; but also bending modes (linked to mode type E) not very much representative of the laminated stack E modes. The core length is not taken into account so modes involving  $n_z$  order components are not calculated.
- Shearing strains are neglected.
- The laminated nature of the core is supposed not to have any effect on the natural frequencies, and is therefore not considered.

## 5.4 3D FE model with homogenized material properties

Researchers mostly focus on 3D-element meshes to model the laminated core. The emulation of the laminated nature of the core is done by homogenization which is a more than 100 year old technique [102]. This Section reviews the available homogenization techniques available in literature. A detailed review of homogenization techniques is also very well explained in the thesis of Millithaler [84].

Since the FE mesh is composed of perfectly connected 3D elements, the only way to emulate the laminated nature of the core is to tune the material properties of the structure. Fundamentally, any material is in fact characterized by its mass density  $\rho$  and its elasticity matrix  $[C]$  in pascal. This fourth-order tensor is defined by Hooke's law  $\{\sigma\} = [C]\{\epsilon\}$  [104] in its general (*i.e.* anisotropic) formulation; where  $\{\sigma\}$  is the stress tensor,  $\{\epsilon\}$  the strain tensor and  $[C]$  a  $6 \times 6$  matrix with 36 independent coefficients:

$$\begin{Bmatrix} \sigma_{11} \\ \sigma_{22} \\ \sigma_{33} \\ \sigma_{23} \\ \sigma_{31} \\ \sigma_{12} \end{Bmatrix} = \begin{bmatrix} C_{11} & C_{12} & C_{13} & C_{14} & C_{15} & C_{16} \\ C_{21} & C_{22} & C_{23} & C_{24} & C_{25} & C_{26} \\ C_{31} & C_{32} & C_{33} & C_{34} & C_{35} & C_{36} \\ C_{41} & C_{42} & C_{43} & C_{44} & C_{45} & C_{46} \\ C_{51} & C_{52} & C_{53} & C_{54} & C_{55} & C_{56} \\ C_{61} & C_{62} & C_{63} & C_{64} & C_{65} & C_{66} \end{bmatrix} \begin{Bmatrix} \epsilon_{11} \\ \epsilon_{22} \\ \epsilon_{33} \\ 2\epsilon_{23} \\ 2\epsilon_{31} \\ 2\epsilon_{12} \end{Bmatrix} \quad (5.1)$$

where the subscripts 1, 2 and 3 refer to the respective directions (x,y,z) for Cartesian coordinates and (r, $\theta$ ,z) for cylindrical coordinates. Hence the simplification of the complex steel stack to a homogeneous component referring

to an equivalent elasticity matrix  $[C]$  is homogenization by definition. In the case of conservative material, the elasticity matrix is symmetric so it reduces the number of unknown coefficients to 21 (plus the mass density  $\rho$ ).  $[C]$  becomes:

$$[C] = \begin{bmatrix} C_{11} & C_{12} & C_{13} & C_{14} & C_{15} & C_{16} \\ & C_{22} & C_{23} & C_{24} & C_{25} & C_{26} \\ & & C_{33} & C_{34} & C_{35} & C_{36} \\ & & & C_{44} & C_{45} & C_{46} \\ & sym. & & & C_{55} & C_{56} \\ & & & & & C_{66} \end{bmatrix} \quad (5.2)$$

However the difficulty arises when trying to identify the 21 coefficients  $C_{ij}$  of  $[C]$  which best represent the stack behavior. To that matter researchers describe numerous identification techniques that use different assumptions regarding material orientation.

### 5.4.1 Isotropic behavior

Several authors firstly assume that the steel stack behaves identically in every direction such as a homogeneous solid stator, *i.e.* it behaves isotropically [74][51][109]. It reduces the number of unknowns to 3: Young's modulus  $E$ , poisson ratio  $\nu$  and mass density  $\rho$ . The advantage is that manufacturers usually provide such data for electrical steel so that its corresponding elasticity matrix can be calculated easily without any experiments or calculations.  $[C]$  is simply given by

$$[C] = \frac{E}{(1 + \nu)(1 - 2\nu)} \begin{bmatrix} 1 - \nu & \nu & \nu & 0 & 0 & 0 \\ & 1 - \nu & \nu & 0 & 0 & 0 \\ & & 1 - \nu & 0 & 0 & 0 \\ & & & \frac{(1-2\nu)}{2} & 0 & 0 \\ & sym. & & & \frac{(1-2\nu)}{2} & 0 \\ & & & & & \frac{(1-2\nu)}{2} \end{bmatrix} \quad (5.3)$$

Although some authors find good correlations for the natural frequencies using isotropic properties and raw data obtained from manufacturers [127, 142, 27], improvements may be achieved using experimental-based model updating *e.g.* M. van der Griet explains in [124] an empirical method to identify the 3 constitutive unknowns. Yet the isotropic modelling approach limits the model tuning capabilities and makes strong assumptions which do not necessarily



make much physical sense; the mechanical phenomena added by the laminated nature of the compound are not considered at all in such model.

This method is used later in the thesis and referred to as **Iso**.

### 5.4.2 Orthotropy and Transverse isotropy

Indeed Van der Giet et al. [125] show that the Young’s modulus in the axial direction  $E_3$  is much lower than in the other directions. Hubert et al. [61] as well state experimentally that the core is significantly more flexible in the axial direction, leading to a necessity of taking into account the dependency of the homogenized material on the directions. Material orthotropy is then supposed because it allocates for behavior dependencies on directions. The general elasticity matrix  $[C]$  becomes

$$[C] = \begin{bmatrix} \frac{1-\nu_{23}\nu_{32}}{E_2 E_3 \Delta} & \frac{\nu_{21}+\nu_{31}\nu_{23}}{E_2 E_3 \Delta} & \frac{\nu_{31}+\nu_{21}\nu_{32}}{E_2 E_3 \Delta} & 0 & 0 & 0 \\ \frac{\nu_{12}+\nu_{13}\nu_{32}}{E_3 E_1 \Delta} & \frac{1-\nu_{31}\nu_{13}}{E_3 E_1 \Delta} & \frac{\nu_{32}+\nu_{31}\nu_{12}}{E_3 E_1 \Delta} & 0 & 0 & 0 \\ \frac{\nu_{13}+\nu_{12}\nu_{23}}{E_1 E_2 \Delta} & \frac{\nu_{23}+\nu_{13}\nu_{21}}{E_1 E_2 \Delta} & \frac{1-\nu_{12}\nu_{21}}{E_1 E_2 \Delta} & 0 & 0 & 0 \\ 0 & 0 & 0 & G_{23} & 0 & 0 \\ 0 & 0 & 0 & 0 & G_{31} & 0 \\ 0 & 0 & 0 & 0 & 0 & G_{12} \end{bmatrix} \quad (5.4)$$

$$\text{with } \Delta = \frac{1 - \nu_{12}\nu_{21} - \nu_{23}\nu_{32} - \nu_{31}\nu_{13} - 2\nu_{12}\nu_{23}\nu_{31}}{E_1 E_2 E_3}$$

The symmetry condition reads

$$\begin{aligned} \frac{\nu_{12} + \nu_{13}\nu_{32}}{E_3 E_1 \Delta} &= \frac{\nu_{21} + \nu_{31}\nu_{23}}{E_2 E_3 \Delta} \\ \frac{\nu_{13} + \nu_{12}\nu_{23}}{E_1 E_2 \Delta} &= \frac{\nu_{31} + \nu_{21}\nu_{32}}{E_2 E_3 \Delta} \\ \frac{\nu_{23} + \nu_{13}\nu_{21}}{E_1 E_2 \Delta} &= \frac{\nu_{32} + \nu_{31}\nu_{12}}{E_3 E_1 \Delta} \end{aligned} \quad (5.5)$$

However by looking more into the topology of the laminated core, researchers have come to consider a variant of orthotropy: transverse isotropy, *i.e.* the structure has particular material properties in one plane (parallel to the cross section, *e.g.* (1,2) corresponding to  $(x, y)$  or  $(r, \theta)$ ), and different properties in

the direction normal to this plane (direction 3 =  $z$ ). This leads to  $C_{11} = C_{22}$ ,  $C_{13} = C_{23}$  and  $C_{44} = C_{55}$ . The stiffness matrix  $[C]$  for this type of material is then:

$$[C] = \begin{bmatrix} \frac{1-\nu_{13}\nu_{31}}{E_1 E_3 \Delta} & \frac{\nu_{12}+\nu_{13}\nu_{31}}{E_1 E_3 \Delta} & \frac{\nu_{13}+\nu_{12}\nu_{31}}{E_1 E_3 \Delta} & 0 & 0 & 0 \\ & \frac{1-\nu_{13}\nu_{31}}{E_1 E_3 \Delta} & \frac{\nu_{13}+\nu_{12}\nu_{31}}{E_1 E_3 \Delta} & 0 & 0 & 0 \\ & & \frac{1-\nu_{12}}{E_1^2 \Delta} & 0 & 0 & 0 \\ & \text{sym.} & & G_{31} & 0 & 0 \\ & & & & G_{31} & 0 \\ & & & & & \frac{E_1}{2(1+\nu_{12})} \end{bmatrix} \quad (5.6)$$

$$\text{with } \Delta = \frac{(1 + \nu_{12})(1 - \nu_{12} - 2\nu_{13}\nu_{31})}{E_1^2 E_3}$$

Either 9 (orthotropy) or 5 (transverse isotropy) independent variables  $E_1$ ,  $E_3$ ,  $\nu_{12}$ ,  $\nu_{13}$  and  $G_{31}$  have to be determined and are not available in manufacturer data sheets. Hence a variety of identification methods are proposed in literature, from model updating to analytical and multi-scale methods.

## Model updating

Wegerhoff et al. [138] present a straightforward model updating technique. The 5 transversally isotropic variables are determined iteratively by fitting the measured natural frequencies to the model predicted ones. The procedure proposed by the author states that:

- $E_1 = E_2$  is set by  $f_{A(n_r,0)}$ ; modes A (pure radial) are used to tune  $E_1 = E_2$
- Poisson ratios  $\nu_{12}$  and  $\nu_{13}$  can be set to the steel datasheet value
- $G_{31}$  is set by  $f_{B(n_r,1)}$ ; modes B (radial motion with radial shearing) are used to tune  $G_{31}$
- $E_3$  is set by  $f_{E(n_r,n_z)}$ ; modes E (axial bending modes) are used to tune  $E_3$

Model updating is also proposed by Schwarzer et al. [110], where the stiffness matrix is updated comparing natural frequencies of modes A and B antisymmetric. However, the explanations are not extensive and the material category is not mentioned. Mair et al. [81] do assume transverse isotropy for their model by demonstrating that isotropic material model does not fit with

the measured data. Moreover, they update their material model by manually fitting every natural frequency occurring from 500 Hz to 3,000 kHz. Similarly as in [138], the effects of each elasticity variable are considered in an uncorrelated way, which in the end supports the optimization process.

Nevertheless the expensive construction of a prototype limits the experimental model updating use such that it becomes interesting to calculate the constitutive parameters as accurately as possible prior to any prototyping phase. Thus model updating procedures are not further considered in the thesis. In fact it will be shown in Section 5.5 that a single linear material model cannot capture every natural frequency with high accuracy.

### Rules of Mixture (RoM) (RoM)

In the **Rules of Mixture (RoM)** procedure [106], the matrix coefficients of Equation 5.4 are determined analytically. The steel stack is a composition of insulating resin (i) and steel (s) layers which form a composite material. The idea is to take the volume ratio  $\phi$  of each of the components into account to calculate the weighed averages of each constitutive parameters. This method is employed by Van der Griet [125] and Millithaler [86, 84] as a first step towards more advanced homogenization techniques. The following equations from (5.7) to (5.14) give the values of the five independent constitutive variables using the **RoM**, where superscripts  $(i)$ ,  $(s)$  and  $(total)$  refer respectively to insulation, steel and total parameters and  $V$  is the volume of each component:

$$\phi^{(i)} = \frac{V^{(i)}}{V^{(total)}} \quad \text{and} \quad \phi^{(s)} = \frac{V^{(s)}}{V^{(total)}} \quad (5.7)$$

$$\rho = \phi^{(i)}\rho^{(i)} + \phi^{(s)}\rho^{(s)} \quad (5.8)$$

$$E_1 = E_2 = \phi^{(i)}E^{(i)} + \phi^{(s)}E^{(s)} \quad (5.9)$$

$$E_3 = \left( \frac{\phi^{(i)}}{E^{(i)}} + \frac{\phi^{(s)}}{E^{(s)}} \right)^{-1} \quad (5.10)$$

$$\nu_{12} = \phi^{(i)}\nu^{(i)} + \phi^{(s)}\nu^{(s)} \quad (5.11)$$

$$\nu_{13} = \nu_{23} = \nu_{12} \frac{E_3}{E_1} \quad (5.12)$$

$$G_{12} = \frac{E_1}{2(1 + \nu_{12})} \quad (5.13)$$

$$G_{13} = G_{23} = \frac{1}{2} \left( \frac{\phi^{(i)} \cdot (1 + \nu^{(i)})}{E^{(i)}} + \frac{\phi^{(s)} \cdot (1 + \nu^{(s)})}{E^{(s)}} \right)^{-1} \quad (5.14)$$

## INRIA

A more elaborated analytical method is developed by Begis et al. [16][15] and referred to as Institut National de Recherche en Informatique et en Automatique (**INRIA**). The  $Y$ -periodic composite structure's equivalent elasticity matrix  $[C]$  is obtained from an asymptotic homogenization approach. The global idea is to get  $Y$ -periodic vectors  $\{W^{pq}(y)\}$  by solving the following equation,

$$\frac{\partial}{\partial y_j} \left( C_{ijkl}(y) \epsilon_{kl}(\{W^{pq}(y)\}) \right) = \frac{-\partial}{\partial y_j} C_{ijkl}(y) \quad (5.15)$$

and finally obtain the homogenized coefficients  $C_{ijkl,eq}$ ,

$$C_{ijkl,eq} = \frac{1}{vol_Y} \int_Y \left[ C_{ijkl}(y) - C_{ijpq}(y) \epsilon_{kl}(\{W^{pq}(y)\}) \right] dy \quad (5.16)$$

where  $vol_Y$  is the volume of the unit cell. Although the computational time is significantly reduced and the steel stacks can be assumed to be a composite material, mathematical difficulties may emerge to resolve equation (5.15). Nevertheless Begis et al. [16] apply it for the interesting case of  $N$  isotropic layers stacked along the 3rd axis ( $z$ ). By assuming isotropy for each constitutive layer one obtains the equivalent elasticity matrix coefficients  $C_{ij}$  from Lamé's coefficients  $\lambda^{(n)}$  and  $\mu^{(n)}$  [16, 84] for each layer  $n$ :

$$C_{11} = C_{22} = \frac{I_1^2 - I_0 I_2}{I_0} + \sum_{n=1}^N (\lambda^{(n)} + 2\mu^{(n)}) V^{(n)} \quad (5.17)$$

$$C_{12} = \frac{I_1^2 - I_0 I_2}{I_0} + \sum_{n=1}^N \lambda^{(n)} V^{(n)} \quad (5.18)$$

$$C_{13} = C_{23} = \frac{I_1}{I_0} \quad (5.19)$$

$$C_{33} = \frac{1}{I_0} \quad (5.20)$$

$$C_{44} = C_{55} = \frac{1}{J_0} \quad (5.21)$$

$$C_{66} = \sum_{n=1}^N \mu^{(n)} V^{(n)} \quad (5.22)$$

with

$$I_h = \sum_{n=1}^N \frac{(\lambda^{(n)})^h}{\lambda^{(n)} + 2\mu^{(n)}} V^{(n)} \quad h = 0, 1, 2 \quad (5.23)$$

$$J_0 = \sum_{n=1}^N \frac{V^{(n)}}{\mu^{(n)}} \quad (5.24)$$

It is worth noting that the matrix verifies transverse isotropy property  $C_{11} = C_{12} + 2C_{66}$ .

### Multi-scale methods

The homogenized structural behavior can also be obtained using a two-step approach, often referred to as a multi-scale technique. Hirschberger et al. describe in [59] the process of modelling heterogeneous material layers. Firstly the behavior of a Representative Volume Element (RVE) is studied. It represents a microscopic portion of the macroscopic structure where the heterogeneous property takes its origin. Secondly one can relate the macro level deformations to the averaged stress and strain tensors at micro level by applying correct RVE volumes and boundary conditions, using an iterative nested solution procedure. One of the advantages of the multi-scale method is the possibility to emulate nonlinear behavior without increasing greatly the model complexity. Hence, it is applied by Luchscheider et al. in [78] in the case of laminated stack. In order to simulate the nonlinear contact between the laminations, the authors make use of a repeated RVE which integrates the nonlinearity by assuming the contact surfaces' roughness to be stack pressure dependent. This periodic RVE corresponds to a portion of the stacks as thick as a single sheet which contains the plane contact in the middle as shown in Fig. 5.2. The stack's material properties, *i.e.* non-linear stiffness and damping matrices, are then identified by applying different static load conditions to the RVE. Being more accurate with the nonlinear implementation in the model, this multi-scale

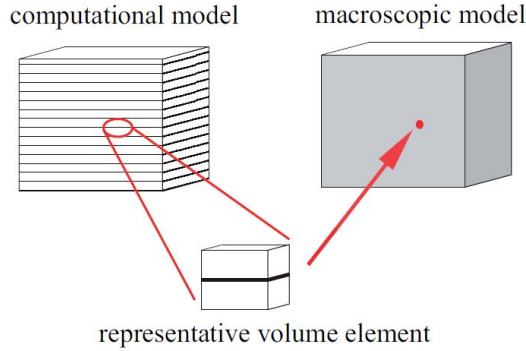


Figure 5.2: Principle of multi-scale homogenization for a laminated stack - Figure taken from [78]

homogenization technique might still require high computational effort because of the non-linearities themselves.

The most recent referenced multi-scale approach is by Millithaler et al. [84][86][85], and is later referred as (**Ortho**). Their work introduces a novel approach in which orthotropic [86] equivalent material properties are identified for laminated steel stacks. The technique uses a base unit cell composed of three isotropic layers (here steel, epoxy and steel) perfectly connected to each other that is put in different pre-stress conditions to collect the equivalent constitutive parameters. In short, static displacements are enforced at particular nodes of the unit cell and output reaction forces and displacements permit to calculate the constitutive parameters [84]. Several combinations of enforced displacements  $\delta$  are then necessary to provide every equivalent constitutive component  $C_{ij}$  since they activate different independent motions *e.g.* pure tension, transverse shear, sliding shear, etc.

Let us consider the cuboid RVE for a laminated stator core stack, composed of 16 nodes (numbered from 1 to 8 and from 11 to 18) as depicted in Fig. 5.3. They form a cuboid of three 8-node elements whose dimensions are  $L_1$ ,  $L_2$  and  $L_3$ , with respective areas  $A_1 = L_2L_3$ ,  $A_2 = L_3L_1$  and  $A_3 = L_1L_2$ .

Six simulations with dedicated enforced displacements  $\delta_i$  (input) applied to specific nodes  $P_{\delta_i}$  along direction  $i = (-1, 1, -2, 2, -3, 3)$ , with proper fixed reference planes for system stability purposes, are performed. They are summarized in Table 5.3 and permit to determine the homogenized material parameters via the calculation of the reaction forces  $F_k(P_{\delta_i})$  and the nodal displacements  $\Delta l_k(P_{\delta_i})$  along direction  $k$  and at the nodes  $P_{\delta_i}$ .

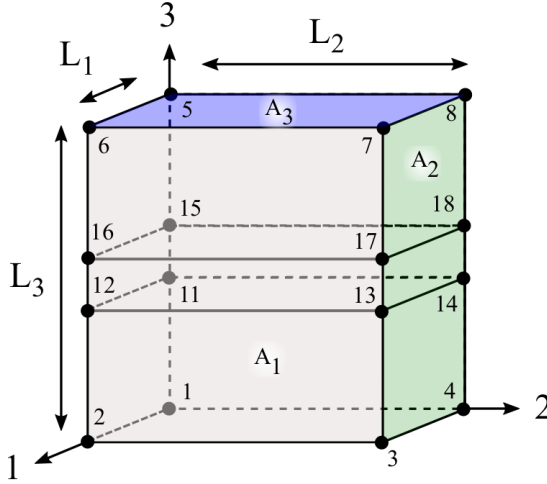


Figure 5.3: Base unit cell used for parameter identification

Table 5.3: Simulations performed for parameter identification

Simulation type	Forced displacements $\delta_i$	Fixed reference Plane	DoF	Evaluated parameters	
	Dir. $i$	$P_{\delta_i}$			
Pure tension 1	-1	1,4,5,8,11,14,15,18	(1,2,3,4)	3	$E_1, \nu_{12}, \nu_{13}$
	+1	2,3,6,7,12,13,16,17	(1,2,6,5)	2	
Pure tension 2	-2	1,2,5,6,11,12,15,16	(1,2,3,4)	3	$E_2, \nu_{23}$
	+2	3,4,7,8,13,14,17,18	(1,4,5,8)	1	
Pure tension 3	-3	1,2,3,4	(1,2,5,6)	2	$E_3$
	+3	5,6,7,8	(1,4,5,8)	1	
Shear 1	-1	1,2,3,4	(1,2,3,4)	3	$G_{31}$
	+1	5,6,7,8	(5,6,7,8)	3	
Shear 2	-2	1,2,3,4	(1,2,3,4)	3	$G_{32}$
	+2	5,6,7,8	(5,6,7,8)	3	
Shear 3	-2	2,3,6,7,12,13,16,17	(2,3,6,7)	1	$G_{12}$
	+2	1,4,5,6,11,14,15,16	(1,4,5,6)	1	

Fig. 5.4 illustrates pure tension 1 and sliding shear 2 simulations as well. It is important to mention that two different shear schemes can be obtained from non-isotropic materials: pure sliding shear (considering  $G_{32}$ ) and pure transverse shear (considering  $G_{23}$ ). In this work, pure sliding shear is used since it gives more accuracy in the results and is more consistent regarding the structure to model, as argued in [86].

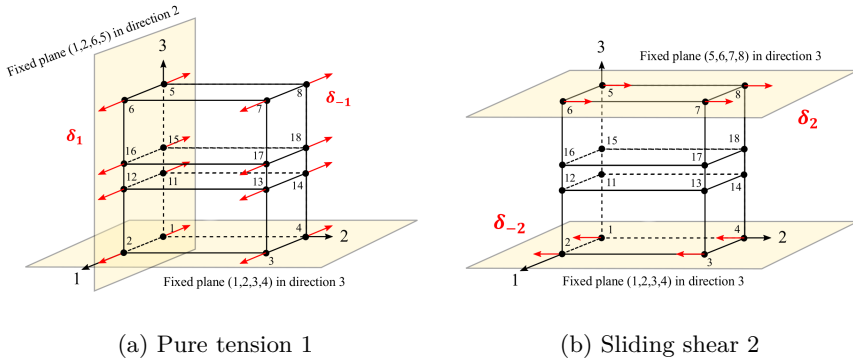


Figure 5.4: Examples of two RVE simulations

Then the equivalent material parameters  $E_1$ ,  $E_2$ ,  $E_3$ ,  $\nu_{12}$ ,  $\nu_{13}$ ,  $\nu_{23}$ ,  $G_{32}$ ,  $G_{31}$  and  $G_{12}$  are derived from the following equations: note that the equivalent mass density  $\rho$  is immediately derived from equation 5.8.

$$E_1 = \frac{\sigma_{11}}{\epsilon_{11}} = \frac{L_1}{\delta_1 A_1} \sum_{P_{\delta_1}} \frac{F_1(P_{\delta_1})}{2} \quad (5.25)$$

$$E_2 = \frac{\sigma_{22}}{\epsilon_{22}} = \frac{L_2}{\delta_2 A_2} \sum_{P_{\delta_2}} \frac{F_2(P_{\delta_2})}{2} \quad (5.26)$$

$$E_3 = \frac{\sigma_{33}}{\epsilon_{33}} = \frac{L_3}{\delta_3 A_3} \sum_{P_{\delta_3}} \frac{F_3(P_{\delta_3})}{2} \quad (5.27)$$

$$\nu_{12} = -\frac{\epsilon_{22}}{\epsilon_{11}} = -\frac{\sum_{P_{\delta_2}} \Delta l_2(P_{\delta_2})}{8 \times 2\delta_1} \cdot \frac{L_1}{L_2} \quad (5.28)$$

$$\nu_{13} = -\frac{\epsilon_{33}}{\epsilon_{11}} = -\frac{\sum_{P_{\delta_3}} \Delta l_3(P_{\delta_3})}{4 \times 2\delta_1} \cdot \frac{L_1}{L_3} \quad (5.29)$$

$$\nu_{23} = -\frac{\epsilon_{33}}{\epsilon_{22}} = -\frac{\sum_{P_{\delta_3}} \Delta l_3(P_{\delta_3})}{4 \times 2\delta_2} \cdot \frac{L_2}{L_3} \quad (5.30)$$

$$G_{32} = \frac{\sigma_{32}}{2\epsilon_{32}} = \frac{L_3}{\delta_3 A_3} \sum_{P_{\delta_2}} \frac{F_2(P_{\delta_2})}{2} \quad (5.31)$$



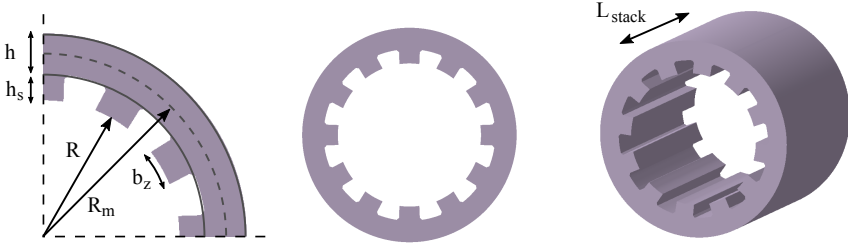


Figure 5.5: Cross-section and profile of the stator core under study

$$G_{31} = \frac{\sigma_{31}}{2\epsilon_{31}} = \frac{L_3}{\delta_3 A_3} \sum_{P_{\delta_1}} \frac{F_1(P_{\delta_1})}{2} \tag{5.32}$$

$$G_{12} = \frac{\sigma_{12}}{2\epsilon_{12}} = \frac{L_1}{\delta_1 A_1} \sum_{P_{\delta_2}} \frac{F_2(P_{\delta_2})}{2} \tag{5.33}$$

The calculated data fills the equivalent elasticity matrix which serves as material definition of the laminated core compound in FEA. It is interesting to note that the **Ortho** method applied to laminated stator stacks actually leads to a transverse isotropic material model.

It is also interesting to note that researchers who assume anisotropy (*i.e.* 21 coefficients to identify) for the homogenized medium do not gain significant accuracy compared to the orthotropic and transverse isotropic models [16, 80, 84, 85]. Hence anisotropy is not assumed in this thesis.

## 5.5 Model comparison and validation: A case study

The different modeling approaches presented in the previous Sections are further developed for a chosen stator core. The predicted natural frequencies are compared with experimental results to assess model validity and limitations.

### 5.5.1 Reference experimental tests

The laminated stator core under study is a 12/8 SRM from industry. Its characteristics are given in Table 5.4 and its cross-section is depicted in Fig. 5.5. It is composed of electrical steel laminations of type M300-35A.

Table 5.4: Characteristics of the stator core under study

Parameter	Symbol	Unit	Value
Mass	$m$	kg	20.45
Number of slots/teeth	$Q_s$		12
Mean tooth width	$b_z$	mm	18.4
Tooth height	$h_s$	mm	13.6
Number of laminations	$n_s$		529
Stack length	$L_{stack}$	mm	185
Yoke mean radius	$R_m$	mm	85.5
Yoke height	$h$	mm	20.5

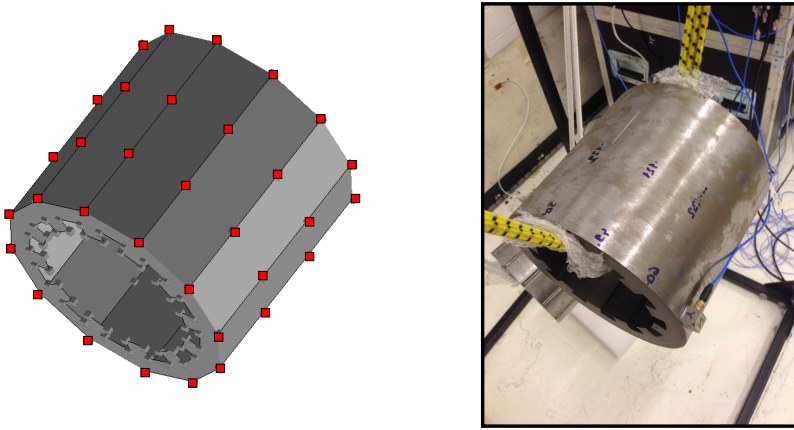


Figure 5.6: Experimental setup; (left) Test.lab geometry, (right) Test setup

A standard-manufactured specimen is tested for EMA purposes. Elastic ropes are used to hang the system and emulate free-free boundary conditions. A miniature shaker (LMS Qsource SN045) is used for radial excitation and provides reliable results up to 5.5 kHz [7]. Its settings are the following: white noise input from 100 Hz to 8 kHz as a burst random signal (80% burst time, 25ms burst ramp time) and 50 averages used for H1 FRF estimation [58]. Tri-axial accelerometers (PCB Piezotronics SN 356A22) are employed and located along the complete stator circumference. Fig. 5.6 illustrates the Test.lab geometry definition and the test setup. The discretization of the 48 (12 circumferentially and 4 axially) accelerometer positions ensures the capture of all modes of interest without spatial aliasing.

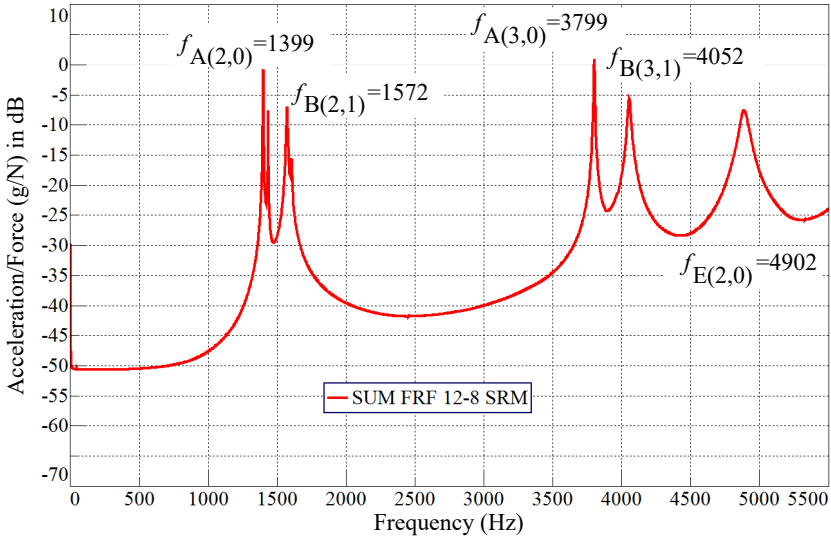


Figure 5.7: FRF-sum for the 12-8 SRM under study

It is important to notice that EMA relies on the linearity principle hence it was consistently checked throughout the test campaign following the described procedure in Section 2.2. The FRF-sum  $S_H(\omega)$  is defined from the full set of  $N_H = 48 \times 3$  FRFs:

$$S_H(\omega) = \frac{1}{N_H} \sum_{N_H} |\Re(H_{O/I}(\omega))| + j|\Im(H_{O/I}(\omega))| \quad (5.34)$$

$S_H(\omega)$  is plotted in Fig. 5.7, together with the undamped natural frequencies corresponding to each mode.

Within the investigated frequency range, the first two pure radial modes  $A(n_r, 0)$  are captured together with their respective twin mode. The two first antisymmetric radial modes with axial shear  $B(n_r, 1)$  and the axial bending mode  $E(2, 0)$  are also captured. These results serve as a reference to compare the developed models and support their updating in the following Sections.

## 5.5.2 Stator core models

The laminated stator core under study is modelled using the different models described in Sections 5.2 and 5.4, *i.e.* **Ring**, **Iso**, **RoM**, **INRIA**, **Ortho** and

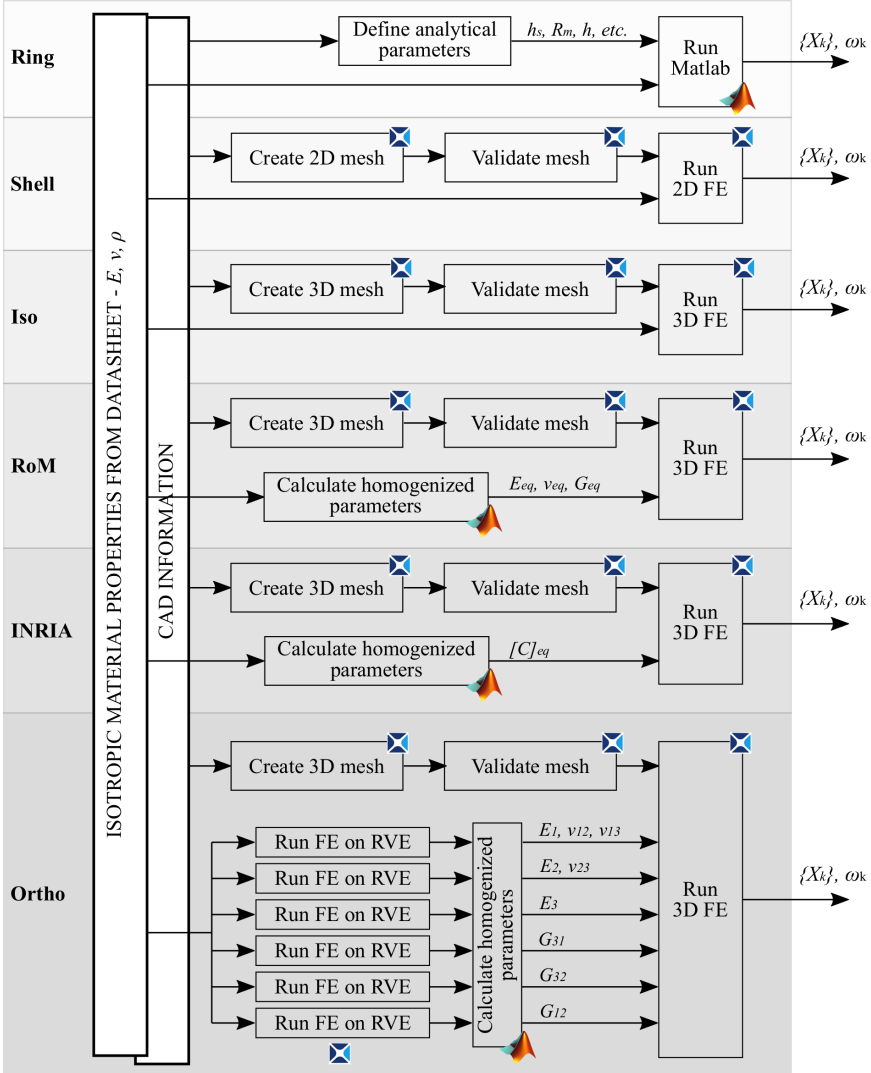


Figure 5.8: Illustration of the stator core models modeling flow

**Shell.** Their practical implementation is illustrated in Fig. 5.8.

The constitutive materials of the laminated stator, *i.e.* the electrical steel M300-35A and the resin plus epoxy glue, have the datasheet properties listed in Table 5.5. The resin plus glue compound is supposed isotropic with properties taken from [84]. It is important to note that the filling ratio for the steel  $\phi^{(s)}$

Table 5.5: Isotropic material properties of the composite compounds

Name	$k$	$E^{(k)}$ GPa	$\rho^{(k)}$ kg/m <sup>3</sup>	$\nu^{(k)}$ -	$\phi^{(k)}$ -
Steel M300-35A	$s$	185	7,650	0.287	99.1%
Resin + epoxy	$i$	2	1,350	0.36	0.9%

corresponds to the stacking factor  $s_f$  and is commonly between 95% and 99.5% [2]. Here the same value as taken by Millithaler et al. [84], *i.e.* 99.1%, is assumed. Additionally the test specimen mass is known and can be used jointly with the 3D CAD volume of the stator core for mass density updating. It leads to an equivalent mass density of  $\rho_{eq} = 7,322 \text{ kg/m}^3$ . The specimen volume is not measured for this updating phase because the emphasis is on mass fit rather than mass density fit.

## Ring

The **Ring** model follows the assumptions and equations of Section 5.2. The geometry parameters of the **Ring** model are detailed by Table 5.4. The material model is considered isotropic and corresponds to the electrical steel grade M300-35A. The mass density corresponds to an updated value  $\rho_{eq}(Ring) = 7,883 \text{ kg/m}^3$  that correlates with the measured stator mass.

## Shell

The **Shell** model follows the assumptions and equations of Section 5.3. It requires a mesh of 2D shell elements. The 2D mesh results from a validation process in which a trade-off between accuracy and computational efforts is made. The chosen mesh is composed of 1,462 nodes and 1,261 4-node isoparametric quadrilateral elements and actually corresponds to the cross-sectional surface mesh of the 3D mesh displayed in Fig. 5.9. As explained in Section 5.3, the material properties are defined only by the electrical steel properties available in Table 5.6. The thickness of the shell elements is then set to  $350 \mu\text{m}$  which does not take the stacking factor into account: the steel is supposed to dominate the dynamic behavior.

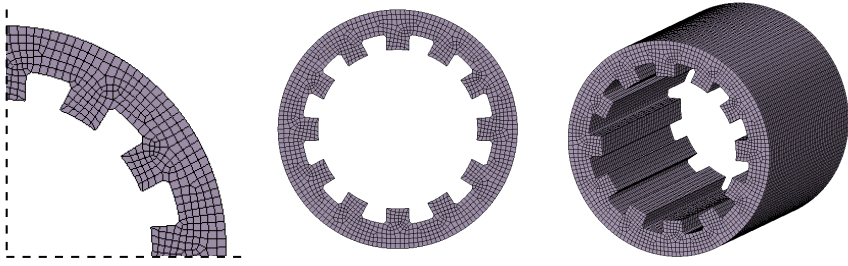


Figure 5.9: 3D-mesh validated

### Iso

The **Iso** model follows the assumptions and equations of Section 5.4.1. Alike for the 2D mesh created previously, the 3D mesh results from a validation process in which a trade-off between accuracy and computational efforts is made. The chosen mesh is composed of 68,714 nodes and 58,006 8-node trilinear hexahedral elements and is pictured in Fig. 5.9. The material model does not incorporate the laminated nature of the stator such that it is considered isotropic and corresponds to the electrical steel grade M300-35A whose properties are detailed in Table 5.5. The mass density corresponds to the updated value  $\rho_{eq}$ .

### RoM

The **RoM** model follows the assumptions of Section 5.4.2. The validated mesh defined in the previous Section and in Fig. 5.9 is used. The material model includes the effects of the laminations following the equations of Section 5.4.2. However the mass density corresponds to the updated value  $\rho_{eq}$  and not to the value obtained by equation 5.8 in order to fit the system mass and thus investigate the model validity from a stiffness point of view.

### INRIA

Similarly to the **RoM** model, **INRIA** follows the assumptions and equations of Section 5.4.2. The validated mesh defined in Fig. 5.9 is used. For the same reason, the mass density corresponds to the updated value  $\rho_{eq}$  and not to the value obtained by equation 5.8.

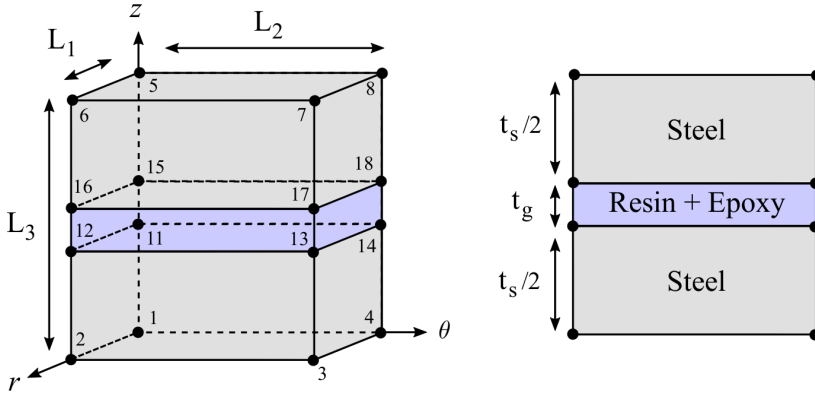


Figure 5.10: **Ortho** RVE representation

**Ortho**

The **Ortho** model follows the assumptions and equations of Section 5.4.2. The RVE taken into consideration is illustrated in Fig. 5.10; two half layers of steel sandwich a layer of resin plus epoxy glue. The manufacturer states that the lamination thickness is equal to  $350 \mu\text{m}$ . However, given the stacking factor (or filling ratio)  $\phi^{(s)}$  of 99.1%, one obtains the steel sheet thickness  $t_s = \phi^{(s)} \times 350 = 347 \mu\text{m}$ . As a consequence, each steel layer on the RVE has a thickness of  $t_s/2 = 178.5 \mu\text{m}$  and a resin plus epoxy thickness  $t_g = \phi^{(i)} \times 350 = 3.15 \mu\text{m}$ .

The pure tension and shear static analyses are performed as described in Section 5.4.2 and permit to estimate the material parameters for a transversally isotropic medium.

**5.5.3 Comparisons**

The stator models described above have the material parameters summarized in Table 5.6. One can already notice several discrepancies:

- The stator model masses are different. The **Ring** model and the models using 3D meshes obviously estimate well the mass since the mass densities were updated. **Shell** does not take the core length into account, so one can relate its mass to a single lamination mass.

Table 5.6: Model parameters

Parameter	Unit	Model					
		<b>Ring</b>	<b>Iso</b>	<b>RoM</b>	<b>INRIA</b>	<b>Ortho</b>	<b>Shell</b>
Mass	kg	20.45	20.49	20.49	20.49	20.49	0.041
$\rho$	kg/m <sup>3</sup>	7,883	7,322	7,322	7,322	7,322	7,650
$E_r$	GPa	185.0	185.0	183.4	183.4	183.2	185.0
$E_\theta$	GPa	185.0	185.0	183.4	183.4	183.2	185.0
$E_z$	GPa	-	185.0	103.7	126.0	115.7	185.0
$\nu_{r\theta}$	-	-	0.287	0.287	0.287	0.287	0.287
$\nu_{rz}$	-	-	0.287	0.163	0.288	0.287	0.287
$\nu_{\theta z}$	-	-	0.287	0.163	0.288	0.287	0.287
$G_{z\theta}$	GPa	-	71.87	39.29	39.29	30.55	71.87
$G_{zr}$	GPa	-	71.87	39.29	39.29	30.55	71.87
$G_{r\theta}$	GPa	-	71.87	71.23	71.26	71.07	71.87

- **RoM** has a lower axial Young's modulus  $E_z$ , and lower transverse Poisson ratios  $\nu_{rz}$  and  $\nu_{\theta z}$ , and transverse shear moduli  $G_{z\theta}$  and  $G_{zr}$ . On the other hand the in-plane parameters  $E_r$ ,  $E_\theta$ ,  $\nu_{r\theta}$  and  $G_{r\theta}$  are not affected.
- **INRIA** is very similar to **RoM** but without changes on the Poisson ratios. It seems to allocate for higher stiffness in the axial direction, while shear stiffnesses are equal.
- **Ortho** is similar to **INRIA**, but with lower axial stiffness. Transverse shear values are reduced but in-plane shear are the same and does not seem to be affected by any of the models.

The natural frequencies obtained with the different models are computed and compared to the experimental values obtained in Section 5.5.1. The relative difference between the measured and simulated natural frequencies is denoted  $\epsilon$ .

At this stage, it is possible to draw conclusions on the capabilities of each model to capture the natural frequencies. **Ring** guarantees an impressive accuracy below 3.1% of relative error, which can be adequate for advanced design and an interesting fast-to-compute approach, given its simplicity. However it is important to remark that the mass density was significantly modified (from 7,650 to 7,883 kg/m<sup>3</sup>), which discredits the model usage because of the need for a testing-prototype. Moreover B modes are not captured by the **Ring** model. **Iso** provides relevant accuracy as well for A modes and captures B



Table 5.7: Model and experimental results comparisons of the natural frequencies

	$f_{A(2,0)}$ Hz	$\epsilon$ %	$f_{B(2,1)}$ Hz	$\epsilon$ %	$f_{A(3,0)}$ Hz	$\epsilon$ %	$f_{B(3,1)}$ Hz	$\epsilon$ %
Measured	1399		1572		3799		4052	
<b>Ring</b>	1389	-0.7	-	-	3681	-3.1	-	-
<b>Iso</b>	1449	+3.6	2009	+27.8	3884	+2.2	4703	+16.1
<b>RoM</b>	1357	-3.0	1705	+8.5	3569	-6.1	4085	+0.8
<b>INRIA</b>	1378	-1.5	1718	+9.3	3619	-4.7	4124	+1.8
<b>Ortho</b>	1348	-3.7	1617	+2.9	3503	-7.8	3905	-3.6
<b>Shell</b>	1377	-1.6	-	-	3699	-2.6	-	-

modes, although the complete structure shows too stiff behavior compared to the laminated system, especially for B modes that show errors higher than 16%. Both **RoM** and **INRIA** give similar results, with increasing accuracy for the natural frequencies of B modes. **Ortho** shows higher accuracy for the B modes but the accuracy is lost for A modes in comparison with **Iso** model. The advantages of **Ortho** are not significantly demonstrated here, knowing the required static analyses that prolongate the model implementation time. On the other hand **Shell** permits to have a decent accuracy in terms of A modes natural frequencies, while using immediate material data from the manufacturer. It means that the cross-section of the core and the steel dominate the dynamics of pure radial shape, which is validated as well in Section 5.6. But the B modes are not captured with this type of model.

In general, the isotropic models, *i.e.* **Iso** and **Shell** capture very well the pure radial modes  $A(n_r, 0)$  but transverse isotropy is necessary to capture correctly the antisymmetric  $B(n_r, 1)$  modes. In fact, laminating a stator core decreases the difference  $f_{A(n_r, 0)} - f_{B(n_r, 1)}$ . Yet it is not sure whether the linear transverse isotropy is a suitable assumption to tune this difference for perfect natural frequency fit. Indeed while it is clear that  $E_r = E_\theta$ ,  $G_{\theta z} = G_{zr}$  and  $\nu_{rz} = \nu_{\theta z}$  for geometrical reasons, it is not trivial to complete the condition  $G_{r\theta} = \frac{E_r}{2(1+\nu_{r\theta})}$ . The next Section 5.5.4 verifies this transverse isotropy assumption.

### 5.5.4 Material parameter sweep and optimization

Mair et al. [81] perform a parameter sweep study for the values  $E_r$ ,  $E_z$ ,  $\nu_{r\theta}$  and  $G_{rz}$  and look at the resulting natural frequencies. They find that the Poisson ratios do not affect significantly the frequencies and that the material parameters have different influences on the natural frequencies depending on the

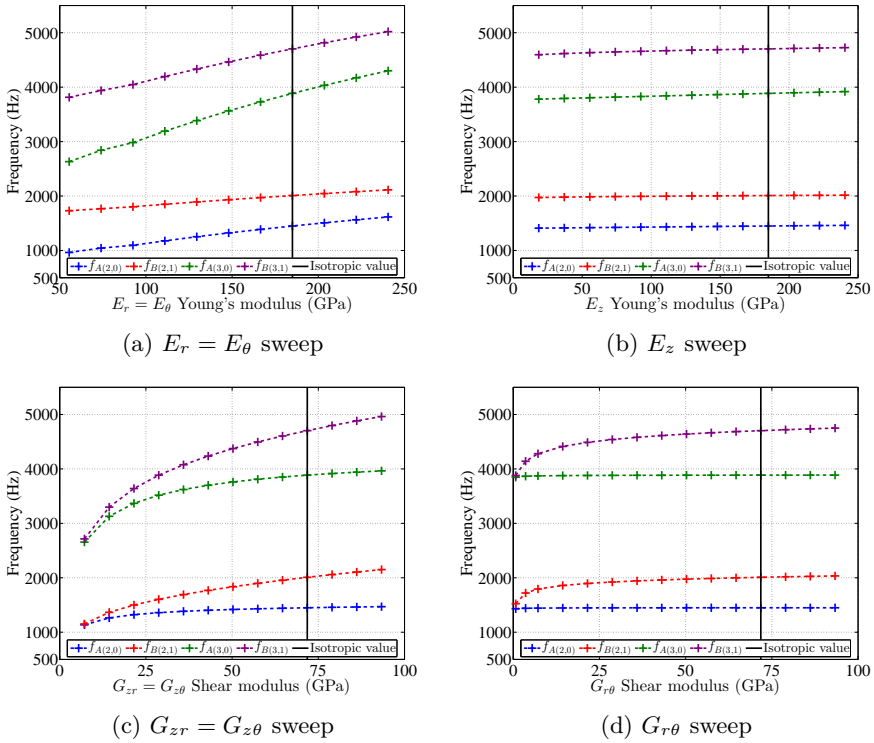


Figure 5.11: Parameter sweep analyses

mode shape. However they do not clearly show the link between parameters and mode shapes, essentially because the parameter variation analyses involve only 3 values per parameter. Therefore in this thesis, a more extensive parameter sweep analysis is performed in order to study the effects of each parameter on the natural frequencies. Based on the trends, an optimization loop finds the optimum parameters for all the natural frequencies to match.

The four parameters of the transverse isotropic material model  $E_r$ ,  $E_z$ ,  $G_{zr}$  and  $G_{r\theta}$  are swept from 10% to 130% of their initial value corresponding to isotropic properties while the others ones are kept constant equal to their isotropic value. Modal analyses are run for each parametrization. The results for each mode between 500 Hz and 5 kHz together with their trend lines are shown in Fig. 5.11.

From this set of FE experiments, one can clearly notice that tuning of the axial Young's modulus  $E_z$  is relatively unnecessary since its effect on any

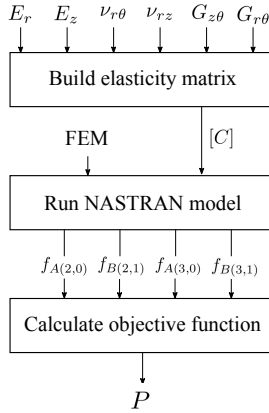


Figure 5.12: Simulation process for optimization (1 iteration)

natural frequency is minor. To some extent, shear moduli have low impact on pure radial mode frequencies  $f_{A(n_r,0)}$  but affect significantly the frequency difference  $f_{A(n_r,0)} - f_{B(n_r,1)}$ . Additionally  $E_r$  (and  $E_\theta$ ) is demonstrated to be the parameter to change for global natural frequency fitting. However, these results do not give a trivial relationship between modal frequencies and related material parameters.

Based on the parameter sweep results an optimization procedure is proposed [52], such that the trends-knowledge is leveraged into the algorithm. The initial parents, *i.e.* the isotropic values of the parameters, are input of the simulation process displayed in Fig. 5.12. The computed output objective function allows selecting a new parent population which serves as new input for the simulation process, etc. Therefore the termination criterion is not qualitative (*e.g.* such as the minimum objective function to achieve) but quantitative: the number of iterations of the simulation process sets the computational effort; 100 iterations are used in the following study. Moreover it is necessary to define constraints to the input values; they are defined from the trends described earlier and summarized in equation 5.35.

$$\begin{aligned}
148.0 &= 80\% \cdot E_r^{iso} \leq E_r \leq 120\% \cdot E_r^{iso} = 222.0 \quad (\text{GPa}) \\
92.5 &= 50\% \cdot E_r^{iso} \leq E_z \leq 120\% \cdot E_r^{iso} = 222.0 \quad (\text{GPa}) \\
7.19 &= 10\% \cdot G_{zr}^{iso} \leq G_{zr} \leq 110\% \cdot G_{zr}^{iso} = 79.6 \quad (\text{GPa}) \\
7.19 &= 10\% \cdot G_{r\theta}^{iso} \leq G_{r\theta} \leq 110\% \cdot G_{r\theta}^{iso} = 79.6 \quad (\text{GPa}) \\
0.258 &= 90\% \cdot \nu_{rz}^{iso} \leq \nu_{rz} \leq 110\% \cdot \nu_{rz}^{iso} = 0.316 \\
0.258 &= 90\% \cdot \nu_{r\theta}^{iso} \leq \nu_{r\theta} \leq 110\% \cdot \nu_{r\theta}^{iso} = 0.316
\end{aligned} \tag{5.35}$$

Since the interest is limited to the first four natural frequencies, the objective function  $P$  is defined as the sum of squared differences between simulated and measured frequencies:

$$P = (f_{A(2,0)} - 1399)^2 + (f_{B(2,1)} - 1572)^2 + (f_{A(3,0)} - 3799)^2 + (f_{B(3,1)} - 4052)^2 \tag{5.36}$$

with the optimization constraints,

$$\begin{aligned}
\frac{|f_{A(2,0)} - 1399|}{1399} &\leq 1.5\%, & \frac{|f_{B(2,1)} - 1572|}{1572} &\leq 1.5\% \\
\frac{|f_{A(3,0)} - 3799|}{3799} &\leq 2.5\%, & \frac{|f_{B(3,1)} - 4052|}{4052} &\leq 2.5\%
\end{aligned} \tag{5.37}$$

The optimum parameters obtained are compared (shown in Fig. 5.13) with their isotropic values to verify the trends evaluated earlier. The shear moduli are significantly decreased as they affect the  $f_{A(n_r,0)} - f_{B(n_r,1)}$  difference. The transverse shear modulus  $G_{zr}$  becomes half the isotropic value, while the in-plane shear  $G_{r\theta}$  is reduced by 90%. Given the high reductions of shear moduli that lead to downward frequency shifts, the Young's moduli are slightly increased to counter-act this effect.  $E_r$  and  $E_z$  then stand respectively around 110% and 105% of their isotropic values. It is also interesting to note that there is more freedom in  $E_z$  variations since its effects on the targeted modes are minor. Finally the Poisson ratios do not change significantly the frequency results but the variations make physical sense:  $\nu_{rz}$  decreases as for the **RoM** model of Table 5.7 ( $\nu_{rz} \approx 92\% \cdot \nu_{rz}^{iso}$ ), *i.e.* compared with a solid block, for the same contraction in axial ( $z$ ) direction there is more extension in radial ( $r$ ) direction.

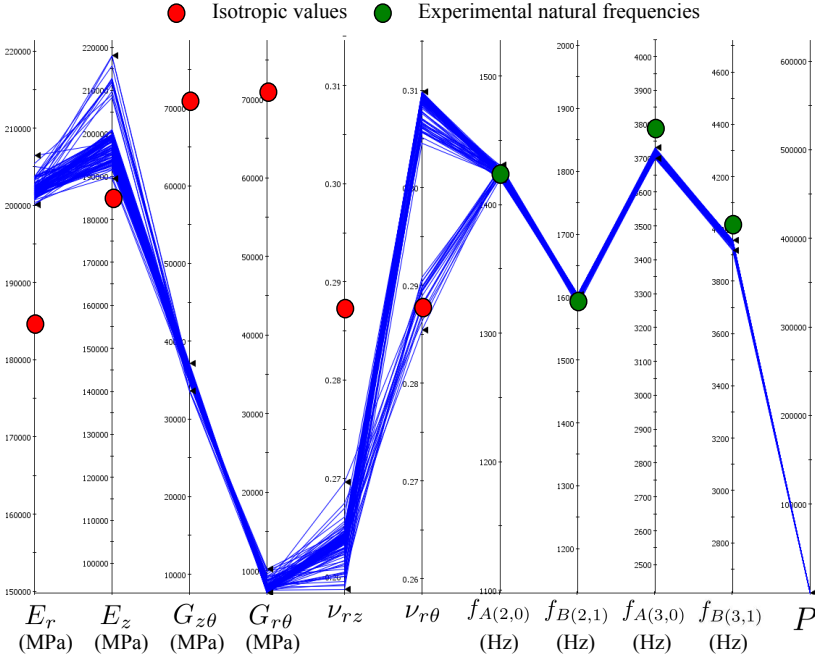


Figure 5.13: Optimization results, each blue line corresponds to a parametrization that permits to reach the optimum P-value

Table 5.8: Optimal material parameters compared to **Iso**'s

	$\rho$ kg/m <sup>3</sup>	$E_r$ GPa	$E_z$ GPa	$\nu_{rz}$ -	$\nu_{r\theta}$ -	$G_{zr}$ GPa	$G_{r\theta}$ GPa
<b>Iso</b>	7,322	185.0	185.0	0.287	0.287	71.9	71.9
Optimized	7,322	201.2	193.7	0.264	0.309	37.3	7.3
(%age of <b>Iso</b> )	100.0	108.8	104.7	92.0	107.7	51.9	10.2

$\nu_{r\theta}$  also increases ( $\nu_{r\theta} \approx 106\% \nu_{r\theta}^{iso}$ ), *i.e.* for the same contraction in azimuthal ( $\theta$ ) direction there is less extension in radial ( $r$ ) direction.

From these remarks, the optimal material parameters are defined for this study case. Table 5.8 details the parameters and compares them to the isotropic values, while Table 5.9 gives the resulted natural frequencies from this optimal material model.

The four simulated natural frequencies with the optimized material are close

Table 5.9: Natural frequencies: calculated with optimal material parameters compared to measured

	$f_{A(2,0)}$ Hz	$\epsilon$ %	$f_{B(2,1)}$ Hz	$\epsilon$ %	$f_{A(3,0)}$ Hz	$\epsilon$ %	$f_{B(3,1)}$ Hz	$\epsilon$ %
Measured	1399		1572		3799		4052	
Optimized	1426	+0.6	1606	+1.1	3726	-1.9	3959	-2.3

to the experimental values with errors below 2.5%. It is possible to obtain a representative material model when considering orthotropic material model. On the other hand, it is important to note that the transverse isotropic condition  $G_{r\theta} = \frac{E_r}{2(1+\nu_{r\theta})}$  is not fulfilled with the optimized parameters. In other words, material transverse isotropy is not a valid assumption for our laminated stator core.

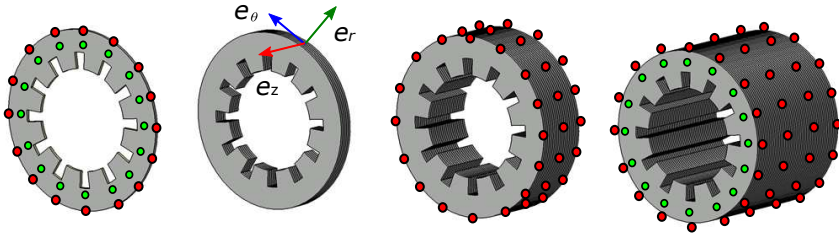
## 5.6 Effects of the number of laminations

The effects of the axial length on the natural frequencies of laminated cores are investigated in literature. Singal et al. [113, 142] investigate analytically these effects and Wang et al. [133, 135, 132] studied them numerically and experimentally. It was found that the natural frequencies of pure radial modes  $A(n_r, 0)$  are independent of the lamination thickness, the number of laminations and the clamping pressure. On the other hand the number of laminations affect other types of modes that activate in-plane shear. Beside the already known trends on the natural frequency variations from different axial lengths, no study looks into the modal damping values. This issue is addressed from an experimental point of view in this Section.

### 5.6.1 Experimental setup and validation

#### Test specimens

EMAs are carried out for test specimens of increasing stack length  $L_{stack}$  from  $n_s = 1$  lamination to  $n_s = 528$  laminations corresponding to the stator of a 16/12 SRM. The laminations are stacked together by means of interlocks (a punched dent in each lamination, that aligns and locks itself with the adjacent lamination [95]). For confidentiality reasons, its detailed geometry cannot be shown, however Fig. 5.14 depicts four representations of the test specimens



- Axial measurement point
- Radial measurement point

Figure 5.14: Representation of some samples (from left to right): 1, 10, 178 and 528 laminas, with their measurement discretization

Table 5.10: Lamination stacks under investigation; H = Hammer, S = Shaker

	Number of laminations $n_s$					
	1	5	10	20	178	528
# Samples	3	2	1	1	1	1
$L_{stack}$ (mm)	0.35	1.75	3.50	7.00	62.3	185.0
Mass (kg)	0.0268	0.1327	0.2682	0.5366	4.750	14.250
Axial points	16	16	16	16	0	16
Radial points	0	16	16	16	16×3	16×4
Excitation	H	H	H	H	S	S

under study with their corresponding cylindrical coordinates, and measurement point discretization. Their measured thickness, mass and the number of samples available are given in Table 5.10.

Flexible ropes are used to hang each specimen to a static frame. They reproduce free-free vibrations by avoiding the rigid body modes to interfere with the flexible modes of the specimen. The ropes' flexibility is of the up-most importance and depends on each specimen's mass. It should be reminded that two main excitation directions are necessary to excite the most critical modes within the frequency range of interest: the axial and radial directions. The axial excitation permits to capture the axial bending modes  $E(n_r, 0)$  while the radial excitation allows capturing the radial modes of type  $A(n_r, 0)$  and  $B(n_r, n_z)$ . Since they are uncoupled, the influence of the number of laminations on the structural dynamics of each stack is studied separately for the two different mode orientations. It is also self-evident that the specimen's length and mass bring constraints to the possible excitation device; for example, radial excitation

is practically not feasible for a single lamination specimen because of its small thickness. Bearing those limitations in mind, two different experimental setups, referred to as setups A and B, are built involving two different rope types. The setup A concerns the specimens lighter than 1 kg, *i.e.* from 1 to 20 lamination stacks and the setup B is used for the heavier specimens, *i.e.* from 128 to 528 lamination stacks. For setup A, a lightweight impact hammer (PCB Piezotronics SN14893) is used in combination with a unidirectional accelerometer (PCB Piezotronics 352A24 of 0.8g). For setup B, an integral shaker (LMS Qsource SN045) is used together with 8 tri-axial accelerometers (PCB Piezotronics SN 356A22) spread around the stator circumference. The data acquisition system is a SCADAS III.

It should be noted that the additional mass of the sensors is minimized by using lightweight sensors. Performing multiple runs allows for the reduction of mass load as well since the amount of sensors used is lowered for each run. The measurement points resolution to run the EMA is specimen-dependent and detailed in Table 5.10.

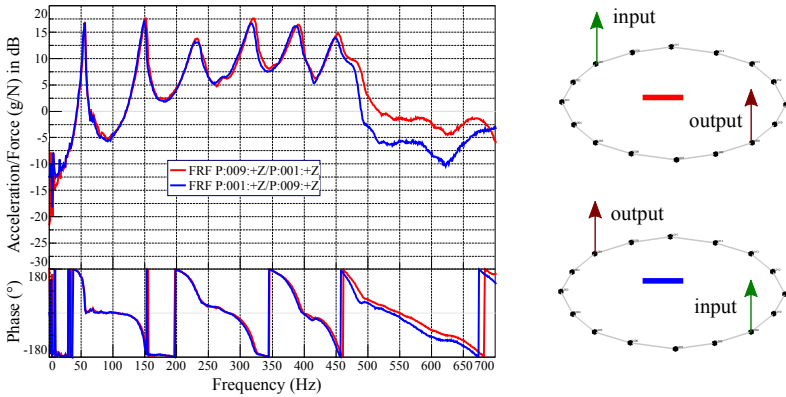
### **Validity of the measurements**

Following the theory of Section 2.2, one has to check that the linearity assumption holds for our specimens in order to perform EMAs. Fig. 5.15 presents two reciprocity checks for the 10 lamination stack and the full stator samples.

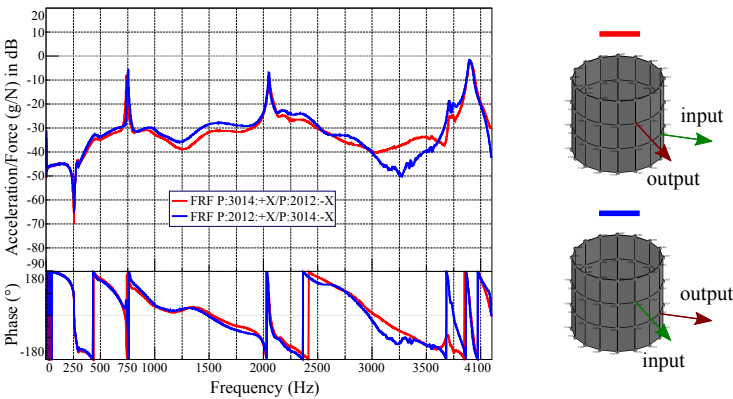
The repeatability principle states that two identical samples tested within the same operational configuration should demonstrate an equal structural behavior. Thus, for example, temperature, errors of the operators, inaccuracies in the excitation and imperfect manufacturing process should not heavily affect the final results. Given that multiple samples are available for the specimens with low number of laminations, *i.e.* the 1 and 5 lamination stacks, several tests on their specimens would validate the repeatability. Another consistent estimator of a reliable measurement is the coherence [58], which is also checked during the experimental campaign.

All the validity tests are performed and allow to assume linearity of each sample under study. They permit to obtain trustworthy FRFs within certain frequency ranges, *i.e.* from 20 Hz to 700 Hz for the axial vibrations and from 150 Hz to 4,100 Hz for radial vibrations.





(a) Example for 10 lamination stack axial reciprocity



(b) Example for 528 lamination stack radial reciprocity

Figure 5.15: Reciprocity checks for different stacks and directions

## 5.6.2 Results

The modal parameters are estimated for each test specimen and excitation direction using the method described in Section 2.2. It is important to mention that for the test specimens having multiple samples (1 and 5 lamination stacks), only the averaged results (averaged FRFs-sum, natural frequency, modal damping) are shown given the validated repeatability.

### Axial excitation for axial-type modes $E(n_r, 0)$

Fig. 5.16 and Fig. 5.17 show the first estimated mode shapes and the FRFs-sum obtained for each specimen respectively in the case of axial excitation. Table 5.11 compiles the natural frequencies and modal damping output from the EMAs for each test specimen. Fig. 5.18 pictures the natural frequencies depending on the number of laminations for each axial bending mode and every specimen that allows such experiment.

It is important to notice that the thicker the specimen, the higher the natural frequency of all modes. The magnitude of the FRFs also decreases considerably with the number of laminations, due to the added mass. In addition, several high frequency modes disappear with stack length  $L_{stack}$  increase. The single lamination has a low-damping behavior while the full stator corroborates quite low amplitudes. Overall, the modal damping is quite high, above 2%, except for the single lamination, such that it is evident that stacking laminations brings significant amount of damping to the axial modes. Yet no trivial trends for the natural frequencies and the damping ratios can be derived for increasing lamination stacks.

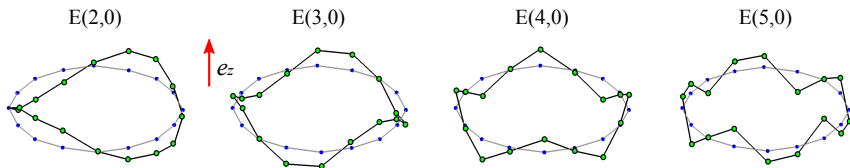


Figure 5.16: Axial bending mode shapes  $E(n_r, 0)$  of 10 lamination stack

### Radial excitation for radial-type modes $A(n_r, 0)$ and $B(n_r, n_z)$

Fig. 5.19 and Fig. 5.20 show the first estimated mode shapes and the FRFs-sum obtained for each specimen respectively in the case of radial excitation. Table

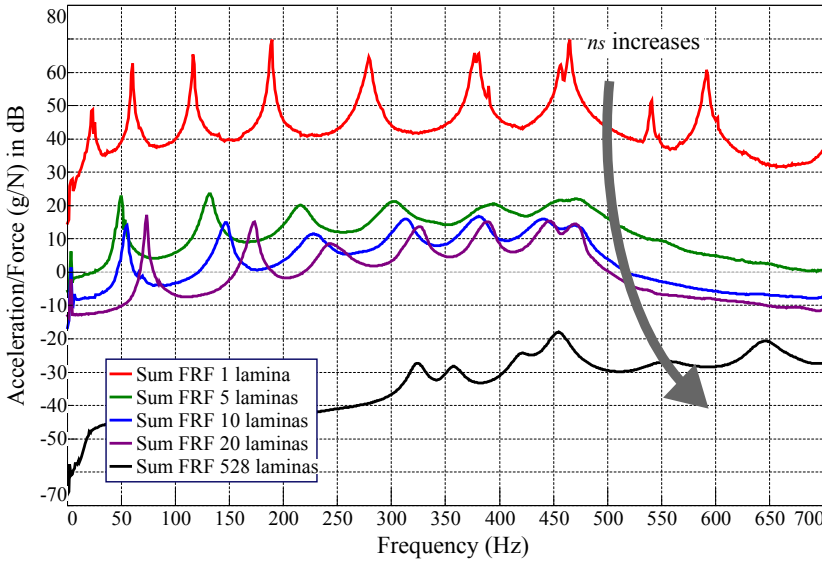


Figure 5.17: FRFs-sum in axial excitation case for different lamination stacks

5.12 compiles the natural frequencies and modal damping output from the EMAs for each test specimen. Fig. 5.21 pictures the natural frequencies for the radial modes depending on the number of laminations and every specimen that allows such experiment.

The radial modes occurring are essentially the pure radial modes  $A(n_r, 0)$  and the anti-symmetric radial modes with shear  $B(n_r, 1)$ . Unlike axial-type modes the natural frequencies of the first ones are not significantly affected by the number of laminations. This agrees with remarks in literature [135, 22, 23] but also is in line with simulation results (see Section 5.5). The magnitude of the FRFs also decrease considerably with the number of laminations due to the added mass. Therefore the natural frequencies of pure radial modes  $A(n_r, 0)$  uniquely depend on the stiffness and mass distributions of the cross-section. Their modal dampings are considerably lower than for the axial modes.

## 5.7 Effects of the stacking technology

The laminations of a stator core hold together by different means [32]. Interlocks are small dents/notches that are implemented in each lamination, such that they hold together by applying a simple axial pre-load to the structure. One can

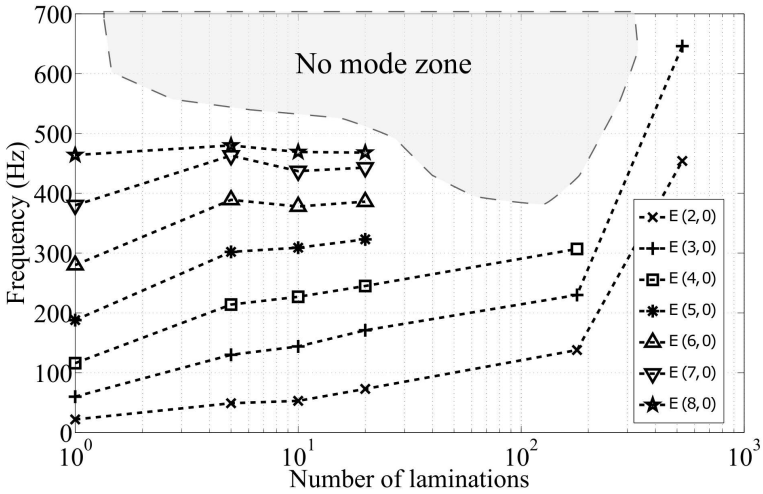


Figure 5.18: Estimated natural frequencies for axial bending modes  $E(n_r, 0)$

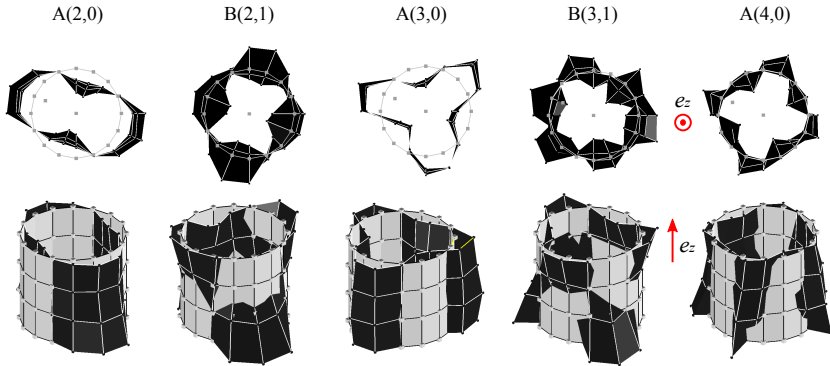


Figure 5.19: Main radial mode shapes of the full stator; undeformed (grey) and deformed (black)

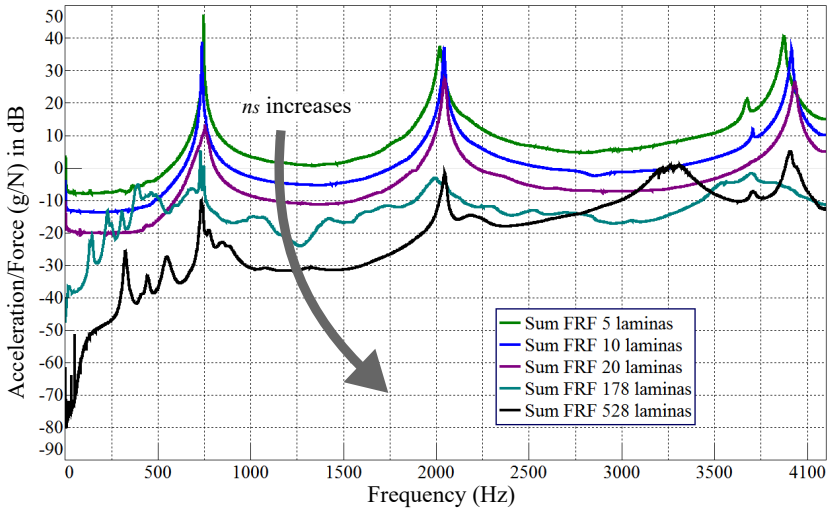


Figure 5.20: FRFs-sum in radial excitation case for different lamination stacks

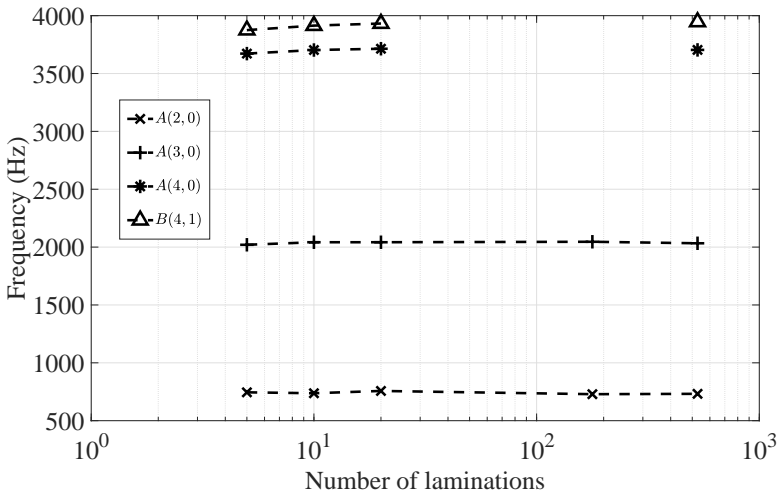


Figure 5.21: Estimated natural frequencies for radial modes  $A(n_r, 0)$  and  $B(n_r, 1)$

Table 5.11: Modal characteristics for axial modes  $E(n_r, 0)$ ; (-) Not appearing

Mode		Number of laminations					
Value	Unit	1	5	10	20	178	528
$f_{E(2,0)}$	Hz	22	49	53	73	138	454
$\xi_{E(2,0)}$	%	<i>5.79</i>	<i>1.95</i>	<i>2.25</i>	<i>0.92</i>	<i>3.91</i>	<i>1.50</i>
$f_{E(3,0)}$	Hz	60	130	144	171	230	646
$\xi_{E(3,0)}$	%	<i>0.85</i>	<i>2.43</i>	<i>2.32</i>	<i>1.41</i>	<i>1.76</i>	<i>1.76</i>
$f_{E(4,0)}$	Hz	116	214	227	245	307	-
$\xi_{E(4,0)}$	%	<i>0.50</i>	<i>3.02</i>	<i>3.50</i>	<i>2.85</i>	<i>1.98</i>	-
$f_{E(5,0)}$	Hz	188	302	309	323	-	-
$\xi_{E(5,0)}$	%	<i>0.31</i>	<i>3.15</i>	<i>2.23</i>	<i>1.80</i>	-	-
$f_{E(6,0)}$	Hz	280	389	378	386	-	-
$\xi_{E(6,0)}$	%	<i>0.90</i>	<i>2.91</i>	<i>1.98</i>	<i>1.48</i>	-	-
$f_{E(7,0)}$	Hz	380	463	437	443	-	-
$\xi_{E(7,0)}$	%	<i>0.38</i>	<i>1.87</i>	<i>1.45</i>	<i>1.33</i>	-	-
$f_{E(8,0)}$	Hz	464	480	469	468	-	-
$\xi_{E(8,0)}$	%	<i>0.24</i>	<i>3.26</i>	<i>1.37</i>	<i>1.03</i>	-	-

Table 5.12: Modal characteristics for radial modes  $A(n_r, 0)$  and  $B(n_r, 1)$ ; (-) Not captured

Mode		Number of laminations				
Value	Unit	5	10	20	178	528
$f_{A(2,0)}$	Hz	745	737	757	729	732
$\xi_{A(2,0)}$	%	<i>0.17</i>	<i>0.17</i>	<i>1.08</i>	<i>0.14</i>	<i>0.30</i>
$f_{A(3,0)}$	Hz	2020	2042	2042	2046	2033
$\xi_{A(3,0)}$	%	<i>0.41</i>	<i>0.23</i>	<i>0.36</i>	<i>0.41</i>	<i>0.75</i>
$f_{A(4,0)}$	Hz	3672	3703	3714	-	3704
$\xi_{A(4,0)}$	%	<i>0.20</i>	<i>0.18</i>	<i>0.35</i>	-	<i>0.34</i>
$f_{B(4,1)}$	Hz	3875	3914	3932	-	3946
$\xi_{B(4,1)}$	%	<i>0.29</i>	<i>0.17</i>	<i>0.29</i>	-	<i>0.20</i>

also glue bond the insulated steel sheets and then apply a clamping pressure to ensure a large stacking factor after the curing process. Finally it is possible to weld axially the laminations after clamping them all together. In any situation

an axial clamping pressure is required, which possibly affects the structural dynamics of the stator core.

The works of Watanabe et al. [137] outline the fact that the natural frequencies of radial modes with shear  $B(n_r, 1)$  of a segmented-core stator tend to increase as the clamping pressure increases. Dias et al. confirm this conclusion experimentally [37], and observe that pure radial modes  $A(n_r, 0)$  are not affected by any variations of the clamping force.

Additionally the stacking technology shows different contact scenarios between the laminations and may pre-constrain steel sheets. These structural changes might lead to variations in the structural dynamics. For instance the residual stresses generated by the heat flow of the welding event have a non-reversible influence on the core integrity and therefore affect the structural dynamics. Tan-Kim et al. [120] investigate the effects of welding on the stator shape and consequently on the acoustic noise emitted. They show better correlation between simulation and measurement results of the acoustic pressure when incorporating the stator geometry changes due to the residual stress from the welding events. However, despite the importance of the damping on the vibrations and acoustic noise, no published study, to our knowledge, presents the advantages and disadvantages of a stacking technology in terms of damping.

This Section studies experimentally the effects of the stacking technology (gluing and welding) for a defined stator core, on the structural characteristics, *i.e.* natural frequencies, mode shapes and modal damping values.

### 5.7.1 Experimental setup

In order to identify the effects of the stacking technology on the structural dynamics of the stator core, two test specimens are investigated. They have the same geometry as the stator core studied in Section 5.5. The first one corresponds to the tested specimen of Section 5.5 and has its laminations glued together by means of a two-component epoxy glue, while the laminations of the second one are welded axially through 12 welding lines. They are referred to as glue-bonded and welded cores in this Section. Fig. 5.22 pictures the two specimens with the corresponding measurement point discretization for the further EMAs.

Elastic ropes are used to hang the system and emulate free-free boundary conditions. A miniature shaker (LMS Qsource SN045) provides a white noise radial excitation input from 100 Hz to 8 kHz as burst random signal (80% burst time, 0.025s burst ramp time). Tri-axial accelerometers (PCB Piezotronics SN 356A22) are employed and 50 averages are performed for FRF H1 estimation.

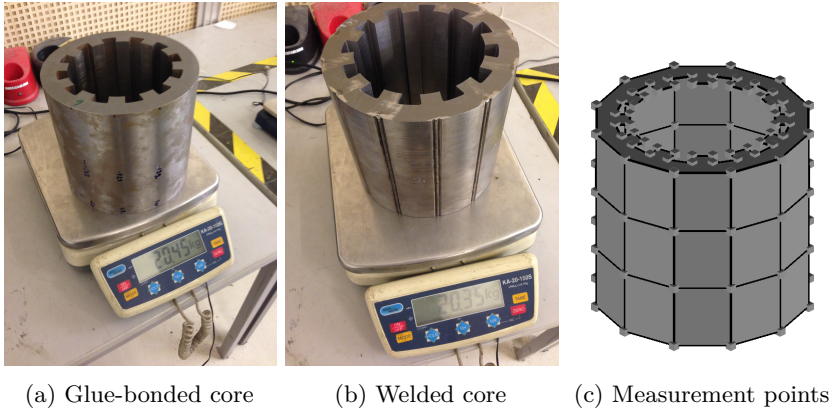


Figure 5.22: Pictures and test discretization of the specimens

Furthermore, linearity checks (linearity and reciprocity) are performed and consolidate the utilization of linear modal models during the EMAs. It is important to note that only radial excitation is performed in this study. The focus originates from the conclusions drawn in Section 5.6 that pinpoint high damping of axial modes  $E(n_r, n_z)$  for complete stator cores, compared to the radial modes  $A(n_r, 0)$  and  $B(n_r, 1)$ .

## 5.7.2 Results

Fig. 5.23 shows the first estimated mode shapes for the welded core and Fig. 5.24 shows the FRFs-sum obtained for each specimen. Table 5.13 compiles the natural frequencies and modal damping output from the EMAs for each test specimen.

The glue-bonded and stator cores show discrepancies in structural dynamics although they have similar mass. As in Section 5.6, the radial modes are easily identified, in particular pure radial modes  $A(n_r, 0)$  and radial with shear modes  $B(n_r, 1)$ . For the first ones, the natural frequencies are not affected by the stacking technology which indicates that the two specimens have similar radial distribution of stiffness and mass. Modal damping values for  $A(n_r, 0)$  are reduced when welding is used compared to gluing. On the other hand  $B(n_r, 1)$  modes become so damped by the welding process that they cannot be estimated. The dry friction between the laminations and the constraint brought by the welding lines along the stack length seem to eliminate these modes. But welding introduces another type of shear mode: the  $B(1, 2)$ . The same phenomenon



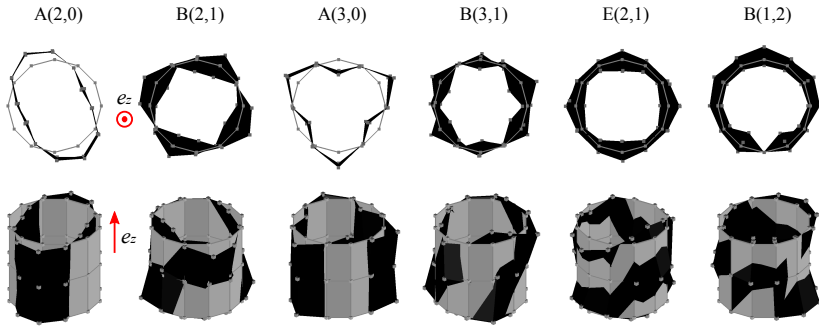


Figure 5.23: Main mode shapes of the welded stator core; undeformed (grey) and deformed (black)

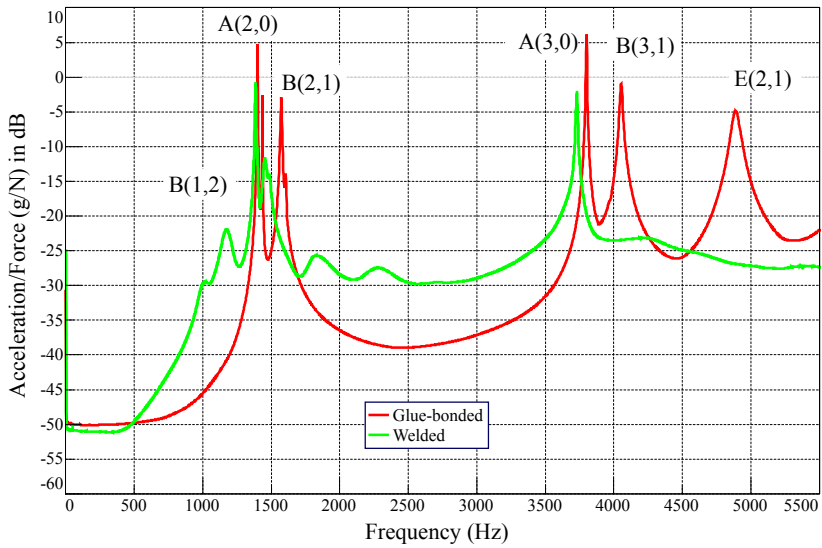


Figure 5.24: FRFs-sum of radial components for glue-bonded and welded stator cores

Table 5.13: Modal characteristics for radially excited modes; (-) Not appearing

Value	Unit	Glue-bonded	Welded
Mass	kg	20.45	20.35
$f_{A(2,0)}$	Hz	1,399	1,385
$\xi_{A(2,0)}$	%	0.09	0.62
$f_{B(2,1)}$	Hz	1,572	-
$\xi_{B(2,1)}$	%	0.3	-
$f_{A(3,0)}$	Hz	3,799	3,728
$\xi_{A(3,0)}$	%	0.09	0.13
$f_{B(3,1)}$	Hz	4,052	-
$\xi_{B(3,1)}$	%	0.27	-
$f_{B(1,2)}$	Hz	-	1,216
$\xi_{B(1,2)}$	%	-	0.65
$f_{E(2,1)}$	Hz	4,902	1,461
$\xi_{E(2,1)}$	%	0.61	0.56

was remarked in Section 5.8.2, and  $B(1, 2)$  appears at lower frequency than the ovalization mode  $A(2, 0)$ .

Furthermore, several axial modes are observed. In fact  $E(n_r, n_z)$  modes do not uniquely show axial bending, but they also involve radial deformations. That is the reason why by exciting in the radial direction, one can still capture  $E(2, 1)$ . It is interesting to note that its characteristics depend on the stacking technology, especially its frequency from 1,461 Hz for the welded core versus 4,902 Hz for the glued core. Naturally the gaps between the laminations affects axial stiffness which inherently shifts the corresponding modal frequencies to lower values.

## 5.8 Intermediate conclusions

### 5.8.1 Final remarks on stator model comparisons

Applying all the models described in Sections 5.2, 5.4 and 5.3 to the stator core tested in Section 5.5.1 permits to compare them in terms of required modeling implementation time, simulation time and accuracy. Table 5.14 gives a qualitative view at the different model advantages and disadvantages.

Table 5.14: Model advantages and disadvantages; (- -) Very bad, (-) Bad, (+) Good, (++) Very good

	Ring	Iso	RoM	INRIA	Ortho	Shell
Implementation time	++	+	-	-	--	+
Simulation time	++	-	-	-	--	+
Accuracy $f_{A(n_r,0)}$	--	++	+	+	-	++
Accuracy $f_{B(n_r,1)}$	N/A	--	+	+	+	N/A
Tuning capabilities	-	-	+	+	++	-

It was noted that the gap between pure radial modes  $A(n_r, 0)$  and antisymmetric modes  $B(n_r, 1)$  natural frequencies is the tuning motivation for further model refinement, since great correlation of both these frequencies is not possible by any of the used models. Introduced by a material parameter sweep analysis that highlights the effects of each parameter on each mode of interest (partly introduced in [81, 138]), an optimization scheme allowed to define equivalent orthotropic material properties that lead to relevant correlation with the experimental values. In particular the in-plane shear modulus  $G_{r\theta}$  needs a significant reduction, such that transverse isotropy was shown not to be assumable for our laminated core.

Therefore it is necessary to think of other material parameter identification methods; two modeling options are suggested:

1. Find an appropriate model for both mode types; *i.e.*  $A(n_r, 0)$  and  $B(n_r, 1)$ . Although it is not aimed here at defining the true solution that uses 3D homogenization, one might orientate the studies towards the modeling of the contact between laminations especially regarding their relative motion; representative of the in-plane shear modulus  $G_{r\theta}$ . For instance contact elements could be incorporated between the epoxy and the laminations that allow for friction. However the added complexity of such model consequently generates other parameters, which are sources of uncertainties.
2. Choose a model per mode of interest. If one requires accuracy for antisymmetric modes  $B(n_r, 1)$ , 3D homogenized models are prescribed, while if one needs pure radial modes accuracy  $A(n_r, 0)$ , isotropic models are sufficient and more reliable. It is particularly important to emphasize that simple isotropic models employing known steel properties show great results for pure radial modes frequencies  $f_{A(n_r,0)}$ , which are the commonly critical modes for acoustic noise emission (see Section 5.1). However this

option might require more simulation workload (time and resources) than option 1.

## 5.8.2 Conclusions on the effects of the number of laminations

Although all the proposed models merely permitted to compute the natural frequencies and shapes from an equivalent material model and geometry, a crucial aspect that cannot be investigated numerically is the modal damping  $\xi_n$ . In order to understand better the physics behind the laminated compound, the effects of the number of laminations were investigated in Section 5.6 and conclusions were drawn on modal characteristics of different mode types.

### Axial modes $E(n_r, 0)$

- $n_s(1) > n_s(2) \Rightarrow f_{E(n_r,0)}(1) > f_{E(n_r,0)}(2)$ :

The longer the stack, the higher the natural frequencies. The axial mode stiffness directly depends on the stack length.

- $n_s(1) > n_s(2) \Rightarrow |H(1)| < |H(2)|$ :

The longer the stack, the lower the FRFs magnitudes; also referring as a larger modal damping, *e.g.* above 2% for more than 1 lamination stacks. For a lamination stack corresponding to a stator core, the modes are difficult to capture because of their high damping and the difficulties to excite strongly enough at high frequencies.

### Radial modes $A(n_r, 0)$ and $B(n_r, n_z)$

- $|H(f = f_{A(n_r,0)})| \gg |H(f = f_{B(n_r,n_z)})|$ :

The pure radial modes  $A(n_r, 0)$  show the largest peaks in terms of FRF magnitudes compared to radial with shear modes  $B(n_r, n_z)$ . In fact  $B(n_r, n_z)$  modes do not occur systematically, supposedly because of the interlocks that constrain the laminations to follow in-phase motions.

- $f_{A(n_r,0)}(\mathcal{D}_s)$ :

The pure radial mode natural frequencies  $f_{A(n_r,0)}$  do not depend on the number of laminations  $n_s$  (stack length), as mentioned in [135, 22, 23]. The stiffness and mass distribution of the stator cross-section dictate the modal frequencies for this type of modes, such that the suggested modeling guidelines regarding 2D **Shell** model from Section 5.8.1 are validated.

- $\xi_{A(n_r,0)} < 0.005$ :

Modal damping values are below 0.5% for pure radial modes, which is considered low damping.

### 5.8.3 Conclusions on the effects of the stacking technology

The tested specimens in Section 5.6 are stacked by means of interlocks, but several other stacking technologies are used industrially. They can affect differently the structural dynamics behavior given the different nature of the contacts between the laminations they introduce. By investigating experimentally these discrepancies in Section 5.7, conclusions were drawn and summarized below.

#### Radial modes $A(n_r, 0)$ and $B(n_r, n_z)$

- $f_{A(n_r,0)}(\text{welded}) \simeq f_{A(n_r,0)}(\text{glue-bonded})$ :

The natural frequencies of pure radial modes  $A(n_r, 0)$  are not affected significantly, despite the mass removal due to the welding areas cuts for the welding lines. The radial mass distribution is changed for the welded core but its stiffness as well. Removing some steel leads to a reduction of radial stiffness and consequently a slight reduction of the natural frequencies  $f_{A(n_r,0)}$  (see Section 5.8.2)

- $\xi_{A(n_r,0)}(\text{welded}) \gg \xi_{A(n_r,0)}(\text{glue-bonded})$ :

Welding considerably increases modal damping of the pure radial modes  $A(n_r, 0)$ . The ovalization mode is particularly damped compared to the triangle mode. It is most likely due to the distribution pattern of the welding lines. The physics behind this phenomenon are explained further in Section 6.2.1.

- $\xi_{B(n_r,1)}(\text{welded}) \geq 1$ :

Welding also damps  $B(n_r, 1)$  modes by adding a constraint-like feature at the welding lines, which is a good indicator of modal damping improvement through manufacturing optimization. The damping might even be so large that the modes cannot be captured anymore using EMA. Again, it is most likely due to the distribution pattern of the welding lines that constrain the deformation of the core to be symmetric. The physics behind this phenomenon are explained further in Section 6.2.1.

- $\exists f_{B(1,2)}(\text{welded}), \nexists f_{B(1,2)}(\text{glue-bonded})$ :

Gluing the laminations together seems to eliminate any type of low frequency modes, such as the ones identified in Section 5.6. But welding introduces the  $B(1, 2)$  mode similarly to the interlocked stator core of Section 5.6. The in-plane shear is low enough to allow relative motion between the laminations, yet without much radial deformation.

### Axial mode $E(n_r, 1)$

- $\exists f_{E(n_r, n_z)}$  with radial excitation:

Some axial modes  $E(n_r, n_z)$  are captured due to their non-unique deformation direction. Actually they also involve radial displacements which helps detecting them during EMAs with radial excitation.

- $f_{E(2,1)}(\text{welded}) \ll f_{E(2,1)}(\text{glue-bonded})$ :

Gluing shifts axial modes to very high frequencies by stiffening the structure axially.

The major point is that the residual stresses generated by the heat flow of the welding event incorporate mechanical constraints to the laminations at the welding areas. Here 12 welding lines permit to damp the ovalization mode  $A(2, 0)$  more than the triangle mode  $A(3, 0)$ . Moreover the antisymmetric modes  $B(n_r, 1)$  vanish completely by applying welding. Therefore it is expected that dedicated welding locations can damp critical modes. This hypothesis is thoroughly formulated and validated in the next Chapter.

## Chapter 6

# On a novel attachment method of the laminations of the stator core for improved NV performances

Predicting correctly the NV behavior of an electric machine is not only interesting to detect critical operating points, but it can be used to propose solutions to minimize undesired phenomena. Immediate phenomena to be attenuated are the resonances, which originate from a multi-physical vibro-acoustic process, as seen in earlier chapters. Their characteristics (frequency, mode shape, etc) are dominated by the stator core structural dynamics which, by being laminated, provides an immense tool set of tuning capabilities. This chapter proposes an alternative solution to the resonance attenuation that benefits from this laminated nature of the stator core to passively damp particular modes.

At first Section 6.1 reviews the current solutions to magnetic noise mitigation by resonance diminution. Section 6.2 hypothesizes on the developed original manufacturing technology for the laminated stator core. The methodology is then carefully validated experimentally in Section 6.3 and its consistency is evaluated successfully using statistical metrics.

## 6.1 Vibration reduction techniques

Based on the source-transfer-receiver approach for NVH behavior explanation of Section 1.1.1 and the necessary multi-physical approach for rotating electric machines, one can define several vibration reduction techniques aimed at acoustic noise mitigation. Two categories emerge from the reduction techniques: active and passive methods.

Active methods refer to techniques that use external sources to counter-act and/or mitigate vibrations via closed-loop control. It is possible to program the modulation such that it is randomized [65] or controlled such that it avoids resonance effects during starting and breaking phases [92]. It is also possible to inject current harmonics which supposedly eliminate magnetic force components responsible for high noise [72]. However this technique has limited applications and risks exciting resonances as well if not properly implemented. Takahashi et al. define optimum switching schemes for an IM that permit significant acoustic power decrease [118]. Takiguchi et al. also propose to eliminate particular force harmonics to reduce vibrations and acoustic pressure and find successful amplitude decreases around 20 dB [119]. Another active solution is to act after the vibration is produced by means of vibration-canceling at the stator/machine surface. Piezo-electrical devices can be used to that purpose [87]. It is also possible to program the modulation such that it is randomized [65] or controlled such that it avoids resonance effects during starting and breaking phases [92].

On the other hand, passive methods are generally related to design refinements that include the rotor/stator geometries, the slot/pole ratio choice and the component and system-level manufacturing. Numerous studies investigate passive vibration because of their reduced cost. The optimum number of slots and poles can also be determined [63] but specific control schemes need to be adapted. With the same constraint and as suggested in Section 4.1, rotor (or stator) skewing is another common method to reduce torque ripple and acoustic noise [144, 48]. The implementation of rotor radial asymmetry proposed by Chitroju et al. also allows reducing NV levels [30]. More recently Zhou et al. implemented rotor notching on an IM and showed impressive vibration damping [148]. In parallel the stator geometry can be refined for the same purposes [50, 126, 22]. In fact the rotor/stator cross section optimization serves the radial magnetic force distribution tuning, *i.e.* to play on the source. But it is possible to act on the vibration transfer system, and more importantly on the main contributor to it: the laminated stator core. It is particularly important to emphasize this component since it is the structural part that dominates the mode responsible for resonance phenomena.

Two design optimization objectives of the laminated stator core can be defined



for improved sound quality. Firstly one aims at shifting the resonance frequencies to higher values because higher frequency components are more easily canceled by acoustic insulation panels. Yet fundamentally the thicker the stator yoke, the higher the natural frequencies of pure radial modes  $A(n_r, 0)$  [77]. Secondly one aims at damping improvements. Hence Hong et al. investigate a few types of stator yokes for an SRM and obtain vibration reduction [60]. Verma et al. particularly explain the importance of damping components (lamination, windings and potting insulation) on the vibration output using experimental analyses [128]. Different mounting scenarios obviously also affect the damping of the system and may reduce noise [149].

Regarding the laminations, viscous and Coulomb (friction) damping occur. A method of making internally damped cores (including stator cores) is patented and consists in introducing viscous damping between steel sheets [71]. However, no concept is available in literature that investigates the possibilities of using the laminations to induce more Coulomb or viscous damping for acoustic noise mitigation purposes. It is believed that this originates from a not-yet published thorough understanding of the lamination dynamics, partly available in Chapter 5.

## 6.2 Conceptualization

### 6.2.1 Motivation

The proposed technique aims at improving damping properties of the laminated stator core by making use of its laminated nature, and especially the attachment method for the laminations to hold together. It emerges from a conclusion of Section 5.7 that states, from an industrial laminated stator core, that welding brings damping of all the antisymmetric modes  $B(n_r, 1)$  in comparison with glue-bonding.

Depending on the attachment technique the structural dynamics changes. For instance Tan-Kim et al. [120] investigate the effects of welding on the stator shape which consequently affects the acoustic noise radiated. The heat from welding causes localized expansion of the steel laminations which, by cooling in a second stage, shrink. Residual stresses  $\sigma_{res}$  are generated and define the non-reversible influence of the welding event on the core geometry and integrity. Beside their influence on the force profiles due to air gap variations, they can be seen as stiffness variations around the welding spots as modeled by Millithaler et al. [84] and induce axial asymmetry of the core stiffness. Fig. 6.1 pictures

the residual stress creation from the welding events for the stator core studied in Section 5.7.

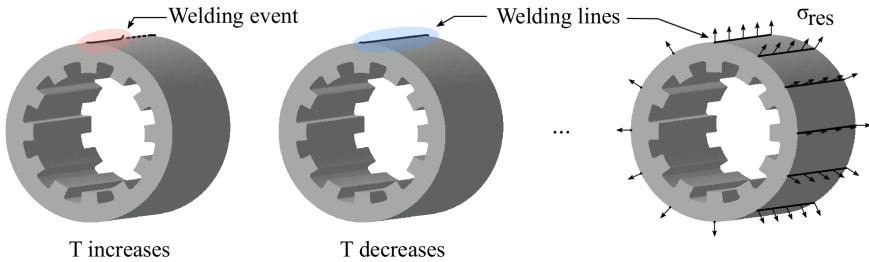


Figure 6.1: Welding event and induced residual stresses -  $T$  = temperature

The change in stiffness distribution of the core due to welding is the first reason why some modes are damped compared to the glue bonded core of Section 5.7. Taking this stator core as an example, the twelve welding lines tend to attract the core yoke back to its equilibrium position. Fig 6.2 shows these attractions for pure radial deformations of modes  $A(2, 0)$  and  $A(3, 0)$ . Fig 6.3 shows the phenomenon for the anti-symmetric mode  $B(2, 1)$ . For these latter modes,  $\sigma_{res}$  varies axially as well which stiffens the structure even more. This is one explanation of the vanishing anti-symmetric modes of Section 5.7.

The second reason why modal damping is increased for certain modes is related to the amplitude reduction effects due to damping (Coulomb, viscous) phenomena involved in the structure. Beside the intrinsic damping properties of steel, the inter-laminar contact nature can influence the overall damping. Viscous damping occurs in the inter-laminar interface of glue-bonded cores as pictured in Fig. 6.4a. Friction is induced between the glue and the moving boundaries (*i.e.* laminations) and causes the glue to shear. On the other hand, Coulomb (or friction) damping relates to the welded core where energy is absorbed via sliding friction [79] and retransmitted as heat, as shown in Fig. 6.4b.

The dry-contact at the inter-laminar interface accentuates sliding friction in the case when the laminations are undergoing relative motion, *e.g.* for anti-symmetric modes  $B(n_r, 1)$ . However in the case of pure radial modes  $A(n_r, 0)$ , the thin sheets deform in phase with each other such that it does not activate this friction. Fig. 6.5 illustrates this damping occurrence by showing the cut plane ( $z, x$ ) of the stator core for undeformed structure,  $A(2, 0)$  mode and  $B(2, 1)$ .

In short, the combination of distributed stiffness through welding and the sliding friction due to the relative motion of neighboring laminations (emphasized by welding) are both physical phenomena that permit to increase structural

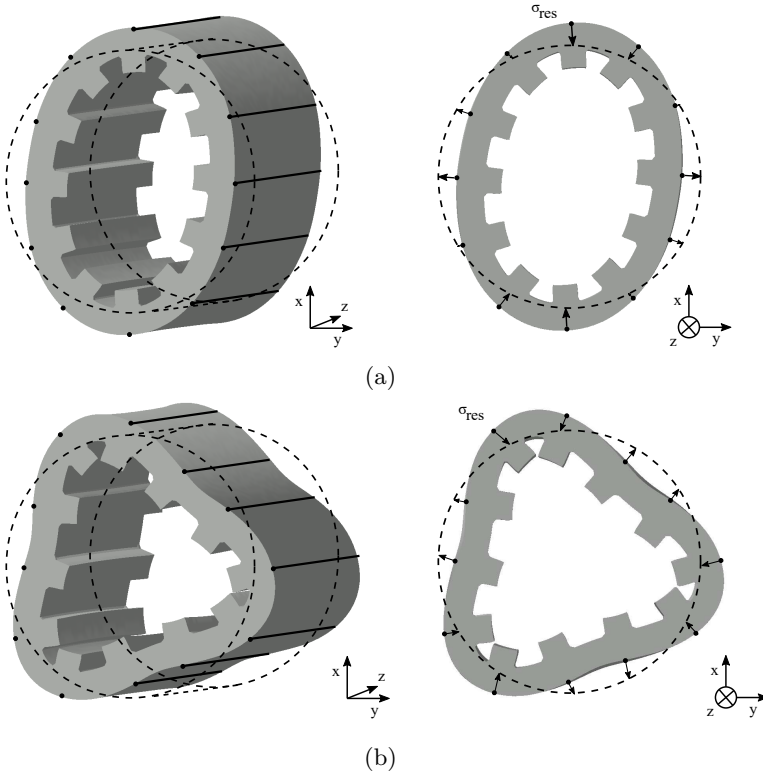


Figure 6.2: Residual stresses effects on mode  $A(2,0)$  (a) and  $A(3,0)$  (b)

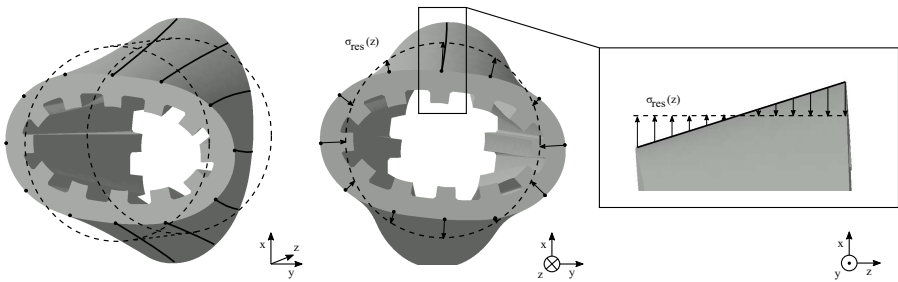


Figure 6.3: Residual stresses effects on mode  $B(2,1)$

damping. It is also important to note that the induced change in the mode shape also affects the transformation of the magnetic force wave to the modal domain and reduce the force's participation factor (see Eq. (2.16)); immediately

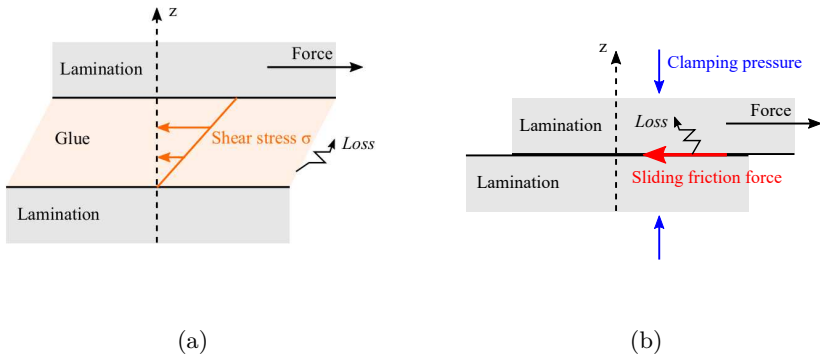


Figure 6.4: Illustration of viscous (a) and Coulomb (b) damping in the case relative displacement occurs

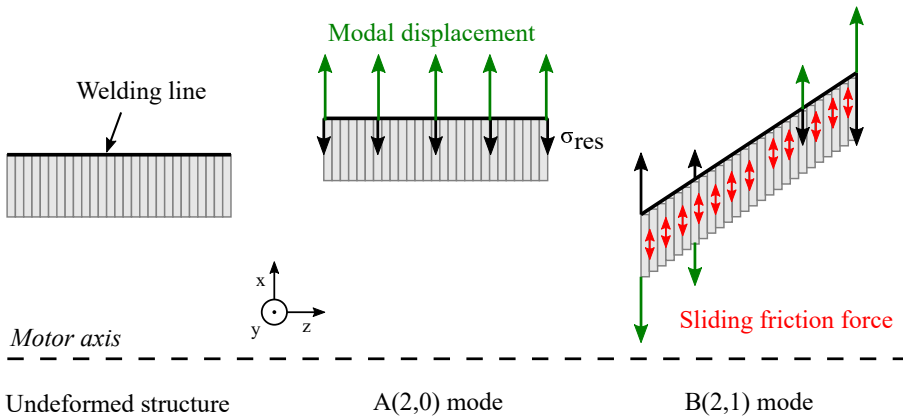


Figure 6.5: Illustration of the damping occurrence for specific modes - NB: Vector amplitudes are informative only

attenuating vibration amplitude from resonances.

In parallel, the geometrical aspect of the phenomena towards targeted modes damping can orientate further damping strategies. The pure radial modes  $A(n_r, 0)$  are commonly the most critical in terms of acoustic noise of magnetic origin for the following reasons:

- they occur at the lowest natural frequencies
- they are excited by radial magnetic forces, because the core cross-section

remains the same along its axis (transversally symmetric) so as the forces distribution

- they are acoustically efficient, meaning that they translate vibration energy into acoustic energy with lower levels of losses, *i.e.* high acoustic noise emission

Therefore the next Sections propose an original lamination stacking method for  $A(n_r, 0)$  modal damping, by using efficiently the two capabilities of damping that stacking manufacturing brings.

### 6.2.2 On forcing transversal asymmetry

Pure radial modes  $A(n_r, 0)$  are transversally symmetric (see Appendix A for thorough explanations of symmetries) and it has been explained previously why transversally symmetric welding brings damping of transversally anti-symmetric modes  $B(n_r, 1)$ . Hence the idea of the proposed attaching method is to connect the stator core laminations such that transversal stiffness asymmetry is introduced. A skew attachment distribution along the shaft axis of the machine is the proposed solution and is depicted in Fig. 6.6.

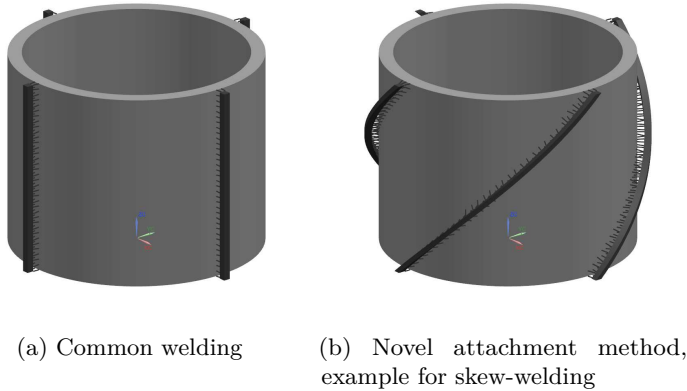


Figure 6.6: Illustration of the novel lamination attachment method for welding with four weld lines

Welding and gluing can be used for attachment process. The stator core stiffness then becomes axially asymmetric (but radially symmetric due to the connection locations), and more importantly transversally asymmetric (from the skew distribution). Moreover the induced relative displacements between

laminations encourages sliding friction to occur, which supposedly increases damping properties. Fig. 6.7 helps explain why modal damping is induced with this technique. Now the residual stresses have azimuthal dependencies which introduces sliding friction for  $A(n_r, 0)$  modes as well, suggesting higher modal damping. Additionally the distributed stiffness tends to reduce modal vibration amplitude of  $A(n_r, 0)$  modes by attracting the yoke to its equilibrium as mentioned in the last Section.

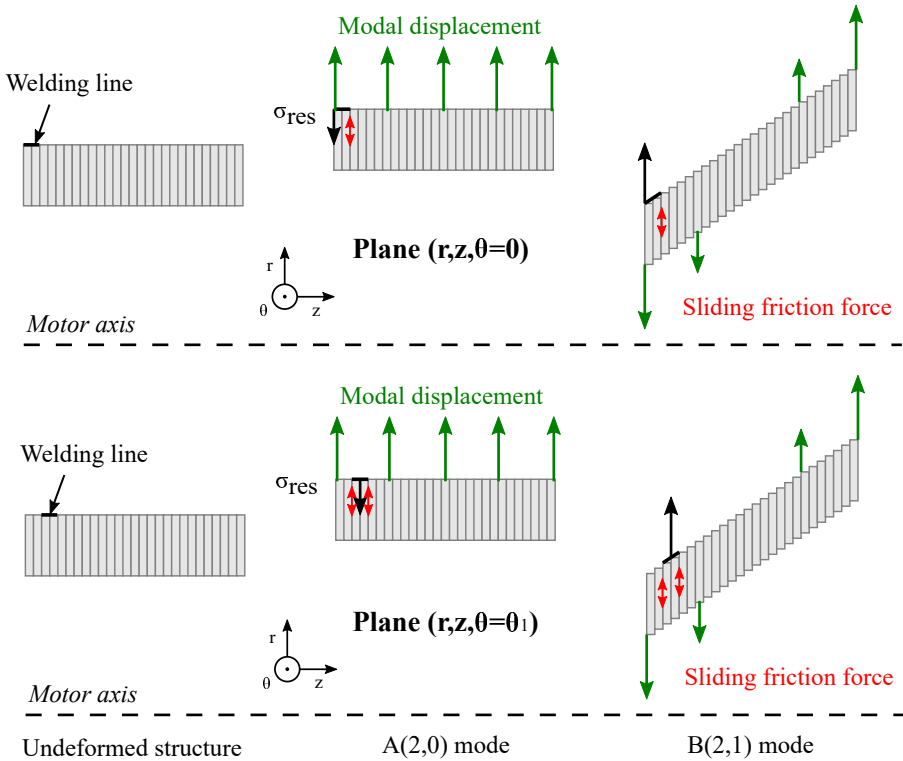


Figure 6.7: Illustration of the damping occurrence when using skew-weld/glue - NB: Vector amplitudes are informative only

The advantages of this technique are three-fold:

- Keep the same cross-section geometry, such that changes on the electromagnetic properties and housing designs are not necessary. The stator core stays axially, radially and transversally symmetric.
- Force the structure to behave non-symmetrically, such that the vibration modes are either damped or deleted. Transversally-asymmetric stiffness

is introduced while relative displacements between laminations are encouraged via dry-friction.

- Use a production technique already implemented in chain manufacturing, *e.g.* gluing and welding, thus making it not more expensive to realize than common techniques

## 6.3 Experimental validations

### 6.3.1 Manufacturing procedure

An appropriate manufacturing was developed for each attachment technique and schematized in Fig. 6.8. For gluing, the sheets are spread evenly on a stinger (Fig. 6.8 (1)) such that a single phase gluing event (2) is carried out for the entire stack. The glue used is a two-component 3M Epoxy DP 460. Then the alignment (4) is carefully performed by the use of gravity and two clamps (5) at the sides that fix the structure while aligned. The glued stator is then put in a pre-heated oven at 50°C for curing (6). For welding, the same alignment setup (4) is utilized. The laminations are clamped (5) and welded (6bis) at the dedicated welding lines. Each welding line is realized one after the other with a few minutes delay in between in order to allow for cooling the structure and minimize the combined residual stresses.

Several test specimens are constructed, defined in Table 6.1 and illustrated in Fig. 6.9. The laminated cores resemble stator cores without teeth, *i.e.* simple cylinders. They are made of either M330-35A or M470-50A electrical steel. These electrical steels are chosen in agreement with what has already been studied earlier in the thesis, and such that the mechanical characteristics of the thinner and thicker sheets are the same. The mechanical properties given by the manufacturers are summarized in Table 6.2. Each specimen is named according to a structure: the lamination thickness (*e.g.* 35 for 0.35mm), the cylinder outer diameter  $D$  in mm, and the attachment process. For instance 35\_180\_g is 180 mm outer diameter cylinder made of M330-35A steel sheets glued together.

35\_180\_g is the reference glued core. 50\_180\_g is built with the same geometry but thicker laminations. It is supposed that by inducing smaller lamination contact area, viscous and Coulomb damping capabilities (Fig. 6.4) are reduced; *i.e.* stacks with thicker laminations are less damped than stacks with thinner laminations. 35\_180\_w and 35\_180\_sw are built to identify the effects of welding and skew-welding, respectively, compared to gluing. 35\_180\_gsw is built from 35\_180\_g in order to show the influence of skew-welding (*i.e.* residual

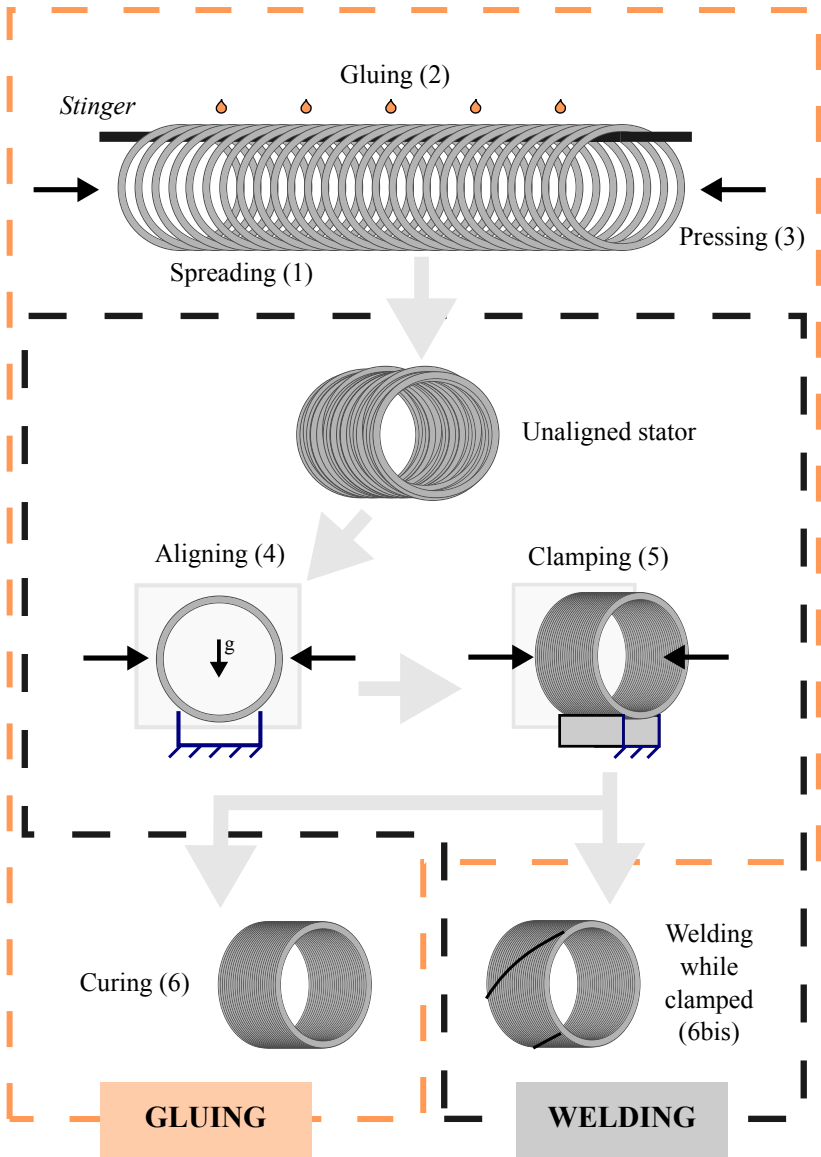


Figure 6.8: Production line process - Gluing and welding cases

stresses) on a glued core. Finally 35\_200\_g and 35\_200\_sg are built with the same stack length ratio  $D/L$  as the previous specimens to keep the same apparent structure, but in a different scale. In particular these last specimens



Table 6.1: Test specimens built

Specimen	Stacking	Outer/Inner Diameter $D/d$ (mm/mm)	Lam. thickness $t$ (mm)	Stack length $L$ (mm)	Ratio $D/L$	Mass (kg)
35_180_g	Glue	180/160	0.35	140	1.3	5.31
50_180_g	Glue	180/160	0.50	140	1.3	5.54
35_180_w	Weld	180/160	0.35	140	1.3	5.34
35_180_sw	Skew-Weld	180/160	0.35	140	1.3	5.38
35_180_gsw	Glue + Skew-Weld	180/160	0.35	140	1.3	5.39
35_200_g	Glue	200/180	0.35	155.4	1.3	6.68
35_200_sg	Skew-Glue	200/180	0.35	155.4	1.3	6.69

Table 6.2: Material characteristics

Steel	Density ( $\text{kg}/\text{dm}^3$ )	Yield Strength ( $\text{N}/\text{mm}^2$ )	Tensile Strength ( $\text{N}/\text{mm}^2$ )	Young's Modulus ( $\text{N}/\text{mm}^2$ )
M330-35A	7.65	300	430	200,000
M470-50A	7.70	300	435	200,000

are useful to determine the effectiveness of the proposed attachment method using glue instead welding. The specimen 35\_200\_sg is built with 2 gluing lines both being opposite from each other, while 35\_180\_w is composed of 4 straight weld lines, and 35\_180\_sw of 4 skewed weld lines as illustrated in Fig. 6.6.

The complexity of realizing repeatable samples of the same specimens, given non-automated production line available, was coped by statistic analyses performed in Section 6.3.3 to evaluate manufacturing and testing uncertainties.

### 6.3.2 Testing procedure

EMAs are performed on the built samples to estimate the modal parameters. As described in Section 2.2, the analyses require Output/Input FRFs  $H_{O/I}$  measurements in a dedicated testing setup environment. Flexible ropes are chosen to hang the sample under test, in order to only capture the intrinsic dynamics of the specimen while eliminating the interference of rigid body modes. A miniature shaker (LMS Qsource SN045) is used as the input excitation

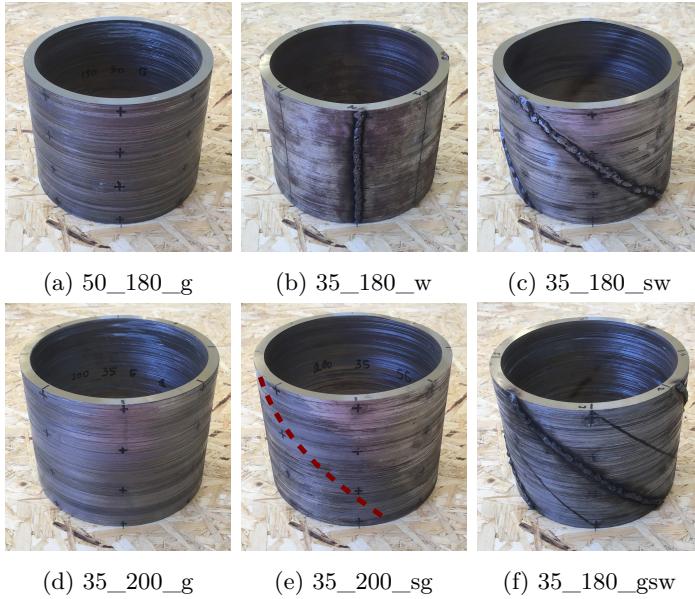


Figure 6.9: Test specimens under study

technique and allows consistent, repeatable and coherent measurements up to 5,500 Hz. The measurement points are defined such that no information is lost due to spatial aliasing, thus leading to 32 measurement points: 8 along the circumference and 4 along the stacking axis. Triaxial accelerometers (PCB Piezotronics SN 356A22) are used for the vibration sensing.

Given that the modal model is linear, see Section 2.2, the structure linearity is validated during all the measurement campaign and for every test sample by means of common reciprocity and linearity checks [58]. PolyMAX [100] is then used as the curve-fitting algorithm and modal parameter estimation. Additionally the peak amplitude  $G_n$  of the acceleration FRF-sum  $S_H$  at each natural frequency is collected.

The uncertainty of realizing perfectly repeatable experiments was coped by statistical analyses performed in Section 6.3.3 to allocate as well for measurement deviations.

### 6.3.3 Significance evaluation

As mentioned in the two previous Sections 6.3.1 and 6.3.2, the uncertainties in the significance of the manufacturing processes to affect a particular parameter, *e.g.* natural frequency or damping. An ANalysis Of VAriances (ANOVA) [131] is performed in order to evaluate the significance of the different factors, namely the manufacturing processes.

#### Repeatability assessment with pooled variance

The perfect repeatability of the manufacturing, testing and post-processing are not always guaranteed. Hence specimen 35\_180\_g of Table 6.1 is subject to an extensive repeatability assessment study which serves as the basis to potential deviations of the other specimens. Three groups of 35\_180\_g generate variance calculations:

- $n_1 = 2$  samples of the 35\_180\_g supposedly identical by using the same attachment production allow assessing the manufacturing repeatability, via generating the variance  $\sigma_1^2$
- $n_2 = 2$  different tests of the same sample permit to assess the testing repeatability, generating the variance  $\sigma_2^2$
- $n_3 = 10$  different EMA post-processing of the same test permit to assess the post-processing repeatability, *i.e.* PolyMAX consistency, generating the variance  $\sigma_3^2$

Each variance  $\sigma_k^2$  ( $k = 1, 2, 3$ ) is calculated as follows:

$$\sigma_k^2 = \frac{1}{n_k - 1} \sum_{p=1}^{n_k} (x_p - \bar{x})^2 \quad (6.1)$$

where  $x_p$  and  $\bar{x}$  represent the  $p^{th}$  population quantity and the arithmetic mean of the population, respectively. In this study, the natural frequencies  $f_{A(2,0)}$ ,  $f_{A(3,0)}$ ,  $f_{A(4,0)}$ , the modal damping  $\xi_{A(2,0)}$ ,  $\xi_{A(3,0)}$ ,  $\xi_{A(4,0)}$  and the peak FRF-sum amplitude  $G_{A(2,0)}$ ,  $G_{A(3,0)}$ ,  $G_{A(4,0)}$  are the quantities of which variances are computed. Then, a pooled variance  $\sigma_m^2$  is computed:

$$\sigma_m^2 = \frac{(n_1 - 1)\sigma_1^2 + (n_2 - 1)\sigma_2^2 + (n_3 - 1)\sigma_3^2}{n_1 + n_2 + n_3 - 3} \quad (6.2)$$

It represents the variance of several populations when the mean of each population might be different, under the assumption that each population variance is the same.  $\sigma_m^2$ , which depends on the mode  $A(n_r, 0)$  and the modal parameter  $f$  or  $\xi$ , will be used as the variance for all the factors studied.

### ANOVA

In order to define the significance of a manufacturing process (factor) compared to another in terms of natural frequency and damping, ANOVA is performed. It compares the differences of means among more than two groups of factors [131]. Each group is populated by samples that are attributed the same factor. From ANOVA, the probability (P-value) of obtaining equal means from all populations is calculated through the F-ratio output of the analysis. A P-value lower than 0.05 suggests that at least one factor is significant from the others. ANOVA assumes that the populations follow a normal distribution, that the population variances are all equal and that the quantities are taken randomly inside the populations.

Generally, let us have  $m$  different factors each having  $N_m$  samples of mean value  $\bar{x}_m$ . The factorial variance  $\sigma_F^2$ , representing the deviation importance due to the factors, is defined as follows,

$$\sigma_F^2 = \frac{1}{m-1} \sum_{i=1}^m N_i (\bar{x}_i - \bar{x})^2 \tag{6.3}$$

where  $\bar{x}$  is the global mean of all the samples. Similarly the residual variance, reflecting the importance of individual variations inside each factor, is defined by

$$\sigma_R^2 = \frac{1}{\left(\sum_{i=1}^{N_m} N_i\right) - m} \sum_{i=1}^m (N_i - 1) \sigma_i^2 \tag{6.4}$$

In our case, the residual variance corresponds to the pooled variance calculated earlier:  $\sigma_R^2 = \sigma_m^2$ . The *F-ratio* is simply the ratio of factorial and residual variances.

$$F - ratio = \frac{\sigma_F^2}{\sigma_R^2} = \frac{\sigma_F^2}{\sigma_m^2} \tag{6.5}$$

The P-value is finally derived from the F-distribution cumulative distribution function [131] and compared to the critical P-value set to 0.05. In total 12 ANOVAs are carried out: two studies that investigate the significance of skew-gluing and skew-welding against regular gluing strategy, that themselves incorporate analyses on three natural frequency variances and 3 modal damping variances.

## 6.4 Results

The results of the EMAs together with the ANOVAs are presented in this Section. First, the FRF-sums with their associated EMA allow drawing conclusions on the effects of each attachment technique on the axial, shearing and anti-symmetric modes. Next, the effects of the lamination thickness, the skew-gluing, the skew-welding and both gluing with skew-welding on the pure radial modes are assessed separately in terms of natural frequencies, modal damping and FRF-sum peak amplitudes.

### 6.4.1 The effects on axial, shearing and anti-symmetric modes

The EMAs of the test specimens described in Table 6.1 give the results compiled in Table 6.3. At this stage no significance evaluation is carried out, as such these are raw EMAs without any deviation calculations. The deviations are calculated later in Section 6.4.2 for pure radial modes which are the most interesting ones for acoustic radiation reduction purposes. Additionally, the measured FRF-sums  $S_H$  for each specimen are shown in Fig. 6.10, 6.11, 6.12 and 6.13.

From this new set of experiments, one can observe other trends than the ones seen in Chapter 5:

- Fig. 6.10 does not show relatively large variations in the FRF-sum. No conclusions on the effect of the lamination thickness on the structural dynamics are drawn for now.
- Fig. 6.11 does show quite some variations. The skew-gluing seems to damp most of the anti-symmetric modes, although (0, 1) shearing modes apparent to noise at low frequencies are generated. Damping effects on pure radial modes are detailed in the next Section.

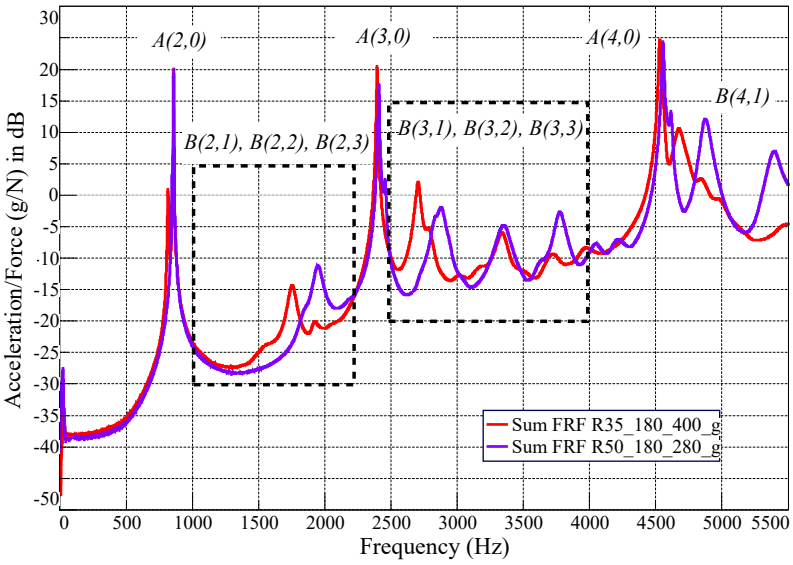


Figure 6.10: FRF-sum for 35\_180\_g and 50\_180\_g

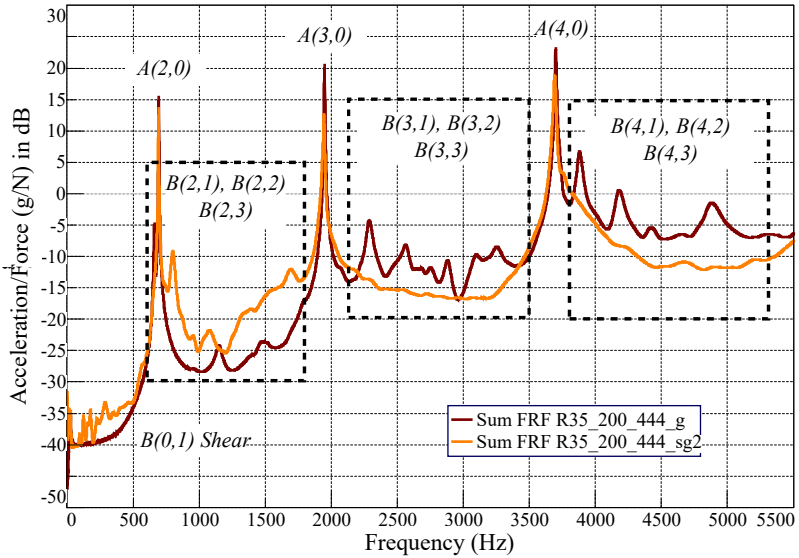


Figure 6.11: FRF-sum for 35\_200\_g and 35\_200\_sg2

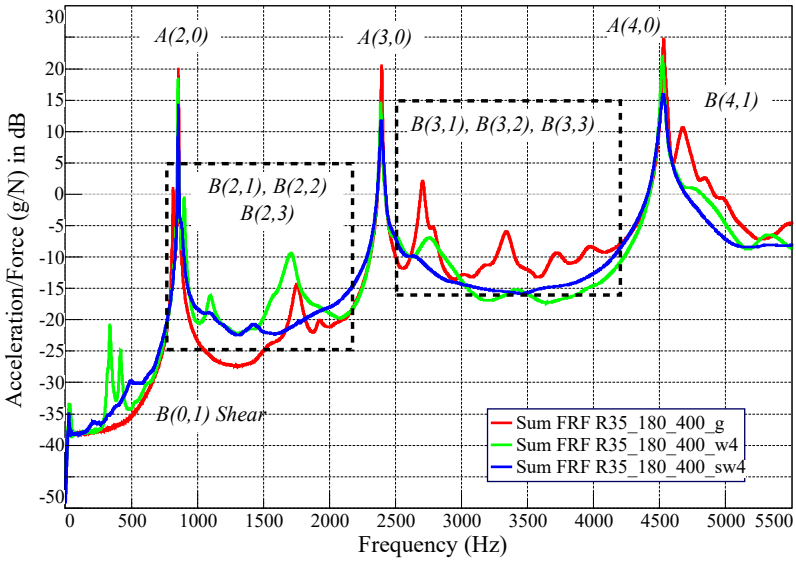


Figure 6.12: FRF-sum for 35\_180\_g, 35\_180\_w and 35\_180\_sw

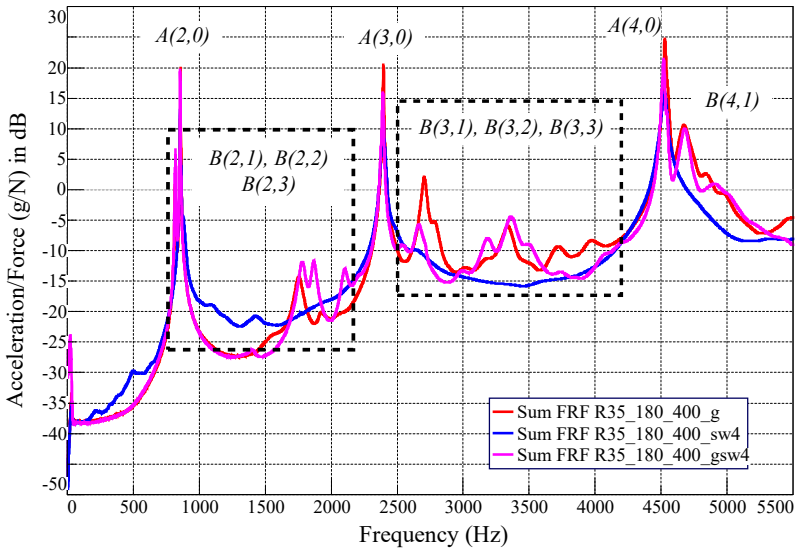


Figure 6.13: FRF-sum for 35\_180\_g, 35\_180\_sw and 35\_180\_gsw

- Fig. 6.12 validates the known trends and validate the pure radial modes damping, which is detailed in the next Section.
- Fig. 6.13 shows a combined glue + skew-weld core behavior very similar to the simple glued specimen. This attachment combination does not seem at this point to be beneficial in any way; a deeper analysis on the pure radial modes is carried out in the next Section to confirm this statement.
- No axial mode occurs for our specimens, since they are estimated to be at higher natural frequencies.

It is also interesting to note the global trends given in Chapter 5:

- High damping of modes  $B(n_r, n_z \neq 0)$  is identified, especially for the welded cores.
- The modal damping values stand in the same range as the glued and welded industrial stators' tested in Chapter 5, which reinforces the representability of the manual manufacturing against industrial manufacturing. For instance for 35\_180\_g,  $\xi_{A(2,0)} = 0.07\%$ , while for the glued stator of Section 5.7, it is equal to 0.09 %.
- Axial stiffening and thus removal of axial/shear modes before the ovalization mode  $A(2, 0)$  happens as well, when comparing 35\_180\_g with 35\_180\_w (see Fig. 6.12).
- The pure radial modes  $A(2, 0)$ ,  $A(3, 0)$  and  $A(4, 0)$  dominate the structural dynamics due to their low modal damping. That is the reason why an extensive study of these modes is presented in the next Section 6.4.2.



Specimen		Modes													
		$B(0,1)$ shear	$B(0,1)$ shear	$A(2,0)$	$B(2,1)$	$B(2,2)$	$B(2,3)$	$A(3,0)$	$B(3,1)$	$B(3,2)$	$B(3,3)$	$A(4,0)$	$B(4,1)$	$B(4,2)$	$B(4,3)$
35_180_g	$f_n$ (Hz)			856	816	1753	-	2394	2662	2702	3330	4530	4674	4825	N/A
	$\xi_n$ ( $\times 10^2$ )			0.07	0.41	1.97	-	0.11	1.35	0.70	1.39	0.17	0.84	1.07	-
50_180_g	$f_n$ (Hz)			860	847	1944	-	2407	2448	2862	3350	4552	4607	4868	5376
	$\xi_n$ ( $\times 10^2$ )			0.03	0.25	1.96	-	0.15	0.27	0.80	1.58	0.14	0.17	0.55	0.86
35_180_w	$f_n$ (Hz)	334	417	853	899	1100	1702	2387	2418	2516	2763	4519	4605	4761	N/A
	$\xi_n$ ( $\times 10^2$ )	2.12	1.12	0.11	0.57	3.14	2.70	0.22	1.02	1.8	3.01	0.24	1.1	2.06	-
35_180_sw	$f_n$ (Hz)			855	-	1098	-	2385	-	2657	-	4526	4606	-	-
	$\xi_n$ ( $\times 10^2$ )			0.17	-	6.09	-	0.78	-	3.5	-	0.53	2.91	-	-
35_180_gsw	$f_n$ (Hz)			854	817	1779	-	2388		2670	-	4516	4679	4881	-
	$\xi_n$ ( $\times 10^2$ )			0.07	0.18	1.51	-	0.16	-	1.18	-	0.16	0.67	1.61	-
35_200_g	$f_n$ (Hz)			694	660	1151	1486	1949	-	2285	2882	3699	3883	4181	4866
	$\xi_n$ ( $\times 10^2$ )			0.08	0.50	2.59	2.42	0.07	-	0.93	0.91	0.11	0.51	1.04	1.28
35_200_sg	$f_n$ (Hz)			693	-	797	-	1942	-	-	-	3692	-	-	-
	$\xi_n$ ( $\times 10^2$ )			0.13	-	1.37		0.29	-	-	-	0.19	-	-	-

Table 6.3: EMAs results

### 6.4.2 The effects on pure radial modes $A(n_r, 0)$

#### The effects of the lamination thickness

Different lamination thicknesses immediately induce different number of lamination sheets for the same stack length. There are consequently higher total contact area between laminations in the case of thinner lamination sheets, which suggest higher inter-laminar frictional contacts, and thus more damping in general. The next results permit to compare specimens 35\_180\_g and 50\_180\_g in order to assess that physical insight. Table 6.4 gives the averaged natural frequencies (Hz), the modal damping values and summation FRFs peak values for every occurring mode, their associated pooled standard deviation coming from the pooled variance  $\sigma_m^2$  and finally the P-value output from the ANOVAs. Fig. 6.4 illustrates the modal damping variations depending on the lamination thickness.

Table 6.4: Significance levels for the samples tested, effect of lamination thickness

	35_180_g	50_180_g	Pooled standard deviation $\sigma_m$	P-value
Natural frequency $f_n$ (Hz)				
$f_{A(2,0)}$	856	860	0.1	1.35e-7
$f_{A(3,0)}$	2394	2407	1.0	1.66e-5
$f_{A(4,0)}$	4530	4552	1.0	2.04e-6
Modal damping $\xi_n$				
$\xi_{A(2,0)}$	0.0007	0.0003	0.0001	6.09e-4
$\xi_{A(3,0)}$	0.0011	0.0015	0.0002	7.43e-2
$\xi_{A(4,0)}$	0.0017	0.0014	0.0002	1.46e-1
Peak Amplitude $G_n$ (g/N) in dB				
$G_{A(2,0)}$	20.0	20.0	3.4	1
$G_{A(3,0)}$	20.5	17.6	3.1	3.16e-1
$G_{A(4,0)}$	24.7	24.4	1.9	8.56e-1

Given the P-values, one can state that the natural frequency shifts are significant. It is interesting to note that the specimen 50\_180\_g is made of thicker laminations and is stiffer than 35\_180\_g. In parallel, the modal damping values are not affected in such a way that conclusions can be drawn; so as the FRF-sum peak amplitudes. The lamination thickness does not play a significant

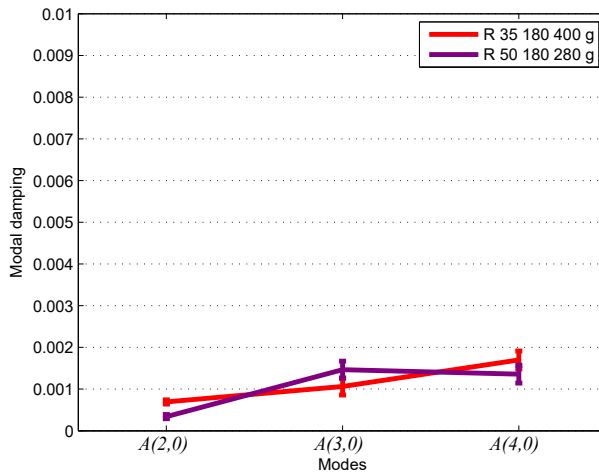


Figure 6.14: Modal damping comparison for glued cores of different lamination thicknesses

enough role on the structural dynamics to envisage design optimizations based on this parameter for NVH improvements.

### The effects of skew-gluing

The skew-gluing brings transversal asymmetry by forcing lamination connections unevenly along the stack. It is therefore expected to have more modal damping of pure radial modes. Table 6.5 gives the same parameters as Table 6.4 but for the glued and skew-glued samples 35\_200\_g and 35\_200\_sg. Fig. 6.15 illustrates particularly the damping obtained from these two specimens.

The natural frequencies do not vary much depending on the attachment technique, although the statistical P-value reflects the significance of the skew-glue factor. The most interesting remark comes with damping variations that for every mode, increases significantly while using skew-glue technique. In fact the mode  $A(3,0)$  shows the greatest damping, about 3 times more damping than 35\_200\_g, which makes physical sense: the two skew lines bring extra stiffness to more vibration nodes in the case of  $A(3,0)$  than for  $A(2,0)$ . The FRF-sum peak amplitudes do not show significant variations coming from the skew-glue, but the global trend of lower energy transfer capabilities (inducing less vibration, thus less noise) is present.

Table 6.5: Significance levels for the samples tested, effects of skew-gluing

	35_200_g	35_200_sg	Pooled standard deviation $\sigma_m$	P-value
Natural frequency $f_n$ (Hz)				
$f_{A(2,0)}$	694	693	0.1	2.55e-4
$f_{A(3,0)}$	1949	1942	1.0	1.02e-3
$f_{A(4,0)}$	3699	3691	1.0	6.08e-4
Modal damping $\xi_n$				
$\xi_{A(2,0)}$	0.0008	0.0013	0.0001	5.46e-3
$\xi_{A(3,0)}$	0.0007	0.0029	0.0002	1.60e-4
$\xi_{A(4,0)}$	0.0011	0.0019	0.0002	6.23e-3
Peak Amplitude $G_n$ (g/N) in dB				
$G_{A(2,0)}$	20.2	13.6	3.4	7.62e-2
$G_{A(3,0)}$	16.2	12.7	3.1	2.39e-1
$G_{A(4,0)}$	20.4	18.8	1.9	3.61e-1

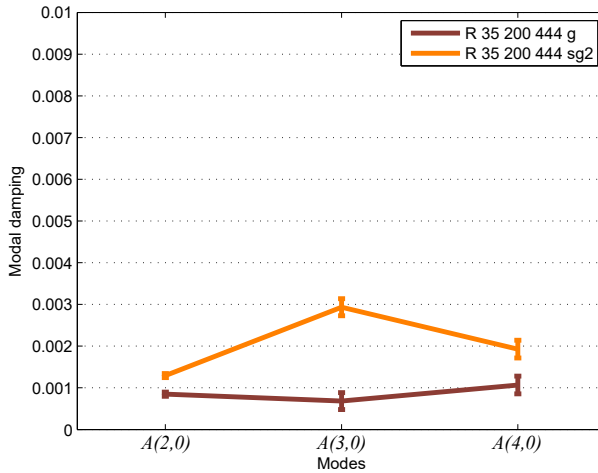


Figure 6.15: Modal damping comparison for glued and skew-glued cores

### The effects of skew-welding

The skew-welding is the most promising of the proposed techniques because the hot welding process generates residual stresses. If the welding lines are

chosen such that the stator structural integrity shows strong anti-symmetries, the damping of pure radial modes increases. Hence, Table 6.6 details the results for 35\_180\_g, 35\_180\_w and 35\_180\_sw. Fig. 6.16 illustrates the damping obtained from these three specimens with their standard deviation  $\sigma_m$ .

Table 6.6: Significance levels for the samples tested, effects of skew-welding

	35_180_g	35_180_w	35_180_sw	Pooled standard deviation $\sigma_m$	P-value
Natural frequency $f_n$ (Hz)					
$f_{A(2,0)}$	856	853	855	0.1	7.77e-8
$f_{A(3,0)}$	2394	2387	2385	1.0	3.05e-5
$f_{A(4,0)}$	4530	4519	4526	1.0	7.87e-5
Modal damping $\xi_n$					
$\xi_{A(2,0)}$	0.0007	0.0011	0.0017	0.0001	4.39e-5
$\xi_{A(3,0)}$	0.0011	0.0022	0.0078	0.0002	2.94e-8
$\xi_{A(4,0)}$	0.0017	0.0024	0.0053	0.0002	1.33e-6
Peak Amplitude $G_n$ (g/N) in dB					
$G_{A(2,0)}$	20.0	18.3	12.5	3.4	7.5e-2
$G_{A(3,0)}$	20.5	14.5	11.7	3.1	3.2e-2
$G_{A(4,0)}$	24.7	21.9	15.9	1.9	3.9e-3

The natural frequencies are not significantly impacted by the attachment technique used. However, modal damping is influenced drastically (significant P-value obtained), especially for mode  $A(3,0)$ . From gluing (35\_180\_g) to welding (35\_180\_w), there is an overall damping increase, but more important for  $A(3,0)$ . Here, the 4 welding lines are spread such that they correspond exactly to 4 vibration nodes of  $A(2,0)$  while they bring stiffness to the nodes of  $A(3,0)$ . On the other hand from welding (35\_180\_w) to skew-welding (35\_180\_sw), one can note a drastic difference of damping values. Similarly to the previous conclusions, the skew distribution of the welding lines adds stiffness to non-nodal points which is translated in higher damping. In that sense, mode  $A(3,0)$  is 7 times more damped from 35\_180\_g to 35\_180\_sw, compared to  $A(2,0)$  that is 2.4 times more damped. The FRF-sum peak amplitudes do show significant changes for  $A(3,0)$  and  $A(4,0)$  but not for  $A(2,0)$ . Yet the trend shown on damping previously is strengthened by acceleration transfer reductions of around 10 dB for the modal peaks, which is another validation of the novel lamination technique potential.

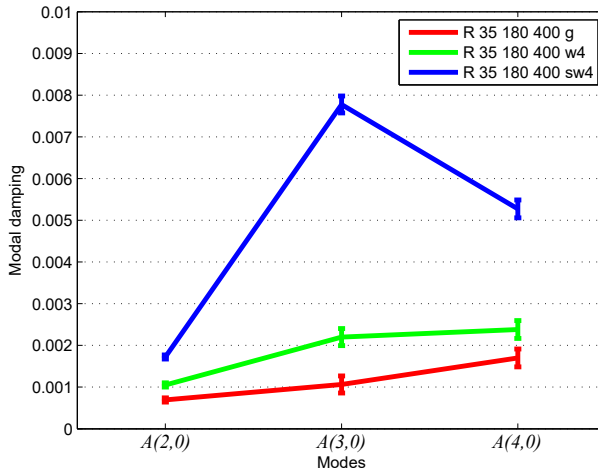


Figure 6.16: Modal damping comparison for glued, welded and skew-welded cores

### The effects of both gluing with skew-welding

The previous results showing strong pure radial modes damping capabilities thanks to dedicated welding patterns, and the removal of axial modes when using gluing, encourage us to combine these two techniques. Table 6.7 gives the results of the glued with skew-welding core 35\_180\_gsw, to be compared with results from glued 35\_180\_g and skew-welded 35\_180\_sw specimens. The modal damping is illustrated in Fig. 6.17 as well.

The natural frequencies are not affected drastically. But the P-value shows significant differences for the modal damping values. Here, the significance comes from the large difference brought by the skew-welded specimen 35\_180\_sw. When one compares the glued stator with the glued + skew-welded stator, it is clear that welding does not bring significant changes to the structure. This shows clearly that gluing dominates welding in terms of structural dynamics contributions to the core, so that one loses the interesting welding features while when gluing the core. In other words, the inter-laminar friction is the key-component from which welding can take advantage compared to gluing that cancels it.

Table 6.7: Significance levels for the samples tested, glue + skew-welding effect

	35_180_g	35_180_sw	35_180_gsw	Pooled standard deviation $\sigma_m$	P-value
Natural frequency $f_n$ (Hz)					
$f_{A(2,0)}$	856	855	854	0.1	9.71e-7
$f_{A(3,0)}$	2394	2385	2388	1.0	9.39e-5
$f_{A(4,0)}$	4530	4526	4516	1.0	6.72e-6
Modal damping $\xi_n$					
$\xi_{A(2,0)}$	0.0007	0.0017	0.0007	0.0001	2.12e-5
$\xi_{A(3,0)}$	0.0011	0.0078	0.0016	0.0002	2.35e-8
$\xi_{A(4,0)}$	0.0017	0.0053	0.0016	0.0002	7.42e-7
Peak Amplitude $G_n$ (g/N) in dB					
$G_{A(2,0)}$	20.0	12.5	19.6	3.4	7.5e-2
$G_{A(3,0)}$	20.5	11.7	15.9	3.1	3.2e-2
$G_{A(4,0)}$	24.7	15.9	24.5	1.9	3.9e-3

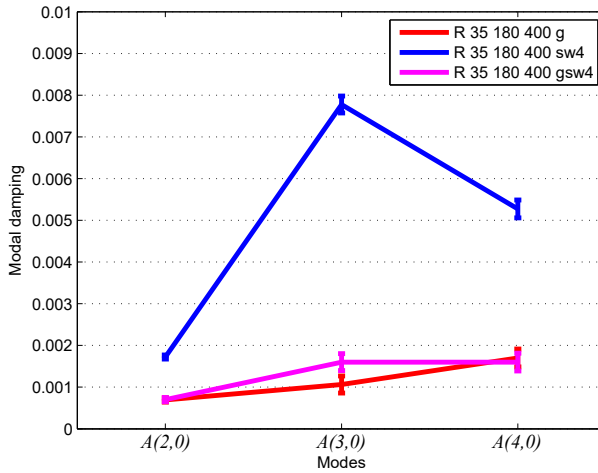


Figure 6.17: Modal damping of glued, skew-welded and glued + skew-welded cores

### 6.4.3 Hypotheses validations

Since the skew-welding method has been previously proved to work experimentally in Section 6.4.2, it is interesting to validate the three hypotheses made in Section 6.2 that were motivating its implementation, *i.e.* skewed distribution of stiffness, increased Coulomb friction between laminations and change in force's participation factor due to changes in mode shapes. The next studies focus on the most promising technique that promotes skew-welding capabilities compared to gluing, *i.e.* Section 6.4.2 *The effects of skew-welding*.

#### Hypothesis 1: the skewed distribution of stiffness

At first it is important to note that the stiffness brought by the welding lines is not significant given that with similar masses, the natural frequencies of the samples are not affected, see Table 6.6. Hence the skewed distribution of stiffness was already shown in Section 6.4.2 not to play a significant role in damping vibrations of the laminated structure. Additionally, vibration damping due to extra stiffness is very limited in general [58], because it would require large differences in stiffness values.

#### Hypothesis 2: the induced inter-laminar dry friction

Then it was assumed that dry friction induced between laminations may be responsible for higher damping. However it is well known that friction force is nonlinear and can be subdivided into static and dynamic friction components [101]; the first occurs between non-moving surfaces while the second occurs between moving surfaces after a force threshold, also called traction, is reached. This threshold depends on several parameters eventually difficult to predict numerically such as normal force to the friction motion direction, surface deformation, roughness and contamination. Through dynamic friction occurring between laminations, the energy lost in the form of heat was assumed here to generate vibration damping.

In order to verify this assumption, several linearity checks as described in Section 2.2.2 were performed. The input voltage level is gradually increased from 1 V to 4 V, up to the maximum level allowed by the miniature shaker, *i.e.* corresponding to a force of 2 newtons, and the FRFs are measured consequently. An example of such linearity check is given in Fig. 6.18 with four different input force levels as used in Section 6.3.2. Additionally, damping ratios are collected through the half-power technique [58] in order to quantify possible effects from



non-linearities. Table 6.8 shows the difference of modal damping with respect to the referenced value assigned to the lowest force level of input.

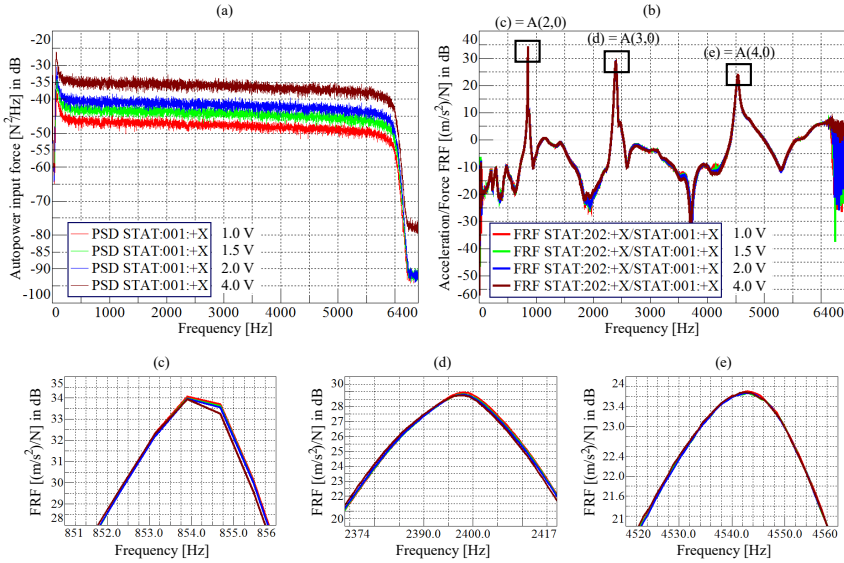


Figure 6.18: Example of a linearity check for the skew-welded core: (a) input autopower (RMS) spectrum, (b) FRF results for different input levels, (c-d-e) zooms on the FRF peaks

While the apparent constancy of the measured FRFs for different levels of input forces have permitted to assume linear behavior of the skew-welded laminated core previously in Section 6.4.2, the damping values still increase with the input forces. It eventually indicates that energy is also lost by friction phenomena as it was hypothesized. However the damping variations do not exceed 6%, and can be considered insignificant when looking at the 700% increase obtained between the glued and the skew-welded cores of Section 6.4.2. Therefore one can assume that nonlinearities from dynamic friction forces are not responsible for higher damping values in the present studies.

Yet it is important to mention that greater forces, such as the electromagnetic ones going up to 300 newtons (see Fig. 3.12), might activate more effectively dry-friction. Due to hardware exciter limitations, this aspect could not be investigated in this dissertation work.

Table 6.8: Modal damping estimations (half-power technique) for skew-welding core and different input voltage levels to the shaker (equivalent to force levels)

Mode	Voltage input [V]	Modal damping $\xi_n$	Difference [%]
A(2,0)	1.0	0.003162	ref.
	1.5	0.003185	+0.74
	2.0	0.003197	+1.11
	4.0	0.003349	+5.93
A(3,0)	1.0	0.009852	ref.
	1.5	0.009998	+1.48
	2.0	0.010015	+1.65
	4.0	0.010202	+3.55
A(4,0)	1.0	0.008310	ref.
	1.5	0.008305	-0.05
	2.0	0.008354	+0.53
	4.0	0.008433	+1.48

**Hypothesis 3: the changes in mode shapes**

Next, since transverse asymmetry is introduced by the use of skewed welding, it is interesting to correlate further the mode shapes. So far they were assumed not affected by any of the manufactures, but a change in modal participation factor can induce vibration damping phenomena as well, as expressed in Eq. (2.16). In order to analyse this effect, the MAC matrix can be used to compare two mode shapes  $\{X_r\}$  and  $\{X_s\}$  [58],

$$MAC(\{X_r\}, \{X_s\}) = \frac{|\{X_r\}\{X_s\}|^2}{(\{X_r\}^{*T}\{X_r\})(\{X_s\}^{*T}\{X_s\})} \tag{6.6}$$

It varies between 0 and 1 and represents how much two mode sets correlate with each other; a perfect correlation would show a MAC number of 1, while a 0 value means no correlation. Two different MAC analyses can be carried out to understand how skew-weld is beneficial in terms of vibration damping. On the one hand, the MAC analysis can be performed on the full stators where different manufactures are compared. On the other hand, the influence of the manufacture can be investigated by doing a MAC analysis for different cross-sections along the stator.

At first, a MAC analysis is performed for the glued, welded and skew-welded cores under study, and is shown in Fig. 6.19. The same accelerometer discretization is used as in Section 6.4.2, *i.e.* 32 points with 1 input. Table 6.9 also shows the diagonal values of the matrices. The reference specimen is the glued stator.

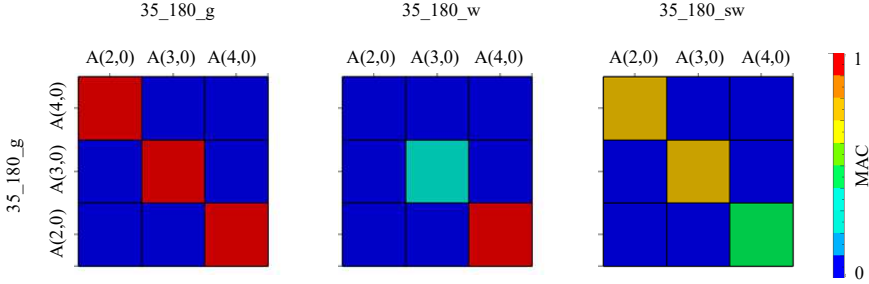


Figure 6.19: Complete MAC analysis for different stator manufactures - matrices

Table 6.9: Complete MAC analysis for different stator manufactures - diagonal values

Reference specimen	Mode	35_180_g	35_180_w	35_180_sw
35_180_g	A(2,0)	1.00	0.00	0.77
	A(3,0)	1.00	0.21	0.71
	A(4,0)	1.00	0.92	0.47

Obviously auto-correlation between the two same test specimens (left matrix) gives the maximum MAC number of 1. Looking at the middle matrix, the  $A(2,0)$  mode does not correlate between the glue and welded cores. In fact only one twin mode of  $A(2,0)$  is captured per experiment and they are not equivalent for the two specimens such that a poor correlation is obtained. The  $A(3,0)$  mode is not well correlated between the glued and welded cores. Last regarding the right matrix, every mode is badly correlated with the reference glued mode shapes. Jointly with the previous results of Sections 5.7 and 6.4.2, this MAC analysis presupposes that mode shapes are affected such that vibrations are reduced through modal participation factor variations. However the influence of transverse asymmetry on the mode shapes is hardly comprehensible by solely performing this analysis.

Hence in order to reinforce the claim, another set of MAC analyses are performed. This time, the mode shapes for different cuts, referred to as layers, along the stator axial axis are correlated. Evidently, EMAs were performed in order to estimate the mode shapes corresponding to each layer. The reference mode set

corresponds to the layer 1. The analysis is carried out for every specimen of this study, *i.e.* the glued, welded and skew-welded cores.

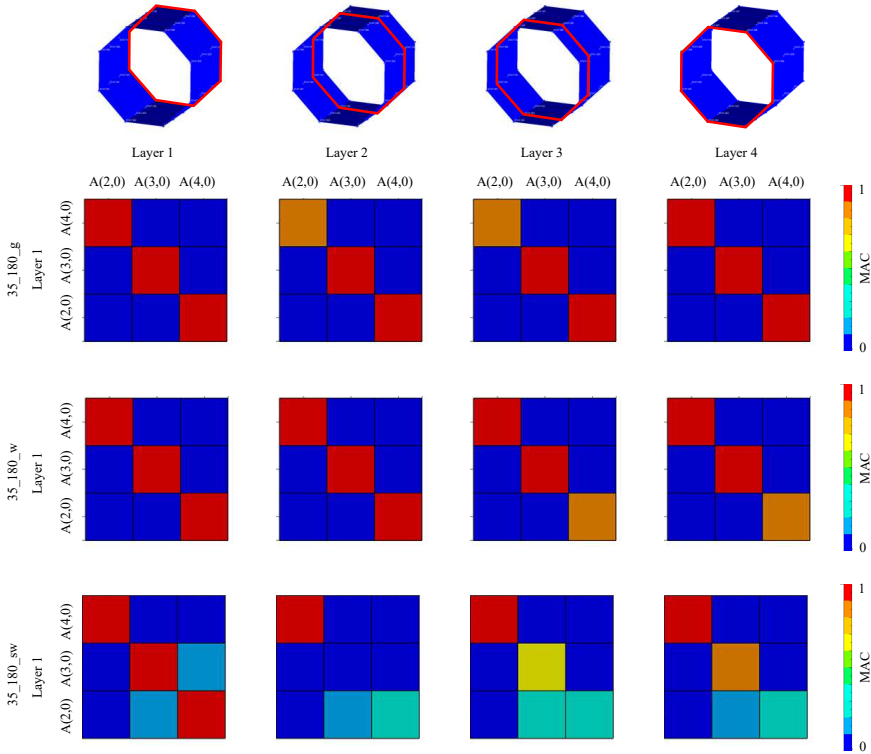


Figure 6.20: Layered MAC analysis for different stator manufactures

Looking at the two first rows of Fig. 6.20, the correlation between each layer is acceptable with values above 0.8. For these two specimens (glued and welded), the transverse symmetry is kept and therefore the mode shapes are not varying along the axial axis. However when transverse asymmetry is introduced (third row) in the skew-welded core, significant mode shape discrepancies occur between layers. This suggests that, originally transversally symmetric, the pure radial modes  $A(n_r, 0)$  become transversally asymmetric by skew-welding; thus shaping the modal participation factor presupposing vibration amplitude reduction.

Table 6.10: Layered MAC analysis for different stator manufactures - diagonal values

Specimen	Mode	Layer 1	Layer 2	Layer 3	Layer 4
35_180_g	$A(2, 0)$	1.00	0.82	0.87	0.91
	$A(3, 0)$	1.00	0.93	0.90	0.93
	(Layer 1) $A(4, 0)$	1.00	0.98	0.99	0.99
35_180_w	$A(2, 0)$	1.00	0.99	0.98	0.99
	$A(3, 0)$	1.00	0.97	0.98	0.98
	(Layer 1) $A(4, 0)$	1.00	0.91	0.89	0.87
35_180_sw	$A(2, 0)$	1.00	0.96	0.92	0.91
	$A(3, 0)$	1.00	0.09	0.69	0.83
	(Layer 1) $A(4, 0)$	1.00	0.25	0.20	0.20

## 6.5 Intermediate conclusions

In this chapter, an alternative solution to the attenuation of resonance phenomena responsible for high magnetic noise has been proposed and validated experimentally. The technique takes advantage of the laminated nature of the stator core that contributes to the most critical resonance effects, to passively damp vibration, and finally mitigate magnetic noise. It essentially proposes an original attachment of the laminations which distributes gluing and/or welding with a skew pattern along the axis of the stator core. Three hypotheses have motivated the implementation of this technique:

1. Change in stiffness distribution: Residual stresses from the attachment technique (particularly welding) tend to attract the core back to its equilibrium position (see Fig. 6.2 and Fig. 6.3), which changes the stiffness distribution of the core. It is expected to be able to stiffen the structure for specific modes by tuning the attachment location distribution patterns.
2. Increase of inter-laminar contact damping: Viscous and Coulomb damping are supposedly involved at the interface between laminations for glue-bonded and welded cores, respectively. The relative motion of neighboring laminations can induce shear stress and sliding friction (see Fig. 6.4) at the interface and can be forced to increase modal damping (see Fig. 6.7).
3. Reduction of modal participation factor: The induced change of the mode shapes from the different stiffness distributions affects the transformation

of the magnetic force wave to the modal domain and reduces the modal participation factor (see Eq. (2.16)), thus the vibration amplitude.

The three hypotheses could be verified experimentally by building several lamination stacks with different manufacturing techniques (glue, weld, skew-glue, skew-weld). It was shown that:

- For every test specimen, axial, shearing and anti-symmetric modes are highly damped while pure radial modes  $A(n_r, 0)$  dominate the structural dynamics, which justifies the focus on these modes for vibration damping.
- Natural frequencies of pure radial modes  $f_{A(n_r, 0)}$  are not significantly affected by any of the manufacturing techniques.
- The change of total contact area brought by different lamination thicknesses does not play a significant role on the structural damping, see Table 6.4.
- Skew-gluing increases significantly modal damping compared to gluing (see Table 6.5), especially for  $A(3, 0)$  mode. The two glue lines bring stiffness to more vibration nodes in the case of  $A(3, 0)$  than for  $A(2, 0)$  (hypothesis 1).
- Skew-welding increases significantly modal damping compared to gluing and welding (see Table 6.6), especially for  $A(3, 0)$  mode. Similarly as for skew-gluing, the four skewed welding lines bring stiffness to more vibration nodes in the case of  $A(3, 0)$  than for  $A(2, 0)$  (hypothesis 1).
- Skew-welding a glued core does not bring significant damping improvements (see Table 6.7), essentially because the glue prevents the inter-laminar dry-friction (Coulomb damping) to occur by decreasing relative motion of neighboring laminations (hypothesis 2). Viscous damping replaces Coulomb damping and shows to be less effective due to lower relative motions.

The hypotheses were partially validated further looking more into the skew-welded stator core, and consolidated the potential of this alternative stacking technique. While the skewed distribution of stiffness does not bring significant changes in terms of vibration damping (hypothesis 1), it was shown by means of linearity checks that Coulomb induced friction is not necessarily activated when skew-welding is introduced (hypothesis 2). Although it is important to recognize that forces higher than available shaker excitation (*e.g.* from electromagnetic phenomena) occur, linearity could be assumed within the present study boundaries and hardware limitations. On the other hand, MAC analyses

showed the importance of tuning mode shapes in order to decrease vibrations from resonances (hypothesis 3). However, the difficulties of measuring magnetic forces and/or of determining the stiffness variations due to welding/gluing made this third hypothesis delicate to validate completely.

It is finally important to note that the proposed technique benefits from keeping the same cross-section geometry, from forcing the structure to behave non-symmetrically such that the vibration modes are damped and from using a production technique already implemented in chain manufacturing.





# Chapter 7

## Conclusions

The main objective of this dissertation was to thoroughly understand the structural behavior of rotating electric machines for traction applications, in order to propose appropriate modeling strategies for their magnetic noise radiation prediction and finally to suggest efficient vibration damping solutions. The thesis is therefore divided into three major topics:

- the system-level approach; related to multi-physical modeling strategy,
- the component-level approach; related to rotor influences on assembly structural dynamics and to the laminated stator core structural dynamics,
- an original lamination stacking for vibration damping purposes.

### 7.1 Multi-physical nature of magnetic noise

Chapter 3 has introduced the typical system-level results of magnetic noise radiation from testing and modeling points of view. In general accelerating or decelerating machines are tested such that one would need to carry out run-up or coast down simulations. However practically the involved transient simulations in such modeling strategies require large computational resources. Therefore it has been proposed in this work to fragment an accelerating transient event into a discrete set of steady-state operations that each correspond to a load and rotational speed. Two different modeling strategies were employed: a detailed multi-physical model that contains only FE simulations for all physical domains (electromagnetic, structural and acoustic), and an analytical model

that simplifies the vibro-acoustic modeling part. In both cases, the stator core was assumed to be the major contributor to the structural dynamics of the machine.

Both FE and analytical models give similar acceleration and acoustic pressure results with the predominance of  $A(2, 0)$  mode resonance effect. It is important to mention that the significantly lower computational resource demand from the analytical model compared to the FE models led its integration into the multi-physic vehicle system-level virtual platform of the ADEPT project. Nonetheless there is a non-negligible discrepancy on the resonance amplitude along every operation point when one compares the simulated results with the experimental measurements. In fact this is entirely due to the assumption of steady-state operation that only include order frequencies (with zero components elsewhere). On the contrary transient phenomena incorporate extra harmonics to the force profile which are then more subject to mode excitation. Consequently the limitations of the multiple steady-state approach motivate further work that is presented in the upcoming Section 7.4.

Additionally, it has been validated that the stator core can be assumed the major contributor to the structural dynamics of an electric machine. Nevertheless it is highly suggested to predict the natural frequencies and modal damping as accurately as possible for more reliable magnetic noise prediction. In parallel, a low-frequency mode is identified experimentally which is not captured with current models. These remarks have motivated thorough investigations on component-levels such as the stator core and the rotor.

## 7.2 The laminated cores structural dynamics

Chapter 4 and Chapter 5 have focused on the necessity to investigate the structural behavior of the laminated cores of an electric machine.

The rotor affects the machine's structural dynamics due to its significant mass and direct link to the output shaft. It possibly disturbs the acoustic comfort and the operational safety. Relatively small variations of the rotor topology have been shown to affect considerably the radiated magnetic noise using a multi-physical numerical simulation process, which shows the importance of rotor design optimization for improved noise performances. Then based on numerous publications that show the occurrence of a critical (high vibration and acoustic perturbations) low frequency mode of full assemblies while not giving clear explanation of the phenomenon, it has been decided to investigate this mode occurrence, entitled RHC mode. Experiments and FEAs have identified the RHC mode as being a combination of rotor and stator bending motions,

which depends on the rotor plus shaft dynamics. The criticality of the mode resides in its capability to induce shaft vibrations leading to unsafe operation and acoustic noise similar to whirling. An original analytical beam-structure model has hence been developed to explain fundamentally its occurrence, and has been validated against experiments.

The laminated stator core is of particular interest because of its strong contribution to the vibro-acoustic behavior of a rotating electric machine, and eventually to resonance phenomena that are unpleasant to the human ear. Additionally the apparent mechanical behavior complexity brought by the hundreds of laminations that compose it introduces modeling challenges. Therefore several models of increasing complexities have been implemented going from simplified analytical **Ring** models to detailed 3D FE models using homogenized orthotropic material properties to emulate the laminated compound. By closely correlating every model with experimental sets, it has been noticed that the gap between pure radial modes  $A(n_r, 0)$  and antisymmetric modes  $B(n_r, 1)$  natural frequencies is the motivation for further model refinement. In fact the frequencies  $f_{A(n_r, 0)}$  are well estimated by analytical and 2D **Shell** models, while the frequencies  $f_{B(n_r, 1)}$  may be well estimated by 3D homogenized models; yet not both accuracies are reachable simultaneously by the state-of-the-art models. Thus two modeling options have been suggested:

**Option 1:** Find an appropriate model for both mode types. Given the incapability of the current models to estimate properly all mode types at the same time, further modeling recommendations are developed in Section 7.4.

**Option 2:** Choose a model per mode of interest. Isotropic material properties give high accuracy for pure radial mode frequencies  $f_{A(n_r, 0)}$  (supposedly the most critical in terms of acoustic radiation) and 3D homogenized FE models provide greater reliability on antisymmetric modes  $f_{B(n_r, 1)}$ . However this option 2 involves more simulation work than option 1, since two models are to be run separately to identify every mode inside the frequency range of interest.

In parallel several experimental campaigns have been carried out to identify how the laminations affect the structural dynamics. The number of laminations (see Section 5.6 for more exhaustive conclusions) certainly affects the machine mass, but the radial stiffness over cross-section mass distribution ratio stays constant as well, such that the natural frequencies of pure radial modes are unchanged from a thin steel sheet to a complete stack. Moreover in-plane shear between laminations is not activated for these modal deformations. Those two

phenomena confirm the suitability of analytical and 2D models for natural frequency estimation of pure radial modes.

Another important modal parameter that plays a significant role in the vibro-acoustic behavior of the machine is the damping. It has been shown experimentally that modal damping stands lower than 0.5% in general for pure radial modes  $A(n_r, 0)$ , whereas it is much higher for antisymmetric modes  $B(n_r, 1)$ . For the latter this higher damping is caused by the relative displacements between the laminations that activate in-plane shear and dry-friction. Furthermore a study on the effects of the stacking technology has indicated the possibility to play on these relative displacements for damping purposes by showing higher damping values for welded stator cores compared with glue-bonded cores. The remark has motivated an original passive solution to vibration damping of resonances of rotating electric machines.

### 7.3 Original lamination stacking for vibration damping purposes

Chapter 6 has investigated an original passive vibration damping solution for the laminated stator core, which leads to resonance mitigation in the acoustic spectrum as well.

For resonance mitigation, vibro-acoustic optimizations can focus on the biggest energy transfer contributor *i.e.* the laminated stator core. Passive vibration strategies for the stator core are made possible by its laminated nature. As opposed to a solid core, low in-plane shear is incorporated in-between laminations by forcing friction to happen through relative displacements between laminations. Viscous friction is ensured by glue-bonding laminations, while dry-friction is ensured via welding. The novel vibration damping idea uses both lamination attachment techniques and hypothesizes on a transversally asymmetric distribution (called skewed) of the attachment compounds (glue or weld) in order to force more relative displacements of the laminations. Three hypotheses have motivated the implementation of this technique: (1) a change in stiffness distribution, (2) an induced inter-laminar dry-friction and (3) a change in mode shapes that affects modal participation factor, thus resonance induced vibration amplitudes.

The novel method has been employed to build cylinders corresponding to the size of the studied machines so far. It has been compared with usual methods, *i.e.* common gluing and welding, by looking at the estimated modal parameters from EMA. The repeatability of the measurement procedure, the post-processing and

the sample manufacturing have been assessed through numerous experimental sets combined with statistical analyses. The results have shown that:

- For every built cylinder, pure radial modes  $A(n_r, 0)$  are the most dominant modes with the lowest damping as previously noticed, whereas antisymmetric modes  $B(n_r, 1)$  are extremely damped.
- The natural frequencies are not affected significantly by any of the attachment methods. It indicates even more that the cross-section geometry and material determines most of the stiffness allocation to pure radial modes.
- Gluing gives the worst modal damping properties, essentially because inter-laminar contact is of viscous nature, which does not promote relative displacement between laminations.
- Skew-gluing shows better damping performances for pure radial modes, especially for  $A(3, 0)$ , which is logical since the two skewed lines bring extra stiffness to more vibration nodes in the case of  $A(3, 0)$  than for  $A(2, 0)$  or  $A(4, 0)$ .
- Welding brings extra damping compared to gluing. The four welding lines are spread such that they correspond exactly to four vibration nodes of  $A(2, 0)$ , while they bring stiffness to the nodes of  $A(3, 0)$ .
- Skew-welding gives the highest damping improvements, particularly for  $A(3, 0)$ . Again the four skewed welding lines add stiffness to non-nodal points, which is translated in higher damping for  $A(3, 0)$  than for other modes.
- Glue plus skew-welding shows the limitations of gluing for damping purposes. The glue prevents dry-friction from occurring, which is the principle on which skew-welding takes its advantage.
- Hypotheses (1) and (2) are eventually not the main causes of vibration damping at resonances. Hypothesis (3) seems the best explanation to resonance amplitude reduction when using skew-welding technique.

The advantages of this technique are three-fold:

1. Keep the same cross-section geometry, such that changes on the electromagnetic properties and housing designs are not necessary. The stator core stays axially, radially and transversally symmetric.
2. Force the structure to behave non-symmetrically, such that the vibration modes are either damped or deleted. Transversally-asymmetric stiffness is introduced, while relative displacements between laminations are encouraged via dry-friction.

3. Use production techniques already implemented in chain-manufacturing, *e.g.* gluing and welding, thus making it not more expensive to realize than common techniques.

## 7.4 Future work

While this dissertation has shown how to predict and passively mitigate the acoustic noise of a rotating electric machine for traction purposes by considering component and system level contributions, many questions are raised and permit to extend the scope of this dissertation. This section presents some of these directions.

A problem to tackle concerns how a run-up is simulated. A multiple steady-states approach does not bring enough precision to the vibro-acoustic behavior of a machine, while a complete multi-physical transient analysis is computationally too expensive. An original idea that has been partially implemented by one of the Master students I supervised (Egi Nazera), is a two-step approach. A look-up table is built from numerous FE simulations and collects radial forces depending on the rotor position and the phase currents. The transient forces are then computed based on drive-cycle (*e.g.* run-up) requirements, and injected in a common vibro-acoustic model. This work was not in the scope of this dissertation but was performed in parallel. The look-up table approach has great modeling potential but still requires implementation improvements.

In this dissertation, it has been shown that the current linear models estimate well the pure radial modes  $A(n_r, 0)$  responsible for resonance phenomena and that two modeling options are suitable for the laminated core structural dynamics. Yet the temperature, which may reach high values in the machine environment, might have non-negligible effects on the modal parameters that justifies investigations in the future. Beside the accurate prediction of the mode shapes and natural frequencies, the modal damping is mostly empirically determined. Chapter 5 and Chapter 6 have identified modal damping values trend which is possibly predictable using inter-laminar friction models.

Additionally it would be valuable to integrate the identified RHC mode of the assembly to the multi-physical modeling process. Connecting a rotor to the stator component in FE models or using the developed analytical model of Chapter 4 as modal analysis, extra input to the analytical models would allow having better correlation at low frequencies.

Several ideas concern the original passive noise mitigation of Chapter 6. It has been confirmed that the developed lamination stacking improves damping

properties of a stator core and experiments have shown the importance of choosing the welding patterns for maximized damping of critical modes. Hence, depending on the electric machine configuration and its exciting force generation, optimized welding patterns can be defined in order to target optimum damping of the most excited modes. On the practical side, it is suggested to ameliorate the construction of the novel stacked cores by using advanced manufacturing (welding) available in industry. Finally after optimizing the welding patterns and having a more consistent manufacturing, it is encouraged to apply the method to an electric machine prototype and investigate on the sound quality improvements.





# Appendix A

## Cylindrical symmetries formulation

The symmetries for cylindrical components are defined in their symbolic mathematical formulation in Table A.1 for object parameter  $\Upsilon$  that can represent the object geometry, stiffness or modal displacement deformations.

Table A.1: Symmetry definitions of global parameter  $\Upsilon, \forall(r, \theta, z)$ , N/A - Not Applicable

Direction	Symmetric	Asymmetric	Anti-symmetric
Axial	$\Upsilon(r, \theta, z) = \Upsilon(r, z)$	$\exists(\theta_0, \theta_1) / \Upsilon(r, \theta_0, z) \neq \Upsilon(r, \theta_1, z)$	N/A
Radial	$\exists k \in \mathbb{N} \setminus \{0, 1\}, \Upsilon(r, \theta, z) = \Upsilon(r, \theta + 2\pi/k, z)$	$\forall k \in \mathbb{N} \setminus \{0, 1\}, \Upsilon(r, \theta, z) \neq \Upsilon(r, \theta + 2\pi/k, z)$	N/A
Transversal	$\Upsilon(r, \theta, z) = \Upsilon(r, \theta, -z)$	$\Upsilon(r, \theta, z) \neq \Upsilon(r, \theta, -z)$	$\Upsilon(r, \theta, z) = -\Upsilon(r, \theta, -z)$

The *axial symmetry* represents the symmetry around the z axis, and relates to the independence of the object parameter of azimuthal direction  $\theta$ . Therefore the  $C(0, 0)$  mode is considered axially symmetric (Fig. A.1) while  $A(2, 0)$  is axially asymmetric (Fig. A.2) because the mode deformation depends on the azimuthal location  $\theta$ .

The *radial symmetry* represents the condition of having the object parameter  $\theta$ -periodic. Thus the mode  $A(2, 0)$  is radially symmetric because half of its deformation pattern is repeated twice for the full mode shape composition; see Fig A.3. But the mode  $B(1, 1)$  is radially asymmetric because no pattern can be repeated such that the complete mode shape is reconstructed; see Fig A.4.

The (perpendicular) *transversal symmetry* is the symmetry related to the middle

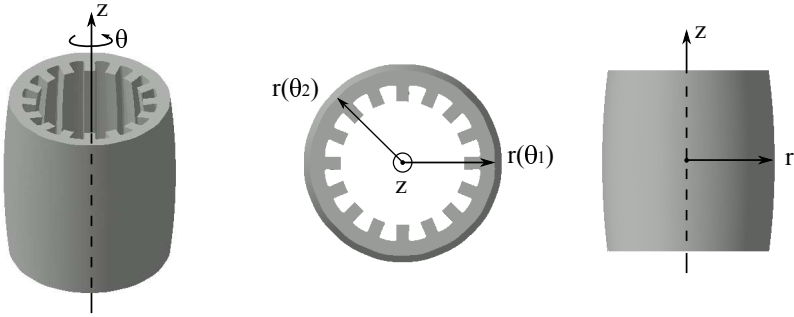


Figure A.1: Representation of axial symmetry; the example of  $C(0,0)$  mode deformation

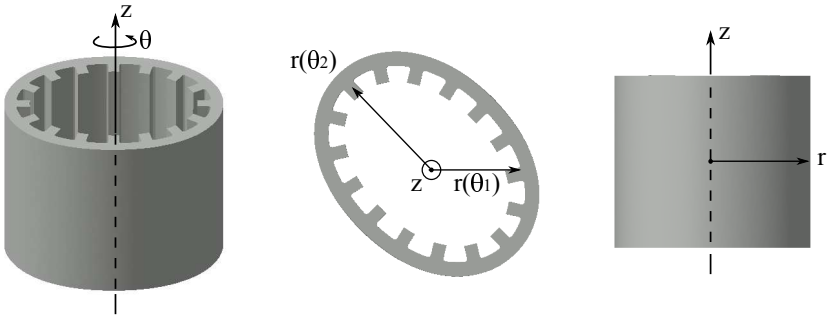


Figure A.2: Representation of axial asymmetry; the example of  $A(2,0)$  mode deformation

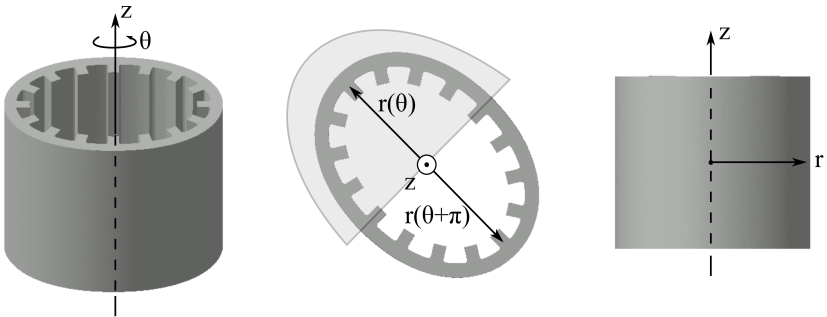


Figure A.3: Representation of radial symmetry; the example of  $A(2,0)$  mode deformation

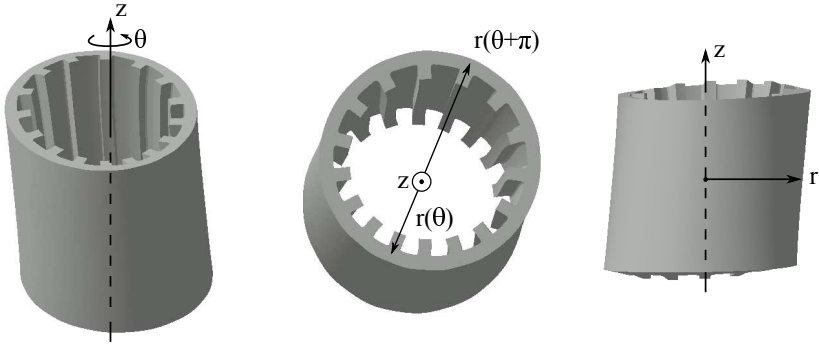


Figure A.4: Representation of radial asymmetry; the example of  $B(1, 1)$  mode deformation

plane parallel to the cross-section of the stator core. As such the mode  $A(2, 0)$  is transversally symmetric because any mode displacement is exactly mirrored in confront with the transverse plane as shown in Fig. A.5. On the contrary mode  $B(2, 3)$  is transversally asymmetric since the modal displacement amplitude is not mirrored against the transverse plane as shown in Fig. A.6. However it can be categorized in the transversal anti-symmetric modes such as mode  $B(2, 1)$ . The anti-symmetry refers to opposite displacement amplitudes for two points located at the same distance  $z$  from the transverse plane. In Fig. A.7, anti-symmetry is pictured by radial displacement equality:  $|r(z_1) - r_{median}| = |r(-z_1) - r_{median}|$ .

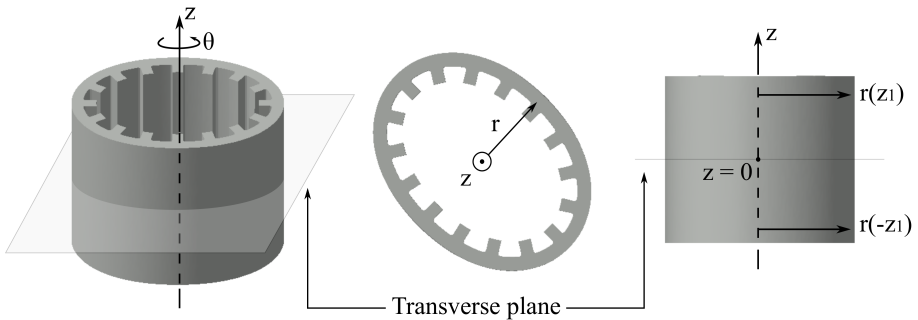


Figure A.5: Representation of transversal symmetry; the example of  $A(2, 0)$  mode deformation

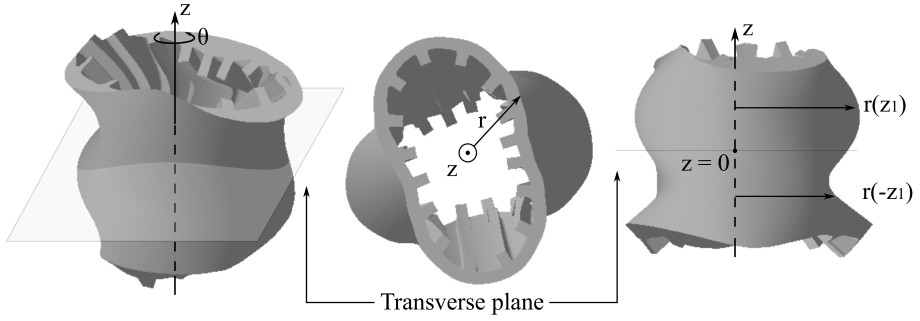


Figure A.6: Representation of transversal asymmetry; the example of  $B(2,3)$  mode deformation

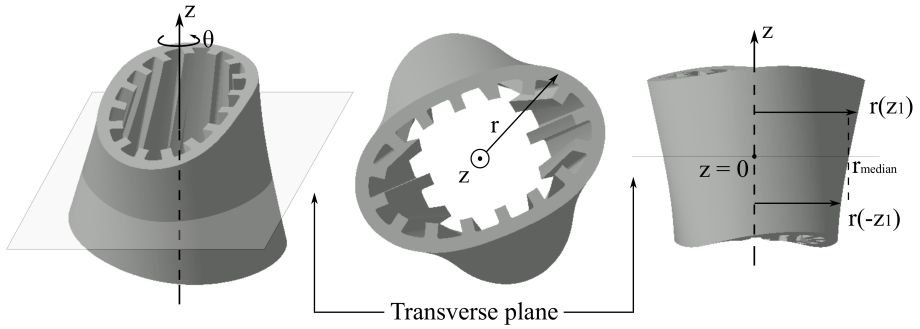


Figure A.7: Representation of transversal antisymmetry; the example of  $B(2,1)$  mode deformation

## Appendix B

# Steady-state versus Transient responses

This annex explains why a resonance is not necessarily excited at every operating speed of a rotating machine when multiple steady-states are computed in comparison with experimental results that take transient run-up into the signal post-processing. Two transient phenomena are responsible for this discrepancy: the transient excitation and the transient response.

The transient state defines a system whose state variables still vary with time. Ultimately the state variables tend to be constant over time, we talk of the system steady-state. In the case of vibrations, the vibration displacement expresses the state variable. Let us take the example of a SDOF system with a natural frequency  $\omega_n/2\pi = 350$  Hz. Subjected to a harmonic force excitation at 400 Hz and the instant  $t = 0$  s, its forced vibration displacement response is derived and pictured in Fig. B.1 (a). A transient state is defined at the beginning of the signal up to 0.3 second where the excited resonance vanishes due to damping, while the steady-state may be defined starting from 0.3 second where vibrations due to resonance are damped out. For both operations, Fig. B.1 (b) gives the frequency spectrum of the response for both states, calculated by FFT.

Clearly the steady-state operation does not contain the resonance frequency in its frequency response. But the transient operation contains both the resonance phenomenon and the excitation frequency. From this set of simple simulations, it is clear that a steady-state operation that involves steady-state input signal (force excitation) only can excite a resonance mode if the excitation frequencies

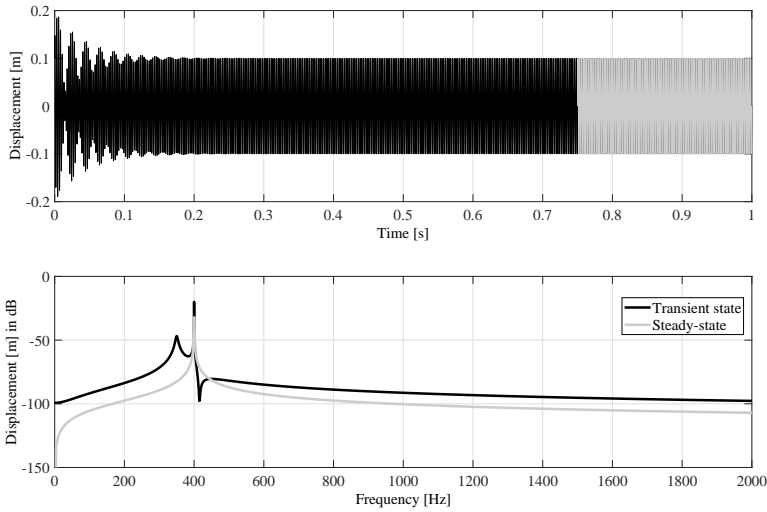


Figure B.1: Transient and steady-state responses of a SDOF system in time (a) and frequency (b) domain

(fundamental and harmonics) match the resonance frequency.

In order to get even closer to the application to rotating machines and to show the response difference between transient and multiple steady-states input signals, a stepped-sine sweep and a linear sweep input force signal is applied to the SDOF system. The stepped-sine sweep reflects the multiple steady-state analysis of Section 3.1 and is a sine-sweep signal with frequency increments of 100 Hz from 0 Hz to 1 kHz. The linear sine-sweep also goes from 0 to 1 kHz but linearly as pictured Fig. B.2 (a). The frequency content of such signals is displayed in Fig. B.2 (b) and the response of the SDOF to these excitations is given in Fig. B.2 (c).

The frequency spectrum of the transient-like signal represented by the linear sine-sweep shows an even distribution of input energy while the stepped-sine sweep spectrum shows higher amplitudes for the frequencies that build the steps. As a consequence the forced response shows higher vibration displacement amplitude at the resonance frequency of 350 Hz.

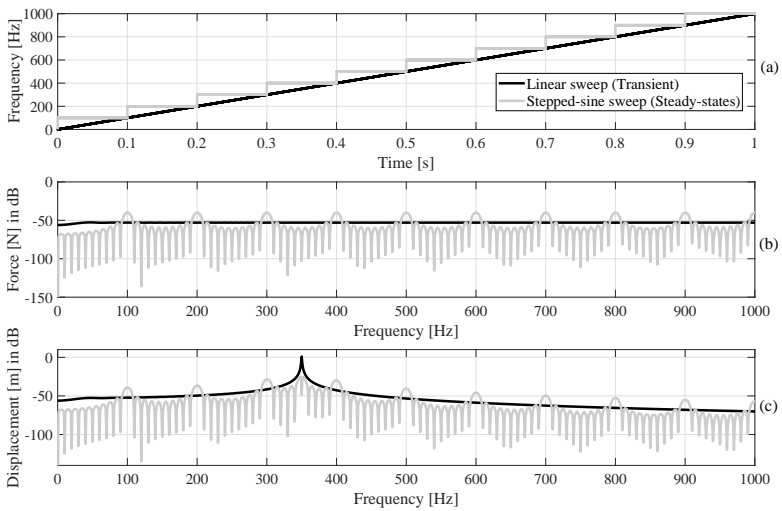


Figure B.2: Excitation frequency versus time (a), its frequency spectrum (b) and the response (c) of the SDOF system to linear sweep and stepped-sine sweep excitations





# Bibliography

- [1] MD/MSC Nastran manual - Quick reference guide, 2010.
- [2] Rule of thumb for calculating stacking factor as a function of lamination thickness, emetor website, 2012.
- [3] Virtual.Lab Help Documentation, 2015.
- [4] Siemens plm community website: <https://community.plm.automation.siemens.com/>, 2016.
- [5] Siemens plm community website: What is an order? [https://community.plm.automation.siemens.com/t5/tkb/articleprintpage/tkb-id/Simcenter\\_Test\\_tkb/article-id/25](https://community.plm.automation.siemens.com/t5/tkb/articleprintpage/tkb-id/Simcenter_Test_tkb/article-id/25), 2016.
- [6] Infolytica website <https://www.infolytica.com/en/applications/ex0185/>, 2017.
- [7] LMS Qsources - Structural and acoustic exciters, 2017.
- [8] Siemens global website: <https://www.siemens.com/press/en/feature/2016/corporate/2016-04-electric-flight.php>, 2017.
- [9] Electrical academia website: <http://electricalacademia.com/>, 2018.
- [10] ADHIKARI, S. *Damping models for structural vibration*. PhD thesis, University of Cambridge, 2001.
- [11] ATKINS, P. W. *Physical Chemistry*. 5th ed. New York: W.H. Freeman and Company, 1994.
- [12] AZIZI, H., AND VAHEDI, A. Rotor geometry parameter optimization of synchronous reluctance motor using Taguchi Method. *Przegląd Elektrotechniczny 1* (2013), 197–201.

- [13] BARTALOTTA, A. On the influence of the rotor dynamics on the vibro-acoustic response of electric machines. Master's thesis, Politecnico di Torino, Torino, 2016.
- [14] BASSETT, T. W., TATE, S., AND MAUNDER, M. Study of high frequency noise from electric machines in hybrid and electric vehicles. In *INTER-NOISE and NOISE-CON Congress and Conference Proceedings* (2014), vol. 249, Institute of Noise Control Engineering, pp. 3909–3918.
- [15] BEGIS, D., BESTAGNO, A., DUVAUT, G., HASSIM, A., AND NUC, M. A new method of computing global elastic moduli for composite materials. Tech. Rep. RR-0195, 1983.
- [16] BEGIS, D., DUVAUT, G., AND HASSIM, A. Homogénéisation par éléments finis des modules de comportements élastiques de matériaux composites. Tech. Rep. RR-0101, 1981.
- [17] BELKHAYAT, D., ROGER, D., AND BRUDNY, J. F. Active reduction of magnetic noise in asynchronous machine controlled by stator current harmonics. In *Eighth International Conference on Electrical Machines and Drives (Conf. Publ. No. 444)* (Sep 1997), pp. 400–405.
- [18] BELMANS, R., AND HAMEYER, K. Impact of inverter supply and numerical calculation techniques in audible noise problems. In *Proceedings of International seminar on Vibrations and acoustic noise of electric machinery* (Bethune, France, 1998), pp. 9–23.
- [19] BOESING, M., HOFMANN, A., AND DONCKER, R. D. Universal acoustic modelling framework for electrical drives. *IET Power Electronics* 8, 5 (2015), 693–699.
- [20] BOLDEA, I., TUTELEA, L. N., PARSA, L., AND DORRELL, D. Automotive Electric Propulsion Systems With Reduced or No Permanent Magnets: An Overview. *IEEE Transactions on Industrial Electronics* 61, 10 (Oct. 2014), 5696–5711.
- [21] BOWEN, D. Use of Principal Components Analysis in establishing correlations between sound quality metrics and jury ratings of product sound. In *INTER-NOISE and NOISE-CON Congress and Conference Proceedings* (2008), vol. 2008, Institute of Noise Control Engineering, pp. 80–86.
- [22] CAI, W., AND PILLAY, P. Resonant frequencies and mode shapes of switched reluctance motors. *Energy Conversion, IEEE Transactions on* 16, 1 (2001), 43–48.

- [23] CAI, W., PILLAY, P., AND ONEKANDA, A. Analytical formulae for calculating srm modal frequencies for reduced vibration and acoustic noise design. In *IEMDC 2001. IEEE International Electric Machines and Drives Conference (Cat. No.01EX485)* (2001), pp. 203–207.
- [24] CHAN, C. C., AND CHENG, M. *Vehicle Traction Motors vehicle traction motors*. Springer New York, New York, NY, 2013, pp. 1103–1132.
- [25] CHAU, K., AND LI, W. Overview of electric machines for EVs and HEVs. *International Journal of Vehicle Design* (2014).
- [26] CHAU, K., SUN, Q., FAN, Y., AND CHENG, M. Torque Ripple Minimization of Doubly Salient Permanent-Magnet Motors. *IEEE Transactions on Energy Conversion* 20, 2 (June 2005), 352–358.
- [27] CHAUVICOURT, F., ORLANDO, S., DESMET, W., GYSELINCK, J., VAN DER AUWERAER, H., AND FARIA, C. Experimental and numerical validation of laminated structure dynamics from a SRM stator. In *International Conference on Structural Engineering Dynamics (ICEDyn)* (Lagos, Portugal, 2015).
- [28] CHAUVICOURT, F., ORLANDO, S., DESMET, W., GYSELINCK, J. J. C., AND FARIA, C. T. Experimental Study on the Impact of the Number of Laminas on the Dynamics Behavior of an Electric Machine Stator. In *Topics in Modal Analysis & Testing, Volume 10*. Springer, 2016, pp. 73–79.
- [29] CHEN, X., YUAN, S., AND PENG, Z. Nonlinear vibration for pmsm used in hev considering mechanical and magnetic coupling effects. *Nonlinear Dynamics* (2015).
- [30] CHITROJU, R. *Improved performance characteristics of induction machines with non-skewed asymmetrical rotor slots*. PhD thesis, KTH, 2009.
- [31] CROLLA, D. *Encyclopedia of Automotive Engineering*. No. vol. 3. Wiley, 2015.
- [32] CROW, A. Stator and rotor laminations from prototype to volume production. In *UKMAG seminar Advances in Machine Manufacture* (Newcastle University, 2013).
- [33] DALCALI, A., AND AKBABA, M. Comparison of 2d and 3d magnetic field analysis of single-phase shaded pole induction motors. *Engineering Science and Technology, an International Journal* (June 2015).
- [34] DEN HARTOG, J. *Mechanical Vibrations*, 4th ed. Dover Publications Inc, 1985.

- [35] DESMET, W., AND MEYERS, J. Numerical Modelling in Mechanical Engineering Part II: The finite element method. Katholieke Universiteit Leuven course [https://onderwijsaanbod.kuleuven.be/syllabi/e/H04U3AE.htm#activetab=doelstellingen\\_idp1430784](https://onderwijsaanbod.kuleuven.be/syllabi/e/H04U3AE.htm#activetab=doelstellingen_idp1430784) (2017).
- [36] DEVILLERS, E., HECQUET, M., LE BESNERAIS, J., AND RÄ©GNIEZ, M. Tangential effects on magnetic vibrations and acoustic noise of induction machines using subdomain method and electromagnetic vibration synthesis. In *Electric Machines and Drives Conference (IEMDC), 2017 IEEE International* (2017), IEEE, pp. 1–8.
- [37] DIAS, M. The effect of the clamping force on the dynamic behavior of a stator core. In *Proceedings of the 17th International Modal Analysis Conference* (1999), pp. 201–207.
- [38] DIJK, M., ORSATO, R. J., AND KEMP, R. The emergence of an electric mobility trajectory. *Energy Policy* 52, Supplement C (2013), 135 – 145. Special Section: Transition Pathways to a Low Carbon Economy.
- [39] DONAVAN, P. R., AND SCHUMACHER, R. *Exterior Noise of Vehicles—Traffic Noise Prediction and Control*. John Wiley & Sons, Inc., 2008, pp. 1427–1437.
- [40] DONG, J., JIANG, J. W., HOWEY, B., LI, H., BILGIN, B., CALLEGARO, A. D., AND EMADI, A. Hybrid Acoustic Noise Analysis Approach of Conventional and Mutually Coupled Switched Reluctance Motors. *IEEE Transactions on Energy Conversion* 32, 3 (Sept. 2017), 1042–1051.
- [41] DOS SANTOS, F. L. M., ANTHONIS, J., NACLERIO, F., GYSELINCK, J. J. C., VAN DER AUWERAER, H., AND GOES, L. C. S. Multiphysics NVH Modeling: Simulation of a Switched Reluctance Motor for an Electric Vehicle. *IEEE Transactions on Industrial Electronics* 61, 1 (Jan. 2014), 469–476.
- [42] DUPONT, J.-B., AND BOUVET, P. Multiphysics Modelling to Simulate the Noise of an Automotive Electric Motor. Tech. rep., SAE Technical Paper, 2012.
- [43] DZIECHCIARZ, A., AND MARTIS, C. New shape of rotor flux barriers in SynRMs based on Zhukovski curves.pdf. In *The 9th International Symposium on Advanced Topics in Electrical Engineering* (Bucharest, Romania, May 2015), IEEE.
- [44] ELSEA, P. Hearing and perception - <http://artsites.ucsc.edu/>.

- [45] FIEDLER, J. O., KASPER, K. A., AND DE DONCKER, R. W. Calculation of the Acoustic Noise Spectrum of SRM Using Modal Superposition. *IEEE Transactions on Industrial Electronics* 57, 9 (Sept. 2010), 2939–2945.
- [46] FULTON, D., AND TETELA, P. Liquid cooling system of an electric machine, Sept. 18 2008. US Patent App. 12/048,327.
- [47] FYFE, K. R., AND MUNCK, E. D. S. Analysis of computed order tracking. *Mechanical Systems and Signal Processing* 11, 2 (1997), 187–205.
- [48] GAN, C., WU, J., SHEN, M., YANG, S., HU, Y., AND CAO, W. Investigation of Skewing Effects on the Vibration Reduction of Three-Phase Switched Reluctance Motors. *IEEE Transactions on Magnetics* 51, 9 (Sept. 2015), 1–9.
- [49] GÉRARD, F., TOURNOUR, M., EL MASRI, N., CREMERS, L., FELICE, M., AND SELMANE, A. Numerical modeling of engine noise radiation through the use of acoustic transfer vectors—a case study. Tech. rep., SAE Technical Paper, 2001.
- [50] GIERAS, J. F., WANG, C., AND LAI, J. C. *Noise of polyphase electric motors*. No. 129 in Electrical and computer engineering. CRC/Taylor & Francis, Boca Raton, Fla., 2006.
- [51] GIRGIS, R. S., AND VERMA, S. P. Method for accurate determination of resonant frequencies and vibration behaviour of stators of electrical machines. *Electric Power Applications, IEE Proceedings B* 128, 1 (1981), 1.
- [52] GLOGER, B. *Self Adaptive Evolutionary Algorithms*. Fachbereich: Universitat Paderborn, 2004.
- [53] GRIFFITHS, D. J. *Introduction to Electrodynamics*. Benjamin Cummings Inc., 2008.
- [54] GROCHENIG, K. *The Short-Time Fourier Transform*. In: *Foundations of Time-Frequency Analysis*, 1 ed. Birkhäuser, Boston, MA, 2001.
- [55] GUILLAUME, P., VERBOVEN, P., AND VANLANDUIT, S. Frequency-domain maximum likelihood identification of modal parameters with confidence intervals. In *Proceedings of the international seminar on modal analysis* (1998), vol. 1, Katholieke Universiteit Leuven, pp. 359–366.
- [56] HENDERSHOT, J. R. Causes & Sources of audible noise in electric motors. In *22nd Incremental Motion Control Systems and Devices Symposium* (Champaign IL, 1993), B.C. Kuo Ed., pp. 259–270.

- [57] HENDERSHOT, J. R., AND MILLER, T. J. E. *Design of brushless permanent-magnet motors / J.R. Hendershot, Jr., T.J.E. Miller*. Magna Physics Pub. ; Clarendon Press Hillsboro, OH : Oxford, 1994.
- [58] HEYLEN, W., LAMMENS, S., AND SAS, P. *Modal analysis theory and testing*, 2 ed. Katholieke Universiteit Leuven, Faculty of Engineering, Department of Mechanical Engineering, Division of Production Engineering, Machine Design and Automation, 1997.
- [59] HIRSCHBERGER, C., RICKER, S., STEINMANN, P., AND SUKUMAR, N. Computational multiscale modelling of heterogeneous material layers. *Engineering Fracture Mechanics* 76, 6 (Apr. 2009), 793–812.
- [60] HONG, J.-P., HA, K.-H., AND LEE, J. Stator pole and yoke design for vibration reduction of switched reluctance motor. *IEEE Transactions on Magnetics* 38, 2 (2002), 929–932.
- [61] HUBERT, A. *Contribution à l'étude des bruits acoustiques générés lors de l'association machines électriques - convertisseurs statiques de puissances - application a la machine asynchrone*. PhD thesis, Université de Technologie de Compiègne, Compiègne, Dec. 2000.
- [62] INMAN, D. J. *Engineering Vibration*, fourth ed. Pearson Education, Inc., 2014.
- [63] JIAN LI, XUEGUAN SONG, AND YUNHYUN CHO. Comparison of 12/8 and 6/4 Switched Reluctance Motor: Noise and Vibration Aspects. *IEEE Transactions on Magnetics* 44, 11 (Nov. 2008), 4131–4134.
- [64] JONG-BIN IM, WONHO KIM, KWANGSOO KIM, CHANG-SUNG JIN, JAE-HAK CHOI, AND JU LEE. Inductance Calculation Method of Synchronous Reluctance Motor Including Iron Loss and Cross Magnetic Saturation. *IEEE Transactions on Magnetics* 45, 6 (June 2009), 2803–2806.
- [65] KIM, K.-S., JUNG, Y.-G., AND LIM, Y.-C. Shaping the spectra of the acoustic noise emitted by three-phase inverter drives based on the new hybrid random PWM technique. In *37th IEEE Power Electronics Specialists Conference* (2006), pp. 1–6.
- [66] KIM, S., CHOI, J.-H., AND LEE, J. Magnet shape optimization for high performance single-phase line start synchronous motor. *Journal of Applied Physics* 93, 10 (2003), 8695–8697.
- [67] KIRKUP, S. *The boundary element method in acoustics: a development in Fortran*. No. 1 in Integral equation methods in engineering. Integrated Sound Software, Hebden Bridge, 1998. OCLC: 833422597.

- [68] KNIGHT, A. University of calgary website <http://people.ucalgary.ca>.
- [69] KOLEHMAINEN, J. Synchronous Reluctance Motor With Form Blocked Rotor. *IEEE Transactions on Energy Conversion* 25, 2 (June 2010), 450–456.
- [70] KRISHNAN, R., AND VIJAYRAGHAVAN, P. State of the art: acoustic noise in switched reluctance motor drives. In *Industrial Electronics Society, 1998. IECON'98. Proceedings of the 24th Annual Conference of the IEEE* (1998), vol. 2, IEEE, pp. 929–934.
- [71] LANDIN, D., JOHNSON, G., MCCUTCHEON, J., AND HILDERBRAND, L. Internally damped stator, rotor, and transformer and a method of making, Dec. 31 2002. US Patent 6,499,209.
- [72] LANFRANCHI, V. *Optimisation de la commande en vitesse variable des machines asynchrones, conception d'une methode de filtrage actif optimise*. PhD thesis, 2000. Thèse de doctorat dirigée par Goedel, Clément Sciences et techniques Reims 2000.
- [73] LASKARIS, K. I., AND KLADAS, A. G. Permanent magnet shape optimization for high efficiency electric traction motors. In *Electromagnetic Field Computation (CEFC), 2010 14th Biennial IEEE Conference on* (2010), IEEE, pp. 1–1.
- [74] LE BESNERAIS, J. *Réduction du bruit audible d'origine magnétique dans les machines asynchrones alimentées par MLI - règles de conception silencieuse et optimisation multi-objectif*. PhD thesis, Ecole Centrale de Lille, 2008.
- [75] LEE, C. *Vibration Analysis of Rotors*. Solid Mechanics and Its Applications. Springer Netherlands, 1993.
- [76] LIN, F., ZUO, S., DENG, W., AND WU, S. Noise Prediction and Sound Quality Analysis of Variable-Speed Permanent Magnet Synchronous Motor. *IEEE Transactions on Energy Conversion* 32, 2 (June 2017), 698–706.
- [77] LONG, S. A., ZHU, Z. Q., AND HOWE, D. Vibration behaviour of stators of switched reluctance motors. *IEE Proceedings - Electric Power Applications* 148, 3 (May 2001), 257–264.
- [78] LUCHSCHEIDER, V., WILLNER, K., AND MAIDORN, M. Computation of the Effective Lamination Stack's Behavior Considering the Contact Simulation with a Multi-Scale Homogenization. In *Proceedings of the 11th World Congress on Computational Mechanics* (Barcelona, Spain, July 2014).

- [79] LUCHSCHEIDER, V., WILLNER, K., AND MAIDORN, M. A material model for lamination stacks based on rough contacts. In *Electric Drives Production Conference (EDPC), 2014 4th International* (2014), IEEE, pp. 1–6.
- [80] LUCIANO, R., AND BARBERO, E. J. Formulas for the stiffness of composites with periodic microstructure. *International Journal of Solids and Structures* 31, 21 (1994), 2933–2944.
- [81] MAIR, M., WEILHARTER, B., RAINER, S., ELLERMANN, K., AND BÍRÓ, O. Numerical and experimental investigation of the structural characteristics of stator core stacks. *COMPEL - The international journal for computation and mathematics in electrical and electronic engineering* 32, 5 (Sept. 2013), 1643–1664.
- [82] MALITI, K. *Modelling and analysis of magnetic noise in squirrel-cage induction motors*. PhD thesis, Kungl Tekniska Högskolan, Stockholm, 2000.
- [83] MARBJERG, G. Noise from electric vehicles - A literature survey (COMPETT project), 2013.
- [84] MILLITHALER, P. *Dynamic behaviour of electric machine stators*. PhD thesis, Université de Franche-Comté, 2015.
- [85] MILLITHALER, P., SADOULET-REBOUL, E., OUISE, M., DUPONT, J. B., AND BOUHADDI, N. Identification of Equivalent Anisotropic Material Properties of 3d-Heterogeneous Structures. *interface 105* (2015), 108.
- [86] MILLITHALER, P., SADOULET-REBOUL, E., OUISE, M., DUPONT, J.-B., AND BOUHADDI, N. Structural dynamics of electric machine stators: Modelling guidelines and identification of three-dimensional equivalent material properties for multi-layered orthotropic laminates. *Journal of Sound and Vibration* (Mar. 2015).
- [87] MININGER, X. *Réduction des vibrations des machines à réductance variable à l'aide d'actionneurs piézoélectriques*. PhD thesis, 2005. Thèse de doctorat dirigée par Gabsi, Mohamed Khémis Électronique, électrotechnique et automatique Cachan, Ecole normale supérieure 2005.
- [88] MOGHADDAM, R. *Synchronous Reluctance Machine in Variable Speed Drives (VSD) Applications*. PhD thesis, Stockholm, 2011.
- [89] MOLLET, Y. *Fault-tolerance and noise and vibration aspects of electrical drives*. PhD thesis, ULB, Bruxelles, 2017.



- [90] MOSQUERA-SANCHEZ, J., VILLALBA, J., JANSSENS, K., AND DE OLIVEIRA, L. A multi-objective sound quality optimization of electric motor noise in hybrid electric vehicles. In *ISMA* (Leuven, Belgium, 2014).
- [91] MYRRIA, G., CHAUVICOURT, F., AND FARIA, C. Evaluation of the influence of the control strategy of the electric vehicles motor on its radiated noise using 1d simulation. In *European Acoustic Conference - EuroRegio* (June 2016).
- [92] NAYEB HASHEMI, N., AND LISNER, R. *A new strategy for active control of acoustic noise in converter-fed induction motors*. Monash University Press, 2002, pp. 1 – 6.
- [93] NAZERAJ, E. Detailed vibro-acoustic analysis of a reluctance machine. Master's thesis, Université Libre de Bruxelles, Bruxelles, 2015.
- [94] NELSON, F. C. Rotor Dynamics without Equations. 9.
- [95] NEUENSCHWANDER, T. Lamination stack with center interlock, Jan. 10 2006. US Patent 6,984,913.
- [96] NYBERG, C. Understanding factors that cause shaft failures. *Pumps and Systems magazine*, available at <http://www.peerlessænet.com/documents/408.pdf> (2007).
- [97] OFFERMANN, P., AND HAMEYER, K. Analysis of Finite Element mesh discretization for faster and more accurate probabilistic simulations: applied to cogging torque calculations in electrical machines. In *XVI International Symposium on Electromagnetic Fields in Mechatronics, Electrical and Electronic Engineering* (2013), p. 6.
- [98] OPREA, C., DZIECHCIARZ, A., AND MARTIS, C. Comparative analysis of different synchronous reluctance motor topologies. In *15th IEEE International Conference on Environment and Electrical Engineering (EEEIC)* (2015), pp. 1904–1909.
- [99] PARK, J.-M., PARK, S.-J., LEE, M.-M., CHUN, J.-S., AND LEE, J.-H. Rotor Design on Torque Ripple Reduction for a Synchronous Reluctance Motor with Concentrated Winding using Response Surface Methodology. In *12th Biennial IEEE Conference on Electromagnetic Field Computation* (2006), pp. 424–424.
- [100] PEETERS, B., VAN DER AUWERAER, H., GUILLAUME, P., AND LEURIDAN, J. The PolyMAX frequency-domain method: a new standard for modal parameter estimation? *Shock and Vibration* 11, 3-4 (2004), 395–409.

- [101] PIRNAT, M., ČEPON, G., AND BOLTEŽAR, M. Introduction of the linear contact model in the dynamic model of laminated structure dynamics: An experimental and numerical identification. *Mechanism and Machine Theory* 64 (June 2013), 144–154.
- [102] POISSON, S. *Second mémoire sur la théorie du magnétisme*. Imprimerie royale, 1825.
- [103] PYRHONEN, J., JOKINEN, T., AND HRABOVCOVA, V. *Design of Rotating Electrical Machines*. Wiley, 2013.
- [104] RAO, S. S. *Vibration of continuous systems*. Wiley, Hoboken, NJ, 2007.
- [105] RATAZZI, A. R., BAMBILL, D. V., AND ROSSIT, C. A. Free Vibrations of Beam System Structures with Elastic Boundary Conditions and an Internal Elastic Hinge. *Chinese Journal of Engineering* 2013 (2013), 1–10.
- [106] REDDY, J. *Mechanics of Laminated Composite Plates and Shells, Theory and Analysis*, 2nd ed. CRC Press, 2004.
- [107] SADOWSKI, N., LEFEVRE, Y., LAJOIE-MAZENC, M., AND CROS, J. Finite element torque calculation in electrical machines while considering the movement. *IEEE Transactions on Magnetics* 28, 2 (Mar. 1992), 1410–1413.
- [108] SARRAZIN, M., ANTHONIS, J., VAN DER AUWERAER, H., MARTIS, C., AND GYSELINCK, J. Signature analysis of switched reluctance and permanent magnet electric vehicle drives. In *Electrical Machines (ICEM), 2014 International Conference on* (2014), IEEE, pp. 1831–1837.
- [109] SCHLENSOK, C., VAN DER GIET, M., HERRANZ GRACIA, M., VAN RIESEN, D., AND HAMEYER, K. Structure-Dynamic Analysis of an Induction Machine Depending on Stator – Housing Coupling. *IEEE Transactions on Industry Applications* 44, 3 (2008), 753–759.
- [110] SCHWARZER, M., ZIMMERLING, C., BARTI, E., DANNEMANN, M., BOCHYNEK, R., AND BEIN, T. Analytical Prediction of the Effective Dynamic behaviour and the Damping Characteristics of Laminated Steel Stacks as used in Electric Machines.
- [111] SHEN, C., TSUEI, Y., ALLEMANG, R., AND BROWN, D. Analytical and experimental study of inextensional modes of a circular cylinder. *International Journal of Analytical and Experimental Modal Analysis* (1986).
- [112] SIEMENS. *NX Nastran - Numerical Methods User's Guide*. Siemens PLM Software Inc., 2014.

- [113] SINGAL, R., VERMA, S., AND WILLIAMS, K. Vibrations of long and short laminated stators of electrical machines, PartIII: results for short stators and validity of simplified frequency equation. *Journal of Sound and Vibration* 129(1) (1989), 31–44.
- [114] STEFANSKYI, A., DZIECHCIARZ, A., CHAUVICOURT, F., SFAKIANAKIS, G., RAMAKRISHNAN, K., NIYOMSATIAN, K., CURTI, M., DJUKIC, N., ROMANAZZI, P., AYAT, S., WIEDEMANN, S., PENG, W., STIPETIC, S., AND TAMAS, A. Researchers within the EU funded Marie Curie ITN project ADEPT, grant number 607361, 2013.
- [115] STEMMLER, H., AND EILINGER, T. Spectral analysis of the sinusoidal PWM with variable switching frequency for noise reduction in inverter-fed induction motors. In *Power Electronics Specialists Conference, PESC'94 Record., 25th Annual IEEE* (1994), vol. 1, IEEE, pp. 269–277.
- [116] SUGIURA, M., ISHIHARA, Y., ISHIKAWA, H., AND NAITOH, H. Improvement of efficiency by stepped-skewing rotor for switched reluctance motors. In *Power Electronics Conference (IPEC-Hiroshima 2014-ECCE-ASIA), 2014 International* (2014), IEEE, pp. 1135–1140.
- [117] SWANSON, E., POWELL, C. D., WEISSMAN, S., AND WASSERMAN, A. A Practical Review of Rotating Machinery Critical Speeds and Modes. *SOUND AND VIBRATION* (2005), 8.
- [118] TAKAHASHI, I., AND MOCHIKAWA, H. Optimum PWM waveforms of an inverter for decreasing acoustic noise of an induction motor. *IEEE transactions on industry applications*, 5 (1986), 828–834.
- [119] TAKIGUCHI, M., SUGIMOTO, H., KURIHARA, N., AND CHIBA, A. Acoustic Noise and Vibration Reduction of SRM by Elimination of Third Harmonic Component in Sum of Radial Forces. *IEEE Transactions on Energy Conversion* 30, 3 (Sept. 2015), 883–891.
- [120] TAN-KIM, A., HAGEN, N., LANFRANCHI, V., CLÉNET, S., COOREVITS, T., MIPO, J.-C., LEGRANGER, J., AND PALLESCHI, F. Influence of the manufacturing process of a claw-pole alternator on its stator shape and acoustic noise. In *XXIIIth International Conference on Electrical Machines (ICEM)*, (2016), IEEE, pp. 2273–2279.
- [121] TIMAR, P. *Noise and Vibration of electrical machines*, vol. 34. Elsevier, 1989.
- [122] TIMAR, P. L., AND LAI, J. C. S. Acoustic noise of electromagnetic origin in an ideal frequency-converter-driven induction motor. *IEE Proceedings-Electric Power Applications* 141, 6 (1994), 341–346.

- [123] VAN DER AUWERAER, H., AND JANSSENS, K. A source-transfer-receiver approach to nvh engineering of hybrid/electric vehicles. In *SAE Technical Paper* (2012), SAE International.
- [124] VAN DER GIET, M., AND HAMEYER, K. Identification of homogenized equivalent materials for the modal analysis of composite structures in electrical machines. In *The 9th International Conference on Vibrations in Rotating Machinery, VIRM 2008* (2008), pp. 437–448.
- [125] VAN DER GIET, M., KASPER, K., DE DONCKER, R. W., AND HAMEYER, K. Material parameters for the structural dynamic simulation of electrical machines. In *XXth International Conference on Electrical Machines (ICEM)* (2012), IEEE, pp. 2994–3000.
- [126] VEREZ, G., BARAKAT, G., AND AMARA, Y. Influence of slots and rotor poles combinations on noise and vibrations of magnetic origins inu'-core flux-switching permanent magnet machines. *Progress In Electromagnetics Research B* 61 (2014), 149–168.
- [127] VERMA, S., SINGAL, R., AND WILLIAMS, K. Vibration behaviour of stators of electrical machines, part I: Theoretical study. *Journal of Sound and Vibration* 115 (1987), 1–12.
- [128] VERMA, S. P., AND BALAN, A. Experimental investigations on the stators of electrical machines in relation to vibration and noise problems. *IEE Proceedings - Electric Power Applications* 145, 5 (Sep 1998), 455–461.
- [129] VIJAYRAGHAVAN, P., AND KRISHNAN, R. Noise in electric machines a review. *IEEE Transactions on Industry Applications* 35, 5 (Oct. 1999), 1007–1013.
- [130] VON ESTORFF, O. *Boundary elements in acoustics: advances and applications*. Advances in boundary elements series. WIT, 2000.
- [131] WALCK, C. *Handbook on statistical distributions for experimentalists*. University of Stockholm Internal Report SUF-PFY/96-01, 2007.
- [132] WANG, C., AND LAI, J. C. S. Vibration analysis of an induction motor. *Journal of sound and vibration* 224, 4 (1999), 733–756.
- [133] WANG, H., AND WILLIAMS, K. The vibrational analysis and experimental verification of a plane electrical machine stator model. *Mechanical Systems and Signal Processing* 9, 4 (1995), 429–438.
- [134] WANG, H., AND WILLIAMS, K. Vibrational modes of thick cylinders of finite length. *Journal of Sound and Vibration* 191, 5 (1996), 955–971.

- [135] WANG, H., AND WILLIAMS, K. Effects of laminations on the vibrational behaviour of electrical machine stators. *Journal of Sound and Vibration* 202, 5 (1997), 703–715.
- [136] WANG, X., STROUS, T. D., LAHAYE, D., POLINDER, H., AND FERREIRA, J. A. Effects of rotor skew on the performance of brushless doubly-fed induction machine. In *IEEE International Electric Machines & Drives Conference (IEMDC)* (2015), IEEE, pp. 260–265.
- [137] WATANABE, S., KENJO, S., IDE, K., SATO, F., AND YAMAMOTO, M. Natural frequencies and vibration behaviour of motor stators. *IEEE Transactions on Power Apparatus and Systems*, 4 (1983), 949–956.
- [138] WEGERHOFF, M., DRICHEL, P., BACK, B., SCHELENZ, R., AND JACOBS, G. Method for determination of transversely isotropic material parameters for the model of a laminated stator with windings. In *22nd International Congress on Sound and Vibration (ICSV)* (2015).
- [139] WEI CAI, PILLAY, P., AND ZHANGJUN TANG. Impact of stator windings and end-bells on resonant frequencies and mode shapes of switched reluctance motors. *IEEE Transactions on Industry Applications* 38, 4 (July 2002), 1027–1036.
- [140] WEILHARTER, B., BIRO, O., LANG, H., OFNER, G., AND RAINER, S. Validation of a Comprehensive Analytic Noise Computation Method for Induction Machines. *IEEE Transactions on Industrial Electronics* 59, 5 (May 2012), 2248–2257.
- [141] WEILHARTER, B., MAIR, M., LANG, H., ELLERMANN, K., AND BIROX, O. Experimental investigation of the vibration behaviour of a laminated stack with winding. In *Industrial Electronics Society, IECON 2013-39th Annual Conference of the IEEE* (2013), IEEE, pp. 2816–2820.
- [142] WILLIAMS, K., SINGAL, R., AND VERMA, S. Vibrations of long and short laminated stators of electrical machines PartII: Results for long stators and validity of simplified frequency equation. *Journal of Sound and Vibration* 129(1) (1989), 15–29.
- [143] XU, X., HAN, Q., AND CHU, F. Dynamic responses and vibration characteristics for an inclined rotor with unbalanced magnetic excitation. In *14th IFToMM World Congress* (2015).
- [144] YANG, H.-Y., LIM, Y.-C., AND KIM, H.-C. Acoustic Noise/Vibration Reduction of a Single-Phase SRM Using Skewed Stator and Rotor. *IEEE Transactions on Industrial Electronics* 60, 10 (Oct. 2013), 4292–4300.

- [145] YANG, S. *Low-Noise electric motors*. Oxford University Press, Oxford, 1981.
- [146] ZHANG, A., BAI, Y., YANG, B., AND LI, H. Analysis of nonlinear vibration in permanent magnet synchronous motors under unbalanced magnetic pull. *MDPI - Applied Sciences* (2018).
- [147] ZHANG, Z., LIU, H., AND SONG, T. Optimization Design and Performance Analysis of a PM Brushless Rotor Claw Pole Motor with FEM. *Machines* 4, 3 (July 2016), 15.
- [148] ZHOU, G.-Y., AND SHEN, J.-X. Rotor Notching for Electromagnetic Noise Reduction of Induction Motors. *IEEE Transactions on Industry Applications* 53, 4 (July 2017), 3361–3370.
- [149] ZHU, Z. Q., XU, L., AND HOWE, D. Influence of mounting and coupling on the natural frequencies and acoustic noise radiated by a pwm controlled induction machine. In *9th International Conference on Electrical Machines and Drives (Conf. Publ. No. 468)* (1999), pp. 164–168.
- [150] ZIENKIEWICZ, O. C., AND TAYLOR, R. L. *The finite element method. Vol. 1: The basis*, 5. ed., reprinted ed. Butterworth-Heinemann, Oxford, 2002. OCLC: 249013082.

# Curriculum Vitae

## Fabien Chauvicourt

Research Engineer & PhD candidate  
French, 27 year-old

Address: Platte Lostraat 59-101  
3010, Kessel-Lo, Belgium  
tel.: +32 (0) 483 26 90 70  
e-mail: fabien.chauvicourt@gmail.com



## EDUCATION

### Joint Ph.D. Degree in Engineering Science (Mechanical Engineering (KUL) & Electrical Engineering (ULB))

*Vibro-acoustics of rotating electric machines* June 2018  
Katholieke Universiteit Leuven, BE  
Promotor: Prof. dr. ir. Wim Desmet (wim.desmet@kuleuven.be)  
Université Libre de Bruxelles, BE  
Promotor: Prof. dr. ir. Johan Gyselinck (johan.gyselinck@ulb.ac.be)

### Master's Degree in Mechanical Engineering (engineering school)

*Specialty in Acoustic and Industrial Vibrations* February 2014  
Université de Technologie de Compiègne, FR  
Advisor: Prof. dr. ir. Jean Michel Ville (jean-michel.ville@utc.fr)

### 2-year intense technical program (Distinction of excellence)

Lycée Paul Valéry (College), Paris, FR June 2010  
Advisor: Prof. Christophe Berthault (christophebertault@free.fr)

## PROFESSIONAL EXPERIENCE

**Early Stage Researcher** May 2014 - ...  
*Siemens Industry Software NV, Leuven, BE*

This research position allows young engineers to build technical experience within a complete industrial and academic partnership that is gathered through the EU funded Marie Curie ITN project ADEPT (ADvanced Electrical Powertrain Technologies, <http://adept-itn.eu/>). Soft skills and technical trainings about multi-physic knowledge of electric powertrain technologies are organized within the consortium. The understanding and prediction of the NVH behavior of electric machines is done using novel numerical, analytical and testing solutions, bearing in mind the multi-physics aspect of the electric powertrain. Among the responsibilities, several M.Sc. students are constantly trained and supervised during the years as well.

### **Marie Curie Representative**

June 2015 - ...

*Siemens Industry Software NV, Leuven, BE*

Elected position at Siemens Industry Software NV in which one of the responsibilities is to represent the other Marie Curie fellows/students in quarterly meetings gathering every corresponding research managers/leaders.

### **Visiting Fellow**

*University of Bristol, Bristol, UK*

March 2017

Carried out power loss measurements involving thermal, impedance and calorimetric tests in order to calibrate the FE model electric and thermal parameters.

*Politecnico di Milano, Milan, IT*

May & December 2016

Improved the analytical model developed earlier and supported Polimi on the NVH predictions of specific machine topologies.

*Motor Engineer, Grenoble, FR*

February 2016

Built a standalone analytical model which permits to compute vibration and acoustic output of an electric motor from its topology and control strategy. Emphasizes was put on the machine design influence given the available knowledge in Motor Engineer.

### **Final-year study intern**

September 2013 – February 2014

*Siemens SAS, Lille, FR*

Identified and defined the signature of every noisy equipment of the future metro NeoVAL. Found and recommended some soundproofing techniques to use as solutions to a better insulation.

### **Visiting student**

August 2012 – January 2013

*Linköpings Universiteit, Linköping, SE*

Followed courses within the Erasmus program, mainly on automotive and aerospace domain. Collaborated in international team projects involving aircraft design.



**Student intern** September 2011 – February 2012  
*Accord Acoustique, Maudétour-en-Vexin, FR*

Assisted the engineers. Determined and recommended some soundproofing materials for several different application areas e.g. swimming pool, building, theater, etc... Participated in acoustic and vibratory studies and wrote reports.

## LANGUAGE SKILLS

<b>French</b>	Mother tongue
<b>English</b>	Fluent: Common European Framework Level C1, TOEIC score: 910/990 (June 2012)
<b>Italian, Dutch</b>	Common European Framework Level A1
<b>Spanish</b>	Basics

## SOFTWARE SKILLS

<b>Office</b>	Microsoft Office Package, L <sup>A</sup> T <sub>E</sub> X
<b>CAE</b>	LMS Virtual.Lab, NX, NX/MSc Nastran, JMAG Designer, Pro-Engineer
<b>Coding</b>	Matlab-Simulink, LMS AMESIM.Lab
<b>Testing</b>	LMS Test.Lab, B&K Pulse
<b>Other</b>	CadnaA, Google Sketchup, CATT-Acoustic, dBTrait, dBbâti

## PERSONAL INTERESTS

<b>Abroad experiences</b>	February 2013 – June 2013: Gap semester volunteering as a “WOOOFer” (World Wide Opportunities in Organic Farms) in 5 different families in Ireland, the UK and Belgium. Life: Tourism around the world – Finland, Russia, Estonia, Denmark, Norway, Netherlands, Belgium, UK, Italy, Switzerland, Greece, Crete, Caribbean Islands.
<b>Sports Activities</b>	Swimming, Cycling, Hiking, Basketball Amateur practice of music (Bass guitar, Guitar), Gardening, Video games
<b>Association</b>	2013: Engaged in Larsen association to improve the acoustics in music rehearsal room Compiègne, FR



# List of publications

## Articles in proceedings of international conferences

1. Chauvicourt F., Faria C., Dziechciarz A., Martis C., (2015). Influence of Rotor Geometry on NVH Behavior of Synchronous Reluctance Machine. *Proceedings of the 10th IEEE International Conference on Ecological Vehicles and Renewable Energies (EVER)*, 31 March - 2 April 2015, Monte Carlo, Monaco.
2. Faria C., Santos F., Chauvicourt F., Orlando S., (2015). Noise emissions on switched reluctance motors: evaluation of different structural models. *Electric Symposium Vehicle & Exhibition 28 (EVS)*, May 2015, South Korea.
3. Chauvicourt F., Orlando S., Desmet W., Gyselinck J.J.C., Van der Auweraer H., Faria C., (2015). Experimental and Numerical Validation of Laminated Structure Dynamics from a Switched Reluctance Machine Stator. *International Conference on Structural Engineering Dynamics (ICEDyn)*, June 2015, Lagos, Portugal.
4. Chauvicourt F., Orlando, S, Desmet W., Gyselinck J.J.C., Faria C., (2016). Experimental Study on the Impact of the Number of Laminas on the Dynamics Behavior of an Electric Machine Stator. *Proceedings of IMAC XXXIV*, January 2016, Orlando, USA.
5. Chauvicourt F., Romanazzi P., Howey D., Dziechciarz A., Martis C., Faria C., (2016). Review of the Multidisciplinary Homogenization Techniques applied to Electric Machines. *Eleventh International Conference on Ecological Vehicles and Renewable Energies (EVER)*, April 2016, Monte-Carlo, Monaco.
6. Myrria G., Chauvicourt F. and Faria C., (2016). Evaluation of the influence of the control strategy of the electric vehicle's motor on its

radiated noise using a 1D simulation. *European Acoustic Conference - EuroRegio2016*, June 2016, Porto, Portugal.

7. Chauvicourt F., Faria C., Gyselinck J.J.C., Desmet W., (2016). Validation of homogenization technique used for accurate predictions of laminated structures' mechanical behavior. *Proceedings of ISMA XXVII*, September 2016, Leuven, Belgium.
8. Myrria G., Chauvicourt F., Faria C., (2016). Fast computation of the acoustic response of electrical machines via analytical means. *Proceedings of ISMA XXVII*, September 2016, Leuven, Belgium.
9. Chauvicourt F., Ballweg M., Desmet W., Van der Auweraer H., Faria C., (2017). Experimental Study on the Rotor Dynamics Influence upon the Modal Characteristics of an Induction Machine. *Proceedings of IMAC XXXV*, January 2017, Hyatt Regency Orange County, USA.
10. Chauvicourt F., Ramakrishnan K., Faria C., Mastinu G., (2017). Analytical Multi-physics Methodology for fast Acoustic Noise Prediction of an External Rotor SPMSM. *Proceedings of IEEE International Electric Machines and Drives Conferences (IEMDC)*, May 2017, Miami, FL, USA.
11. Bervoets S., Debal P., Chauvicourt F., Faria C., Faïd S., Kok D., (2017). Cost Optimised Integrated Electric Powertrain Containing the First Silent Switched Reluctance Motor for Passenger Vehicles. *Electric Symposium Vehicle & Exhibition 30 (EVS)*, October 2017, Stuttgart, Germany.

### Articles in international refereed journals

1. Chauvicourt F., Faria C., Desmet W., Gyselinck J., (2017). Equivalent beam model for the fundamental explanation of a low frequency rotor-dependent mode shape of an electric machine assembly. *Elsevier Comptes Rendus Mécaniques*. (*Manuscript submitted for publication*)
2. Chauvicourt F., Faria C., Desmet W., Gyselinck J., (2017). Transversally-Asymmetric Stiffness of Laminated Stator Core: A solution for Noise Mitigation of Electric Machines. *IEEE Trans. On Energy Conversion*. (*Manuscript submitted for publication*)



KUL: PRODUCTION ENGINEERING, MACHINE DESIGN AND AUTOMATION (PMA) SECTION - ULB: BIO, ELECTRO AND

FACULTY OF ENGINEERING SCIENCE  
DEPARTMENT OF MECHANICAL ENGINEERING  
MECHANICAL SYSTEMS (BEAMS) DEPARTMENT  
Celestijnenlaan 300 box 2402  
B-3001 Leuven

